DEVELOPMENT OF REDUCED-ORDER MODELS AND STRATEGIES FOR FEEDBACK CONTROL OF HIGH-SPEED AXISYMMETRIC JETS

Dissertation

Presented in Partial Fulfillment of the Requirements for
the Degree Doctor of Philosophy in the
Graduate School of The Ohio State University

By

Aniruddha Sinha, B.S.

Graduate Program in Department of Mechanical Engineering

The Ohio State University

2011

Dissertation Committee:

Mo Samimy, Advisor

Andrea Serrani, Co-Advisor

Datta V. Gaitonde

Jeffrey P. Bons

Abstract

Localized arc filament plasma actuators have demonstrated significant potential in controlling high-speed and high Reynolds number jets in open-loop. The two primary goals of jet control are either noise reduction or bulk mixing enhancement. This research develops the tools for implementing feedback for this flow control system. The particular jet considered is a Mach 0.9 axisymmetric configuration with Reynolds number 6.7×10^5.

The jet near-field pressure is well-suited for real-time non-intrusive observation of the flow state. Its response to forcing is similar to that of the far acoustic field. Forcing near the jet column mode results in amplification; forcing close to the shear layer mode yields attenuation. As a preliminary effort, two model-free feedback control algorithms are developed and implemented for online optimization of the forcing frequency to extremize the near-field pressure fluctuations. The steady-state behavior of the jet under closed-loop control matches the optimal open-loop results. However, the responsiveness of the controllers is poor since the dynamics of the jet are neglected.

The first step in model-based feedback control is the development of a reduced-order model for the unforced jet. A cylindrical domain spanning the end of the jet potential core is chosen for the significance of its dynamics to the applications at hand. A combination of proper orthogonal decomposition and Galerkin projection is used to reduce the Navier-Stokes equations into a small set of ordinary differential equations employing empirical data. Extensive validation is performed on two existing numerical simulation databases

of jets spanning low and high Reynolds numbers, and subsonic and supersonic speeds. Subsequently, a 35-dimensional model is derived from experimental data and shown to capture the most important dynamical aspects. The short-term prediction accuracy is found to be acceptable for the purpose of feedback control. The statistics from intermediate-term simulations also display good agreement with experimental observations. However, the simulated trajectories from the model grow unbounded beyond about 50 flow time steps.

The model of the unforced jet is augmented to incorporate the effects of plasma actuation. The periodic forcing is modeled as a deterministic pressure wave specified on the boundary of the modeling domain. Forcing of the 35-dimensional model around the jet column mode produces acceptable simulation of the nonlinear response that is observed in experiments. However, the sensitivity of the response is sharper than expected.

Various strategies are adapted and implemented for real-time estimation of the flow state from near-field pressure information. These are assessed using the numerical database of the low Reynolds number Mach 0.9 jet. The most useful strategy is the linear time invariant filter employing a linearized version of the dynamic model developed for the unforced jet. This is shown to be more accurate than the more common stochastic estimation techniques, while requiring minimal processing resources.

The actual design of the feedback laws in this very challenging problem remains an open question. The possible directions to take in addressing this in the future are discussed.

Acknowledgments

Vita

August 22, 1978 .... Born - Kolkata, India

2001 .... B.S. Mechanical Engineering,
Jadavpur University, Kolkata, India

2001-2006 .... Engineer,
Tata Consultancy Services (TCS), India

2003-2006 .... Design Team Member,
Zimmer Inc., Warsaw, IN, USA,
On deputation from TCS, India

2006-2007 & 2010 .... Distinguished University Fellow,
The Ohio State University

2007-2009 & 2011 .... Graduate Research Assistant,
The Ohio State University

Publications

Research Publications

A. Sinha, A. Serrani, and M. Samimy, "Development of Empirical Estimators for Feedback Control of High-Speed Axisymmetric Jets," *AIAA Journal*, 49(9), 2011.

C. Rethmel, J. Little, K. Takashima, **A. Sinha**, I. Adamovich, and M. Samimy, "Flow Separation Control over an Airfoil with Nanosecond Pulse Driven DBD Plasma Actuators," accepted for publication in *Experiments in Fluids*.

M. Samimy, J.-H. Kim, M. Kearney-Fischer, and **A. Sinha**, "High-Speed and High Reynolds Number Jet Control Using Localized Arc Filament Plasma Actuators," accepted for publication in *Journal of Propulsion and Power*.

M. Samimy, J.-H. Kim, M. Kearney-Fischer, and **A. Sinha**, "Acoustic and Flow Fields of an Excited High Reynolds number Axisymmetric Supersonic Jet," *Journal of Fluid Mechanics*, 656:507–529, 2010.

A. Sinha, A. Serrani, and M. Samimy, "Initial Development of Reduced-Order Models for Feedback Control of Axisymmetric Jets," *Inernational Journal of Flow Control*, 2(1):39–60, 2010.

A. Sinha, K. Kim, J.-H. Kim, A. Serrani, and M. Samimy, "Extremizing Feedback Control of a High-Speed and High Reynolds Number Jet," *AIAA Journal*, 48(2):387–399, 2010.

Conference Publications

A. Sinha, A. Serrani, and M. Samimy, "Incorporating Actuation Effects in Reduced-Order Models for Feedback Control of Axisymmetric Jets," In *17th AIAA/CEAS Aeroacoustics Conference, AIAA Paper 2011-2937*, 2011.

M. Samimy, J.-H. Kim, M. Kearney-Fischer, and **A. Sinha**, "High speed and high Reynolds number jet control using arc filament plasma actuators for noise mitigation and for flow and noise diagnostics," In *49th AIAA Aerospace Sciences Meeting, AIAA Paper 2011-0022*, 2011.

C. Rethmel, J. Little, K. Takashima, **A. Sinha**, I. Adamovich, and M. Samimy, "Flow Separation Control over an Airfoil with Nanosecond Pulse Driven DBD Plasma Actuators," In *49th AIAA Aerospace Sciences Meeting, AIAA Paper 2011-0487*, 2011.

A. Sinha, A. Serrani, and M. Samimy, "Development of Empirical Estimators for Feedback Control of Axisymmetric Jets," In *5th AIAA Flow Control Conference, AIAA Paper 2010-4419*, 2010.

A. Sinha, A. Serrani, and M. Samimy, "Development of Reduced-order Models for Feedback Control of Axisymmetric Jets," In *48th AIAA Aerospace Sciences Meeting, AIAA Paper 2010-0015*, 2010.

A. Sinha, K. Kim, J.-H. Kim, A. Serrani, and M. Samimy, "Extremizing Feedback Control of a High-Speed and High Reynolds Number Jet," In *47th AIAA Aerospace Sciences Meeting, AIAA Paper 2009-0849*, 2009.

A. Sinha, K. Kim, J.-H. Kim, A. Serrani, and M. Samimy, "Towards Feedback Control of High-Speed and High-Reynolds Number Jets," In *4th AIAA Flow Control Conference, AIAA Paper 2008-3862*, 2008.

Fields of Study

Major Field: Mechanical Engineering

Studies in:

Feedback Control
Flow Control
Fluid Mechanics
Reduced-Order Modeling
Turbulence

Abbreviations

2C − PIV   Two-component particle image velocimetry

3C − PIV   Three-component particle image velocimetry

DNS   Direct numerical simulation

EKF   Extended Kalman filter

GP   Galerkin projection

IIR   Infinite impulse response (filter)

ILES   Implicit large-eddy simulation

KF   Kalman filter

KWA   Kiefer-Wolfowitz algorithm

LAFPA   Localized arc filament plasma actuator

LSE   Linear stochastic estimation

LTIF   Linear time-invariant filter

NMA   Nelder-Mead algorithm

ODE   Ordinary differential equation

PIV   Particle image velocimetry

POD   Proper orthogonal decomposition

PSD   Power spectral density

QSE   Quadratic stochastic estimation

RMS   Root mean square

ROM   Reduced-order model

SE   Stochastic estimation

SLSE   Spectral linear stochastic estimation

SPL   Sound pressure level

mKWA   Modified Kiefer-Wolfowitz algorithm

mNMA   Modified Nelder-Mead algorithm

Table of Contents

List of Tables

List of Figures

xviii

Chapter 1

INTRODUCTION

The rapid expansion of computing power combined with the development of sophisticated but economical sensing technologies have opened new vistas for application of feedback control to complex large-scale systems. This has shifted the onus to the appropriate approximation of the dynamics of such systems. Thus, this branch of science and engineering, termed reduced-order modeling, has seen burgeoning activities in recent times. Although general-purpose tools have been successfully developed for approximating large-scale linear systems (Antoulas, 2005), nonlinear systems must still be addressed on a case-by-case basis using deep physical understanding.

One of the frontiers of feedback control today is high-speed flows, which represent highly nonlinear and very large-scale (actually infinite-dimensional) systems. System reduction techniques for flows are still in their infancy. Useful linear models have been proposed for some flow control problems. Examples include — near-wall turbulence (Bewley and Liu, 1998), flow over a cavity (Rowley et al., 2006), and transitional channel flow (Ilak and Rowley, 2008). Kim and Bewley (2007) provide a review of the application of linear systems theory to such flows. However, for most flows, nonlinear effects cannot be neglected. One of the best-studied benchmark problems in this regard is the natural vortex shedding

occurring in the flow past a cylinder. Elegant nonlinear models have been proposed to model the strong oscillations in this flow (e.g. Noack et al., 2005). Some flows of practical interest are also dominated by oscillatory wakes and are therefore amenable to similar modeling approaches. Examples are — ameliorating optical path variations over turrets (Seidel et al., 2010; Andino et al., 2011), drag-reduction for bluff bodies (Pastoor et al., 2008), and lift-increase in airfoil configurations (Luchtenburg et al., 2009; Heinz et al., 2010). The natural feedback loop developing in the flow over a cavity has also been modeled for the implementation of closed-loop control by several researchers (Rowley et al., 2004; Samimy et al., 2007a; Caraballo et al., 2008).

The modeling is considerably difficult if the flow is *not* dominated by oscillations at a few discrete frequencies. The most practical flows in this category are turbulent planar shear layers, axisymmetric shear layers or jets, and high-speed boundary layers, that are characterized by large-scale structures with broadband frequency content. One of the pioneering works in reduced-order modeling of flows was in fact aimed at isolating and analyzing the essential dynamics of the turbulent near-wall flow in an open channel (Aubry et al., 1988; Sanghi and Aubry, 1993; Berkooz et al., 1993; Holmes et al., 1996). Notable advances have also been made in the modeling of axisymmetric jets (Glauser et al., 1989; Zheng and Glauser, 1990) as well as planar shear layers (Delville et al., 1999; Ukeiley et al., 2001). However, none of these researchers were considering controlled flows. The present research is an effort to develop a feedback-oriented dynamical model of a high-speed and high Reynolds number axisymmetric jet. For this, the two main ingredients are the known but practically intractable governing Navier-Stokes equations, and empirical experimental data. The research is motivated by the following brief introduction to the dynamics of the jet as well as the particular objectives of jet control.

A shear layer is a canonical flow configuration that forms when two fluids with dissimilar but nominally parallel velocities interact. Turbulent interaction lead to gradual broadening or growth of the shear layer starting from its point of inception. The additional aspect of a free jet is that the high-speed flow is confined within the low-speed (or ambient) fluid. These fluid dynamic configurations are attended by several natural instability mechanisms, that must be understood for effective control.

The mean velocity profile in a shear layer has an inflection point which is steepest at its initiation, at the end of the splitter plate in case of a planar configuration, or at the nozzle lip in case of a jet. Linear stability theory shows that such an inflected velocity profile is unstable to a broad range of frequencies (e.g. Michalke, 1965). This mechanism is called the initial shear layer instability or Kelvin-Helmholtz instability. Naturally-occurring or artificially-seeded perturbations in the initial shear layer are amplified selectively, and roll up into large-scale coherent structures. Such structures were first observed in the 1970's in low-speed but turbulent shear layers and jets (Crow and Champagne, 1971; Brown and Roshko, 1974). Coherent structures were soon recognized as a universal flow characteristic of immense engineering significance. The purely stochastic description of turbulence prevalent until that time could be augmented, if not surpassed, by a quasi-deterministic formulation, with consequent opportunities for manipulation. In fact, one of the main goals of flow control is to affect the flow through the appropriate shaping of the coherent structures.

The center f of the range of unstable frequencies in the shear layer scales with the initial momentum thickness θ_0 and the mean of the velocities of the two streams $\overline{U}$. The appropriate non-dimensional frequency, known as the Strouhal number, is $St_\theta := f\theta_0/\overline{U}$. The maximum growth of naturally-occurring perturbations is observed for $St_\theta \approx 0.012$, and this is termed the 'shear layer mode' (Zaman and Hussain, 1981). Excitation at $St_{\theta F} \approx$

0.017 produces the most rapid growth and early saturation and breakdown of the rolled-up structures, leading to turbulence suppression (Zaman and Hussain, 1981). The subscript 'F' indicates that the forcing frequency f_F replaces the natural frequency f in the definition

In a jet, the shear layer wraps on itself around the periphery. Thus, the growth of the shear layer eventually leads to a three-dimensional interaction. The body of the high-speed stream remains irrotational until it encounters this interaction region, and is hence called the 'potential core' or the 'jet column'. The interaction of the shear layer with itself results in an instability mechanism, termed the 'jet column mode', that causes the potential core to naturally undulate. The most amplified flow frequency, observed at the end of the core, scales with the jet diameter D (or width, for a rectangular jet) and the exit velocity U_j (Crow and Champagne, 1971; Hussain and Zaman, 1981). The corresponding Strouhal number $St_D := fD/U_j$ is around 0.2 to 0.6 (Gutmark and Ho, 1983). Broadband turbulence amplification as well as far-field noise amplification is observed by forcing the jet at $St_{DF} \approx 0.3$ (Bechert and Pfizenmaier, 1975; Moore, 1977; Crighton, 1981; Hussain and Zaman, 1981; Ahuja and Blakney, 1985).

An axisymmetric jet is susceptible to an additional instability, whereby perturbations in certain azimuthal Fourier modes are selectively amplified by the natural dynamics of the jet. The primary parameter affecting the 'azimuthal instability' is D/θ_0 (Cohen and Wygnanski, 1987; Corke et al., 1991).

One of the by-products of turbulent interactions in the jet shear layer is noise. Jet noise has been a cause for concern since the commercialization of jet engine technology for civil and military aviation. In recent years, the problem has worsened with increasing number of flights, growth of residential population around airports, enactment of more stringent regulations, and deployment of significantly noisier high-performance military jets. Although

jet noise is a mature research area with a history spanning almost six decades, there is still a lack of consensus on the fundamental mechanisms involved (Jordan and Gervais, 2008). However, a common ground among the divergent viewpoints is the recognition of the importance of the large-scale coherent structures in the jet mixing layer, especially near the end of the potential core.

Apart from jet noise mitigation, research effort is also focused on enhancing bulk mixing in jets. Specifically, the hot gases exiting from the jet nozzle undergo bulk mixing with the ambient fluid in a process that ultimately leads to dissipation. It is of military interest to enhance this mixing so that the high-temperature of the jet vanishes quickly. The rate of dissipation is clearly correlated with the dynamics of the large-scale structures in the jet shear layer (Gutmark et al., 1995).

From the above discussion, one can conclude that the disparate research fields of noise mitigation and bulk mixing enhancement in jets have the large-scale structures as a common denominator. Affecting the turbulence characteristics of flows by manipulating large-scale structures is within the realm of flow control, which is therefore appropriate for both these applications.

Localized arc filament plasma actuators (LAFPA) have been developed and continuously improved for flow control applications in the Gas Dynamics and Turbulence Laboratory (GDTL) at the Ohio State University (OSU) (Samimy et al., 2004; Utkin et al., 2007; Kim et al., 2010). LAFPAs are capable of generating high-amplitude and high-bandwidth control signals, which are crucial actuator characteristics for manipulating high-speed and high Reynolds number flows. These actuators provide intense but controlled localized Joule heating to manipulate the large-scale structures in the mixing layer by exciting the natural instabilities of the jet. Eight of these actuators have been deployed in a uniform azimuthal

array at the periphery of the nozzle exit of axisymmetric jets with Mach numbers of 0.9, 1.3, and 1.65. The effects of various forcing azimuthal modes and frequencies on the response of the mixing layer were investigated (Samimy et al., 2007b; Kim et al., 2009a; Kearney-Fischer et al., 2009). At particular forcing Strouhal numbers and azimuthal modes of operation, the length of the jet potential core was significantly reduced with an increase in the jet centerline velocity decay rate beyond the end of potential core. Plasma actuation was also shown to attenuate far-field noise, with reductions of 0.5 to over 1.0 dB over a range of forcing Strouhal numbers (Samimy et al., 2007c; Kastner et al., 2009b). The above explorations were performed on unheated jets. Significant improvements in effectiveness of the LAFPAs have been observed in heated jets for both mixing enhancement (Kearney-Fischer et al., 2009), and noise attenuation (Kearney-Fischer et al., 2011b). Thus, open-loop forcing results have demonstrated that the LAFPAs have significant control authority on high-speed and high Reynolds number jet flows for applications involving both noise attenuation and bulk-mixing enhancement.

The above investigations also showed that the optimal actuator parameters for a certain application exist in a limited region of the parameter-space. Moreover, as in any control system, the performance of the LAFPAs in open-loop is a function of the jet operating conditions, for example the Mach number and exit temperature, which are subject to variations and uncertainties in flight. Thus, a natural advancement towards practical implementation is to incorporate feedback control, which may guarantee robustness in the presence of such uncertainties.

The present research is reliant on experiments in two crucial ways. First, the development of the dynamical model of the jet is directly based on empirical data. Moreover, the feedback control technique proposed herein is validated in experiments. Thus the thesis

begins by presenting the experimental methodology in Chapter 2. No less important to the modeling effort is the availability of two numerical simulation databases of jets. These are also discussed briefly in Chapter 2.

The pressure in the near irrotational field of the jet is correlated with the velocity field in the shear layer. As such, it is proposed to use real-time measurement of the pressure to estimate the velocity field for feedback control. Moreover, the pressure-velocity correlations are also exploited as an integral part of the model-development procedure starting from empirical data. The near-field pressure is studied for the jet in open-loop forcing in Chapter 3.

A simple yet robust form of closed-loop control is model-free feedback, and this is pursued in Chapter 4. In this paradigm, the noise mitigation problem is posed as real-time minimization of near-field pressure fluctuations. Conversely, the bulk-mixing enhancement problem is replaced by online maximization of the pressure. In both cases, experimental validation demonstrates that the optimal forcing frequency found in open-loop parameter sweeps can be replicated in closed-loop.

Although the simplicity of model-free controllers is attractive for flow control, their responsiveness is generally slowed by the necessity of neglecting the system dynamics. Significant improvements in performance may be realized with a model-based feedback controller, which is the most common paradigm in feedback control. The considerable challenges involved in obtaining a dynamical model of the jet have been discussed at the outset. A necessary first step in the proposed approach is to model the dynamics of the system without any actuation. The development and validation of a reduced-order dynamical model of the unforced jet forms the main thrust of this thesis, and this is presented in Chapter 5.

The work presented in the above chapter lays the groundwork for the two other avenues of research pursued here. Chapter 6 discusses the incorporation of the effects of plasma actuation in the reduced-order model of the jet. Chapter 7 presents and compares various strategies for real-time estimation of the flow velocity field for feedback control, the most effective of which are shown to be those that exploit the dynamical model developed above.

The research is summarized in Chapter 8. In addition, this chapter also discusses the directions of further research in this area.

Chapter 2

EXPERIMENTAL AND NUMERICAL SIMULATION METHODOLOGIES

This chapter provides a description of the general experimental setup and methodology used in several components of the research. These include a discussion of the flow facility, the anechoic chamber, the plasma actuators, and several diagnostic tools. Some details require extensive background information to be discussed meaningfully, and these appear in subsequent chapters. Finally, some pertinent details of the numerical databases employed in this work are also presented here.

2.1 Anechoic Chamber and Flow facility

All experiments were conducted in the anechoic chamber at the Gas Dynamics and Turbulence Laboratory (GDTL) at the Ohio State University (OSU); a schematic appears in Figure 2.1. The anechoic chamber and jet facility has been described in detail by Kerechanin et al. (2001) and complies with ANSI Standard S12.35. The chamber has a cutoff frequency of 250 Hz provided by foam wedges. The floor wedges are removable to allow the easy setup of measurement systems when anechoicity is not required. Apart from this, several of the wall wedges can be removed to provide optical access with cameras while still retaining hemi-anechoic testing conditions (see Figure 2.1).
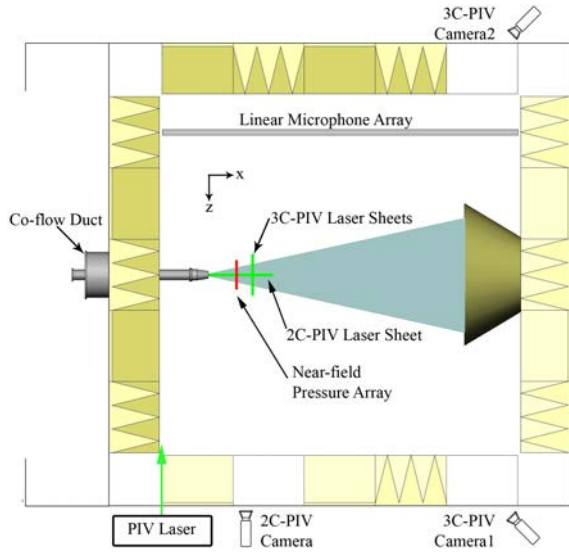
Figure 2.1: Schematic of jet experimental facility at GDTL.

The ambient air is compressed using three 5-stage reciprocating compressors, filtered, dried, and stored in two cylindrical 36 m^3 tanks at up to 16 MPa. The stagnation pressure is controlled by a Fisher Type 667-D control valve capable of maintaining the pressure within 0.2 psi of the desired value. The facility is designed for continuous operation of an axisymmetric jet with an exit diameter of $D = 25.4$ mm (1.0 inch) and Mach number up to 2.5.

The present work employed an axisymmetric Mach 0.9 jet with an exit diameter of 25.4 mm. The subsonic jet is formed through a converging nozzle with an internal contour designed using a 5th order polynomial. The stagnation temperature typically stayed between 0 and 10°C depending on the operating conditions. Quasi-one-dimensional isentropic compressible flow relations (Anderson, 2003) were used to compute the flow variables at the jet exit. In particular, the above variation in the stagnation temperature resulted in a variation in the computed exit velocity U_j between 277 m/s and 282 m/s. Sutherland's

formula (White, 1991) was used to calculate the dynamic viscosity at the jet exit. Then the Reynolds number Re based on D and the exit conditions was $\sim 6.7 \times 10^5$.

The state of the boundary layer at the jet nozzle exit plays a significant role in the initial development of structures in the shear layer, and hence the response of the jet to excitation at the nozzle lip (see Samimy et al. (2010) for a review). The thickness of the boundary layer in the present operating condition is estimated to be on the order of 1 mm, making it extremely difficult to study experimentally. Recently, Kearney-Fischer et al. (2009) used hot-wire anemometry to study the initial shear layer of a 1.5 inch converging nozzle attached to the current jet facility. For experimental feasibility, the jet was operated at Mach numbers between 0.25 and 0.65 with corresponding Reynolds number ranging from 2×10^5 to 6×10^5. The plasma actuators are housed in a nozzle extension as described below, and such an extension was also attached to the above 1.5 inch nozzle. With this setup, a collapse of the suitably scaled velocity profiles was obtained over the range tested, indicating that the boundary layer exiting the nozzle is turbulent. Kearney-Fischer et al. (2009) also performed analysis to conclude that the boundary layer thickness and momentum thickness in the current work are on the order of 1 mm and 0.1 mm, respectively.

2.2 Localized Arc Filament Plasma Actuators

Localized arc filament plasma actuators have been developed and implemented at GDTL over the past decade. Each LAFPA consists of a pair of 1 mm diameter tungsten pin electrodes connected to a high-voltage ($\sim$ kV) source through a dedicated high-frequency switching circuit (see Figure 2.2(a)). A boron nitride nozzle extension with 25.4 mm inner diameter and 15 mm thickness is used to hold the actuators (see Figure 2.2(b)). Eight LAFPAs are distributed uniformly around the azimuth 1 mm upstream of the exit. A 0.5
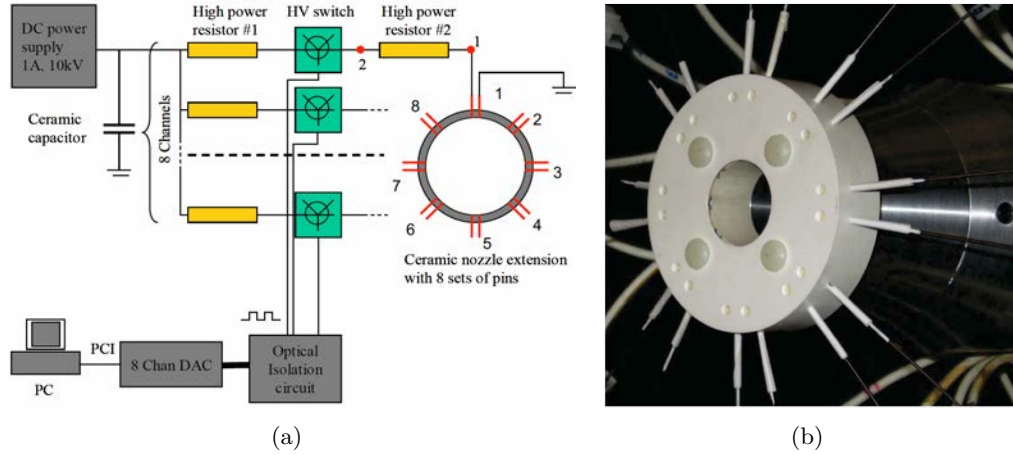
Figure 2.2: (a) Schematic of LAFPA circuit. (b) Picture of LAFPA setup.

mm deep and 1 mm wide ring groove is made in the extension to house the electrodes and shield the plasma. The center-to-center distance between the two electrodes in a LAFPA is 3 mm.

The computer-generated signal that manipulates the switching circuitry is a rectangular pulse train as shown in Figure 2.3(a). When the switch to a LAFPA is closed, the voltage across the electrodes ramps up to the breakdown voltage (which is several kV and depends on the distance between the electrodes, the flow conditions, as well as the frequency of forcing) in ~ 5 μs (see Figure 2.3(a)). The air between the electrodes is ionized and an electric arc is established. Within about 10 ns afterwards (not resolved in the above figure), the voltage across the electrodes drops to a few hundred volts and remains at that level until the switch is opened. The instantaneous power addition to the flow thus reaches ~ 1 MW, although the average cycle power is only ~ 10 W. The resultant effect on the flow is a rapid localized heating that generates compression waves as seen in Figure 2.3(b) (Samimy et al., 2010). More information on the construction and characterization of LAFPAs is available
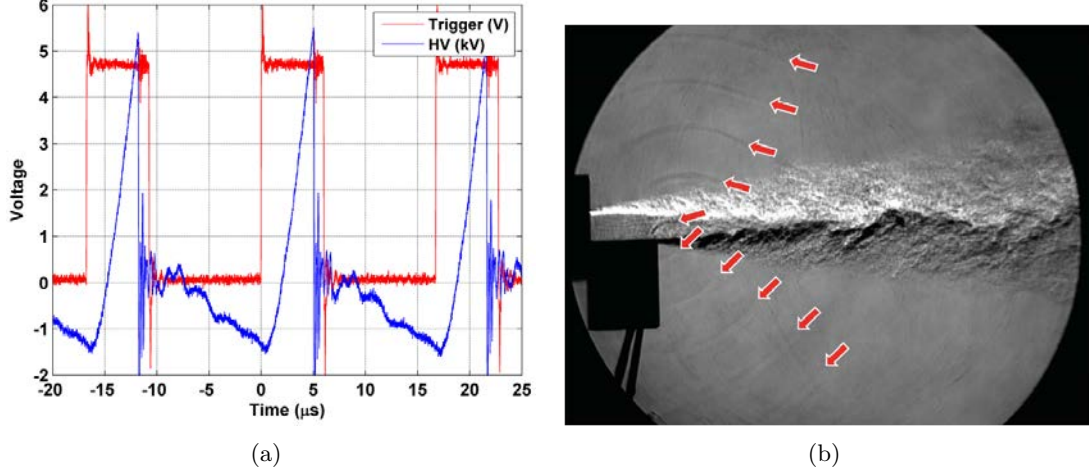
Figure 2.3: (a) Traces of the trigger signal voltage controlling a LAFPA at 60 kHz forcing with 6 μs pulse width and the corresponding high voltage breakdown characteristics. (b) An instantaneous schlieren image of a rectangular Mach 0.9 jet showing the compression waves (indicated by arrows) generated by four aligned LAFPAs forced at 20 kHz (Samimy et al., 2010).

in previous publications from our laboratory (Samimy et al., 2004, 2007b,c; Utkin et al., 2007; Samimy et al., 2010; Kim et al., 2010; Hahn et al., 2011).

The computer program allows for independent control of the frequency, pulse width, and phases of the trigger signals controlling the eight LAFPAs. Note that the amplitude of excitation cannot be controlled independently. The bandwidth of the actuators is 200 kHz, but the maximum forcing frequency used in the present work was $\sim$ 35 kHz. Hahn et al. (2011) recently reported that although complete breakdown of the air is crucial for the effectiveness of the LAFPAs, the pulse width beyond breakdown also has some influence. For the present work, the following empirical relation has been obtained experimentally and used:

$$\text{duty cycle } (\%) = \begin{cases} 0.6(f_F/1000) + 2, & \text{if } f_F \leq 30 \text{ kHz}, \\ 0.29(f_F/1000) + 11.42, & \text{if } f_F > 30 \text{ kHz}, \end{cases}$$

Forcing Azimuthal Mode, m_F	Firing Order
0 (Axisymmetric)	8 actuators fire in phase
1 (1st helical)	1, 2, 3, 4, 5, 6, 7, 8
2 (2nd helical)	(1 & 5), (2 & 6), (3 & 7), (4 & 8)
3 (3rd helical)	1, 4, 7, 2, 5, 8, 3, 6
4 (Nyquist mode)	(1, 3, 5 & 7), (2, 4, 6 & 8)

Table 2.1: Firing order for all possible simple forcing azimuthal modes using eight actuators. All actuators within a set of parentheses fire together.

where f_F is the forcing frequency in Hz, and duty cycle refers to the percentage of the forcing period over which the trigger signal is switched on.

The relative phases of the eight actuators is controlled, and this determines the azimuthal mode of firing. In controlling an axisymmetric jet using acoustic drivers, the input signal to a particular actuator is typically a sinusoid with amplitude given by $A = A_0 \sin(2\pi f_F t - m_F \psi)$, where m_F is a simple (not mixed) forcing azimuthal mode, A_0 is the amplitude, t is time, and ψ is the azimuthal location of the actuator. In the plasma actuator, the input signal is a rectangular on/off pulse, but the phase relation of the actuators is still as above. In particular, the azimuthal angle between two actuators fired successively is determined by $\phi = 2\pi m_F / N$, where N is the number of actuators used (8 in the current work). With the actuator numbering shown in Figure 2.2(a), the firing orders for all possible simple azimuthal modes are shown in Table 2.1. The distinct azimuthal modes that can be resolved with N discrete actuators is given by Nyquist's aliasing theorem as 0 to $\lceil (N-1)/2 \rceil$, where $\lceil \cdot \rceil$ denotes the ceiling function.

The actuators span discrete locations around the azimuth and the time during which they deposit the bulk of energy is a small fraction of the typical forcing period. A temporal

(a) Design 1   (b) Design 2
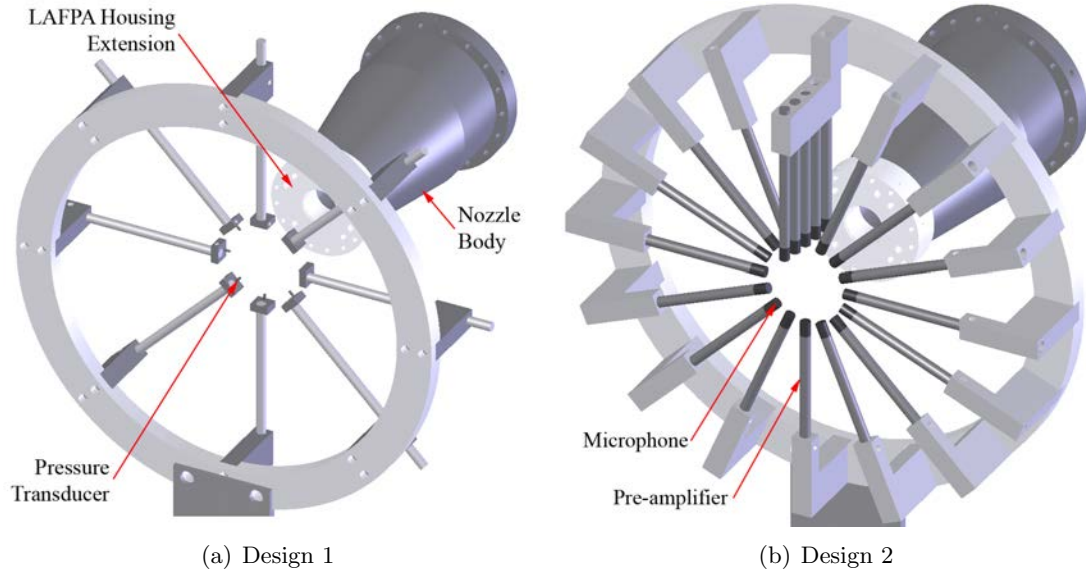
Figure 2.4: Two designs of the near-field pressure measurement setup.

and azimuthal Fourier analysis of this energy would show substantial leakage of energy into unintended azimuthal modes and frequencies. However, the perturbations thus introduced roll-up into more coherent structures in both time and space. Hence, analysis of flow fields acquired in a phase-locked manner to the forcing typically show that the intended azimuthal modes and frequencies are actually preferentially energized (Samimy et al., 2007b; Kastner et al., 2009b; Kearney-Fischer et al., 2009; Kim et al., 2009a; Gaitonde and Samimy, 2010).

2.3 Data Acquisition

2.3.1 Near-Field Pressure

The pressure in the near irrotational field was measured in two main experimental assays separated by two years. During this period, the measurement setup was substantially modified. Both iterations of the design shall be discussed here since results will be presented from both experiments.

15

The first design shown in Figure 2.4(a) incorporated a symmetric circular array of 8 Kulite dynamic pressure transducers (model XCQ-062-25A). The inner diameter of the ring that held the transducers was 254 mm (10 inches), ten times larger than the nozzle diameter. The tip diameter of the pressure transducers was 1.6 mm (1/16 inch), and they were affixed using a silicone-based adhesive in small aluminum blocks of dimensions $0.45 \times 0.50 \times 0.20$ inches. These aluminum blocks in turn were affixed using set-screws to steel 1/4 inch diameter rods. The rods could be slid radially in and out of their respective holders on the outer rim, allowing the pressure transducers to be set at any desired radius using set screws. The ring array itself was mounted on a 2-axis manual slide allowing adjustment of location and orientation with respect to the jet.

The pressure transducers have a usable frequency range up to 10 kHz. The voltage output from the transducers were amplified 1000 times using an in-house-fabricated signal conditioner which also provided the excitation voltage. The signals were low-pass filtered at 100 kHz, and acquired using an eight channel National Instruments (NI) ADC card at a sampling rate of 200 kHz. For all computations of the pressure spectrum, a LabVIEW data acquisition routine collected 100 blocks of 8192 samples each at 200 kHz on the eight channels simultaneously, for a total duration of $\sim$ 3.9 s. The resulting spectra had a frequency resolution of 24.4 Hz.

Subsequently, a need was felt to have greater resolution of the azimuthal content of the near-field pressure. The earlier rig was re-machined to hold twice as many transducers around the azimuth (see Figure 2.4(b)). Moreover,1/4 inch Bruel & Kjaer (B&K) microphones (model 4939) were used instead of Kulite pressure transducers since they were already available in the laboratory. The circuitry of the microphones was also found to

be more robust to the electro-magnetic interference arising from the LAFPAs. The microphones are 9 mm long and are screwed onto B&K pre-amplifiers (model 2690). The diameter and length dimensions of the latter are 6.3 mm (1/4 inch) and 89.5 mm (3.5 inches), respectively. The pre-amplifiers are shown in Figure 2.4(a) as being affixed to the rim holders using set screws, allowing for radial adjustment. The new design also incorporated a linear array of five microphones centered on the plane of the azimuthal array. The linear resolution of this array was 12.7 mm (1/2 inch). The tips of the sensors on the linear array typically formed a line inclined at 8.6° to the jet axis, although this could be adjusted easily. This configuration ensured that the sensors were approximately equidistant from the outer edge of the shear layer of the unforced jet, as measured in earlier PIV assays (Kearney-Fischer et al., 2009). The remaining rig was not modified.

The dynamic range of the microphones is 4 Hz to 80 kHz with the grid cover removed. The signals from the microphones were amplified and filtered between 20 Hz and 100 kHz using B&K Nexus 2690 signal conditioners. The remaining data acquisition hardware and post-processing were similar to that for the pressure transducers.

The results from the near-field pressure measurements will be presented later. The power spectra from the two measurement setups were indistinguishable up to the rated frequency of the Kulite transducers (10 kHz).

2.3.2 Far-Field Acoustics

Limited surveys of the far-field acoustics were conducted, mainly to validate feedback control effects. The measurement rig is depicted in Figure 2.1. The measurement hardware and post-processing were the same as that used in the second design of the near-field pressure measurement rig discussed above. Two microphones were located at 30° and 90° polar angles relative to the downstream jet axis; their radial locations were $103D$ and $48D$

17

respectively, measured from the nozzle exit. The far-field acoustics were normalized to a radius of $80D$.

The presence of the near-field pressure measurement rig was found to have no effect on the far-field sound power spectrum at the 30° location; however, the spectrum measured at the 90° location was found to have an additional 2-3 dB near its peak due to reflection off the rig. So, for proper comparison to the spectra measured with feedback control, the unforced and open-loop forced spectra reported herein were also measured with the near-field rig in place.

2.3.3 Particle Image Velocimetry

A LaVision system was used for 3-component particle image velocimetry (3C-PIV) on the cross-stream plane of the jet at discrete streamwise locations between $x/D = 5.0$ and 7.75 ($\Delta x/D = 0.25$). A final slice was planned for $x/D = 8$, but was abandoned due to experimental exigency. A Spectra Physics model SP-400 dual head Nd:YAG laser was used as the light source. The two cameras used had 2048×2048 pixel CCDs, and the associated lenses resulted in a spatial resolution of about 0.096 mm on any cross-stream plane. The cameras were placed downstream of the jet exit outside the anechoic chamber obeying the Scheimpflug principle, with line-of-sight access afforded by windows in the chamber (see Figure 2.1). Vector maps were computed from image pairs separated in time by 1.4 μs. The cameras were kept fixed while the overhead optics were manipulated to place the laser sheet at various streamwise locations, a new calibration being performed for each PIV plane.

The jet plume was seeded with diethylhexyl-sebecat liquid droplets atomized by a four-jet LaVision atomizer. A 381 mm diameter duct was placed co-axial with the jet to generate a very low speed ($\sim 0.01U_j$) entrained co-flow. The co-flow was seeded by a fogger to avoid statistical bias in the measurements, as well as spurious velocity vectors in the entrained

18

air that has not mixed with the jet yet. The average droplet size was 0.7 and 0.25 μm for the jet flow and co-flow, respectively. For each experimental run, 1000 image pairs were recorded at about 2 Hz.

Three-component PIV processing consisted of a three-pass correlation routine with 64×64 pixel windows for the first pass and 32×32 pixel windows for an additional two passes, each pass having 50% overlap of windows. The resulting spatial resolution of the velocity map was $0.06D$. For the axisymmetric jet, it is natural to transform from rectangular to polar coordinates. For each slice, the jet center was located automatically by best fitting circles to the mean axial velocity contours on the default rectangular grid. The polar grid was centered on the jet center thus found. A triangle-based linear interpolation was used to transform the velocity map from the rectangular grid to the polar grid, before converting the velocity vectors to polar components (Tinney et al., 2008a). The radial resolution was made $D/16$ and 80 grid points were placed around the azimuth. The radial domain was curtailed to $2D$.

For computation of pressure-velocity cross-spectral correlations, the timing of the 3C-PIV snapshots relative to the pressure measurements had to be carefully controlled. The LaVision PIV software was set up to generate a pulse signal 20 ms prior to the acquisition of each PIV snapshot. This pulse was used to trigger the acquisition of the corresponding block of pressure data. These timing characteristics ensured that each PIV snapshot was taken approximately in the middle of each pressure data block. However, instead of relying on this approximate relation, the Q-switch pulse that triggered the first laser was also acquired simultaneously with the pressure at the same sampling characteristics. In post-processing, the unique rising edge of this Q-switch pulse in each block of data was used to determine the time of the corresponding PIV snapshot.

For additional validation, 2-component PIV (2C-PIV) was performed on a vertical meridional plane using much of the equipment and processing described above; the setup is depicted in Figure 2.1. This was *not* accomplished simultaneously with any other data acquisition. The resulting vector map had spatial resolution of $0.093D$ and covered the entire jet plume over the axial domain between $0.3D$ and $12D$. For ensemble-averaged statistics, 1000 image pairs were recorded at about 5 Hz. In addition, sets of 250 images locked to various chosen phases of the actuation signal were also acquired for forced cases. Earlier attempts at locking PIV to LAFPA phases had failed at GDTL owing to high electromagnetic interference from the LAFPA power supply. In the current successful attempt, an intermediate pulse generator (Berkeley Nucleonics Corp. model 565) placed physically close to the LaVision computer was used to perform an additional thresholding of the noise-corrupted raw actuator control signal. The resulting cleaner signal was used to trigger the PIV capture.

2.3.4 Actuation Phase Acquisition

For development of the empirical control-oriented reduced-order model of the jet, the behavior of the flow variables must be known relative to the forcing signal. In each experimental run with forcing, a unique forcing frequency and azimuthal mode was employed. The particular character of LAFPAs described above then means that the only unknown forcing information at any time is its phase. A sampling frequency of the order of MHz would have been required to determine the phase from the rectangular pulse train controlling the LAFPA operation. Instead, the pulse train controlling the first LAFPA was supplied to an Agilent 3320A 20 MHz arbitrary waveform generator, where each of the square rising edges on the rectangular pulse train triggered a rising ramp signal. This sequence of ramp signals was acquired simultaneously with the pressure signals using the NI hardware and

LabVIEW program described above. Each ramp rose from 0 to 10 V within 20 μs, which is shorter than the smallest forcing time-period of interest, while being long enough to be sampled twice at the 100 kHz sampling rate. In post-processing of forcing cases, the ramp signal was decoded to determine the actuation phase at each pressure sample, and more importantly, corresponding to each PIV snapshot.

2.4 Computing Power Spectral Density

Two of the main methods of analyzing time-series data (like measured pressure fluctuations) are Fourier analysis and wavelet analysis. Fourier analysis posits a time-stationary signal and yields the power spectral density (PSD) of the signal as a whole. On the other hand, the wavelet-based technique analyzes the change in frequency content of a signal with time. The near-field and far-field pressure fluctuations in an unforced or forced jet are well-modeled as stationary so that Fourier analysis is almost ubiquitous. Recently researchers have used wavelet analysis on turbulent jet data to study the intermittency of noise events (Everson et al., 1990; Camussi and Guj, 1999; Cavalieri et al., 2010).

The discussion of computation of PSD follows from the presentation of Bendat and Piersol (2000). Consider an arbitrary time-series denoted by $w(t) \in \mathbb{C}$ whose PSD is desired. All practical measurements of w will be for finite time windows; let one such time window be $0 \leq t \leq T$. Then the temporal Fourier transform of w, denoted by $\breve{w}$, is defined as

$$\breve{w}(f) := \int_0^T w(t)\mathrm{e}^{-2\pi \mathrm{i} f t}\mathrm{d}t, \tag{2.1}$$

where f is the temporal frequency, and $\mathrm{i} = \sqrt{-1}$. The PSD of $\breve{w}(f)$ is then defined as

$$\mathrm{PSD}\left\{\breve{w}(f)\right\} := \lim_{T \to \infty} \frac{1}{T} E\left\{\breve{w}^*(f)\breve{w}(f)\right\}. \tag{2.2}$$

Here, the expectation $E(\cdot)$ is over multiple realizations (or measurements) acquired at different time-windows, and $*$ denotes the complex-conjugate.

The auto-correlation of w is defined as

$$\Pi_{ww}(\tau) := E\left\{w^*(t+\tau)w(t)\right\}.$$

The Wiener-Khintchine theorem (see e.g. Bendat and Piersol, 2000) states that the PSD is actually the Fourier transform of the auto-correlation; i.e.

$$\text{PSD}\left\{\breve{w}(f)\right\} = \int_{-\infty}^{\infty} \Pi_{ww}(\tau)\mathrm{e}^{-2\pi\mathrm{i}f\tau}\mathrm{d}\tau.$$

The frequency f in the definition of PSD can take on any real value. However, since the PSD is an even function of f, it is customary to show only the non-negative frequency axis. By Parseval's theorem, the area under the PSD represents the variance of $w(t)$, but this is true only if the area in the neglected 2nd quadrant is accounted for by doubling the PSD in the represented first quadrant. Thus, in all the PSD plots shown here, the PSD for positive f will be depicted as twice the value obtained from the actual definition.

2.5 Numerical Simulation Databases

Two different numerical simulation databases were accessed for guiding the development of feedback control as well as validating the models. Both of them solve the compressible Navier-Stokes equations, and they furnish a database of all pertinent flow quantities in a time-resolved and spatially-resolved manner. These are discussed here.

2.5.1 Direct Numerical Simulation Database of Unforced Jet

Freund (2001) has performed a direct numerical simulation (DNS) of an unforced unheated Mach 0.9 axisymmetric jet with $Re = 3600$. Kastner et al. (2006) compared the results to those from an experimental jet operated in GDTL at Mach 1.3 with $Re = 1.06 \times 10^6$

(a) DNS   (b) Experiment
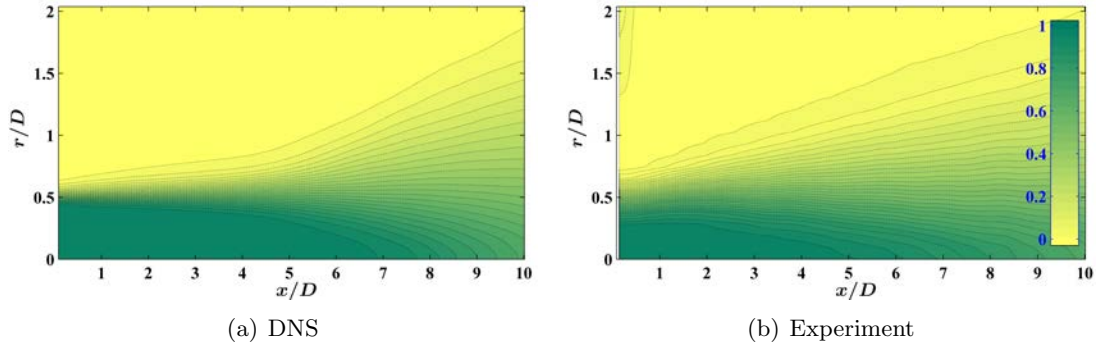
Figure 2.5: Axial velocity contours for the Mach 0.9 jet from DNS and experiments normalized by the jet exit velocity.

to evaluate the effect of Reynolds number on noise sources. Remarkable similarity was noted in most of the essential aspects, including far-field coherence, acoustic spectral shape, and flow field activity during noise events. These overall similarities justify the use of the DNS database to develop and validate the feedback control strategies for the experimental jet.

The details of the database are available in Freund (2001); here, the most pertinent aspects are highlighted. The cylindrical computational grid has 80 uniformly spaced azimuthal grid-points. For ease of implementation, the originally non-uniform rectangular $x - r$ grid is linearly interpolated hereby to a uniform square grid with a spacing of $0.0625D$, where, D is the jet exit diameter. All the results were also assessed in the original grid, and no material difference was observed. The data is saved at 2316 consecutive time instants with uniform separation of 0.071 flow time steps (D/U_j), making for a record length that spans 164 flow time steps.

The boundary layer at the exit of the nozzle in the DNS jet is laminar (Freund, 2001), whereas it is turbulent in the experimental jet (Kearney-Fischer et al., 2009). The most immediate effect of this difference is the disparity in the initial jet spreading and the length

of the potential core. This is evident in the comparative axial velocity contours shown in Figure 2.5. The transition to turbulence also causes the abrupt change in flaring angle of the DNS jet at $x \sim 5D$. Based on this comparison, the domain of interest in the DNS jet was shifted downstream by $2D$ compared to the experimental jet.

2.5.2 Implicit Large-Eddy Simulation Database of Forced Jet

Gaitonde (2011) has performed implicit large-eddy simulation (ILES) of an unheated Mach 1.3 axisymmetric jet with $Re = 1.06 \times 10^6$ under various forcing conditions that mimic the effect of LAFPAs. Note that the operating conditions are identical to the corresponding experimental jet at GDTL. The LAFPAs are modeled as wall-temperature discontinuities and the geometric configuration replicates the experimental arrangement too. The behavior of the jet observed in experiments is captured well by this database. It also offers a unique insight into the detailed temporal and spatial evolution of the structures that are generated by the actuation. The ultimate goal of this simulation effort is to inform the development of optimal control strategies.

The cylindrical computational domain has 100 uniformly spaced azimuthal grid-points. The original axial grid is sampled at $\sim 0.25D$ intervals for the saved data, but the original radial grid data-points are retained. The radial grid is non-uniform, with the smallest spacings being at the centerline and again at the lip-line. However, re-sampling the data on a uniform radial grid with resolution $0.0625D$ was found to be equivalent for the low-order modeling pursued here.

Due to minute differences in the precise exit velocity profiles between the experimental and ILES Mach 1.3 jets, the flow field data from ILES have to be shifted by $2D$ downstream so that their statistics agree with experiments (Gaitonde and Samimy). Such discrepancies are well known for LES databases (Bodony and Lele, 2005). The Mach 0.9 jet was used

exclusively in all the experiments performed as part of this research, and its potential core length is about $2D$ shorter than that of the Mach 1.3 experimental jet (Samimy et al., 2007b; Kearney-Fischer et al., 2009). Thus, when data from the ILES database is used in the model development for the Mach 0.9 jet, no axial shift will be needed.

Chapter 3

FORCING EFFECTS ON NEAR-FIELD PRESSURE

Much of the results presented in this chapter have been published in Sinha et al. (2010a).

3.1 Introduction

Forcing a high-speed and highly turbulent jet with localized arc filament plasma actuators (LAFPAs) produces significant changes in its dynamics. This has been studied in detail at GDTL and an overview of the results has recently been presented in Samimy et al. (2011). These studies have focused on elucidating the effects of forcing in two main regions of the jet.

The flow field within the first 12 to 15 jet diameters of the exit has been studied extensively. Qualitative flow visualization has been instrumental in demonstrating the presence of robust organized large-scale structures on the order of the governing dimension of the jet, i.e. the nozzle exit diameter. These qualitative studies have also shown how different forcing parameters lead to significant flaring or narrowing of the entire jet plume. Quantitative assays have involved two- and three-component particle image velocimetry as well as pressure measurements within the shear layer, typically along the nozzle lip line. These results have not only reinforced the findings from the qualitative measurements, but have

also demonstrated how the mean velocity as well as the turbulent kinetic energy fields are dramatically manipulated by forcing.

One of the main objectives of the development of LAFPAs at GDTL has been the mitigation of jet noise. Hence, the other region of focus has been the far-field acoustics. Data from microphones arrayed over the far-field have shown that the noise could be significantly attenuated with specific forcing parameters in all jets studied so far covering a wide range of operating conditions.

The focus of this thesis is the development and implementation of feedback control for jets, which requires the real-time measurement of the effect of forcing on the jet. The velocity field in the shear layer displays the most direct effect of forcing, but it is impractical to measure over a significant volume of the jet in a real-world implementation. It is also not practical to require direct sensing of far-field noise levels for control applications. However, the hydrodynamic pressure field in the incompressible irrotational region surrounding the jet shear layer is strongly correlated with the dynamics of the shear layer as well as the radiated noise field (e.g. Arndt et al., 1997; Picard and Delville, 2000; Coiffet et al., 2006; Tinney et al., 2007, 2008b; Jordan and Gervais, 2008; Kastner et al., 2010). The measurement of the near-field pressure presents some unique opportunities: (*i*) it is a relatively non-intrusive technique; (*ii*) pressure, being a scalar variable, is considerably easier to measure than the velocity field inside the flow; and (*iii*) unlike some of the velocity measurement tools like particle image velocimetry and laser Doppler velocimetry, pressure sensors are compact and robust and can be feasibly transferred from the laboratory setting to real-world applications (Tinney et al., 2008b).
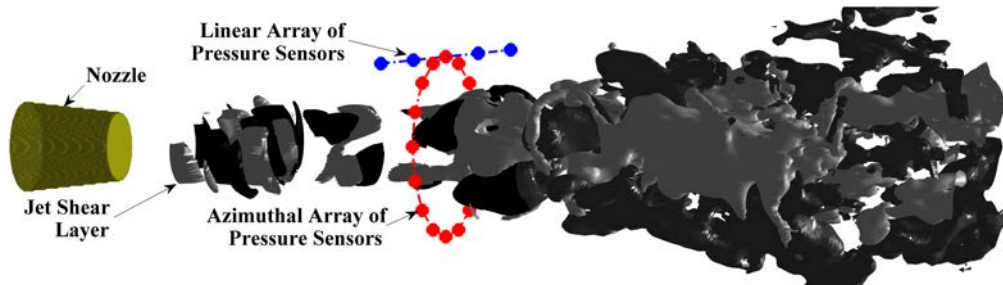
Figure 3.1: Schematic of near-field pressure sensing configuration.

The intensity of pressure fluctuations in the irrotational near-field of the jet is related to the Reynolds stresses in the mixing layer by a weighting function that is inversely proportional to the 4th power of the wavenumber (George et al., 1984). The nature of this rapid roll-off indicates that the pressure field will be dominated by the larger turbulent scales; this is termed wavenumber-filtering. As discussed later, the intensity of hydrodynamic pressure fluctuations in the near field that are the signature of the large-scale structures decrease rapidly with radial distance from the shear layer. Thus, in order to detect the behavior of the actuation-modified large-scale structures, the pressure sensors must be placed close to the shear layer without actually impinging on the jet. A schematic of the pressure measurement setup is presented in Figure 3.1.

In this chapter, the effect of forcing on the near-field pressure is discussed. Previous research investigating the correlation of the near-field pressure with the far-field acoustics is also discussed in some detail, as this pertains to the choice of sensor location.

3.2   Azimuthal Decomposition of Pressure Field

The jet is axisymmetric, which makes it logical to study the azimuthal modal make-up of its near-field pressure. This has been recognized and pursued for decades (e.g. Fuchs,

1972; Hall et al., 2006; Tinney et al., 2007, 2008b). Thus, the discussion of the effects of forcing on the near-field pressure is begun by introducing the necessary measurement setup and the technique of azimuthal modal decomposition.

Let the jet exit velocity and nozzle exit diameter be U_j and D, respectively. All velocities and linear coordinates are normalized by these respective quantities. Time is normalized by the flow time scale D/U_j. Pressure is normalized by $\rho_j U_j{}^2$, where ρ_j is the fluid density at the nozzle exit. With the kinematic viscosity of the fluid at the nozzle exit denoted by ν_j, the pertinent Reynolds number is $Re := U_j D/\nu_j$. The spatial domain is represented in cylindrical coordinates $\mathbf{x} = (x, r, \theta)$.

With reference to Figure 3.1, the measured pressure is denoted by $P : \mathcal{X}_p \times \mathcal{R}_p \times \mathbb{T} \times \mathbb{R} \to \mathbb{R}$, $P : (x, r, \theta, t) \mapsto \mathbb{R}$. Here, $\mathbb{T}$ is the circle group, $\mathbb{R}$ is the real line, and $\mathcal{X}_p$ and $\mathcal{R}_p$ are respectively the set of discrete axial and radial locations of the sensors. The azimuthal decomposition requires simultaneous measurement of pressure at several locations on an azimuthal array concentric with the jet. For the purpose of the current discussion, the simultaneous measurement is not required at multiple axial or radial locations. Although the azimuthal domain will also be measured at discrete locations, the formal derivations are aided by considering it to be continuous for the present. The above notation is natural for measurements on an azimuthal array of the form shown in Figure 3.1. However, by fixing θ, the notation can also be used for representing measurements made on a linear array of sensors (as shown in the figure) as well as using one-off sensors. In these cases, θ can be assumed to be 0 without loss of generality.

The statistical stationarity and axisymmetry of the jet is used to define the time-average or ensemble average pressure as

$$\overline{P}(x, r) := E\left\{\frac{1}{2\pi} \int_{-\pi}^{\pi} P(x, r, \theta, t)\mathrm{d}\theta\right\}. \tag{3.1}$$

29

Henceforth, unless otherwise mentioned, the expectation operator $E(\cdot)$ will signify the ensemble-average. If information is not available at multiple azimuthal locations, as on the linear array depicted in Figure 3.1, then the azimuthal averaging is omitted. Invoking Reynolds decomposition, the fluctuating pressure is

$$p(x, r, \theta, t) := P(x, r, \theta, t) - \overline{P}(x, r). \tag{3.2}$$

The azimuthal Fourier transform of a function $w : \mathbb{T} \to \mathbb{C}$, $w : (\theta) \mapsto \mathbb{C}$, will be denoted by

$$w(\theta) \overset{\mathcal{F}_m}{\mapsto} \hat{w}(m); \quad \hat{w}(m) := \frac{1}{2\pi} \int_{-\pi}^{\pi} w(\theta) \mathrm{e}^{-\mathrm{i}m\theta} \mathrm{d}\theta. \tag{3.3}$$

Here m is the azimuthal mode; it is an integer. The inverse Fourier transform will be denoted by

$$\hat{w}(m) \overset{\mathcal{F}_\theta}{\mapsto} w(\theta); \quad w(\theta) = \sum_{m=-\infty}^{\infty} \hat{w}(m) \mathrm{e}^{\mathrm{i}m\theta}. \tag{3.4}$$

Accordingly, if information is available at multiple azimuthal locations, then the azimuthal Fourier transform of p is defined as $p(x, r, \theta, t) \overset{\mathcal{F}_m}{\mapsto} \hat{p}(x, r, t; m)$. Since p is real, $\hat{p}$ is Hermitian in m.

The pressure is measured at finite locations around the azimuth, say at N_θ uniformly-spaced stations. Then, Nyquist aliasing theory states that the distinct azimuthal modes that can be resolved are $-\lceil (N_\theta - 1)/2 \rceil$ to $\lceil (N_\theta - 1)/2 \rceil$, where $\lceil \cdot \rceil$ denotes the ceiling function. This is evidently similar to the discussion of azimuthal forcing modes obtainable with a finite number of LAFPAs (see Section 2.2).

The statistical stationarity can be used to compute the temporal Fourier transform of the pressure recorded over a time window T that is long enough to resolve the lowest frequencies of interest. The treatment of the physical pressure p has been discussed in Section 2.4. For

30

any azimuthal mode m, the temporal Fourier transform is

$$\check{\hat{p}}(x, r; m, f) := \int_0^T \hat{p}(x, r, t; m) \mathrm{e}^{-2\pi \mathrm{i} f t} \mathrm{d}t. \tag{3.5}$$

Then, following the discussion in Section 2.4, the corresponding power spectral density is defined as

$$\mathrm{PSD}\left\{\check{\hat{p}}(x, r; m, f)\right\} := \begin{cases} \displaystyle\lim_{T\to\infty} \frac{1}{T} E\left\{\check{\hat{p}}^*(x, r; m, f)\check{\hat{p}}(x, r; m, f)\right\}, & \text{if } m = 0, \\[2mm] \displaystyle\lim_{T\to\infty} \frac{2}{T} E\left\{\check{\hat{p}}^*(x, r; m, f)\check{\hat{p}}(x, r; m, f)\right\}, & m > 0. \end{cases} \tag{3.6}$$

For even N_θ, the PSD of the Nyquist azimuthal mode $m = N_\theta/2$ is also given by the first formula. The energies in the positive helical modes are identical to the energies in their negative counterparts, and the above definition accounts for this. This is similar to the consideration in Section 2.4, whereby the PSD was doubled in the positive frequencies to account for the neglected negative frequency axis.

Hall et al. (2006) measured the near-field pressure of a Mach 0.85 and $Re = 9.8 \times 10^5$ jet using an azimuthal array of 15 transducers; they confirmed the low-dimensional character of the azimuthal pressure spectrum that was originally reported by Michalke and Fuchs (1975). In particular, they showed that the instantaneous pressure signal can be almost completely reconstructed from the sum of the axisymmetric mode and the first helical mode. Shifting the reference azimuthal angle to the angle of measurement, (i.e., setting $\theta = 0$), their hypothesis can be written as

$$\begin{aligned} p(x, r, \theta = 0, t) &= \sum_{m=-\infty}^{\infty} \hat{p}(x, r, t; m) \mathrm{e}^{\mathrm{i}m(\theta=0)} \\ &\approx \hat{p}(x, r, t; m = 0) + \hat{p}(x, r, t; m = 1) + \hat{p}(x, r, t; m = -1) \\ &= \hat{p}(x, r, t; m = 0) + 2\Re\left\{\hat{p}(x, r, t; m = 1)\right\}, \end{aligned} \tag{3.7}$$

where $\Re(\cdot)$ signifies the real part of the argument. In the final step, the Hermitian property of $\hat{p}(m)$ is exploited. The above azimuthal-mode-filtered pressure is more useful for feedback

31

control than the raw pressure itself since the spatial filtering enhances the signal-to-noise ratio. It has already been discussed above that the stronger the large-scale structures in the mixing layer, the higher the pressure fluctuations in the near-field. Moreover, stronger coherent structures are associated with enhanced entrainment, and thereby increased bulk-mixing. Thus, the fluctuation energy of $[\hat{p}(0) + 2\Re\{\hat{p}(1)\}]$ may be a suitable surrogate for real-time estimation of the level of mixing in the jet shear layer. In the above expression, the implicit dependencies are omitted for notational convenience.

Hall et al. (2006) also found that the near-field $\hat{p}(0)$ signal correlates better with the far-field noise than just the pressure signal by itself. Moreover, they reported that the correlation is greater with the far-field microphone at downstream angles compared to the sideline angle. This latter finding was to be expected since dynamics of large-scale structures are believed to be responsible for the peak of acoustic radiation to shallow angles with respect to the jet axis. In particular, Hall et al. (2006) observed a maximum normalized correlation coefficient of 0.34 between the signal from a far-field microphone placed at a polar angle of 30° and the $\hat{p}(0)$ signal at $x = 7.5$. For later reference, the corresponding correlation coefficient at $x = 3$ was 0.11. This behavior was later confirmed by Suzuki and Colonius (2006).

3.3 Unforced Jet Characteristics

The near-field pressure of unforced jets has been studied extensively in the past. Here, the data from the unforced Mach 0.9 jet in our facility is analyzed and compared to the results presented in the literature. One of the most well-characterized aspects of the near-field pressure is the demarcation between the hydrodynamic and acoustic signatures. This was first studied by Arndt et al. (1997) and later confirmed in numerous experimental assays

(Harper-Bourne, 2004; Coiffet et al., 2006; Tinney et al., 2008b). Arndt et al. (1997) showed that the noise sources may be modeled as essentially irrotational for predicting the variation of intensity of pressure fluctuations in the near-field. Depending on their frequency and the proximity of the observer, the pressure power spectrum is either dominated by the reactive (or hydrodynamic) pressure fluctuations that are $90°$ out of phase with velocity fluctuations, or the in-phase propagative (or acoustic) pressure fluctuations.

Arndt et al. (1997) showed that the reactive pressure intensity behaves as y^{-6} for constant frequency in the energy-containing range of the velocity spectrum, where y refers to the distance of the observer from the source. The peaks of the near-field pressure spectra typically correspond to this frequency range. The noise source model proposed by Arndt et al. (1997) also predicted that in the frequencies corresponding to the inertial subrange, the intensity decay should be $k^{-6.67}$ for a particular observation location, where k refers to the wavenumber. There is little dispersion in the irrotational near-field, so that $k = 2\pi f/a_0$, where f is the frequency and a_0 is the ambient speed of sound. Finally, the model also predicted that at high enough frequencies, the pressure spectrum should be propagative-pressure-dominated and hence display a $(ky)^{-2}$ decay. The demarcation between the hydrodynamic and acoustic components of the spectrum was reported as $ky \approx 2$ for low subsonic jets (Arndt et al., 1997; Harper-Bourne, 2004; Coiffet et al., 2006). For a Mach 0.85 jet the demarcation was found to be $ky \approx 3.5$ (Tinney et al., 2008b; Hall et al., 2009).

The computation of the power spectral density has been detailed before. The Strouhal number axis from such a spectrum is converted into an equivalent ky axis as follows. Following previous researchers, y is taken as the radial distance of the microphone from the

lip line. Then,

$$ky = \frac{2\pi f}{a_0}(r - 0.5)D = 2\pi\frac{U_j}{a_0}\left(\frac{fD}{U_j}\right)(r - 0.5) = 2\pi\frac{\mathcal{M}_j}{\sqrt{1 + \frac{\gamma - 1}{2}\mathcal{M}_j{}^2}}St_D(r - 0.5). \quad (3.8)$$

In the above, isentropic quasi-1-D compressible flow equations are used, γ represents the ratio of specific heats, $\mathcal{M}_j$ is the jet exit Mach number (0.9 for the present work), and r represents the radial location of the microphone (normalized by D).

The Kulite pressure transducers have a usable frequency range up to 10 kHz, and the demarcation between the hydrodynamic and acoustic parts of the spectrum is typically beyond this range. Hence, for this characterization, the data from the near-field microphones are reported. It must be mentioned that the spectrum computed using the two measurement systems did agree over their common bandwidths (20 Hz to 10 kHz).

The behaviors described above are well-replicated by the data collected at GDTL. Figure 3.2(a) shows the collapse of the spectra in the inertial subrange for multiple radial measurement locations at the same axial location. They also show an approximate acoustic decay behavior beyond $ky \approx 3.5$. Figure 3.2(b) shows collapse of data collected at different axial locations but the same radial location. As the microphone is moved downstream, the intensity increases due to greater proximity with the flaring shear layer. Moreover, the peaks are shifted to lower frequencies indicating the growth of the large-scale structures that account for the peak intensity. In Figure 3.2(c), it is seen that if the microphones are moved downstream in a line at an angle of 8.6° to the axis, then the spectra collapse fully. Thus, on such a line the increasing local noise source strength is being offset by the increase in radial distance of observation from the lip line. Moreover, the downshifting of the peak ky's observed in Figure 3.2(b) is being offset by the upshifting of the peak ky's noticed in Figure 3.2(a) so that the peaks also collapse. In Figure 3.2(d), this behavior is

(a) $x = 3.0$, various r (b) $r = 1.5$, various x

(c) Line array at $8.6°$ to axis, around $r = 1$ (d) Line array at $8.6°$ to axis, around $r = 1.5$
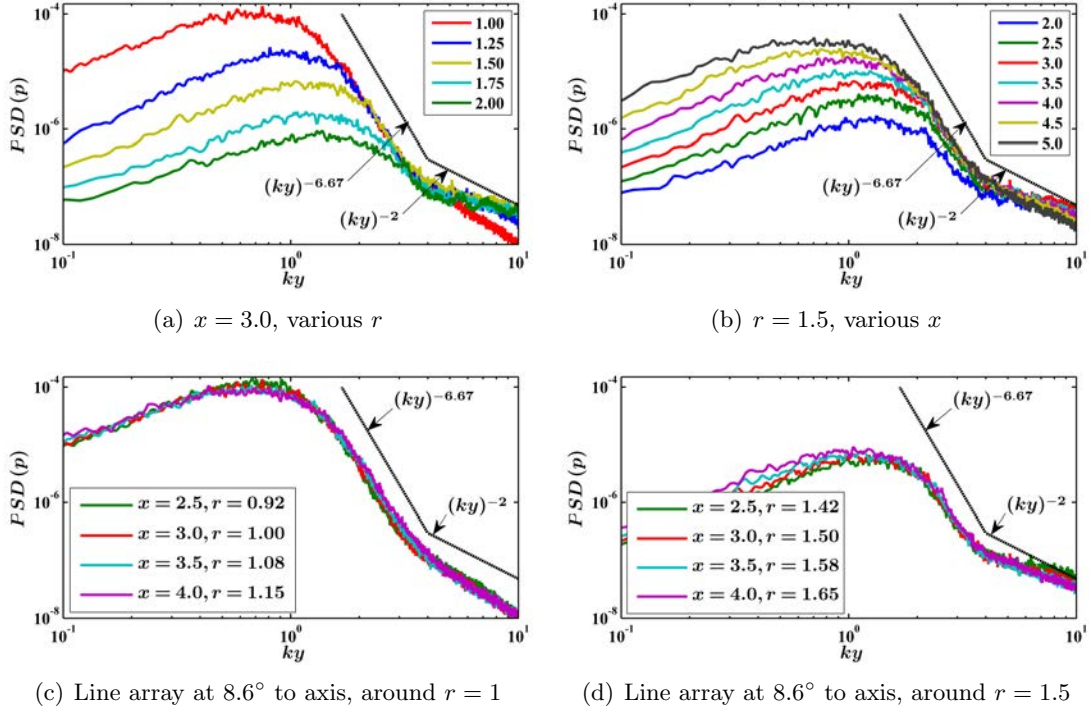
Figure 3.2: Wavenumber spectra.

also replicated by measurements taken on a line shifted further outward radially, but at the same angle.

The objective for studying the near-field pressure was to determine its suitability for feedback control. One of the first issues to be addressed was the positioning of the azimuthal ring array of pressure sensors. In practical applications, one would like to place the sensors as close as possible to the nozzle exit for ease of implementation. However, as mentioned earlier, Hall et al. (2006) reported that the correlation of near-field pressure to the far-field noise is low at the jet exit and reaches a maximum at $x = 7.5$. To balance these opposing constraints, the ring array location was chosen as $x = 3$. Hall et al. (2006) observed that at this location both the axisymmetric and first helical pressure modes have
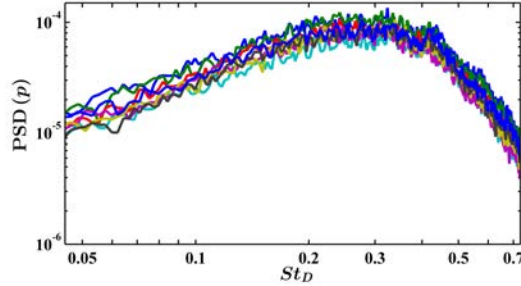
Figure 3.3: Power spectral densities of pressure field at $x = 3$, $r = 1$ for unforced jet from eight sensors around the azimuth line up, demonstrating coaxiality.

the maximum energy compared to all other streamwise locations. As explained earlier, the pressure sensors should be placed outside, but close to, the jet shear layer to be able to capture the signature of the large-scale structures that are to be controlled. Figure 3.2(a) demonstrates that the essential character of the observed spectrum does not change once $r \geq 1$ at $x = 3$, indicating that the shear layer does not extend beyond $r = 1$ at this location, except that the hydrodynamic portion of the spectrum becomes smaller. This was confirmed in PIV studies performed on the same jet at various forcing conditions too (Kearney-Fischer et al., 2009; Kim et al., 2009a). Hence, the tips of the Kulite pressure transducers were located at $x = 3$ and $r = 1$ for the results presented here.

Figure 3.3 demonstrates that the eight channels record almost identical power spectra, verifying that the jet is axisymmetric and the azimuthal array of pressure sensors is coaxially aligned to it. The range of frequencies represented cover the most energetic part of the spectrum. The high end cutoff is dictated by the bandwidth of the Kulite pressure transducers. Figure 3.4 shows the power spectra of the first four azimuthal-mode-filtered pressure signals; this is the most that one can resolve with eight sensors. At this streamwise location, $\hat{p}(1)$ is the strongest, followed by $\hat{p}(0)$. Hall et al. (2006) have observed that

36
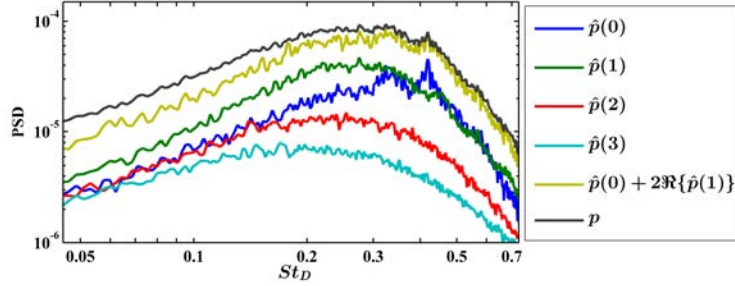
Figure 3.4: Power spectral densities of pressure field at $x = 3$, $r = 1$ for unforced jet at various azimuthal modes.

$[\hat{p}(0) + 2\Re\{\hat{p}(1)\}]$ is a good approximation to the fluctuating pressure p in the physical domain (see discussion related to eqn (3.7)). The spectrum of this composite quantity is indeed found to be quite similar to the mean spectrum from the eight individual channels in Figure 3.4.

A peculiar feature of the spectra in Figures 3.3 and 3.4 is the narrow-band peak at $St_D = 0.42$. Such a peak has not been reported in the literature, and even in the facility at GDTL, it was not very repeatable. The peak was most prominent in the axisymmetric mode of pressure. The amplitude of the peak was found to be most pronounced nearest to the nozzle exit. In particular, such a peak has never been observed in the far-field acoustic spectra studied extensively at GDTL. About two years after the completion of the experiments reported in this and the next chapter, some debris was detected behind the perforated plate just downstream of the stagnation chamber. The data presented in Figure 3.2 were collected after removal of the debris, and the peak is seen to be much reduced. At present, the best guess is that a minor imperfection in the jet plumbing is resulting in a mild resonance behavior.

37
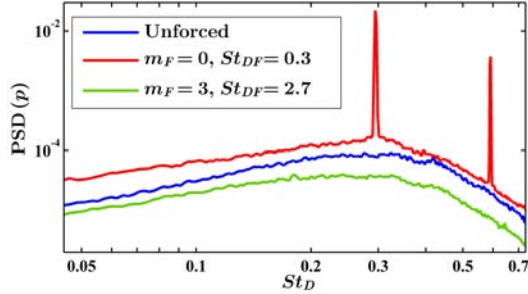
Figure 3.5: Representative near-field pressure spectra with open-loop forcing.

3.4 Forced Jet Characteristics

A comprehensive experimental assay was conducted to document the effect of open-loop forcing parameters on the near-field pressure. Forcing was performed at all possible simple azimuthal modes, viz. $m_F = 0$, 1, 2, and 3. The forcing Strouhal number St_{DF} was varied from 0.09 to 5.44 in varying step sizes. The azimuthal-mode-filtered pressure signals and their associated PSD and root mean square (RMS) were computed in post-processing.

Figure 3.5 shows the mean power spectra from the eight sensors for two representative open-loop forcing experiments compared to the unforced case. It will be shown that the case with $m_F = 0$ and $St_{DF} = 0.3$ corresponds to a maximum in the near-field pressure fluctuations, whereas that with $m_F = 3$ and $St_{DF} = 2.7$ corresponds to a minimum. The broadband amplification at the lower St_{DF} and attenuation at the higher one are noticeable in Figure 3.5. Similar effects and trends have been observed in the far-field noise also (Samimy et al., 2007c).

The energy in a pressure signal is represented by its RMS. This is an efficient computation and particularly suitable for model-free feedback control, as demonstrated in the next chapter. For reference, the reported metric from far-field acoustical experiments is overall

38

sound pressure level, which is actually just the variance of the measured acoustic signal. During feedback control, the signals would be band-pass-filtered in the frequency range depicted in Figure 3.5. For accurate comparison, this filter was also applied to the pressure signals captured in open-loop forcing before computing their respective RMS values.

Figure 3.6 presents the RMS of the near-field pressure and its various azimuthal-mode-filtered versions for a wide range of St_{DF}'s. The $m_F = 0$ and 3 cases are more pertinent for our application; so these forcing cases were explored on a finer grid of St_{DF}'s. The following observations are made regarding the results.

- For all forcing azimuthal modes explored, the RMS of the pressure as well as the RMS of each pressure azimuthal mode have similar characteristics - there is a relatively sharp maximum at a low St_{DF} and a broad minimum at a higher St_{DF}. The maximum clearly corresponds to the jet column mode; previous flow visualization and PIV results have shown that the jet exhibits the largest response to forcing around this St_{DF} (Kim et al., 2009a). The first (slightly lower) peak in RMS (p) for $m_F = 0$ aligns with the jet column mode. The second peak is caused by the unphysical axisymmetric-mode resonant behavior in the jet facility that was noted and discussed in the context of Figures 3.3 and 3.4. This peak is not observed in any of the sub-figures in Figure 3.6 that do not contain any contribution from the axisymmetric mode of pressure. The attenuation at higher St_{DF}'s is associated with the initial shear layer instability (Samimy et al., 2010).

- Figure 3.6(a) shows that the peak in RMS (p) is largest for $m_F = 0$ and smallest for $m_F = 2$ and 3.

(a) Pressure

(b) Axisymmetric mode

(c) First helical mode

(d) Second helical mode

(e) Third helical mode

(f) Sum of 0th and 1st azimuthal modes
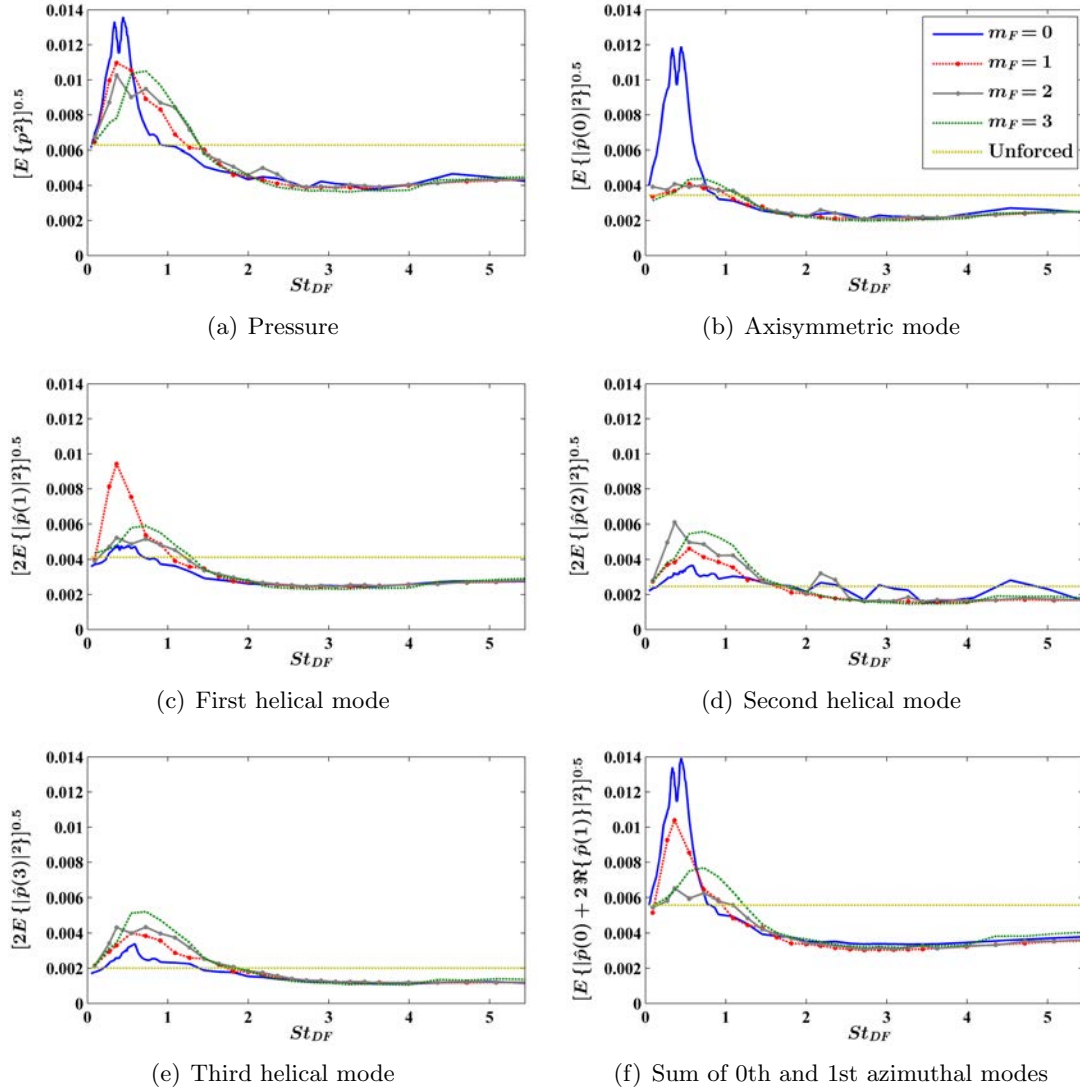
Figure 3.6: Effect of open-loop forcing Strouhal number St_{DF} and azimuthal mode m_F on near-field pressure and its various azimuthal modes. Each graph shows the effect of the four different forcing azimuthal modes explored on the RMS of an azimuthal component of pressure. Also, the RMS of the respective signals in the unforced case are shown for ease of comparison. Note that the $m_F = 0$ and 3 curves do not have markers since they were collected with a fine resolution.

- For a particular m_F, the maximum RMS is noted in the corresponding pressure azimuthal mode. For example, Figure 3.6(c) shows that the maximum value of RMS $\{\hat{p}(1)\}$ is obtained by forcing the jet at $m_F = 1$.

- The RMS of $[\hat{p}(0) + 2\Re\{\hat{p}(1)\}]$ shows characteristics similar to the RMS of the pressure itself.

- The switch-over from amplification to attenuation (the crossing of the curves with the unforced pressure RMS line) follows a set pattern for the pressure as well as all its azimuthal modes. In particular, the curves for $m_F = 0$ attenuate at the lowest St_{DF} and those for $m_F = 3$ attenuate at the highest St_{DF}.

- The different pressure azimuthal modes also exhibit a progression of crossover locations. For example, all the curves for RMS $\{\hat{p}(0)\}$ cross over at $St_{DF} \approx 0.9$ (but with differences therein, as mentioned above). However, this crossover happens at $St_{DF} \approx 1.8$ for RMS $\{\hat{p}(3)\}$.

- The effects of different forcing azimuthal modes become indistinguishable at higher forcing Strouhal numbers.

- The location of the minimum shifts to higher St_{DF}'s for increasing pressure azimuthal modes. While the minima for RMS $\{\hat{p}(0)\}$ and RMS $\{\hat{p}(1)\}$ occur at $St_{DF} \approx 2.7$, the other modes have their minima at $St_{DF} \approx 3.6$.

- The minima become flatter for higher pressure azimuthal modes, especially at the high-St_{DF} end.

3.5 Summary

One of the main objectives of this chapter is to characterize the extent of the hydrodynamic pressure field of the unforced jet, which is well correlated with the velocity field. This relationship will be repeatedly exploited in the rest of the thesis. For example, in Chapter 7, pressure measurements in the near-field are proposed as a means of real-time estimation of the flow velocity field for feedback control. The discussion concerning the wavenumber spectra presented in Figure 3.2 will be important for the correct placement of the near-field pressure sensors.

The other thrust of this chapter is the investigation of the effect of forcing the jet with LAFPAs on the near-field pressure. The overall conclusion from this exercise is that the response of this field is very similar to that of the acoustic far-field. Forcing with frequencies near the jet column mode causes amplification of fluctuations in both fields. Forcing at frequencies that are an order of magnitude higher results in attenuation of fluctuations, again in both fields. These similarities are exploited in Chapter 4 wherein the near-field pressure is treated as a surrogate for real-time extremization of the far-field acoustics.

Chapter 4

Extremizing Feedback Control

The research presented in this chapter was published in Sinha et al. (2010a).

4.1 Introduction

Consider a system (or plant, in control terminology) with one or more controllable input variables, several uncontrollable parameters, and a single measurable output variable. Assume that in the multi-dimensional response surface governing the behavior of the output with varying inputs and parameters, there is an extremum, i.e. a maximum or minimum, which represents a performance objective to be achieved. Consider also that while a controller for this plant only has the ability to modify the inputs, the parameters are uncertain and can vary slowly in time. Extremum-seeking or self-optimizing control refers to a class of techniques that seek to optimize the inputs of such a plant to extremize the output (Ariyur and Krstić, 2003). The only information that such a controller requires is the nature of the extremum, i.e. maximum or minimum. In particular, no explicit model of the plant's input/output behavior needs to be supplied. It is this model-free aspect that makes extremum-seeking control particularly suitable for flow control applications wherein detailed models are difficult to obtain (Beaudoin et al., 2006; Becker et al., 2007; Kim et al., 2009b).

The simplicity of extremum-seeking feedback control comes at the cost of neglected system dynamics. In the absence of a dynamic model, the plant must be assumed to be static, which means that the plant input cannot be varied too fast. This slows down the optimization process. In spite of this drawback, extremum-seeking control is pursued here as a preliminary assay in controller design for jet flows.

In general, jet actuation techniques strive to alter the initial development and dynamics of large-scale structures with the objective of controlling some aspect of the jet's global behavior. Two specific goals of jet control are far-field noise mitigation and bulk mixing enhancement. Both these objectives have been achieved in open-loop forcing experiments at GDTL using LAFPAs. It must be pointed out that the two goals cannot be attained simultaneously as they impose conflicting requirements on the large-scale structure dynamics, and hence on the actuation parameters.

At GDTL, extensive experimentation has revealed significant insight into the actuation mechanisms and parameters that result in far-field noise reduction (Samimy et al., 2007c, 2010). In particular, it has been generally observed that with eight LAFPAs, forcing with azimuthal mode $m_F = 3$ results in the best performance. The goal of extremizing feedback control in this context is to optimize the forcing Strouhal number St_{DF} in real-time to minimize far-field noise. The benefit of incorporating feedback control is that optimal performance may be guaranteed even with time-varying operating conditions by automatically adjusting St_{DF}.

For feedback control, a real-time measurement of the effect of forcing is needed. It is not practical to require direct sensing of far-field noise levels for control applications. In Section 3.2, it has been discussed that the axisymmetric mode of the near-field pressure may be a feasible surrogate for the far-field acoustics. So, for the purpose of extremizing

44

feedback control, the objective of mitigating far-field noise is reframed as the objective of minimizing the fluctuations in the axisymmetric mode of the near-field pressure. In this effort, the forcing azimuthal mode is to be retained as $m_F = 3$, and the St_{DF} is to be optimized in real-time. The actual effect on the far-field acoustics is to be observed in parallel for assessing the effectiveness of this control strategy.

The above investigation will be made by comparing the effect of closed-loop forcing on the far-field acoustics to the optimal case of open-loop forcing. The sense of this optimality is to be clarified here, since the optimal forcing frequency for far-field noise attenuation has been shown to be a function of the measurement polar angle. It has been discussed before that the larger scales in the jet shear-layer dominate the pressure signature in the near-field, as well as the acoustic far-field signature at shallow angles with respect to the downstream jet axis. On the other hand, the smaller scales of turbulence contribute most to the sideline angles in the far-field. Thus, it can be expected that minimizing the fluctuations in the near-field pressure (actually the axisymmetric mode of pressure, as discussed above) may also minimize the far-field noise at downstream angles; the same cannot be expected for sideline angles. This is also supported by the directivity of the near-field/far-field correlation reported by Hall et al. (2006) and discussed in Section 3.2. Hence, it is appropriate to compare the far-field spectrum for the feedback controlled case to the spectrum measured in the open-loop forcing case that resulted in the minimum noise radiated to the 30° location. The forcing parameters for the latter have been established to be $m_F = 3$ and any St_{DF} in the broad range from 1.5 to 3 (Samimy et al., 2007c).

The objective of bulk mixing enhancement has been explored in great depth in open-loop experimentation using LAFPAs at GDTL (Samimy et al., 2007b; Kim et al., 2009a; Kearney-Fischer et al., 2009; Samimy et al., 2010). It has been observed that the greatest centerline

(a) $m_F = 3$ (b) $m_F = 0$
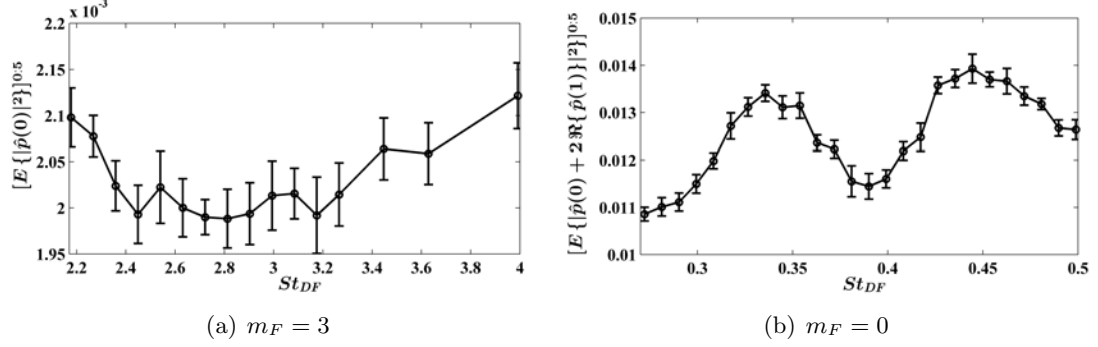
Figure 4.1: Details of open-loop forcing results pertinent to the two extremizing control problems considered.

Mach number decay rate, and centerline and lip-line turbulence growth rates are achieved by forcing the jet in the axisymmetric mode ($m_F = 0$) or the first flapping mode ($m_F = \pm 1$). For extremizing feedback control of bulk mixing enhancement, one needs to assess the degree of mixing in real-time. Measuring the velocity in the shear-layer is impractical and intrusive. However, as discussed in Chapter 1, the robust large-scale structures generated in the process of enhancing bulk mixing also create the greatest pressure fluctuations in the hydrodynamic near-field. Moreover, it was mentioned in Section 3.2 that the sum of the 0th and 1st azimuthal modes of pressure very nearly reconstructs the actual pressure field, while bestowing some noise-filtering characteristic to the measurements. Recall, that one has to consider both the +1 and the −1 azimuthal modes. Thus, for the purpose of extremizing feedback control, the objective of bulk mixing enhancement is reframed as the objective of maximizing the fluctuations in the sum of the 0th and 1st azimuthal modes of the near-field pressure. In this effort, the forcing azimuthal mode is to be retained as $m_F = 0$, and the St_{DF} is to be optimized in real-time. A similar investigation could be done by using $m_F = \pm 1$, but is not pursued here.
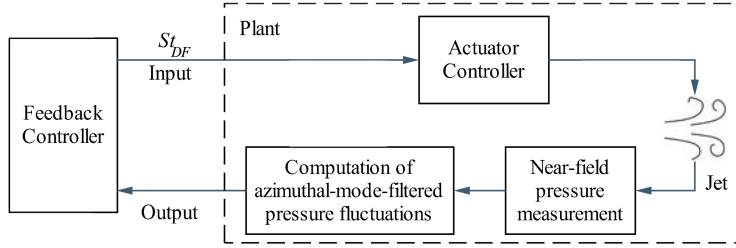
Figure 4.2: Extremizing feedback scheme for jet control.

The open-loop experiments revealing the character of the near-field pressure in the Mach 0.9 and $Re = 6.7 \times 10^5$ jet have been presented in Section 3.4. The relevant details are excerpted in Figure 4.1. Recall that pressure is normalized by $\rho_j U_j^2$, where ρ_j and U_j respectively denote the mean density and axial velocity at the jet exit. The time-resolved pressure signals are measured on an azimuthal array of eight transducers placed at $x = 3$ and $r = 1$. These functional dependencies are omitted for notational convenience, and only the azimuthal modal dependence is specified for the discussion in this chapter. The stochasticity of the plant is indicated by the uncertainty bars in the two curves. The exact formula for computing these uncertainties will be clarified following the presentation of the algorithms below.

To the author's knowledge, all extremum-seeking controllers presented in the literature are gradient-based. A gradient-based extremum-seeking control strategy has been implemented for the present application (Sinha et al., 2008). Although its steady state operation compared well with the optimal open-loop results, the convergence (transient behavior) was found to be very slow. For the highly turbulent flow under consideration, there is an inherent stochasticity that calls for gradient-free approaches. This chapter presents two novel gradient-free extremizing algorithms that are developed and implemented for the online

optimization of the near-field pressure. An overview of the control scheme is presented in Figure 4.2. On initialization with an arbitrary St_{DF}, the controllers automatically adjust the St_{DF} to optimize the plant output. Either controller can be used for maximization or minimization by simply switching the sign of the plant output that is fed back. Another aspect of the application that has bearing on the algorithms developed is that optimization is desired on only one forcing parameter, viz. St_{DF}. This makes the optimization problem 1-D.

The two extremizing feedback control algorithms developed, viz. modified Nelder-Mead and modified Kiefer-Wolfowitz algorithms, are respectively presented in Sections 4.2 and 4.3. The essential implementation details are delineated in Section 4.4. The results are presented in Section 4.5 and conclusions of this chapter are discussed in Section 4.6.

4.2   Modified Nelder-Mead Algorithm

In the optimization literature for deterministic scalar-valued functions, *direct search* is used "to describe sequential examination of trial solutions involving comparison of each trial solution with the 'best' obtained up to that time together with a strategy for determining (as a function of earlier results) what the next trial solution will be" (Hooke and Jeeves, 1961). Although these algorithms were originally proposed as heuristics, recent analysis demonstrates that many of them have provable convergence properties (Lagarias et al., 1998; Lewis et al., 2000). In particular, global convergence has been proven for a subset of these techniques called *pattern search* algorithms (Torczon, 1991, 1997). The present application is a 1D problem, for which pattern search is identical to direct search. Lewis et al. (2000) present a review of direct search methods and their historical evolution. The

most popular direct search technique is the simplex-based Nelder-Mead algorithm (NMA) (Nelder and Mead, 1965).

The present application concerns a *stochastic single-variable* scalar-valued cost function; moreover the optimum of the function may vary with time. Barton and Ivey (1996) recommended modifications to the original NMA for robust behavior in the presence of statistical uncertainty. Torczon (1989, 1991); Dennis and Torczon (1991) designed a pattern search technique, the Multi-Directional Search Method, for provable convergence in a deterministic setting. Torczon (1989) also provided empirical evidence of reliable optimization of stochastic cost functions using this algorithm. The modified Nelder-Mead Algorithm (mNMA) controller proposed herein is a model-free direct search algorithm based on all the above results with several additional enhancements for use in real-time optimization of slowly time-varying cost functions.

The flowchart for the mNMA is presented in Figure 4.3. Let the single-variable scalar-valued cost function to be maximized be denoted by $h : \mathbb{R} \to \mathbb{R}$. For this 1D problem, the simplex is a 2-element set of vertices representing the end points of a line; let this set be $S = \{S_1, S_2\}$. The initial choice of these vertices must be specified by the user, or by another algorithm. In the optimization process, the algorithm adapts the size and location of the simplex so that its vertices tend to converge upon the optimum. However the user specifies the maximum $S_{\max}$ and minimum $S_{\min}$ allowable size of the simplex; the rationale is explained next.

In offline optimization of a static cost function, one is solely concerned with the final optimal simplex; hence the simplex is allowed to collapse to a point. However, in an online optimization application, one not only expects the process to converge upon the optimal value, but to remain 'alive' to possible subsequent changes in the optimal value itself. This
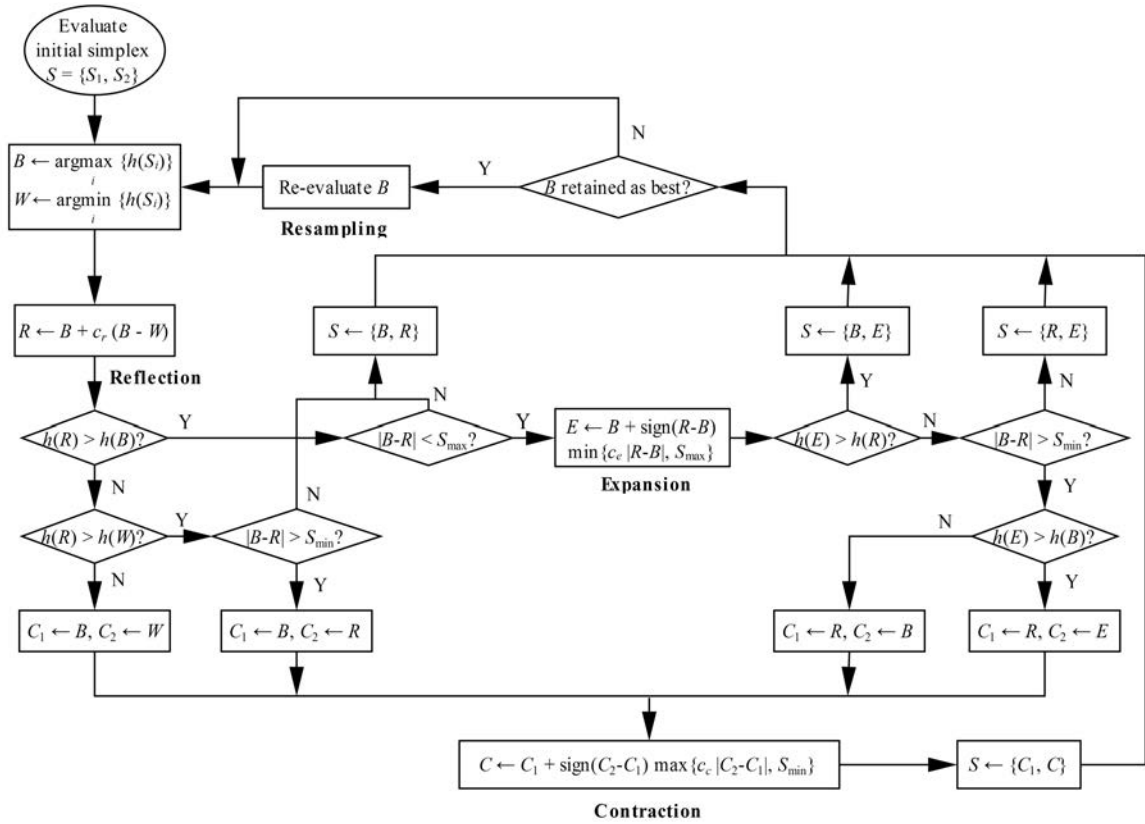
Figure 4.3: Flowchart of the modified Nelder-Mead algorithm for maximizing the cost function $h(\bullet)$.

argues for imposing a lower bound $S_{\min}$ on the simplex size, since a point simplex would be insensitive to the local gradient of the input/output map. This also corresponds to the notion of persistent excitation used in the adaptive control literature since it ensures a minimum amplitude of oscillation of the plant input. As a safety precaution, an upper bound $S_{\max}$ is also applied on the simplex size. In a stochastic setting, a few successive uncertain observations can drive the simplex far away from the optimum. First of all, this might result in actuator saturation. Also, the controller may require a large number of iterations to recover from such a large excursion.

The process begins with the evaluation of $h(\bullet)$ at the vertices of the initial simplex before entering the iterator. The loop starts by ranking the vertices based on their functional values. In a maximization problem, the best vertex B would be the one with the highest function value. Since in a 1-D problem there are only 2 vertices, the other one would be the worst vertex W. This is written as

$$B \leftarrow \arg\max_{i\in\{1,2\}} h(S_i), \quad W \leftarrow \arg\min_{i\in\{1,2\}} h(S_i). \tag{4.1}$$

This use of the mere rank distinguishes the direct-search techniques from the gradient-descent methods which would typically use a finite difference approximation of the local gradient of the cost function.

The next step is *Reflection*. It is based on the hypothesis that a more optimal value of the independent variable can be found on the opposite side of B, away from W. The reflected vertex R is calculated as

$$R \leftarrow B + c_r(B - W), \tag{4.2}$$

where, $c_r \geq 1$ is the reflection coefficient. A typical value of c_r is 1. The expression $h(R)$ is evaluated at this point.

On reflection, if it is found that $h(R) > h(B)$, then it is logical to hypothesize that the optimum is further along the directed line segment $\overrightarrow{BR}$. This would then warrant *Expansion* of the simplex, but only if it is smaller than $S_{\max}$. Also, the expansion step might itself cause the simplex size to exceed its bound, in which case it must be forcibly shortened. Thus, the expanded vertex E is computed as

$$E \leftarrow B + \text{sign}(R - B) \min(c_e |R - B|, S_{\max}), \tag{4.3}$$

where, $c_e > 1$ is the expansion coefficient. Typically, $c_e = 2$. At this point, $h(E)$ is evaluated. If $h(E) > h(R)$, then the expansion step is deemed successful and the new simplex is set to $\{B, E\}$ before looping back to the reflection step. (The return path goes through a *Resampling* step that will be discussed later.) If on the other hand $h(E) \leq h(R)$, then the original NMA would have set the new simplex as $\{B, R\}$ before the ensuing reflection. There is an issue with this scenario that is peculiar to a 1-D application. With the typical values of c_r and c_e as above, the next vertex to be evaluated on reflection of B through R would be E again. Since functional evaluations are typically expensive, one should avoid this successive evaluation of E. A better option is as follows.

Note that this branch of the algorithm is entered only if $h(B) < h(R)$ and $h(E) \leq h(R)$; thus the optimum can be hypothesized to lie in between B and E. Also, it is logical to perform a *Contraction* of the simplex to concentrate the search effort in the most promising sub-interval. An additional complication is introduced by the lower bound $S_{\min}$ on the simplex size. Consider the logical step in case the simplex cannot be contracted any further, i.e. if $|B - R| = S_{\min}$. (Note that $|B - R|$ cannot be less than $S_{\min}$ as $c_r \geq 1$, and $|B - W| \geq S_{\min}$ would have been enforced in the previous iteration.) Since R is the best vertex, it should be retained in the simplex. Furthermore, E has been evaluated most recently, and hence should not be re-evaluated. So, the only option is to re-evaluate B. This

can be achieved by setting the simplex to $\{R, E\}$ and looping back to the reflection step. If on the other hand $|B - R| > S_{\min}$, then Nelder and Mead's idea of the *Inside/Outside Contraction* is employed (Nelder and Mead, 1965). In particular, if $h(E) > h(B)$, then it is logical to contract the $\{R, E\}$ simplex toward R. On the other hand, if $h(E) \leq h(B)$, then the $\{R, B\}$ simplex should be contracted toward R.

Until now, the discussion has concerned the case where $h(R) > h(B)$ and the simplex size has not reached its maximum. In case the first condition is satisfied but not the second, then the simplex cannot be expanded further. However, it is hypothesized that the optimum lies on the other side of R away from B (this is what motivated the expansion in the first place). In this case, the correct option is to set the new simplex as $\{B, R\}$. Note that in the ensuing reflection, B would be reflected through R to give the E vertex that a normal expansion step would have explored. This completes the discussion for the branch of the algorithm wherein the reflection creates a new best vertex.

In case $h(R) \leq h(B)$, the optimum can be hypothesized to lie in between W and R; this would warrant a *Contraction* per the above discussion. Following the NMA, if $h(R) > h(W)$ then an *Outside Contraction* is performed. For the 1D application under consideration, this involves discarding the W vertex and contracting the $\{B, R\}$ simplex toward B. If on the other hand $h(R) \leq h(W)$, then an *Inside Contraction* is effected by contracting the $\{B, W\}$ simplex toward B. There is a (by now familiar) problem with the outside contraction: if the simplex size is the smallest that it can be, then the contraction would not change the worst vertex R, and it would be evaluated twice in succession. A more preferable option in this case would be to set $\{B, R\}$ as the new simplex before looping back to a reflection. Note that the constraint of the lower bound on the simplex size does not affect the *Inside Contraction*. In that case, if the simplex is at its minimum size, then the contraction would

not change the worst vertex W, and it would be evaluated again, but not twice in succession. This would be the correct option under the circumstances.

The above discussion has delineated the four routes by which one can arrive at a contraction step. Also, for each such path, the better vertex (call it C_1) that is to be retained and the worse vertex (call it C_2) that is to be rejected have been indicated. The actual contraction step is identical to the one in the NMA except for the enforcement of the minimum size constraint on the simplex, $S_{\min}$. That is, the contracted vertex C is calculated as

$$C \leftarrow C_1 + \text{sign}(C_2 - C_1)\ \max(c_c|C_1 - C_2|, S_{\min}), \tag{4.4}$$

where, $c_c < 1$ is the contraction coefficient. A typical value of c_c is 0.5. At this stage, $h(C)$ is evaluated. The contracted simplex $\{C_1, C\}$ is accepted unconditionally and the algorithm proceeds to the next reflection step. The original NMA also includes a *Shrink* step. However, for a 1-D problem, it duplicates the contraction step, albeit with a possibly different coefficient; it is therefore not included in the proposed algorithm.

Finally, consider the *Resampling* step adopted from Barton and Ivey (1996) to address stochasticity. In essence, although the vertex B might not be the true optimum, a single observation of its functional value in a stochastic setting might make it appear optimal. So, at the end of an iteration (before the next reflection step), if B is retained as the best vertex, then it is re-evaluated and its old functional value is replaced with the new one in subsequent rank determinations.

In summary, three modifications are proposed for the classical NMA to adapt it for a 1D stochastic cost function with a time-varying optimum: (i) resampling, (ii) imposition of lower and upper bounds on the simplex, and (iii) avoiding the repeated successive evaluation of the same vertex. The flowchart for mNMA in Figure 4.3 indicates a perpetual loop in

accordance with the persistent excitation philosophy. However, the process can be stopped at any time by manually switching off the controller implementing the algorithm.

4.3 Modified Kiefer-Wolfowitz Algorithm

Robbins and Monro (1951) pioneered the field of *stochastic approximation*, the study of search techniques that successfully reach a pre-assigned goal in spite of uncertainty. Kiefer and Wolfowitz (1952) adapted the idea to the problem of finding the extremum of a unimodal function in a stochastic setting. Although the original algorithm was gradient-based, a later variant was developed for gradient-free stochastic optimization (Wilde, 1964). In general, these algorithms evaluate a converging sequence of iterates that extremize the cost function, the stochasticity being addressed by making the convergence gradual.

The discussion begins with a brief presentation of the original Kiefer-Wolfowitz algorithm (KWA). Consider the stochastic cost function $h(y_n)$, where y_n is the independent variable at the nth iteration of the procedure. It is assumed that the stochastic uncertainty is unbiased and that $E\{h(\bullet)\}$ is a convex unimodal function, where $E\{\bullet\}$ is the expectation operator. The goal is to iteratively find the y that maximizes $E\{h(y)\}$ by only evaluating $h(\bullet)$. (For minimization, the negative of $h(\bullet)$ can be passed to the routine.) In KWA, the expected gradient $E\{h'(y_n)\}$ is estimated as a finite difference using a positive and negative perturbation. The center y_{n+1} of the next pair of measurements is then computed as

$$y_{n+1} = y_n + a_n \frac{h(y_n + c_n) - h(y_n - c_n)}{c_n} \tag{4.5}$$

where, $a_n > 0$ and $c_n > 0$ are respectively the step size and perturbation level at the nth iteration. The convergence proof of the technique (Kiefer and Wolfowitz, 1952) makes the following assumptions on the sequences c and a:

$$\lim_{n \to \infty} a_n = 0, \quad \lim_{n \to \infty} c_n = 0, \quad \sum_{n=1}^{\infty} a_n = \infty, \quad \sum_{n=1}^{\infty} \left(\frac{a_n}{c_n}\right)^2 < \infty. \tag{4.6}$$

One common choice for a_n is a_1/n, with $a_1 > 0$. Then, a possible choice for c_n is c_1/n^b, with $0 < b < 0.5$ and $c_1 > 0$.

For real-time optimization of a slowly time-varying cost function, the process must provide persistent excitation. Thus, the modified Kiefer-Wolfowitz algorithm (mKWA) implements lower bounds $a_{\min}$ and $c_{\min}$ on the step size a and perturbation level c, respectively. Note that this would violate the conditions placed on the sequences a and c. Hence, one cannot expect convergence to the local optimum; instead, the independent variable can be expected to oscillate in a neighborhood of this optimum.

The KWA is essentially a gradient-descent algorithm, albeit for a stochastic function. This is not suitable in situations where the cost function, although convex, has a very small slope in the vicinity of the maximum. Also, this will delay convergence in case the function has inflection points. The solution described by Wilde (1964) is termed *normalization*. Essentially, instead of the actual value of the slope, only its sign is used in the optimization. Thus, at the end of each iteration, the new center for the next pair of measurements is computed as

$$y_{n+1} = y_n + a_n \text{sign} \left\{ h(y_n + c_n) - h(y_n - c_n) \right\} \tag{4.7}$$

This normalization transforms the KWA from a gradient-based process to one that uses the rank information of the sampled points only, similar to direct search. It was adopted in the proposed mKWA.

The other important modification is the *acceleration* protocol proposed by Kesten (1958); he argued that a change in the sign of the slope would indicate that the optimum was crossed over from one side to the other between the last two iterations. Thus such a sign change should be followed by a reduction of the step size a for convergence. However, far away from the optimum (signified by a constant sign of the slope), reducing

a would only serve to slow down convergence, and hence must be avoided. In the original KWA, a_n and c_n are modified in lock-step with the iterate y_n; the acceleration method decouples these two processes. So, although y_k is still updated for every step index k, the index n governing the decrease of a_n is incremented only on the detection of a change in the sign of the estimated slope. Additionally, Kesten stipulated that the perturbation level c_n should be a constant.

Kesten's acceleration protocol is adopted in the proposed mKWA, but the perturbation level was not kept constant. Instead, c_n is allowed to decrease from an initial higher value down to the lower bound $c_{\min}$ imposed on it by the first modification proposed above. The reasoning is as follows. The lower bound $c_{\min}$ cannot be too large, otherwise the variable y as well as the cost function $h(\bullet)$ will continue to make large excursions from their respective optima even in the steady state, which is undesirable. However, following Kesten, if relatively small perturbations are used from the beginning of the process, then the process may be overly sensitive to uncertainty, thereby delaying convergence. Thus, in mKWA, the initial perturbation level c_1 is set suitably high and the c_1/n^b formula is used for decrementing it in lock-step with the step-size decrements. Since this adaptation of c only occurs during the initial stages, the constraint of $0 < b < 0.5$ is not binding any longer and one may freely tune this parameter to improve performance. Note that this does not really violate Kesten's stipulation since the perturbation level becomes constant at $c_{\min}$ after a short initial period.

The pseudo-code of the modified Kiefer-Wolfowitz algorithm for maximizing the function $h(\bullet)$ is presented below.

$\text{MKWA}(h, y_1, c_1, a_1, c_{\min}, a_{\min}, b)$

1   $k \leftarrow 1, n \leftarrow 1$
2   **while** (not manually overridden)
3       $s_k \leftarrow \text{sign}\{h(y_k + c_n) - h(y_k - c_n)\}$
4   **if** ($k > 1$ AND $s_k \neq s_{k-1}$)
5          $n \leftarrow n + 1, c_n \leftarrow \max\{c_1/n^b, c_{\min}\}, a_n \leftarrow \max\{a_1/n, a_{\min}\}$
6       $y_{k+1} \leftarrow y_k + a_n s_k$
7       $k \leftarrow k + 1$

4.4   Implementation Details

The experimental setups for the jet, the LAFPAs, and the measurement of the near-field pressure have been discussed in Chapter 2. For assessing the extremizing feedback control algorithms, the near-field pressure signals must be fed to the controller and the commanded actuation frequency must be conveyed to the LAFPA system. The details of this implementation will be discussed here. At the outset, it must be recalled that time is normalized by D/U_j, where D is the jet nozzle exit diameter and U_j is the nominal axial velocity at the exit.

4.4.1   Hardware Setup

The hardware timing parameters are specified in Hz below; for ease of reference, note that 1 kHz corresponds to a Strouhal number of 0.09 for the present application. During unforced jet experiments and open-loop forcing cases, the signals from the pressure transducers were amplified, low-pass filtered at 100 kHz, and acquired using an eight channel National Instrument (NI) PCI-6143 ADC card at a sampling rate of 200 kHz. In closed-loop experiments, a dSpace 1103 DSP board operating at 50 kHz clock rate was used to implement the control algorithm. In these cases, each of the eight channels of output from the 100 kHz low-pass filter was split in two. One signal from each splitter was acquired by the above ADC board for offline computation of statistics in steady-state operation.
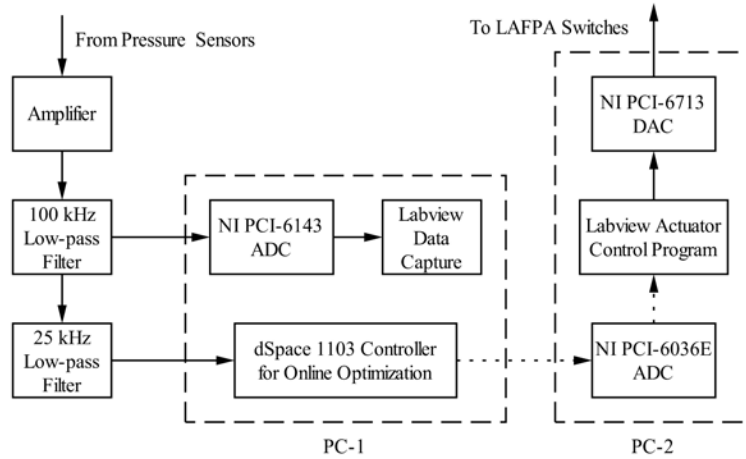
Figure 4.4: Schematic of data flow in closed-loop experiments. During open-loop forcing, the dSpace controller was removed from the loop and the LabVIEW Actuator Control Program accepted a user-entry for the forcing parameters. In unforced jet experiments, both the dSpace controller and PC-2 were disconnected. The solid arrows indicate eight channels of data flow; the dotted arrows indicate control information flow.

The other set of signals were again low-pass filtered at 25 kHz before being routed to the input channels of the dSpace board. The dSpace program captured the transient pressure data along with a number of control variables. A schematic of the data flow is shown in Figure 4.4.

The LabVIEW program for controlling the LAFPAs periodically samples the forcing frequency from an output DAC channel of the dSpace board. For this, the PC-2 running the LabVIEW program is connected to two NI PCI cards. One of them is the 8-channel PCI-6713 output DAC card that conveys the switching signals to the MOSFET switches; it operates at 780 kHz. The second is an 8-channel PCI-6036E ADC input card; only one of its input channels is utilized here.

The azimuthal filtering of the pressure data is performed at each sample instant within the dSpace controller. Only the azimuthal mode pertinent to a particular problem at hand

is computed, and this is sent to the algorithm that computes the RMS that is discussed next.

4.4.2 Real-time Computation of Pressure Fluctuation Level

The offline computation of RMS is a straightforward matter. However, the real-time calculation of the RMS of a turbulent quantity poses some challenges. In a digital hardware implementation, the plant output must be sampled as often as possible over a large enough time window (denoted by T_{rms}) to reliably estimate the RMS over this sample size. An efficient way of implementing this is to keep a running sum of the squares of the sampled output values over the desired time window. At the end of the time window, the final sum is divided by the number of samples in the time window and the square root of the quotient is computed. This computed value is then "held" as the RMS of the output while the running sum is restarted from 0 to repeat the cycle. The choice of T_{rms} is crucial to the performance of the feedback control system aimed at extremizing the RMS. If T_{rms} is too short, then the RMS value would be unreliable. On the other hand, if T_{rms} is too long, then the response time of the extremizing controller will be longer, leading to slower convergence to the optimum.

Figure 4.5 shows the results of a study conducted to determine the effect T_{rms} on the estimated RMS. Four different time windows were used, viz. 440, 1100, 2200 and 4400, all specified in terms of flow time steps. The signals from the eight pressure transducers were sampled at 50 kHz ($St_D = 4.54$) in dSpace. The axisymmetric mode of pressure was computed at each sample instant, and the RMS was computed using the procedure described above. The jet forcing parameters are indicated in the figure caption. As expected, longer values of T_{rms} result in lesser variability in the estimated RMS. Although this result confirms intuition, it is not a complete guide to the optimal choice of T_{rms}, as discussed next.
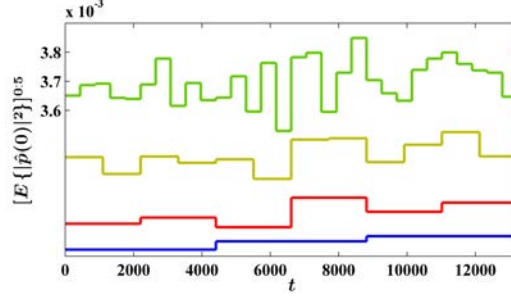
Figure 4.5: Parameter study for real-time estimation of fluctuations with various time-windows indicated by the hold times on the individual curves. The jet was forced at $St_{DF} = 0.91$ and $m_F = 3$. Note that the curves are shifted for visualization.

The variability (or noise) in the output is directly controlled by T_{rms}. However, the acceptable level of variability is determined by the actual output (or signal). This constitutes the signal-to-noise ratio (SNR) that is considered in the design of any measurement system. Figure 4.1 presented the plant input/output maps pertinent to the two extremizing problems at hand. Here, SNR is defined as the ratio of the nominal value of the RMS to the standard deviation of the estimated RMS. It depends on the St_{DF} as well as the T_{rms}. In Figure 4.1(a), the error bars indicate the standard deviations in the RMS values calculated with $T_{\mathrm{rms}} = 2200$. The SNR averaged over the marked data-points was 66. In closed-loop experiments aimed at minimizing the RMS of $\hat{p}(0)$, this T_{rms} was found to be a good balance between reliability and speed of convergence. Next consider the open-loop results presented in Figure 4.1(b). The nominal signal is much higher in this case, and it was found that $T_{\mathrm{rms}} = 1100$ resulted in an average SNR of 64 over the marked data points. The standard deviations computed with this sampling window are indicated by the error bars in Figure 4.1(b). This T_{rms} of 1100 and its corresponding SNR were found to be a good choice in closed-loop control experiments aimed at maximizing $[\hat{p}(0) + 2\Re\{\hat{p}(1)\}]$. For completeness, experiments

(a) $St_{DF} = 0.39$ (b) $St_{DF} = 1.02$
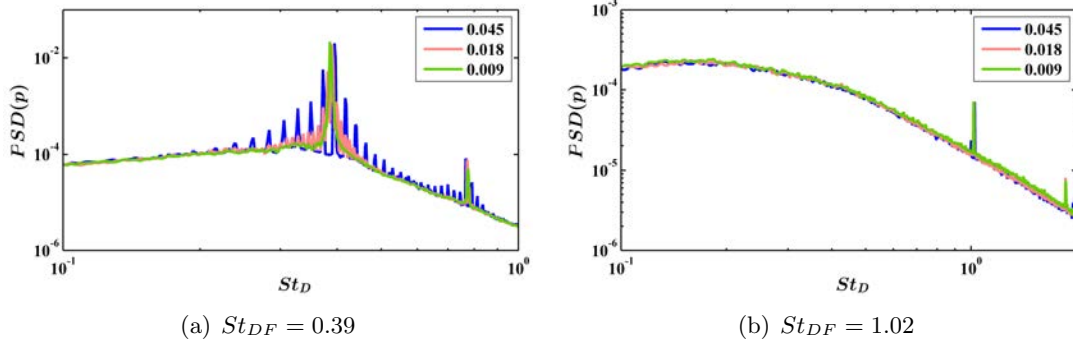
Figure 4.6: PSD of near-field pressure for different listening rates in the closed-loop system, as indicated in the legends. The forcing azimuthal mode is $m_F = 0$, and the constant forcing frequencies in the respective captions are commanded from dSpace.

were conducted to determine the average uncertainty characteristics of the input/output map shown in Figure 4.1(a) with $T_{\mathrm{rms}} = 1100$, and the resulting SNR was found to be 45.

4.4.3   Actuator Controller Listening Rate

The control signal from dSpace is sampled by the LabVIEW program at a finite frequency termed the "listening rate". Immediately after a new control input is sampled, the LabVIEW code uses software signal generators to create eight pulse packets, one for each actuator, with the newly commanded frequency. The packets are automatically sized, so that they can be sent out within the listening time period. Recall that the pulse update rate for the LAFPA control system is 780 kHz ($St_D = 70.8$). Thus, for example, with a listening rate of $St_D = 0.009$, each packet will have 7800 samples. The computation of the pulse packets requires a finite time on the microprocessor during which the actuators are "quiet". Once the pulse trains are computed, they are sent as output on the DAC card using a buffer. On completion of this output task, the LabVIEW code will sample the control signal from dSpace again, and the cycle will be repeated.

Experiments were performed on the closed-loop system to assess the impact of the listening rate. The first investigation was conducted by commanding a constant forcing Strouhal number $St_{DF} = 0.39$ from dSpace with $m_F = 0$; this is a typical value that would be encountered in experiments aimed at maximizing bulk mixing. Figure 4.6(a) compares the PSD of near-field pressure for three different listening rates expressed in non-dimensional Strouhal number: 0.009, 0.018 and 0.045. In another set of experiments, a constant $St_{DF} = 1.02$ was issued from dSpace with $m_F = 0$; this is at the lower extreme of the range of St_{DF} in experiments involving minimizing far-field noise. Figure 4.6(b) compares the PSD for this set of experiments with the same three listening rates. Two distinct behaviors are to be noted: (*i*) increasing the listening rate makes the spectrum noisier for the same commanded forcing frequency, and (*ii*) the spectrum is smoother for higher forcing frequencies with the same listening rate.

It has been discussed above that the minimum time window for RMS computation is 1100 flow time steps. This means that the maximum rate at which the feedback controller would be updating the commanded St_{DF} is 0.0009. For this update rate, a listening rate of 0.009 was deemed to provide adequate responsiveness while resulting in a clean spectrum. This was used in all closed-loop control experiments.

4.4.4 Time Delay and Static Map

An important assumption in the implementation of extremizing controllers is the absence of plant dynamics. Step-response experiments were conducted to verify this.

The following step input was chosen:

$$St_{DF} = \begin{cases} 0.09, & \text{if } 0 \leq t \leq 1100 \\ 0.45, & \text{if } 1100 < t \leq 2200 \\ 0.73, & \text{if } 2200 < t \leq 3300 \text{ flowtimesteps.} \end{cases} \tag{4.8}$$

(a) Listening $St_D = 0.009$

(b) Listening $St_D = 0.018$

(c) Listening $St_D = 0.045$

(d) Listening $St_D = 0.09$
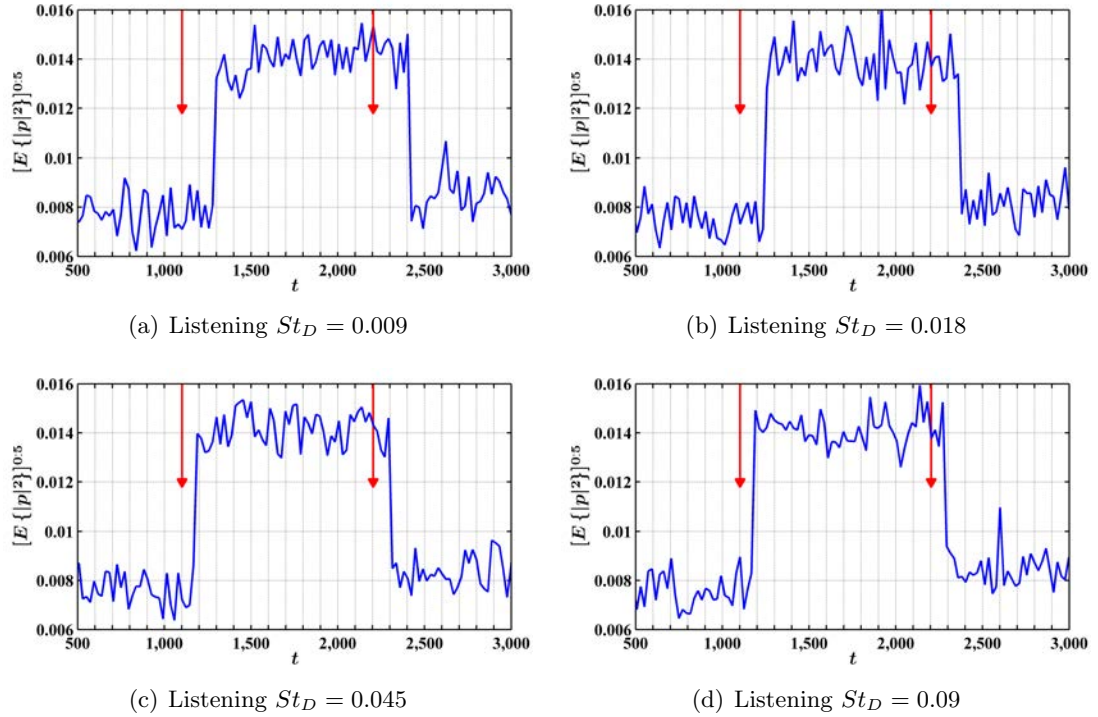
Figure 4.7: Step responses with different listening rates indicated. At the first arrow in each plot, the input St_{DF} was abruptly changed from 0.09 to 0.45; at the second arrow, it was changed again to 0.73. The y-axes show the RMS of near-field pressure measured over 22 flow time steps (100 samples) each.

The forcing azimuthal mode was $m_F = 0$. The signals from the eight pressure sensors were acquired at a sampling rate of 50 kHz ($St_D = 4.5$). In post-processing, the RMS over all channels was computed using a moving window of 22 flow time steps (100 samples) with no overlap. At every 22 time steps, one thus obtains an RMS value representing the pressure fluctuations over the previous 22 time steps; these are reported in Figure 4.7. It is evident that the delay between command and response decreases with increasing listening rate. However, with listening rates set at St_D's of both 0.045 and 0.09, the delay is about 110 flow time steps. This implies that there are other factors that introduce delays in the plant, but that their contributions total less than 10 ms.

It has been discussed above that the listening rate was chosen to be $St_D = 0.009$. For this, the time delay is less than 220 time steps. To account for this delay in the implementation, the control routine incorporated a wait time of 220 time steps (20 ms) between directing the actuators to use a particular forcing frequency and starting to record the corresponding pressure data. Such a strategy makes the plant appear effectively static to the controller.

4.5   Results

Two different sets of experiments were conducted for achieving the two performance objectives established in Section 4.1, viz. minimizing far-field noise and maximizing bulk mixing. The results from these experiments are presented in Sections 4.5.1 and 4.5.2, respectively. In either case, both the mNMA and mKWA extremizing controllers are employed and their performances are compared.

4.5.1 Minimizing Far-field Noise

The far-field noise may be reduced by focusing on reducing the RMS of $\hat{p}(0)$ in the near-field, as discussed in Section 4.1. With the forcing azimuthal mode m_F set to 3, the effect of the forcing Strouhal number St_{DF} on this latter quantity has been presented in Figure 4.1(a). The two extremizing controllers were evaluated for the task of minimizing this cost function after being initiated from various St_{DF}'s in the range of 0.9 to 4.5. From the static input/output map, one is expecting convergence to the broad minimum between St_{DF}'s of 1.5 and 3. At the same time, one expects that once steady-state is reached, the near-field pressure fluctuations and the far-field acoustic levels should be close to their respective minima found in open-loop experiments.

Results with Modified Nelder-Mead Algorithm

The mNMA seeks the optimal forcing Strouhal number and ensures steady-state operation in the vicinity of the optimum by issuing a converging sequence of St_{DF}'s. The operation of mNMA is governed by a number of tunable parameters, many of which are dictated by the input/output map found in open-loop parameter sweep experiments (see Figure 4.1(a)). The map shows a very gradual slope in the range of St_{DF} from 3 to 5; thus a large value of $S_{\max} = 0.45$ was selected. Note that this sets the maximum change in St_{DF} in any one iteration of the mNMA process. With $S_{\max} = 0.27$, convergence to the optimum from an initial St_{DF} of 4.5 was not repeatable. With $S_{\max} = 0.9$, the convergence was repeatable and rapid, but there was a large overshoot that caused delays in settling. The I/O map also indicates that the minimum is broad; hence an appropriate choice of $S_{\min}$ was 0.09. At present, it is unknown as to what constitutes an adequate level of persistent excitation in real applications. Here, the goal is to show that a meaningful level can be

feasibly established by the mNMA controller. Experiments with $S_{\min}$ set to 0 and 0.18 have also shown satisfactory steady state behavior. The timing parameter T_{rms} was set to 2200 flow time steps for reasons discussed in Section 4.4.2; convergence was unreliable with $T_{\mathrm{rms}} = 1100$.

Following the published literature (Nelder and Mead, 1965; Torczon, 1989), the simplex transformation parameters were set as $c_r = 1$, $c_c = 0.5$, and $c_e = 2$. The initiating St_{DF} was set as the first vertex of the initial simplex S_1. The other vertex of the initial simplex, S_2, was determined by the initial size of the simplex chosen. This value should be chosen such that the algorithm can reliably rank its vertices initially; this means that S_1 and S_2 must be spaced far enough apart so that their functional values have the correct rank in spite of uncertainty. For fastest convergence, the initial simplex size was always specified to be $S_{\max}$.

The transient behavior is demonstrated with the process initialized at three different St_{DF}'s. Figure 4.8(b) shows that in all three cases, the plant output $[E\{|\hat{p}(0)|^2\}]^{0.5}$ reaches and settles around 0.002 within $5T_{\mathrm{rms}}$, i.e. using just 5 evaluations of the plant output. This convergence rate represents an order of magnitude improvement compared to the results with the gradient-based extremum-seeking controller (Sinha et al., 2008). Also note that this steady-state value of the plant output is the minimum obtained in open-loop experiments (see Figure 4.1(a)). Figure 4.8(a) indicates that the St_{DF} reaches ≈ 2.7 within the same time, but it varies within 2.4 to 3.0 subsequently, even though $S_{\min} = 0.09$. This can be explained by the broadness of the minimum. Since all initial conditions led to similar steady state behavior, the PSD of the axisymmetric mode of the near-field pressure is presented for just one case in Figure 4.9(a), viz. for an initial St_{DF} of 4.5. The spectrum with mNMA is quite similar to the optimal open-loop spectrum, especially in the high-amplitude
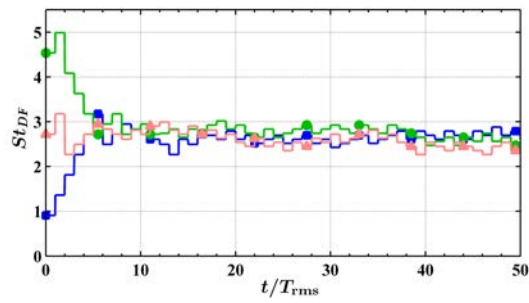
67

(a) Plant input with mNMA
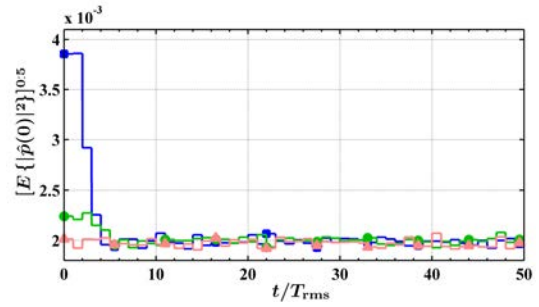
(b) Plant output with mNMA
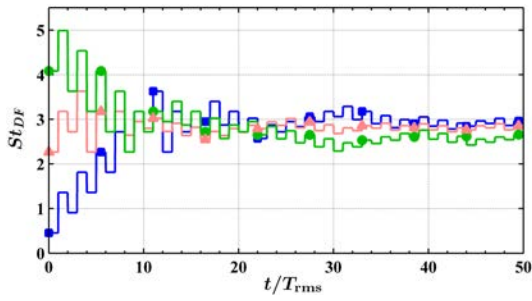
(c) Plant input with mKWA
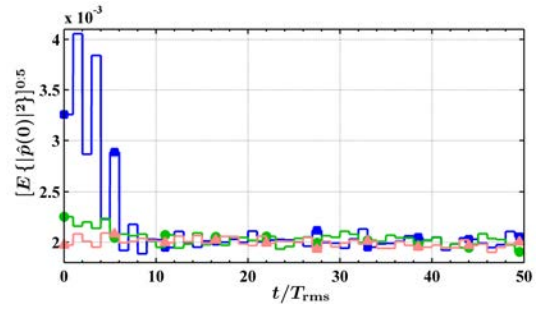
(d) Plant output with mKWA

Figure 4.8: Transient behavior in minimum-seeking experiments starting from various initial conditions. The initial input for a particular curve in the right sub-figure is to be read from the corresponding left sub-figure. Note that $T_{\mathrm{rms}} = 2200$ flow time steps.
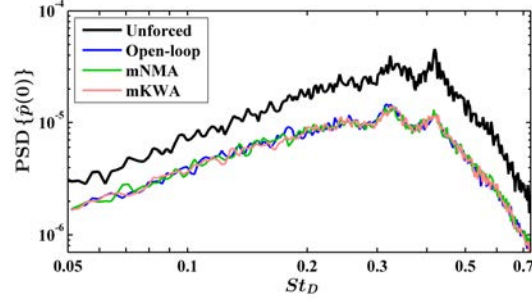
(a) Near-field pressure
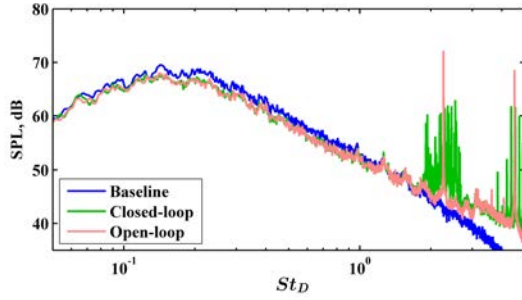
(b) Far-field at 30° mic
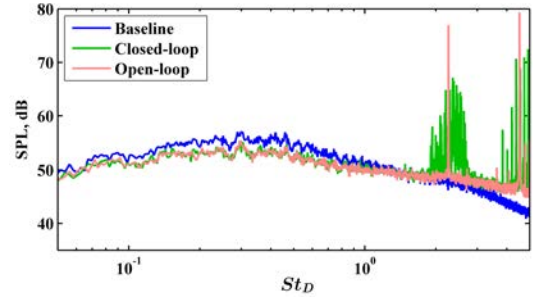
(c) Far-field at 90° mic

Figure 4.9: Steady-state behavior in minimum-seeking experiments compared with the optimal open-loop forcing case.

region of interest. Thus the best open-loop result in minimization of the near-field pressure fluctuations can be replicated in closed-loop by the mNMA with a very short transient phase.

In Figures 4.9(b) and 4.9(c), the steady-state far-field sound pressure level (SPL) spectra at two different polar angles obtained with mNMA are compared with the optimal open-loop forcing case. The sense of this optimality has already been explained in Section 4.1. The two spectra are found to be virtually indistinguishable in the high-amplitude regions. The main forcing tone in the feedback controlled case is smaller but there are several weaker tones near it corresponding to the discrete persistent perturbations in the St_{DF}. This result

69

supports the choice of $[E\{|\hat{p}(0)|^2\}]^{0.5}$ as the quantity to minimize in the near-field for far-field noise attenuation. It also provides succinct evidence of the effectiveness of extremizing feedback control.

Results with Modified Kiefer-Wolfowitz Algorithm

Although the mKWA differs from mNMA in its philosophy, the two have very similar behavior and end-effect. Like the mNMA, the mKWA also issues a converging sequence of St_{DF}'s, but the convergence rate is intentionally made slow for robustness in stochastic applications. In the mKWA, each decision to issue a new St_{DF} is based on two observations of the output with positive and negative perturbations from the previous iterate. On the other hand, in the mNMA, each such decision is based on only one observation of the output. This accounts for the improved robustness of KWA. Recall that the timing parameter T_{rms} had to be set to 2200 flow time steps in mNMA experiments aimed at minimizing the near-field pressure fluctuations. The mKWA showed repeatable convergence to the minimum even with $T_{\mathrm{rms}} = 1100$. However, for reliability, T_{rms} was retained as 2200 in the mKWA experiments also.

The mKWA controller has several tunable parameters that should be set based on available knowledge of the plant input/output map to be minimized (see Figure 4.1(a)). The decrement exponent b was set to 1.0 as a compromise between rapid convergence and reliability. The I/O map possesses a gradual slope at the high-St_{DF} end. If the process uncertainty is higher than the difference in output with the positive and negative perturbations introduced by the mKWA, the convergence (if it happens at all) would be very slow indeed. To address this, the initial perturbation level c_1 in the input forcing Strouhal number was chosen as 0.45. The initial step size a_1 was also set to 0.45 to hasten convergence. This is similar, but not equivalent, to selecting the initial simplex size and

70

$S_{\max}$ as 0.45 in the mNMA experiments. The parameters $c_{\min}$ and $a_{\min}$ together play a role similar to $S_{\min}$ in the mNMA implementation. Following the reasoning for the latter, they were selected as $c_{\min} = a_{\min} = 0.045$. Here, $a_{\min}$ keeps the optimization process "alive" in the long run whereas $c_{\min}$ ensures that the estimation of the sign of the local gradient is relatively robust to uncertainty in the output. In this respect, the mKWA offers more flexibility than the mNMA since in the latter both these effects are controlled by $S_{\min}$.

Figure 4.8(c) demonstrates that starting from three different initial conditions covering a wide range, the St_{DF} reaches around 2.7 within $10T_{\mathrm{rms}}$, but it varies within 0.24 and 0.30 subsequently. Figure 4.8(d) shows that the output reaches and settles around 0.002 within the same interval in all three cases. Except for the doubled settling time, all other characteristics are very similar to the mNMA results, including the representative steady-state output spectrum shown in Figure 4.9(a). The far-field SPL spectra (not shown) were similar too. The doubling of the settling time in the mKWA results compared to those observed in mNMA experiments has been discussed above.

4.5.2 Maximizing Near-Field Pressure Fluctuations

The bulk mixing in the jet shear layer may be enhanced by focusing on maximizing the RMS of $([\hat{p}(0) + 2\Re\{\hat{p}(1)\}]$ in the hydrodynamic near-field, as discussed in Section 4.1. With the forcing azimuthal mode m_F set to 0, the effect of forcing Strouhal number St_{DF} on this latter quantity has been determined in open-loop experiments and shown in Figure 4.1(b). The two extremizing controllers were evaluated for the task of maximizing this cost function after being initiated from various St_{DF}'s in the range of 0.1 to 0.8. There are two distinct maxima in this range, viz. 0.34 and 0.45. As discussed in Section 3.3, the first peak corresponds to the jet column mode, and it is physical. The second peak arises due to a possible imperfection in the jet plumbing, and is not truly characteristic of jets. However,

to the feedback controller, both peaks appear as maxima to aim toward. Although neither controller can guarantee convergence to the global extremum, both maybe expected to latch onto one of the two maxima. Since the ordinates of the two maxima are quite similar, achieving either of them should correspond to significant mixing enhancement.

Results with Modified Nelder-Mead Algorithm

The choice of the parameters of the mNMA controller is dictated by the available knowledge of the I/O map of the plant being optimized. As before, the values of the simplex transformation parameters were set as $c_r = 1$, $c_c = 0.5$, and $c_e = 2$. The maximum allowable simplex size $S_{\max}$ was chosen as 0.09 based on the range of initial conditions and the sharpness of the maxima. Values of 0.07 and 0.18 (not shown here) were also tried with similar results, attesting to the relative robustness of the controller to the specific choice of this parameter. Further reduction of $S_{\max}$ led to delays in convergence as the determination of the sign of the local gradient was hindered by the uncertainty in the measured output. The minimum allowable simplex size $S_{\min}$ determining the level of persistent excitation in the process was set to 0.009 from the knowledge of the sharpness of the maxima being sought. A value of 0.018 did not lead to substantial degradation in performance. However, with $S_{\min} = 0.045$, large oscillations were observed in the forcing frequency and the average output was reduced since the larger perturbations were keeping the output away from its optimum. In the absence of any further knowledge of a suitable level of persistent excitation, the goal was to demonstrate the flexibility of the algorithm. The timing parameter T_{rms} was set to 1100 flow time steps for reasons discussed in Section 4.4.2; convergence was unreliable with $T_{\mathrm{rms}} = 550$.

Figure 4.10(a) shows that the commanded St_{DF} settles within $10T_{\mathrm{rms}}$ from a variety of initial values. In steady state, the St_{DF} remained close to one of the optimal values

(a) Plant input with mNMA

(b) Plant output with mNMA

(c) Plant input with mKWA

(d) Plant output with mKWA
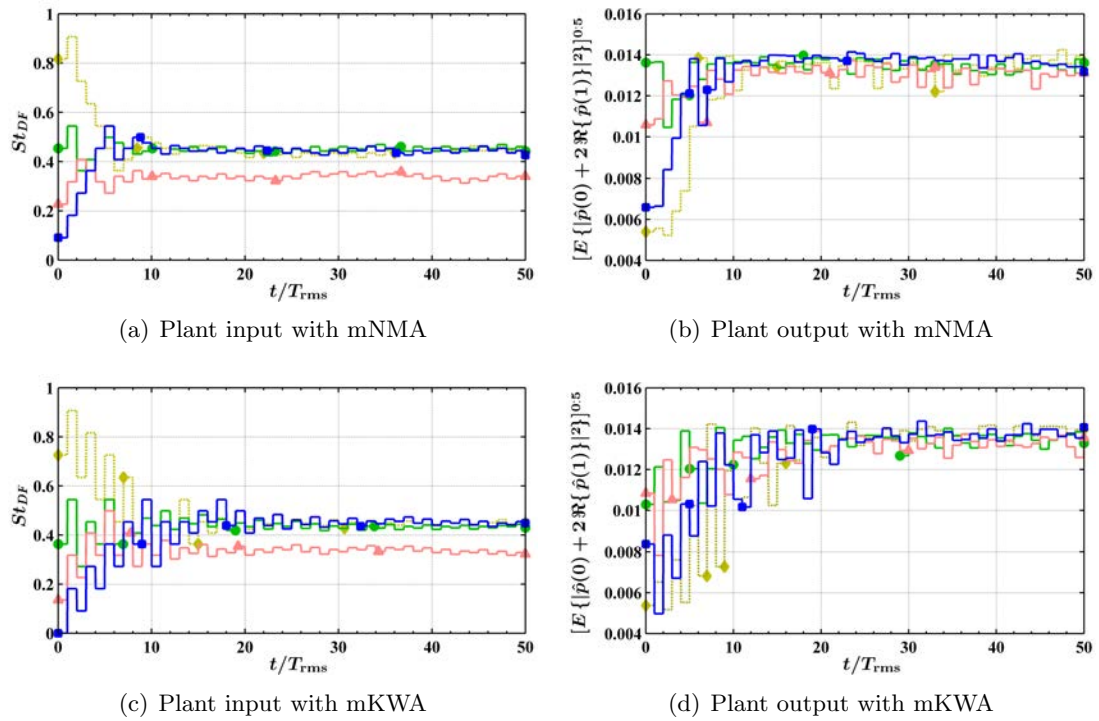
Figure 4.10: Transient behavior in maximum-seeking experiments starting from various initial conditions. The initial input for a particular curve in the right sub-figure is to be read from the corresponding left sub-figure. Note that $T_{\mathrm{rms}} = 1100$ flow time steps.

expected from the I/O map shown in Figure 4.1(b). The plant output also converged to a steady value around 0.0133 within the same time. In steady state, the output is seen to have significant oscillations. Also, the mean output is somewhat lower than the optimal value found in open-loop experiments (≈ 0.014). Both these effects can be explained by the sharpness of the maxima.

Figure 4.11 presents the PSD's corresponding to the two maxima found in open-loop experiments. They are seen to have virtually identical broadband behavior and their forcing tones have similar amplitudes. Overlaid on these spectra from open-loop forcing experiments are two PSD's representing the only two distinct steady-state behaviors observed in closed-loop experiments with mNMA. These two behaviors signify convergence to either of the two maxima in the I/O map presented in Figure 4.1(b). The same two behaviors have also been observed in the steady-state values of the St_{DF} depicted in Figure 4.10(b). In both these closed-loop experiments, the broadband characters of the steady-state spectra are quite indistinguishable from the optimal open-loop cases. The forcing peaks are broader but smaller, as expected from the persistent excitation in the feedback controlled cases. Thus, the extremizing controller based on mNMA is able to closely replicate the optimal open-loop forcing results in maximizing near-field pressure fluctuations within an adequately short time.

Results with Modified Kiefer-Wolfowitz Algorithm

The choice of the parameters of the extremizing controller based on mKWA follow from the arguments laid out previously for minimizing near-field pressure fluctuations using this controller as well as the character of the I/O map in this application. The initial perturbation level c_1 was set to 0.09. In a few experiments with $c_1 = 0.07$, no erroneous convergence behavior was observed. However, transient oscillations took longer to settle down with
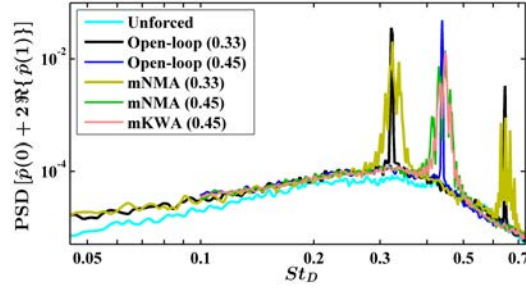
Figure 4.11: Steady-state behavior in maximum-seeking experiments. The numbers in parentheses refer to the mean value of the steady-state St_{DF}.

$c_1 = 0.18$. Similar considerations led to the choice of the initial step size $a_1 = 0.09$. The parameters $c_{\min}$ and $a_{\min}$ were both selected as 0.0045, exploiting their relationship to $S_{\min}$ in the mNMA; the value of the latter has been justified already.

Figure 4.10(c) shows that commanded St_{DF} settles within $22T_{\mathrm{rms}}$ from a range of initial values. The output being maximized is also seen to reach steady state within the same time in Figure 4.10(d). This represents a doubling of the convergence time over the results obtained with mNMA discussed above. The reason for this difference has been discussed in the context of the minimum-seeking experiments in Section 4.5.1. Apart from this disparity, the steady state behavior of the mKWA controller is identical to that of the mNMA controller. This is seen in the time domain plots in Figures 4.10(c) and 4.10(d) as well in the frequency domain spectra in Figure 4.11.

4.6   Conclusions

This chapter was motivated by the results of open-loop forcing using localized arc filament plasma actuators, discussed in Chapter 3. In particular, control authority has been demonstrated on the irrotational near-field pressure of a Mach 0.9 jet with a Reynolds

number based on nozzle exit diameter of 6.7×10^5. These results had shown two distinct effects of actuation on the near-field pressure: a large amplification occurs in the pressure fluctuations at a forcing Strouhal number (St_{DF}) near the jet column mode, whereas a broad attenuation is found at higher values. The peak corresponds to maximum bulk mixing in the jet shear layer; the minimum is important for its potential link to far-field noise attenuation.

A feedback control strategy has been developed that minimizes the RMS of the axisymmetric mode of the near-field pressure in real-time by automatically tuning the St_{DF} of the LAFPAs; this was motivated by the correlation of this signal with the far-field noise. Another feedback controller was designed to maximize the RMS of the sum of the axisymmetric and first helical modal components of the near-field pressure by tuning the St_{DF}; the motivation was the correlation of this signal with the bulk mixing in the shear layer. Thus, both the far-field noise mitigation and the bulk mixing enhancement applications can be regarded as online extremization problems involving single-variable cost functions. An important characteristic of both applications is the high level of uncertainty introduced in the corresponding cost functions by turbulence.

Two different gradient-free offline optimization algorithms were investigated - the Nelder-Mead direct search method and the Kiefer-Wolfowitz stochastic optimization routine. The former is designed for efficient optimization of deterministic cost functions, whereas the latter can also handle stochastic functions. Several novel enhancements were incorporated in the original algorithms before they could be implemented in feedback controllers for online optimization. In closed-loop control experiments for minimum-seeking and maximum-seeking, both controllers were able to replicate the optimal open-loop control effects on the near-field pressure after brief transient phases. It was also demonstrated that feedback

control can attenuate the far-field noise to a degree similar to the maximal observed in previous open-loop forcing experiments. The modified Kiefer-Wolfowitz method was found to be more robust but the convergence rate was typically halved in comparison to the modified Nelder-Mead controller. One shortcoming of the former is the absence of any mechanism to increase the perturbation and increment levels; this might be a disadvantage if the desire is to quickly account for changes in the location of the optimum during operation. The expansion mechanism in the modified Nelder-Mead algorithm would be very useful in this regard.

In summary, both feedback controllers investigated in this chapter demonstrate significant promise for the online optimization of the near-field pressure of axisymmetric jets.

Chapter 5

REDUCED-ORDER MODELING OF UNFORCED JET

The majority of the research presented in this chapter was published in Sinha et al. (2010b).

5.1 Introduction

The previous chapter has presented a simple yet robust form of closed-loop control that is model-free. There, the system input-to-output map is assumed to be static, and the controller is typically set up to vary the input to seek the maximum or minimum output in real-time. Although the simplicity of model-free controllers is attractive for flow control, their responsiveness is generally slowed by the necessity of neglecting the system dynamics. Considerable improvements in performance may be realized with a model-based feedback controller, which is the most common paradigm in feedback control. The motivations for moving to a model-based approach are: (*a*) to gain a deeper understanding of the physics involved in the unforced jet, the forced jet, and the plasma actuation itself, (*b*) to attain faster convergence to the optimal parameter regime than the case of model-free control, by incorporating a knowledge of the dynamics of the jet mixing layer in the model, and (*c*) to

achieve improvements in power consumption. (Collis et al., 2004; Caraballo et al., 2008; Pastoor et al., 2008)

An incompressible flow is uniquely determined by specifying the three components of velocity over the entire flow domain. Considering compressibility effects, two additional thermodynamic variables (e.g. density and pressure) are needed for a full characterization of the flow. In control system terminology, this information constitutes the set of *states* of the system. The dynamics of these states are governed by the infinite-dimensional Navier-Stokes equations, and infinitely many states are needed to fully specify the flow. From the point of view of practical implementation as well as the feasibility of actual design of the control law, it is essential that a small set of ordinary differential equations (ODE) be able to approximately describe the dynamical behavior of the control system. Hence, any model-based flow control strategy must necessarily involve the development of a reduced-order model (ROM) of the flow. In developing the ROM, a change of coordinates is sought such that a small set of the new coordinates may approximately represent the dynamics of the original system.

A number of methods have been employed to develop ROMs of flows of practical interest — they lend themselves to the following broad categorization.

1. Phenomenological models of flows are obtained by invoking intuitive arguments about the essential physics of the flow. Flows dominated by oscillations have been modeled in this manner in the past (Pastoor et al., 2008; Tchieu et al., 2008; Noack et al., 2003; Luchtenburg et al., 2009). Unfortunately, the unforced high Reynolds number jet mixing layer is relatively disorganized and this makes the task of phenomenological modeling quite difficult.

2. Black-box modeling involves starting with an assumed structure of the ROM (number of dynamic states, degree of nonlinearity, form of the forcing term, etc.) before performing well-designed experiments or simulations to identify the dynamical relation between the system input and output. Several implementations have been reported in the recent flow control literature (Perret et al., 2006; Henning et al., 2007; Efe et al., 2008; Siegel et al., 2008). This modeling approach does not incorporate much physical information about the flow, but may be the most viable option in particularly complex applications.

3. The Galerkin procedure involves two steps to arrive at the ROM (Holmes et al., 1996). In the first step, the kinematics of the flow are assumed to reside on a low-dimensional manifold, so that the infinite dimensional flow variables are represented by an expansion on a finite number of modes. This expansion is usually linear, but nonlinear expansions have been found to yield greater accuracy for certain flows in bounded domains (Marion and Temam, 1989; Debussche et al., 1995). In the next step, the dynamics of these modes are also assumed to reside on the same low-dimensional manifold, and this is enforced by the Galerkin projection (GP) of the Navier-Stokes equations onto this manifold. Depending on the origin of the expansion modes, Galerkin models have been categorized as mathematical, physical, or empirical (Noack et al., 2003). Empirical Galerkin models, as the name suggests, derive their modes from experimental data or numerical simulations. They have been generally found to be the most accurate while employing the least number of modes (Noack et al., 2003).

The most common technique of deriving modes from empirical data is the Proper Orthogonal Decomposition (POD) (Lumley, 1967; Holmes et al., 1996). Its popularity stems from the fact that it is a linear procedure, and it objectively educes an orthogonal set

of basis functions that optimally converges in the sense of a suitably-defined $\mathcal{L}_2$ norm of the projection error. The eduction of POD bases for axisymmetric jets was pioneered by Glauser et al. (1985) with several important contributions in recent years (Gamard et al., 2002; Jung et al., 2004; Iqbal and Thomas, 2007; Tinney et al., 2008a,b).

Based on the above discussion of the available options for deriving ROMs, POD and empirical GP were used for the present feedback control application. POD-GP has been used for studying the dynamics of flows over the past 20 years (Aubry et al., 1988; Zheng, 1990; Ukeiley et al., 2001; Rempfer, 2000; Rajaee et al., 1994; Rowley, 2002). In particular, a model-based feedback controller has been implemented for reducing cavity tones using this modeling strategy at GDTL (Samimy et al., 2007a; Caraballo et al., 2007, 2008).

The goal of the present work is to incorporate feedback control for the plasma-actuated high Reynolds number jet. The details of LAFPAs in the jet have not been fully replicated in numerical simulations, although significant fidelity has been achieved in implicit large eddy simulation (Gaitonde and Samimy, 2010; Gaitonde, 2011). As such, the empirical data for the final reduced-order model must be derived from experiments, although intermediate validation is performed on numerical simulation databases. The experimental database required for incorporating compressibility effects in the model has to be built by simultaneously acquiring the velocity and two other thermodynamic quantities over a domain of feasible size. To date, experimentalists have not realized this goal. These practical constraints impose the incompressibility assumption on the present ROM. This may be justified since a control-oriented model only needs to be good enough for representing the short-time-horizon dynamical relation between control inputs and sensor outputs (Kim and Bewley, 2007). Numerical simulation results presented later validate this assumption.
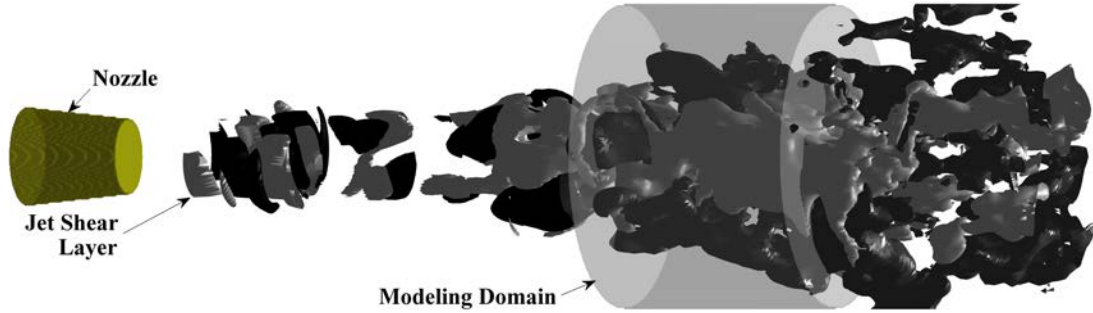
Figure 5.1: Cylindrical modeling domain spanning the end of the potential core.

The flow domain of interest for ROM development is the mixing layer in the vicinity of the end of the potential core, as shown in Figure 5.1. In the axisymmetric jet, the azimuthal direction is homogenous and the radial direction is inhomogeneous. In the past, the axial direction was assumed to be homogenous, and Taylor's hypothesis was used to convert a time-resolved velocity measurement to an axially-resolved velocity database (Zheng, 1990). However, preliminary experience with the DNS database indicated that such an assumption may not be correct for the current modeling purpose. Then, the empirical database for the ROM should consist of the 3-component 2-point velocity cross-correlation tensor with all possible pairs of axial and radial locations, and all possible azimuthal separations over the indicated 3-D region. The acquisition of such a database is quite complicated. Another option is to collect snapshots of the 3-component velocity field over the 3-D region. Although this information is not directly accessible in experiments, Tinney et al. (2008a,b) presented an approximate technique for this purpose using spectral linear stochastic estimation (SLSE), and this would be adopted in this work.

An essential and non-trivial initial step in the design of a model-based feedback controller is the modeling of the unforced flow. The POD-GP procedure can result in ROMs with

widely differing fidelity depending on the simplifying assumptions that are made. The choices made at this point will affect the later development of the actuated model. The present chapter delves into the details of modeling the pertinent near-field mixing layer of the unforced axisymmetric jet. The incorporation of the effect of actuation is deferred to Chapter 6.

A very useful (and, in fact, indispensable) tool for evaluating the various modeling strategies is a time- and spatially-resolved 3-D volumetric database of the axisymmetric jet. Two such numerical databases have been discussed in Section 2.5, and both would be employed here. However, the final validation is performed on experimental data, for which the setup has been described in Chapter 2.

The notation that is followed in this chapter, as well as in the subsequent ones, is first established in Section 5.2, along with other preliminary observations regarding the symmetries in the jet under consideration. The proper orthogonal decomposition is laid out in general terms for the axisymmetric problem at hand in Section 5.3. Sections 5.4–5.6 goes through the successive steps in obtaining the reduced-order description of the jet kinematics. The Galerkin projection for obtaining the dynamical model is presented in Section 5.7. Although not the main thrust of this research, Section 5.8 derives the Galerkin projection for the compressible Navier-Stokes equations (and mass and energy conservation relations) governing the axisymmetric jet. This allows the later assessment of the effects of the incompressibility assumption which is made in the remaining part of the research. Section 5.9 details the results of validation of the various steps in the modeling procedure starting with the DNS database, and culminating in the validation with experimental data. Conclusions are drawn from the research presented in the chapter in Section 5.10.

5.2   Preliminaries

Recall that the jet exit velocity U_j and nozzle exit diameter D normalize all velocities and linear dimensions respectively. Consequently, time is normalized by the flow time scale D/U_j.

In cylindrical coordinates $\mathbf{x} := (x, r, \theta)^{\mathrm{T}}$, the modeling domain is $\Omega := [X_1, X_2] \times [0, R] \times \mathbb{T}$. Here, X_1 and X_2 denote the upstream and downstream bounds of the axial domain, R is the radial extent of the domain, and $\mathbb{T}$ is the circle group. The velocity vector is $\mathbf{U} : \Omega \times \mathbb{R} \to \mathbb{R}^3$, $\mathbf{U} : (\mathbf{x}, t) \mapsto (U_x, U_r, U_\theta)^{\mathrm{T}}$.

Two different proper orthogonal decompositions will be performed in the present work. In the slice POD, the database will consist of snapshots of the 3 components of velocity measured on a single cross-stream slice. Slice POD will be performed independently on several such cross-stream slices. In the volumetric POD, the database will consist of snapshots of the 3 components of velocity measured over the cylindrical domain of interest shown in Figure 5.1. Instead of discussing these cases in isolation, their common aspects will be described first, followed by a presentation of their individual features. The common feature of all these field databases is the presence of the homogenous and periodic azimuthal direction.

In order to unify notation, let the domain of definition of the field be denoted as $(\mathbf{y}, \theta) \in \Omega_y \times \mathbb{T}$. For the slice POD, x is fixed, so that $\mathbf{y} \equiv r$ and a polar domain is obtained with $\Omega_y \equiv [0, R]$. For the volumetric POD, $\mathbf{y} \equiv (x, r)$ and the full cylindrical domain with $\Omega_y \equiv [X_1, X_2] \times [0, R]$ is retrieved. In either case, the notation introduced above can be generalized to write any velocity field belonging to the database as $\mathbf{U} : \Omega_y \times \mathbb{R} \to \mathbb{R}^3$, $\mathbf{U} : (\mathbf{y}, t) \mapsto (U_x, U_r, U_\theta)^{\mathrm{T}}$.

In the Reynolds decomposition, any instantaneous flow variable is decomposed into its steady mean value obtained by ensemble averaging and the residual time-varying fluctuations. To keep the following derivation general, the steady part of the decomposition is specified as a general 'base' field (indicated by the superscript 'b') instead of the specific mean value. The obvious choices for the base field are (a) the mean value, (b) the steady solution of the governing dynamics (if it exists), and (c) the null field indicating no decomposition. In each case, the residuum would be called 'fluctuations' with the meaning implicit from the context. For physical meaningfulness, all pertinent flow variables in a particular problem must be subjected to the same decomposition. Applying this decomposition to the velocity field, one obtains

$$\mathbf{U}(\mathbf{y}, \theta, t) = \mathbf{U}^b(\mathbf{y}) + \mathbf{u}(\mathbf{y}, \theta, t). \tag{5.1}$$

For the axisymmetric flow under consideration, the base field must be axisymmetric too. Hence, the base velocity field $\mathbf{U}^b$ is independent of θ. Moreover, for the non-swirling flow under consideration, the base field for the azimuthal velocity must be null; i.e., $U_\theta^b \equiv 0$. The fluctuating velocity field is denoted by $\mathbf{u}$, with the three components being u_x, u_r, and u_θ, respectively. In particular, the statistical stationarity and axisymmetry of the jet are used to define the mean velocity field as

$$\overline{\mathbf{U}}(\mathbf{y}) := E\left\{\frac{1}{2\pi} \int_{-\pi}^{\pi} \mathbf{U}(\mathbf{y}, \theta, t) \mathrm{d}\theta\right\}. \tag{5.2}$$

The expectation operator $E(\cdot)$ signifies the ensemble-average over all realizations identified by t.

The azimuthal direction is periodic. Then, following the analogous discussion for the pressure field in Section 3.2, the forward and inverse azimuthal Fourier transforms of the
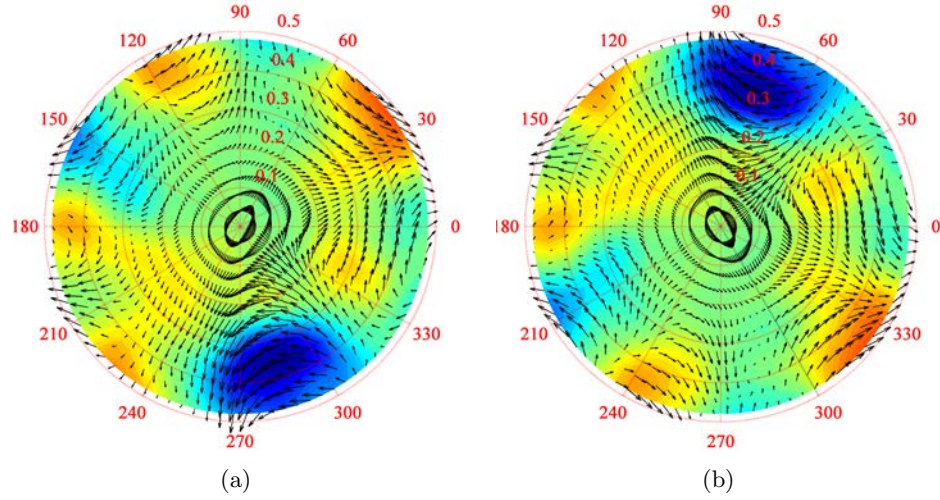
Figure 5.2: Enforcing axisymmetry. (a) Actual velocity field realization. (b) Corresponding co-velocity field.

fluctuating velocity field are defined as

$$\hat{\mathbf{u}}(\mathbf{y}, t; m) := \frac{1}{2\pi} \int_{-\pi}^{\pi} \mathbf{u}(\mathbf{y}, \theta, t) \mathrm{e}^{-\mathrm{i}m\theta} \mathrm{d}\theta, \tag{5.3a}$$

$$\mathbf{u}(\mathbf{y}, \theta, t) = \sum_{m=-\infty}^{\infty} \hat{\mathbf{u}}(\mathbf{y}, t; m) \mathrm{e}^{\mathrm{i}m\theta}. \tag{5.3b}$$

Since $\mathbf{u}$ is real, $\hat{\mathbf{u}}$ is Hermitian in m.

The axisymmetry of the jet can be used to infer a symmetry condition. Consider an actual realization of $\mathbf{u}$ shown in Figure 5.2(a). The contour-map indicates the axial component, and the vector field is in the cross-stream plane. If enough realizations are collected in a perfectly axisymmetric jet, one should also expect to capture the simulated *co-velocity* field $\underline{\mathbf{u}}$ shown in Figure 5.2(b) (Iqbal and Thomas, 2007). Of course, in an actual experiment, one cannot expect to collect both realizations. However, the collected database of realizations can be extended by appending the co-velocity field of each physical velocity

86

field. To be precise, the two fields are related as

$$\underline{u}_x(\mathbf{y}, \theta, t) := u_x(\mathbf{y}, -\theta, t), \quad \underline{u}_r(\mathbf{y}, \theta, t) := u_r(\mathbf{y}, -\theta, t), \quad \underline{u}_\theta(\mathbf{y}, \theta, t) := -u_\theta(\mathbf{y}, -\theta, t). \quad (5.4)$$

Consequently, their azimuthal Fourier transforms are related as

$$\underline{\hat{u}}_x(\mathbf{y}, t; m) := \hat{u}_x^*(\mathbf{y}, t; m), \quad \underline{\hat{u}}_r(\mathbf{y}, t; m) := \hat{u}_r^*(\mathbf{y}, t; m), \quad \underline{\hat{u}}_\theta(\mathbf{y}, t; m) := -\hat{u}_\theta^*(\mathbf{y}, t; m). \quad (5.5)$$

The asterisk denotes complex conjugation.

5.3 Proper Orthogonal Decomposition in Axisymmetric Field

It is well-established (Lumley, 1967; Sirovich, 1987; George, 1988) that in the presence of a homogeneous and/or periodic direction in a flow, its POD devolves into the Fourier decomposition along that direction. This will be pursued for the axisymmetric flow under consideration, and the resulting symmetries will be derived. These symmetries (*a*) augment the database collected from experiments, (*b*) make computations easier, and (*c*) model the flow more accurately (Sirovich, 1987).

5.3.1 Two Point Cross-Correlation Tensor

The two-point cross-correlation tensor is central to the POD; for all $i, j \in \{x, r, \theta\}$, it is defined as

$$\Pi_{ij}(\mathbf{y}, \mathbf{y}', \vartheta) := E\left[\frac{1}{2\pi} \int_{-\pi}^{\pi} \frac{1}{2} \Big\{ u_i(\mathbf{y}, \theta + \vartheta, t) u_j(\mathbf{y}', \theta, t) + \underline{u}_i(\mathbf{y}, \theta + \vartheta, t) \underline{u}_j(\mathbf{y}', \theta, t) \Big\} \mathrm{d}\theta \right],$$

$$(5.6)$$

where azimuthal homogeneity as well as the appended co-velocity field have been used. The full tensor with all 9 components will be denoted by $\mathbf{\Pi}(\mathbf{y}, \mathbf{y}', \vartheta)$. The relations in eqn (5.4) can be invoked to prove the following

$$\Pi_{ij}(\mathbf{y}, \mathbf{y}', \vartheta) = \Pi_{ij}(\mathbf{y}, \mathbf{y}', -\vartheta), \quad (i, j) \in \{(x, x), (r, r), (\theta, \theta), (x, r), (r, x)\}, \quad (5.7\mathrm{a})$$

$$\Pi_{ij}(\mathbf{y}, \mathbf{y}', \vartheta) = -\Pi_{ij}(\mathbf{y}, \mathbf{y}', -\vartheta), \quad (i, j) \in \{(x, \theta), (r, \theta), (\theta, x), (\theta, r)\}. \tag{5.7b}$$

Such properties have indeed been verified in experiments (Jung et al., 2004; Iqbal and Thomas, 2007; Tinney et al., 2008a).

The azimuthal Fourier transform of Π_{ij} is defined in the usual manner:

$$\hat{\Pi}_{ij}(\mathbf{y}, \mathbf{y}'; m) := \frac{1}{2\pi} \int_{-\pi}^{\pi} \Pi_{ij}(\mathbf{y}, \mathbf{y}', \vartheta) e^{-im\vartheta} d\vartheta. \tag{5.8}$$

Since Π_{ij} is real, $\hat{\Pi}_{ij}$ is Hermitian in m. Let the real and imaginary parts of a quantity be denoted by superscripts r and i, respectively. The following properties can be deduced from eqn (5.7) by applying the definition of eqn (5.8):

$$\hat{\Pi}_{ij}(\mathbf{y}, \mathbf{y}'; m) = \hat{\Pi}_{ij}^r(\mathbf{y}, \mathbf{y}'; m), \quad (i, j) \in \{(x, x), (r, r), (\theta, \theta), (x, r), (r, x)\}, \tag{5.9a}$$

$$\hat{\Pi}_{ij}(\mathbf{y}, \mathbf{y}'; m) = i \, \hat{\Pi}_{ij}^i(\mathbf{y}, \mathbf{y}'; m), \quad (i, j) \in \{(x, \theta), (r, \theta), (\theta, x), (\theta, r)\}. \tag{5.9b}$$

Consider the azimuthal Fourier transform of the physical part of the cross-correlation tensor in eqn (5.6) (i.e. ignoring the co-velocity fields for now). One obtains

$$\frac{1}{2\pi} \int_{\vartheta=-\pi}^{\pi} E\left\{ \frac{1}{2\pi} \int_{\theta=-\pi}^{\pi} u_i(\mathbf{y}, \theta + \vartheta, t) u_j(\mathbf{y}', \theta, t) d\theta \right\} e^{-im\vartheta} d\vartheta$$

$$= E\left[\frac{1}{2\pi} \int_{\theta=-\pi}^{\pi} \left\{ \frac{1}{2\pi} \int_{\theta'=\theta-\pi}^{\theta+\pi} u_i(\mathbf{y}, \theta', t) e^{-im\theta'} d\theta' \right\} u_j(\mathbf{y}', \theta, t) e^{im\theta} d\theta \right]$$

$$= E\left\{ \hat{u}_i(\mathbf{y}, t; m) \frac{1}{2\pi} \int_{\theta=-\pi}^{\pi} u_j(\mathbf{y}', \theta, t) e^{im\theta} d\theta \right\}$$

$$= E\left\{ \hat{u}_i(\mathbf{y}, t; m) \hat{u}_j^*(\mathbf{y}', t; m) \right\}.$$

A similar derivation applies to the co-velocity fields appearing in eqn (5.6). Then, the definition in eqn (5.8) yields

$$\hat{\Pi}_{ij}(\mathbf{y}, \mathbf{y}'; m) = \frac{1}{2} \left[E\left\{ \hat{u}_i(\mathbf{y}, t; m) \hat{u}_j^*(\mathbf{y}', t; m) \right\} + E\left\{ \underline{\hat{u}}_i(\mathbf{y}, t; m) \underline{\hat{u}}_j^*(\mathbf{y}', t; m) \right\} \right].$$

Given the relations in eqn (5.5), one obtains the following

$$E\left\{ \underline{\hat{u}}_i(\mathbf{y}, t; m) \underline{\hat{u}}_j^*(\mathbf{y}', t; m) \right\} = E\left\{ \hat{u}_i(\mathbf{y}, t; m) \hat{u}_j^*(\mathbf{y}', t; m) \right\}^*,$$

$$\forall (i,j) \in \{(x,x),(r,r),(\theta,\theta),(x,r),(r,x)\},$$

$$E\left\{\hat{\underline{u}}_i(\mathbf{y},t;m)\hat{\underline{u}}_j^*(\mathbf{y}',t;m)\right\} = -E\left\{\hat{u}_i(\mathbf{y},t;m)\hat{u}_j^*(\mathbf{y}',t;m)\right\}^*,$$

$$\forall (i,j) \in \{(x,\theta),(r,\theta),(\theta,x),(\theta,r)\}.$$

These relations bestow the symmetries observed in eqn (5.9).

Thus, in practice, the following relation is used to compute $\hat{\Pi}_{ij}$

$$\hat{\Pi}_{ij}(\mathbf{y},\mathbf{y}';m) = E\left\{\hat{u}_i(\mathbf{y},t;m)\hat{u}_j^*(\mathbf{y}',t;m)\right\}. \tag{5.10}$$

Subsequently, one neglects the real parts of the azimuthal shear stresses and the imaginary parts of the remaining correlation coefficients. In the past, analogous symmetries have been enforced for the kernel of a POD performed on a fully-developed channel flow (Moin and Moser, 1989).

5.3.2   Vector Proper Orthogonal Decompostion

The field $\mathbf{u}(\cdot,t)$ belongs to the Hilbert space of square-integrable functions $\mathcal{L}_2(\Omega)$ equipped with inner product denoted by $\langle\, \cdot\, ,\, \cdot\, \rangle$. For the purpose of the following development, it will be more advantageous to think of this information as constituting an ensemble of snapshots, with $\mathbf{u}^k$ representing the snapshot of $\mathbf{u}(\cdot,t)$ at $t = t_k$. In the latter perspective, the database is specified as $\left\{\mathbf{u}^k \in \mathcal{L}_2(\Omega)\,\middle|\, k = 1,\ldots,N_s\right\}$, where N_s denotes the total number of snapshots in the ensemble. The notation $\mathbf{u}$ will be used to represent the entire ensemble $\left\{\mathbf{u}^k\right\}$. Note that it implicitly includes both the measured snapshots as well as the corresponding co-fields described in Section 5.2.

Given $\mathbf{u}$, the goal of POD is to find a subspace $S \subset \mathcal{L}_2(\Omega)$ of fixed dimension N, such that the error $E\{||\mathbf{u} - \mathcal{P}_S\mathbf{u}||\}$ is minimized (Rowley, 2002). Here, $||\cdot||$ is the induced norm on $\mathcal{L}_2(\Omega)$, and $\mathcal{P}_S$ is the orthogonal projection onto the subspace S. Let

$\left\{ \mathbf{\Phi}^{(n)} \in \mathcal{L}_2(\Omega) | n = 1, \ldots, N \right\}$ be an orthonormal basis of S, such that the orthogonal projection is given by

$$\mathcal{P}_S \mathbf{u} = \sum_{n=1}^{N} \left\langle \mathbf{u} , \ \mathbf{\Phi}^{(n)} \right\rangle \mathbf{\Phi}^{(n)}. \tag{5.11}$$

The POD theorem (Lumley, 1967; Holmes et al., 1996; Rowley, 2002) states that the functions $\mathbf{\Phi}^{(n)}$ that minimize the projection error of the dataset are the eigenfunctions corresponding to the N largest eigenvalues Λ in the eigenvalue problem

$$E \left(\langle \mathbf{\Phi} , \ \mathbf{u} \rangle \mathbf{u} \right) = \Lambda \mathbf{\Phi}. \tag{5.12}$$

The eigen-solutions are called POD modes.

The meaningful 'vector' inner product for two vector fields $\mathbf{v}^{(1)}, \mathbf{v}^{(2)} \in \mathcal{L}_2(\Omega)$ is defined as

$$\left\langle \mathbf{v}^{(1)} , \ \mathbf{v}^{(2)} \right\rangle := \int_{\Omega} \mathbf{v}^{(2)*}(\mathbf{x}) \mathbf{A}(\mathbf{x}) \mathbf{v}^{(1)}(\mathbf{x}) \mathrm{d}\mathbf{x}. \tag{5.13}$$

The asterisk denotes the complex conjugate transpose that, for the real field under consideration, devolves to the transpose. The weighting matrix function is simply $\mathbf{A}(\mathbf{x}) = \mathbf{A}(\mathbf{y}) = r$, but the generalization is preferred in the following derivation. The above definition of the inner product induces the turbulent kinetic energy-based norm that is most common.

With this inner product definition, the POD problem of eqn (5.12) can be expanded to the integral eigenvalue problem

$$\int_{\Omega} E \left\{ \mathbf{u}(\mathbf{x}) \mathbf{u}^*(\mathbf{x}') \right\} \mathbf{A}(\mathbf{x}') \mathbf{\Phi}(\mathbf{x}') \mathrm{d}\mathbf{x}' = \Lambda \mathbf{\Phi}(\mathbf{x}), \quad \mathbf{x} \in \Omega. \tag{5.14}$$

The kernel is recognized to be the two-point cross-correlation tensor. The co-fields are omitted in the above for notational convenience but are implicitly included in the expectation operation. Separating $\mathbf{x}$ into $\mathbf{y}$ and θ coordinates yields

$$\int_{\theta'=-\pi}^{\pi} \int_{\Omega_y} E \left\{ \mathbf{u}(\mathbf{y}, \theta' + \vartheta) \mathbf{u}^*(\mathbf{y}', \theta') \right\} \mathbf{A}(\mathbf{y}') \mathbf{\Phi}(\mathbf{y}', \theta') \mathrm{d}\mathbf{y}' \mathrm{d}\theta' = \Lambda \mathbf{\Phi}(\mathbf{y}, \theta' + \vartheta).$$

Since the azimuthal direction is homogenous, the above equation becomes

$$\int_{\theta'=-\pi}^{\pi} \int_{\mathbf{y}'=\Omega_y} \mathbf{\Pi}(\mathbf{y}, \mathbf{y}', \vartheta) \mathbf{A}(\mathbf{y}') \mathbf{\Phi}(\mathbf{y}', \theta') \mathrm{d}\mathbf{y}' \mathrm{d}\theta' = \Lambda \mathbf{\Phi}(\mathbf{y}, \theta' + \vartheta),$$

after omitting the domain dependencies. Substituting the azimuthal Fourier decomposition of the cross-correlation tensor in the above,

$$\sum_{m'=-\infty}^{\infty} \int_{\Omega_y} \hat{\mathbf{\Pi}}(\mathbf{y}, \mathbf{y}'; m') \mathbf{A}(\mathbf{y}') \left\{ \int_{\theta'=-\pi}^{\pi} \mathbf{\Phi}(\mathbf{y}', \theta') \mathrm{e}^{\mathrm{i}m'\vartheta} \mathrm{d}\theta' \right\} \mathrm{d}\mathbf{y}' = \Lambda \mathbf{\Phi}(\mathbf{y}, \theta' + \vartheta).$$

Or,

$$\sum_{m'=-\infty}^{\infty} 2\pi \int_{\Omega_y} \hat{\mathbf{\Pi}}(\mathbf{y}, \mathbf{y}'; m') \mathbf{A}(\mathbf{y}') \hat{\mathbf{\Phi}}(\mathbf{y}'; m') \mathrm{e}^{\mathrm{i}m'(\theta'+\vartheta)} \mathrm{d}\mathbf{y}' = \Lambda \mathbf{\Phi}(\mathbf{y}, \theta' + \vartheta),$$

where $\hat{\mathbf{\Phi}}$ is the azimuthal Fourier transform of $\mathbf{\Phi}$.

The mth azimuthal Fourier transform of the above equation is performed and the orthonormality of the Fourier basis is invoked to obtain

$$2\pi \int_{\Omega_y} \hat{\mathbf{\Pi}}(\mathbf{y}, \mathbf{y}'; m) \mathbf{A}(\mathbf{y}') \hat{\mathbf{\Phi}}(\mathbf{y}'; m) \mathrm{d}\mathbf{y}' = \Lambda(m) \hat{\mathbf{\Phi}}(\mathbf{y}; m). \tag{5.15}$$

In the above, a slight abuse of notation is made to incorporate the azimuthal mode dependency of the eigenvalues. The components of the eigenfunction are $\hat{\mathbf{\Phi}} =: \left(\hat{\Phi}_x, \hat{\Phi}_r, \hat{\Phi}_\theta \right)^{\mathrm{T}}$. The eigenvalue problems for the different azimuthal modes are decoupled.

Note that the above POD problem can also be derived by defining the inner product in the azimuthal Fourier domain for two arbitrary fields $\hat{\mathbf{v}}^{(1)}$ and $\hat{\mathbf{v}}^{(2)}$ as

$$\left\langle \hat{\mathbf{v}}^{(1)}, \hat{\mathbf{v}}^{(2)} \right\rangle := 2\pi \int_{\Omega_y} \hat{\mathbf{v}}^{(2)*}(\mathbf{y}) \mathbf{A}(\mathbf{y}) \hat{\mathbf{v}}^{(1)}(\mathbf{y}) \mathrm{d}\mathbf{y}, \tag{5.16}$$

and inducing the corresponding norm. Then the POD problem can be stated as the problem of finding the set of N functions $\hat{\mathbf{\Phi}}^{(n)}$ spanning the subspace S that minimize the projection error $E\left\{ ||\hat{\mathbf{u}} - \mathcal{P}_S \hat{\mathbf{u}}||^2 \right\}$ independently for each azimuthal mode m, given a database of fields $\hat{\mathbf{u}}$. The projection operator is defined as before:

$$\mathcal{P}_S \hat{\mathbf{u}} = \sum_{n=1}^{N} \left\langle \hat{\mathbf{u}}, \hat{\mathbf{\Phi}}^{(n)} \right\rangle \hat{\mathbf{\Phi}}^{(n)},$$

and the general form of the POD problem equivalent to eqn (5.12) is

$$E\left\{\left\langle \hat{\boldsymbol{\Phi}}(\cdot;m) \ , \ \hat{\mathbf{u}}(\cdot;m)\right\rangle \hat{\mathbf{u}}(\cdot;m)\right\} = \Lambda(m)\hat{\boldsymbol{\Phi}}(\cdot;m). \tag{5.17}$$

The projection coefficient in the above resolves the amplitude and is called the POD modal coefficient

$$\hat{\alpha}_k^{(n)}(m) := \left\langle \hat{\mathbf{u}}^k(\cdot;m) \ , \ \hat{\boldsymbol{\Phi}}^{(n)}(\cdot;m)\right\rangle. \tag{5.18}$$

For the slice POD, the coefficient is also parameterized by the axial location of the slice.

The properties of the POD allow one to exactly reconstruct any of the field realizations that formed the original database, using a linear combination of all the eigenfunctions. However, it is typical to assume that any arbitrary field can be approximately reconstructed using the truncated basis obtained above consisting the first N eigenfunctions (Lumley, 1967; Holmes et al., 1996)

$$\hat{\mathbf{u}}^k(\mathbf{y};m) \approx \sum_{n=1}^{N} \hat{\alpha}_k^{(n)}(m)\hat{\boldsymbol{\Phi}}^{(n)}(\mathbf{y};m). \tag{5.19}$$

Thus, in the presence of the homogenous and periodic azimuthal direction in the flow, the POD in that direction results in separable azimuthal Fourier modes, with POD performed in the remaining inhomogeneous directions independently for each Fourier mode. This character of POD is well known in the literature (e.g., Sirovich, 1987; George, 1988).

5.3.3 Scalar Proper Orthogonal Decomposition

The scalar POD is a specializing of the vector POD in which each component of the original vector field is decomposed independently. Consider two arbitrary scalar fields $\hat{v}_i^{(1)}(\cdot)$ and $\hat{v}_i^{(2)}(\cdot)$ with i denoting the component index into the original vector fields. Then, the 'scalar' inner product is defined as

$$\left\langle \hat{v}_i^{(1)} \ , \ \hat{v}_i^{(2)}\right\rangle := 2\pi \int_{\Omega_y} \hat{v}_i^{(2)*}(\mathbf{y})A_i(\mathbf{y})\hat{v}_i^{(1)}(\mathbf{y})\mathrm{d}\mathbf{y}. \tag{5.20}$$

Then, for each $m \in [-\infty, \infty]$ and any i, the scalar POD problem is

$$2\pi \int_{\Omega_y} \hat{\Pi}_{ii}(\mathbf{y}, \mathbf{y}'; m) A_i(\mathbf{y}') \hat{\phi}_i(\mathbf{y}'; m) \mathrm{d}\mathbf{y}' = \lambda_i(m) \hat{\phi}_i(\mathbf{y}; m), \quad \mathbf{y} \in \Omega_y. \tag{5.21}$$

Here the eigenfunctions $\hat{\phi}$ are akin to those for the vector POD, but one obtains individual eigenvalues λ_i for the different components indexed by i. Note that Einstein's summing convention is not implied by the repeated indices here.

5.3.4 Properties of Proper Orthogonal Decomposition

The properties of the vector POD will be discussed here; analogous properties hold for the scalar POD too.

Properties of POD Eigenvalues

Substituting the nth eigensolution in eqn (5.17) and taking an inner product with the nth eigenfunction obtains

$$\left\langle E\left\{ \left\langle \hat{\boldsymbol{\Phi}}^{(n)}(\cdot; m) , \ \hat{\mathbf{u}}(\cdot; m) \right\rangle \hat{\mathbf{u}}(\cdot; m) \right\} , \ \hat{\boldsymbol{\Phi}}^{(n)}(\cdot; m) \right\rangle = \Lambda^{(n)}(m) \left\langle \hat{\boldsymbol{\Phi}}^{(n)}(\cdot; m) , \ \hat{\boldsymbol{\Phi}}^{(n)}(\cdot; m) \right\rangle.$$

Subsequent simplification invoking the properties of the inner product and the unity of the eigenfunctions yields

$$\Lambda^{(n)}(m) = E\left\{ \left| \left\langle \hat{\mathbf{u}}(\cdot; m) , \ \hat{\boldsymbol{\Phi}}^{(n)}(\cdot; m) \right\rangle \right|^2 \right\} \geq 0. \tag{5.22}$$

This proves that the POD eigenvalues are real and non-negative (Lumley, 1967; Holmes et al., 1996; Rowley, 2002).

Comparison of the above expression with the definition of the POD modal coefficient in eqn (5.18) yields

$$E\left\{ \left| \hat{\alpha}_k^{(n)}(m) \right|^2 \right\} = \Lambda^{(n)}(m). \tag{5.23}$$

Thus the mean square of the POD modal coefficient is equal to the corresponding eigenvalue.

93

Orthogonality of Modal Coefficients

The POD eigenfunctions of a particular azimuthal mode are orthonormal by definition. This makes the corresponding modal coefficients orthonormal too. Moreover, the azimuthal Fourier modes themselves are orthonormal. The result is the following property

$$E\left\{\hat{\alpha}_k^{(n)*}(m)\hat{\alpha}_k^{(n')}(m')\right\} = \Lambda^{(n)}(m)\delta_{n,n'}\delta_{m,m'}. \tag{5.24}$$

This is recognized as a generalization of eqn (5.23).

Using the above property along with the properties of the Fourier transform, one may derive the following

$$E\left\{\hat{\alpha}^{(n),r}(t;m)\hat{\alpha}^{(n),r}(t;m)\right\} = E\left\{\hat{\alpha}^{(n),i}(t;m)\hat{\alpha}^{(n),i}(t;m)\right\} = 0.5\Lambda^{(n)}(m), \quad m \neq 0, \tag{5.25a}$$

$$E\left\{\hat{\alpha}^{(n),r}(t;m)\hat{\alpha}^{(n),i}(t;m)\right\} = 0, \tag{5.25b}$$

$$\hat{\alpha}^{(n)}(t;-m) = \hat{\alpha}^{(n)*}(t;m). \tag{5.25c}$$

In the above, the superscripts r and i, respectively denote the real and imaginary components of the complex modal coefficient.

Energy Captured

The energy captured by a particular eigenfunction $\hat{\mathbf{\Phi}}^{(n)}(\cdot;m)$ is defined as the expectation of the squares of the norms of the projections of all fields on this eigenfunction. This is equal to the corresponding eigenvalue owing to the unity of the POD eigenfunctions (Lumley, 1967; Holmes et al., 1996; Rowley, 2002)

$$E\left\{\left\|\left\langle \hat{\mathbf{u}}(\cdot;m) , \ \hat{\mathbf{\Phi}}^{(n)}(\cdot;m)\right\rangle\hat{\mathbf{\Phi}}^{(n)}(\cdot;m)\right\|^2\right\} = \Lambda^{(n)}(m). \tag{5.26}$$

POD for Negative m

Suppose that an eigensolution has been obtained to eqn (5.15) for m; denote this pair by $\left\{\Lambda^{(n)}(m),\ \hat{\boldsymbol{\Phi}}^{(n)}(\cdot\,;m)\right\}$. Then, consider the problem for $-m$:

$$2\pi \int_{\Omega_y} \hat{\boldsymbol{\Pi}}(\mathbf{y},\mathbf{y}';-m)\mathbf{A}(\mathbf{y}')\hat{\boldsymbol{\Phi}}^{(n)}(\mathbf{y}';-m)\mathrm{d}\mathbf{y}' = \Lambda^{(n)}(-m)\hat{\boldsymbol{\Phi}}^{(n)}(\mathbf{y};-m).$$

The kernel is Hermitian in m, the weighting function is real, and the eigenvalue is also real. Using these properties and taking the complex conjugate of the above yields

$$2\pi \int_{\Omega_y} \hat{\boldsymbol{\Pi}}(\mathbf{y},\mathbf{y}';m)\mathbf{A}(\mathbf{y}')\hat{\boldsymbol{\Phi}}^{(n)*}(\mathbf{y}';-m)\mathrm{d}\mathbf{y}' = \Lambda^{(n)}(-m)\hat{\boldsymbol{\Phi}}^{(n)*}(\mathbf{y};-m).$$

On comparison with the original equation for m, the conclusion is

$$\Lambda^{(n)}(-m) = \Lambda^{(n)}(m), \tag{5.27a}$$

$$\hat{\boldsymbol{\Phi}}^{(n)}(\cdot\,;-m) = \hat{\boldsymbol{\Phi}}^{(n)*}(\cdot\,;m). \tag{5.27b}$$

Thus the eigensolutions are also Hermitian in m. Then, one can solve the eigenvalue problem for $m \geq 0$ only, and the results for $m < 0$ can be recovered from the Hermitian property (Sirovich, 1987).

Eigenfunctions from Fields

The eigenfunctions themselves can be expressed as a linear combination of the snapshots in the database, since the range of the kernel is in the span of the snapshots (Sirovich, 1987; Rowley, 2002). Thus

$$\hat{\boldsymbol{\Phi}} = \sum_{k=1}^{N_s} c_k \hat{\mathbf{u}}^k, \tag{5.28}$$

for some scalar coefficients $c_k \in \mathbb{C}$. Recall again that the ensemble includes the co-fields as well.

Symmetry of Eigenfunctions

A property of the POD eigenfunctions will be proved that devolves from the axisymmetry of the flow. For notational convenience, the obvious functional dependencies will be omitted in the following derivation. The real and imaginary parts of a quantity are denoted by superscripts r and i, respectively.

Let $\hat{\mathbf{\Phi}}$ be an eigenfunction of the integral eigenvalue problem eqn (5.15). Consider the following vector field $\left(\hat{\Phi}_x^r, \hat{\Phi}_r^r, -\mathrm{i}\hat{\Phi}_\theta^i\right)^{\mathrm{T}}$. Recalling the properties of the cross-correlation tensor given in eqn (5.9), this vector field satisfies the following set of integral equations:

$$
\int_{\Omega y} \left[\begin{array}{ccc} \hat{\Pi}_{xx}^r(\mathbf{y}, \mathbf{y}'; m) & \hat{\Pi}_{xr}^r(\mathbf{y}, \mathbf{y}'; m) & \mathrm{i}\hat{\Pi}_{x\theta}^i(\mathbf{y}, \mathbf{y}'; m) \\ \hat{\Pi}_{rx}^r(\mathbf{y}, \mathbf{y}'; m) & \hat{\Pi}_{rr}^r(\mathbf{y}, \mathbf{y}'; m) & \mathrm{i}\hat{\Pi}_{r\theta}^i(\mathbf{y}, \mathbf{y}'; m) \\ -\mathrm{i}\hat{\Pi}_{\theta x}^i(\mathbf{y}, \mathbf{y}'; m) & -\mathrm{i}\hat{\Pi}_{\theta r}^i(\mathbf{y}, \mathbf{y}'; m) & \hat{\Pi}_{\theta\theta}^r(\mathbf{y}, \mathbf{y}'; m) \end{array} \right] \mathbf{A}(\mathbf{y}') \left[\begin{array}{c} \hat{\Phi}_x^r(\mathbf{y}'; m) \\ \hat{\Phi}_r^r(\mathbf{y}'; m) \\ -\mathrm{i}\hat{\Phi}_\theta^i(\mathbf{y}'; m) \end{array} \right] \mathrm{d}\mathbf{y}'
$$

$$
= \frac{\Lambda(m)}{2\pi} \left[\begin{array}{c} \hat{\Phi}_x^r(\mathbf{y}; m) \\ \hat{\Phi}_r^r(\mathbf{y}; m) \\ -\mathrm{i}\hat{\Phi}_\theta^i(\mathbf{y}; m) \end{array} \right]. \tag{5.29}
$$

The first two component equations are straightforward; the sign is inverted for the last equation for reasons that become clear in the next step.

The remaining part of the eigenfunction $\left(\mathrm{i}\hat{\Phi}_x^i, \mathrm{i}\hat{\Phi}_r^i, \hat{\Phi}_\theta^r\right)^{\mathrm{T}}$ satisfies the following:

$$
\int_{\Omega y} \left[\begin{array}{ccc} \hat{\Pi}_{xx}^r(\mathbf{y}, \mathbf{y}'; m) & \hat{\Pi}_{xr}^r(\mathbf{y}, \mathbf{y}'; m) & \mathrm{i}\hat{\Pi}_{x\theta}^i(\mathbf{y}, \mathbf{y}'; m) \\ \hat{\Pi}_{rx}^r(\mathbf{y}, \mathbf{y}'; m) & \hat{\Pi}_{rr}^r(\mathbf{y}, \mathbf{y}'; m) & \mathrm{i}\hat{\Pi}_{r\theta}^i(\mathbf{y}, \mathbf{y}'; m) \\ -\mathrm{i}\hat{\Pi}_{\theta x}^i(\mathbf{y}, \mathbf{y}'; m) & -\mathrm{i}\hat{\Pi}_{\theta r}^i(\mathbf{y}, \mathbf{y}'; m) & \hat{\Pi}_{\theta\theta}^r(\mathbf{y}, \mathbf{y}'; m) \end{array} \right] \mathbf{A}(\mathbf{y}') \left[\begin{array}{c} \mathrm{i}\hat{\Phi}_x^i(\mathbf{y}'; m) \\ \mathrm{i}\hat{\Phi}_r^i(\mathbf{y}'; m) \\ \hat{\Phi}_\theta^r(\mathbf{y}'; m) \end{array} \right] \mathrm{d}\mathbf{y}'
$$

$$
= \frac{\Lambda(m)}{2\pi} \left[\begin{array}{c} \mathrm{i}\hat{\Phi}_x^i(\mathbf{y}; m) \\ \mathrm{i}\hat{\Phi}_r^i(\mathbf{y}; m) \\ \hat{\Phi}_\theta^r(\mathbf{y}; m) \end{array} \right].
$$

Here, all three component equations are obtained directly, and it is evident that the similarity of the kernels motivated the sign inversion in the previous equation.

The form of these equations makes it evident that the two parts of the eigenfunctions are themselves solutions of the original eigenvalue problem, and thus must be linearly dependent

on each other. This means that the eigenfunctions can be normalized such that the following hold

$$\hat{\Phi}_x = \hat{\Phi}_x^r, \quad \hat{\Phi}_r = \hat{\Phi}_r^r, \quad \hat{\Phi}_\theta = -i\ \hat{\Phi}_\theta^i. \tag{5.30}$$

The solutions for the scalar POD problem satisfy identical relations. An analogous property was proved for the channel flow with one or two homogenous directions by Sirovich (1987).

For the axisymmetric mode, the kernel is real (since it is Hermitian in m). Thus, the eigenfunctions are real, although they all can be multiplied by i. Along with this, the above normalization argument is also valid. The result is that for $m = 0$, the POD modes belong to one of two categories: (a) $\hat{\Phi}_\theta \equiv 0$, in which case $\hat{\Phi}_x$ and $\hat{\Phi}_r$ are real and non-trivial, or, (b) $\hat{\Phi}_x \equiv 0$ and $\hat{\Phi}_r \equiv 0$, in which can $\hat{\Phi}_\theta$ is non-trivial, and can be normalized to be imaginary.

Equivalent Real Eigenvalue Problem

The above symmetry of the eigenfunctions allows one to reframe the complex eigenvalue problem as an equivalent real problem. This effectively halves the computational overhead.

Note that the normalized eigensolution in eqn (5.30) appears exactly in eqn (5.29), and so this is the complex eigenvalue problem to solve. However, it can be written as

$$\int_{\Omega_y} \begin{bmatrix} \hat{\Pi}_{xx}^r(\mathbf{y}, \mathbf{y}'; m) & \hat{\Pi}_{xr}^r(\mathbf{y}, \mathbf{y}'; m) & \hat{\Pi}_{x\theta}^i(\mathbf{y}, \mathbf{y}'; m) \\ \hat{\Pi}_{rx}^r(\mathbf{y}, \mathbf{y}'; m) & \hat{\Pi}_{rr}^r(\mathbf{y}, \mathbf{y}'; m) & \hat{\Pi}_{r\theta}^i(\mathbf{y}, \mathbf{y}'; m) \\ \hat{\Pi}_{\theta x}^i(\mathbf{y}, \mathbf{y}'; m) & \hat{\Pi}_{\theta r}^i(\mathbf{y}, \mathbf{y}'; m) & \hat{\Pi}_{\theta\theta}^r(\mathbf{y}, \mathbf{y}'; m) \end{bmatrix} \mathbf{A}(\mathbf{y}') \begin{bmatrix} \hat{\Phi}_x^r(\mathbf{y}'; m) \\ \hat{\Phi}_r^r(\mathbf{y}'; m) \\ \hat{\Phi}_\theta^i(\mathbf{y}'; m) \end{bmatrix} d\mathbf{y}'$$

$$= \frac{\Lambda(m)}{2\pi} \begin{bmatrix} \hat{\Phi}_x^r(\mathbf{y}; m) \\ \hat{\Phi}_r^r(\mathbf{y}; m) \\ \hat{\Phi}_\theta^i(\mathbf{y}; m) \end{bmatrix}. \tag{5.31}$$

This is the real integral eigenvalue problem that should be solved. The actual eigensolutions can be retrieved from eqn (5.30).

5.3.5 Implementation Details

Direct POD

In all practical implementations, the domain Ω_y of the field is discretized. This reduces the integral eigenvalue problem to a matrix eigenvalue problem through the invocation of an appropriate quadrature rule. Suppose that there are N_g grid points in the discretization of Ω_y. For slice POD, this will imply the discretization of the radial domain. For volumetric POD, this will imply the discretization of the axial and radial domains together. In either case, the matrix representation of each of the components of the two point correlation tensor $\hat{\Pi}_{ij}$ will be of size $N_g \times N_g$. The eigenfunctions will be column vectors of length N_g.

Indicating matrix representation of any quantity w by $[w]$, the integral eigenvalue problem in eqn (5.15)

$$\left[\hat{\mathbf{\Pi}}\right][\mathbf{W}]\left[\hat{\mathbf{\Phi}}\right] = \Lambda\left[\hat{\mathbf{\Phi}}\right].$$

Here, the weight matrix is $[\mathbf{W}] = 2\pi[\mathbf{A}][\Delta]$, with $[\Delta]$ being the matrix implementing the quadrature rule. The uniform dependency on the azimuthal mode m is omitted for notational convenience. This is recognized as a straightforward matrix eigenvalue problem.

A modification that needs to be made is the avoidance of the centerline data-point. The eigenvalue problem becomes singular at the centerline owing to the zero weight accorded to this location in the inner product. The solution is to remove the centerline from the POD domain altogether.

Efficient matrix algebra routines are commonly available for solving the above problem for large N_g. These routines typically achieve greater efficiency and accuracy when the kernel is Hermitian (Baker, 1977). Although $\left[\hat{\mathbf{\Pi}}\right]$ is indeed Hermitian, $\left[\hat{\mathbf{\Pi}}\right][\mathbf{W}]$ is not so in general. This is because of the dependence of the inner product on the radial coordinate. Glauser et al. (1985) proposed the following technique to address this. The matrix $[\mathbf{W}]$ is

diagonal since both $[\mathbf{A}]$ and $[\Delta]$ are diagonal. So it is very easy to find the square root of this matrix, denoted by $[\mathbf{W}]^{1/2}$, as well as the inverse of the latter. With this in mind, the above equation is pre-multiplied on both sides by $[\mathbf{W}]^{1/2}$, and re-arranged to obtain

$$[\mathbf{W}]^{1/2} \left[\hat{\mathbf{\Pi}} \right] [\mathbf{W}]^{1/2} [\mathbf{W}]^{1/2} \left[\hat{\mathbf{\Phi}} \right] = \Lambda \, [\mathbf{W}]^{1/2} \left[\hat{\mathbf{\Phi}} \right].$$

Since $[\mathbf{W}]^{1/2}$ is real and diagonal, the normalized kernel $[\mathbf{W}]^{1/2} \left[\hat{\mathbf{\Pi}} \right] [\mathbf{W}]^{1/2}$ is Hermitian. Its eigenvalues are the same as those of the original kernel. Its eigenvectors are of the form $[\mathbf{W}]^{1/2} \left[\hat{\mathbf{\Phi}} \right]$, from which the eigenvectors of the original kernel, $\left[\hat{\mathbf{\Phi}} \right]$ can be easily retrieved through pre-multiplication by $[\mathbf{W}]^{-1/2}$.

Method of Snapshots

Recall that N_s denotes the total number of snapshots in the ensemble. Sirovich (1987) introduced the method of snapshots to reduce computational overhead in cases where there are fewer snapshots than grid points. In fact, instead of an N_g-dimensional problem, one has to solve an N_s-dimensional problem, followed by a reconstruction step. In the method of snapshots, one does not explicitly use the two-point cross-correlation tensor as the kernel, so that its symmetries cannot be used directly. Instead, one has to consider the snapshots of the co-field along with those of the measured field. Of course, this means that N_s is actually twice the number of independent snapshots measured, making the method less attractive.

5.4 Proper Orthogonal Decomposition on Cross-Stream Slices

The main objective is to obtain the low-dimensional kinematics of the flow over the entire modeling domain shown in Figure 5.3. As described in the previous section, this requires either the two-point cross-correlation tensor or a database of snapshots of the velocity field. The experimental determination of the correlation is prohibitively expensive for the relatively large domain of interest. Current experimental techniques also cannot measure
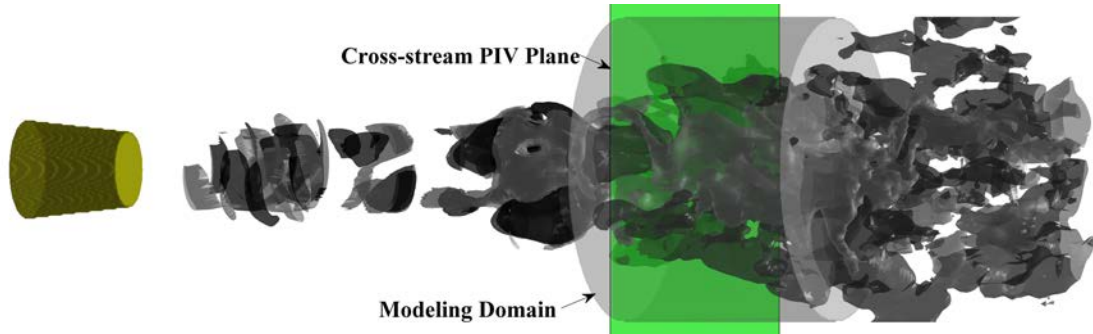
Figure 5.3: Representative cross-stream slice intersecting the modeling domain.

the velocity field simultaneously over the entire modeling domain. The next best option is to obtain an approximation of such a snapshot using stochastic estimation. This involves two major steps: (*i*) determining the correlation between the pressure at a fixed location in the irrotational near-field and the 3-components of the velocity field over a fine-enough grid of points in the desired domain, and (*ii*) using the above correlations and a measurement of pressure at the same location to estimate a snapshot of the velocity field over the entire domain. This is less expensive than the determination of the two-point cross-correlation since the pressure measurement location is fixed. The required correlations may be obtained from point-wise measurements of the velocity field over the entire 3-D domain (say, using hot-wire anemometry or laser Doppler velocimetry). The experimental complexity may be reduced substantially by performing plane-wise measurements of the velocity field on discrete cross-stream sections as shown in Figure 5.3 (Tinney et al., 2008a).

In turbulent flows, two-point correlations (such as required here) are stronger for the larger scales of motion, and tend to vanish for small enough scales. Hence, instead of calculating correlations between the pressure at the fixed location and the velocity at every point in the domain, it is computationally advantageous to first determine the largest scales

of motion in the flow before correlating them to the pressure. As discussed above, slice POD is the technique of choice for obtaining such a low-dimensional description of the flow (Tinney et al., 2008a), and this is pursued here. The derivation has been performed in general terms in the previous section. Here, only the special notation will be established for ease of later discussion. The concept, technique and properties will not be re-iterated.

The velocity field is measured on cross-stream sections at discrete axial locations $x \in \mathcal{X}_u \subset [X_1, X_2]$. Thus, the domain of definition is $\Omega = \mathcal{X}_u \times [0, R] \times \mathbb{T}$. Since the POD is performed independently at each $x \in \mathcal{X}_u$, the pertinent domain for POD for any given x is $\Omega_y \times \mathbb{T}$ with $\Omega_y = [0, R]$.

The appropriate cross-correlation tensor is $\mathbf{\Pi}(r, r', \vartheta; x)$ and its mth azimuthal Fourier transform is $\hat{\mathbf{\Pi}}(r, r'; x, m)$. After the decomposition into azimuthal Fourier modes, one is left with variations in the radial direction only, so that the slice POD problem is actually 1-dimensional. The 1-D slice vector POD problem to be solved independently for each $(x, m) \in \mathcal{X}_u \times [-\infty, \infty]$ is

$$2\pi \int_{r'=0}^{R} \hat{\mathbf{\Pi}}(r, r'; x, m) \hat{\boldsymbol{\phi}}(r'; x, m) r' \mathrm{d}r' = \Xi(x, m) \hat{\boldsymbol{\phi}}(r; x, m). \qquad (5.32)$$

The eigenvalues and eigenfunctions are denoted by Ξ and $\hat{\boldsymbol{\phi}}$. The associated time-dependent POD modal coefficient is

$$\hat{\beta}^{(n)}(t; x, m) := \left\langle \hat{\mathbf{u}}(x, \cdot, t; m) \ , \ \hat{\boldsymbol{\phi}}^{(n)}(\cdot; x, m) \right\rangle. \qquad (5.33)$$

Here, the temporal change of the POD modal coefficients is explicitly indicated as they encode the temporal behavior of the velocity field. Finally, the approximate reconstruction using the truncated basis obtained above consisting of the first N^1 eigenfunctions is

$$\hat{\mathbf{u}}(x, r, t; m) \approx \sum_{n=1}^{N^1} \hat{\beta}^{(n)}(t; x, m) \hat{\boldsymbol{\phi}}^{(n)}(r; x, m). \qquad (5.34)$$

The 1-D slice scalar POD problem to be solved independently for each $(x, m) \in \mathcal{X}_u \times [-\infty, \infty]$ and each component $i \in \{x, r, \theta\}$ is

$$2\pi \int_{r'=0}^{R} \hat{\Pi}_{ii}(r, r'; x, m)\hat{\varphi}_i(r'; x, m)r'\mathrm{d}r' = \xi_i(x, m)\hat{\phi}_i(r; x, m). \tag{5.35}$$

The eigenvalues and eigenfunctions are denoted by ξ and $\hat{\phi}$. The associated time-dependent POD modal coefficient is

$$\hat{\gamma}_i^{(n)}(t; x, m) := \left\langle \hat{u}_i(x, \cdot, t; m) \ , \ \hat{\varphi}_i^{(n)}(\cdot; x, m) \right\rangle. \tag{5.36}$$

Finally, the approximate reconstruction using the truncated basis obtained above consisting of the first N^1 eigenfunctions is

$$\hat{u}_i(x, r, t; m) \approx \sum_{n=1}^{N^1} \hat{\gamma}_i^{(n)}(t; x, m)\hat{\varphi}_i^{(n)}(r; x, m). \tag{5.37}$$

5.5 3-D Velocity Field Reconstruction using Stochastic Estimation

Stochastic estimation was originally introduced to educe coherent structures in turbulent flows (Adrian, 1977). Subsequently, it has also been employed for estimating velocity fields using minimal measurements and a knowledge of the spatial correlations in the flow (Adrian, 1994). The original technique estimated the velocity directly (Adrian, 1994). In the classical version of the complementary technique, the estimated velocity field was projected onto the POD basis, and the projected field was deemed the final estimated field (Bonnet et al., 1994). Subsequently, the complementary technique was modified in two important ways (Boree, 2003; Taylor and Glauser, 2004). The POD modal coefficients of the velocity field were estimated directly so that the estimated velocity field was reconstructed by weighting the POD basis by these coefficients. Additionally, a different physical quantity (eg. pressure, surface shear stress, etc.) was used as the unconditional variable. The concept was later extended by decomposing both the unconditional and conditional fields
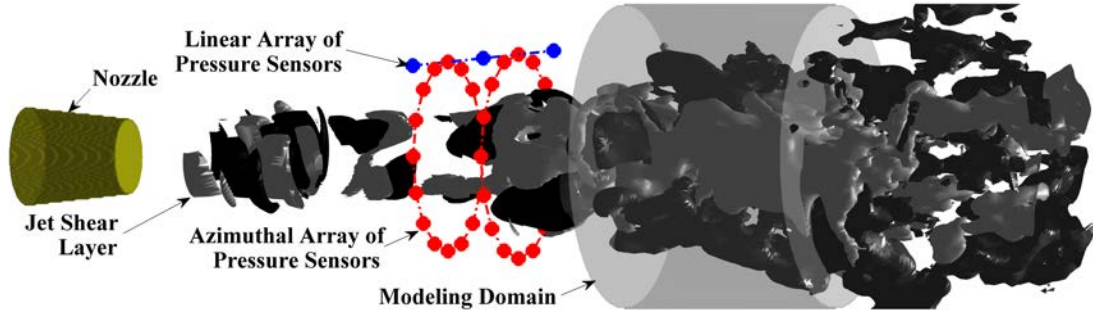
Figure 5.4: Near pressure field measurement schematic.

into their respective low-dimensional modes, be they Fourier or POD, before linking the corresponding modal coefficients through stochastic estimation (Tinney et al., 2008b). The successive modifications were implemented to take advantage of the increased correlations between the low-dimensional quantities, thereby reducing computations without sacrificing (or, in some cases, actually improving) the accuracy of reconstruction. The spectral linear stochastic estimation SLSE was implemented for statistically stationary flows, where the correlation was computed in the temporal Fourier domain (Ewing and Citriniti, 1999; Tinney et al., 2006, 2008b). This was shown to be especially useful whenever the spectral features of the conditional and unconditional variables were disparate, and/or significant time delays existed between them (Tinney et al., 2006). Both these effects are manifest in the present application.

In the modified complementary SLSE formulated by Tinney et al. (2008b), time-resolved pressure measurements in the irrotational near-field of the axisymmetric jet were used as the unconditional variable to simultaneously reconstruct the conditional velocity field on several cross-stream slices through the jet mixing layer. It will soon be evident that this necessitates the computation of the cross-spectral tensor between pressure and velocity.

This was addressed by capturing stereo-PIV snapshots separately on each pertinent cross-stream slice, but at known instants of the pressure-record (Tinney et al., 2008b). The original work relied on a single azimuthal array of pressure sensors, but the reconstruction can be made more accurate by adding an axial linear array of pressure sensors, at little extra cost. Figure 5.4 shows an even more general arrangement of pressure sensors that is used to formulate the problem.

The general notation for the pressure field was introduced in Section 3.2. Here, a specialized notation is introduced for the convenience of discussing the spatially-discrete nature of the measurement. Consider N_p^a azimuthal arrays of pressure transducers arranged at different axial locations $x \in \mathcal{X}_p^a$. In addition, suppose that there are N_p^l individual pressure sensors at different axial locations $x \in \mathcal{X}_p^l$ that do not belong to any azimuthal array. Although the development does not need the individual sensors to form a linear array, they would be assumed to be in a straight line at $\theta = 0$ for notational convenience. Without loss of generality, it is also assumed that all pressure sensors are located on the surface of a virtual cone co-axial with the jet, so that their radial locations are a function of their axial locations. Then, for convenience of notation, the radial coordinate will be omitted and the measurement location will be parameterized by the axial coordinate alone. The choice of such a conical surface was discussed in Section 3.3. Here, the focus is on the correlations of the pressure with the velocity field for modeling purposes. So, the precise location of the surface is not critical as long as it is in the near hydrodynamic range.

With the foregoing discussion, the individual pressure signals from the sensors in the azimuthal arrays are denoted as $P^a : \mathbb{T} \times \mathbb{R} \times \mathcal{X}_p^a \to \mathbb{R}$, $P^a : (\theta, t; x) \mapsto \mathbb{R}$. The decomposition into base and fluctuating pressure is

$$P^a(\theta, t; x) = P^{a,b}(x) + p^a(\theta, t; x). \tag{5.38}$$

In particular, the mean pressure on an azimuthal array is defined as

$$\overline{P}^a(x) := E\left\{\frac{1}{2\pi}\int_{-\pi}^{\pi}P^a(\theta,t;x)\mathrm{d}\theta\right\}.$$

Similarly, the pressure signals on the linear array are denoted as $P^l : \mathbb{R} \times \mathcal{X}_p^l \rightarrow \mathbb{R}$, $P^l : (t;x) \mapsto \mathbb{R}$. The corresponding decomposition is

$$P^l(t;x) = P^{l,b}(x) + p^l(t;x). \tag{5.39}$$

In particular, the mean pressure is $\overline{P}^l(x) := E\left\{P^l(t;x)\right\}$. The azimuthal Fourier transform of p^a is defined in the usual manner: $p^a(\theta,t;x) \xrightarrow{\mathcal{F}_m} \hat{p}^a(t;x,m)$.

The formulation of the SLSE is quite similar for the three cases that are studied here (all are performed in the azimuthal Fourier domain): (a) the original technique for estimating the velocity field $\hat{\mathbf{u}}(x,r,t;m)$, (b) the complementary technique for estimating the vector POD modal coefficients $\hat{\beta}^{(n)}(t;x,m)$, and (c) the complementary technique for estimating the scalar POD modal coefficients $\hat{\gamma}_i^{(n)}(t;x,m)$, $\forall i \in \{x,r,\theta\}$. The equations will be explicitly shown for the last case, as those for the other two cases can be readily deduced from it.

The temporal finite Fourier transforms of the pressure signals are defined as (Bendat and Piersol, 2000):

$$\check{\hat{p}}^a(x,m,f) := \int_{t=t_0-T/2}^{t_0+T/2}\hat{p}^a(t;x,m)\mathrm{e}^{-2\pi\mathrm{i}ft}\mathrm{d}t, \tag{5.40a}$$

$$\check{p}^l(x,f) := \int_{t=t_0-T/2}^{t_0+T/2}p^l(t;x)\mathrm{e}^{-2\pi\mathrm{i}ft}\mathrm{d}t, \tag{5.40b}$$

where f is the temporal frequency, and t_0 locates the mid-point of a time-series of length T. The transforms implicitly depend on t_0 and T. Let the temporal Fourier transform of $\hat{\gamma}_i^{(n)}(t;x',m)$ be denoted as $\check{\hat{\gamma}}_i^{(n)}(x',m,f)$, where $x' \in \mathcal{X}_u$ is the location of the cross-stream slice. Generalizing the formulation of Tinney et al. (2008b), and denoting the estimate of

any quantity w by $\tilde{w}$, the modal coefficient $\check{\tilde{\gamma}}_i^{(n)}(x', m, f)$ is estimated as

$$\check{\tilde{\gamma}}_i^{(n)}(x', m, f) := \sum_{j=1}^{N_p^a} \mathcal{L}_{\gamma_i}^{a*}(x_j, x', n, m, f)\check{\tilde{p}}^a(x_j, m, f) + \sum_{k=1}^{N_p^l} \mathcal{L}_{\gamma_i}^{l*}(x_k, x', n, m, f)\check{\tilde{p}}^l(x_k, f).$$

(5.41)

Einstein's summing convention should not be followed for m and f (Tinney et al., 2008b). To minimize the estimation error $E\left\{ \left| \check{\tilde{\gamma}}_i^{(n)}(x', m, f) - \check{\tilde{\gamma}}_i^{(n)}(x', m, f) \right|^2 \right\}$ for each individual x', i, n, m, and f, the standard least-squares technique yields the following set of $N_p^a + N_p^l$ coupled linear equations for the estimation coefficients $\mathcal{L}$:

$$\mathbf{S}_{pp}(m, f)\boldsymbol{\mathcal{L}}_{\gamma_i}(x', n, m, f) = \mathbf{S}_{p\gamma_i}(x', n, m, f).$$

(5.42)

Here,

$$\mathbf{S}_{pp}(m, f) := \begin{bmatrix} \mathbf{S}_{pp}^{aa}(m, f) & \mathbf{S}_{pp}^{al}(m, f) \\ \mathbf{S}_{pp}^{la}(m, f) & \mathbf{S}_{pp}^{ll}(f) \end{bmatrix},$$

$$\mathbf{S}_{pp}^{aa}(m, f) := \begin{bmatrix} S_{pp}^{aa}(x_1, x_1, m, f) & \cdots & S_{pp}^{aa}(x_1, x_{N_p^a}, m, f) \\ \vdots & \ddots & \vdots \\ S_{pp}^{aa}(x_{N_p^a}, x_1, m, f) & \cdots & S_{pp}^{aa}(x_{N_p^a}, x_{N_p^a}, m, f) \end{bmatrix},$$

$$\mathbf{S}_{pp}^{al}(m, f) := \begin{bmatrix} S_{pp}^{al}(x_1, x_1, m, f) & \cdots & S_{pp}^{al}(x_1, x_{N_p^l}, m, f) \\ \vdots & \ddots & \vdots \\ S_{pp}^{al}(x_{N_p^a}, x_1, m, f) & \cdots & S_{pp}^{al}(x_{N_p^a}, x_{N_p^l}, m, f) \end{bmatrix},$$

$$\mathbf{S}_{pp}^{ll}(m, f) := \begin{bmatrix} S_{pp}^{ll}(x_1, x_1, f) & \cdots & S_{pp}^{ll}(x_1, x_{N_p^l}, f) \\ \vdots & \ddots & \vdots \\ S_{pp}^{ll}(x_{N_p^l}, x_1, f) & \cdots & S_{pp}^{ll}(x_{N_p^l}, x_{N_p^l}, f) \end{bmatrix},$$

$$\mathbf{S}_{pp}^{la}(m, f) = \mathbf{S}_{pp}^{al*}(m, f)$$

$$\boldsymbol{\mathcal{L}}_{\gamma_i}(x', n, m, f) := \begin{bmatrix} \mathcal{L}_{\gamma_i}^a(x_1, x', n, m, f) \\ \vdots \\ \mathcal{L}_{\gamma_i}^a(x_{N_p^a}, x', n, m, f) \\ \mathcal{L}_{\gamma_i}^l(x_1, x', n, m, f) \\ \vdots \\ \mathcal{L}_{\gamma_i}^l(x_{N_p^l}, x', n, m, f) \end{bmatrix},$$

$$
\mathbf{S}_{p\gamma_i}(x', n, m, f) := \begin{bmatrix} S^a_{p\gamma_i}(x_1, x', n, m, f) \\ \vdots \\ S^a_{p\gamma_i}(x_{N^a_p}, x', n, m, f) \\ S^l_{p\gamma_i}(x_1, x', n, m, f) \\ \vdots \\ S^l_{p\gamma_i}(x_{N^l_p}, x', n, m, f) \end{bmatrix}.
$$

The cross-spectral tensors of pressure are defined as

$$
S^{aa}_{pp}(x_j, x_k, m, f) := \lim_{T\to\infty} \frac{1}{T} E\left\{ \check{p}^a(x_j, m, f)\check{p}^{a*}(x_k, m, f) \right\}, \tag{5.43a}
$$

$$
S^{al}_{pp}(x_j, x_k, m, f) := \lim_{T\to\infty} \frac{1}{T} E\left\{ \check{p}^a(x_j, m, f)\check{p}^{l*}(x_k, f) \right\}, \tag{5.43b}
$$

$$
S^{ll}_{pp}(x_j, x_k, f) := \lim_{T\to\infty} \frac{1}{T} E\left\{ \check{p}^l(x_j, f)\check{p}^{l*}(x_k, f) \right\}. \tag{5.43c}
$$

The expectation operator is the un-weighted average over different independent time records of length T. With the experimental realities in mind, the cross-spectral tensors between pressure and the modal coefficients are computed in a different, but equivalent, manner invoking the Wiener-Khintchine theorem (Bendat and Piersol, 2000):

$$
S^a_{p\gamma_i}(x_j, x', n, m, f) := \int_{\tau=-\infty}^{\infty} E\left\{ \hat{p}^a(t+\tau; x_j, m)\hat{\gamma}_i^{(n)*}(t; x', m) \right\} e^{-2\pi i f\tau} d\tau, \tag{5.44a}
$$

$$
S^l_{p\gamma_i}(x_j, x', n, m, f) := \int_{\tau=-\infty}^{\infty} E\left\{ \hat{p}^l(t+\tau; x_j)\hat{\gamma}_i^{(n)*}(t; x', m) \right\} e^{-2\pi i f\tau} d\tau. \tag{5.44b}
$$

Here, t indicates the instant in the pressure record when the snapshot of the velocity field is captured on the cross-stream slice. Several such pairs of pressure records and velocity snapshots must be captured for convergence of the statistics; the expectation operator signifies an ensemble-average over all such pairs. The axisymmetry of the flow can be used to prove that cross-spectral tensors and the estimation coefficients are Hermitian functions of the temporal frequency f; these were enforced here.

Once $\check{\hat{\gamma}}_i^{(n)}(x', m, f)$ is estimated, the estimate of $\hat{\gamma}_i^{(n)}(t; x', m)$ is obtained by inverse Fourier transform. This estimate is most accurate for $t = t_0$, the center of the original

pressure time-series. So, it is best to perform the steps in eqns (5.40) and (5.41), and the inverse transform, separately for each time instant t_0 at which the velocity field is desired. Since the SLSE is intended for off-line implementation, accuracy considerations can be allowed to trump computational efficiency. The actual velocity field is reconstructed using eqn (5.37).

For Tinney et al. (2008b), experimental expediency dictated that the cross-stream PIV slices could not be taken on an axial grid that was fine enough for the reliable computation of the required spatial derivatives. Cubic spline interpolation was used to solve this problem (Tinney et al., 2007; DeBoor, 1978). The same method is adopted here to render the database amenable for the subsequent Galerkin projection. Along with the fluctuating velocity field, the Galerkin projection also requires the spatially-resolved mean velocity field. This can be reconstructed by again using cubic spline interpolation to estimate the mean velocity on a grid of desired axial resolution from the measured mean velocities on the original coarse grid of cross-stream slices.

5.6 Proper Orthogonal Decomposition on Cylindrical Volume

Various methods have been detailed above for obtaining a database consisting of snapshots of the 3 components of velocity on a 3-D cylindrical region of the form shown in Figure 5.1. For validation, one other possibility is to use the numerical database directly. Only the vector POD is pursued here since it produces superior results to the scalar version in the subsequent Galerkin projection (Rowley, 2002). The domain of definition of the velocity field is now $\Omega \equiv \Omega_y \times \mathbb{T}$ with $\Omega_y = [X_1, X_2] \times [0, R]$.

The appropriate cross-correlation tensor is $\mathbf{\Pi}(x, x', r, r', \vartheta)$ and its mth azimuthal Fourier transform is $\hat{\mathbf{\Pi}}(x, x', r, r'; m)$. After the decomposition into azimuthal Fourier modes, one

is left with variations in the axial and radial directions. Then, the 2-D volumetric vector POD problem to be solved independently for each $m \in [-\infty, \infty]$ is

$$2\pi \int_{x'=X_1}^{X_2} \int_{r'=0}^{R} \hat{\mathbf{\Pi}}(x, x', r, r'; m) \hat{\mathbf{\Phi}}(x', r'; m) r' \mathrm{d}r' \mathrm{d}x' = \Lambda(m) \hat{\mathbf{\Phi}}(x, r; m). \tag{5.45}$$

The eigenvalues and eigenfunctions are denoted by Λ and $\hat{\mathbf{\Phi}}$. The associated time-dependent POD modal coefficient is

$$\hat{\alpha}^{(n)}(t; m) := \left\langle \hat{\mathbf{u}}(\cdot, t; m) , \ \hat{\mathbf{\Phi}}^{(n)}(\cdot; m) \right\rangle. \tag{5.46}$$

Finally, the approximate reconstruction using the truncated basis obtained above consisting the first N_m eigenfunctions

$$\hat{\mathbf{u}}(x, r, t; m) \approx \sum_{n=1}^{N_m} \hat{\alpha}^{(n)}(t; m) \hat{\mathbf{\Phi}}^{(n)}(x, r; m). \tag{5.47}$$

The notation allows for different number of POD modes to be retained for the various azimuthal modes, which will be useful subsequently.

5.7 Galerkin Projection of Incompressible Navier-Stokes Equations

5.7.1 The Main Derivation

The low-dimensional description of the flow is recapitulated here for ease of discussion. The decomposition of the velocity and pressure fields into the corresponding base fields and superimposed fluctuations is

$$\mathbf{U}(x, r, \theta, t) = \mathbf{U}^b(x, r) + \mathbf{u}(x, r, \theta, t),$$

$$P(x, r, \theta, t) = P^b(x, r) + p(x, r, \theta, t).$$

The subsequent azimuthal Fourier decomposition of the fluctuations yields

$$\mathbf{U}(x, r, \theta, t) = \mathbf{U}^b(x, r) + \sum_{m=-M}^{M} \hat{\mathbf{u}}(x, r, t; m) \mathrm{e}^{im\theta},$$

109

$$P(x, r, \theta, t) = P^b(x, r) + \sum_{m=-M}^{M} \hat{p}(x, r, t; m)\mathrm{e}^{\mathrm{i}m\theta}.$$

Here, M is the highest azimuthal mode retained. Subsequently, vector POD is performed on the unsteady velocity field and the velocity decomposition becomes

$$\mathbf{U}(x, r, \theta, t) = \mathbf{U}^b(x, r) + \sum_{m=-M}^{M} \sum_{n=1}^{N_m} \hat{\alpha}^{(n)}(t; m)\hat{\boldsymbol{\Phi}}^{(n)}(x, r; m)\mathrm{e}^{\mathrm{i}m\theta}.$$

It was previously discussed that the above truncation represents a finite-dimensional subspace $S \subset \mathcal{L}_2(\Omega)$. However, S is typically not invariant, meaning that for initial conditions of velocities in S, the velocities associated with the evolving flow do not remain in S for all future times. To extend the reduced-order representation of the kinematics to the dynamics, an approximate ROM is needed that renders S invariant. To address this, one performs a Galerkin projection of the governing dynamics onto S. The projection is orthogonal and minimizes the error in approximation defined in the sense of the norm on $\mathcal{L}_2(\Omega)$ that is induced from the inner product used in the POD (Rowley, 2002).

The actual implementation of Galerkin projection proceeds in two steps. First, the velocity fields appearing in the governing dynamical equation are represented in terms of their low-dimensional approximations using the orthonormal basis of S derived from POD. Since one starts with as many dynamical equations as there are independent flow variables, the dynamical equations themselves can be considered to form a vector field in $\mathcal{L}_2(\Omega)$. Taking the inner product of this vector field with each of the basis vector fields of S leads to the desired set of ODE's governing the evolution of the associated POD modal coefficients. This procedure is now discussed for the flow problem at hand.

The reason for assuming the jet flow field to be incompressible has been discussed in Section 5.1. The non-dimensionalized incompressible Navier-Stokes equation is

$$\frac{\partial \mathbf{U}}{\partial t} = \frac{1}{Re}\nabla^2 U - (\mathbf{U} \cdot \nabla)\,\mathbf{U} - \nabla P. \tag{5.48}$$

In cylindrical coordinates, the equations are

$$
\begin{aligned}
\frac{\partial U_i}{\partial t} = \frac{1}{Re} &\left\{ \left(\frac{\partial^2}{\partial x^2} + \frac{\partial^2}{\partial r^2} + \frac{1}{r}\frac{\partial}{\partial r} + \frac{1}{r^2}\frac{\partial^2}{\partial \theta^2} \right) U_i + \left(-\frac{U_r}{r^2} - \frac{2}{r^2}\frac{\partial U_\theta}{\partial \theta} \right) \delta_{i,r} \right. \\
&\left. + \left(-\frac{U_\theta}{r^2} + \frac{2}{r^2}\frac{\partial U_r}{\partial \theta} \right) \delta_{i,\theta} \right\} - \left\{ \left(U_x\frac{\partial}{\partial x} + U_r\frac{\partial}{\partial r} + \frac{U_\theta}{r}\frac{\partial}{\partial \theta} \right) U_i + \left(-U_\theta \delta_{i,r} + U_r \delta_{i,\theta} \right) \frac{U_\theta}{r} \right\} \\
&- \left(\frac{\partial P}{\partial x}\delta_{i,x} + \frac{\partial P}{\partial r}\delta_{i,r} + \frac{1}{r}\frac{\partial P}{\partial \theta}\delta_{i,\theta} \right),
\end{aligned}
$$

where $i \in \{x, r, \theta\}$, and δ is the Kronecker delta. A compact notation for the above set of equations is

$$
\frac{\partial \mathbf{U}}{\partial t} = \frac{1}{Re}L_G(\mathbf{U}) + Q_G(\mathbf{U}, \mathbf{U}) + G_G(P),
$$

where, for vector fields $\mathbf{U}$ and $\mathbf{V}$, and scalar field f, the functions are defined as

$$
\begin{aligned}
L_G(\mathbf{U}) &:= \left(\frac{\partial^2}{\partial x^2} + \frac{\partial^2}{\partial r^2} + \frac{1}{r}\frac{\partial}{\partial r} + \frac{1}{r^2}\frac{\partial^2}{\partial \theta^2} \right) \mathbf{U} + \left(-\frac{U_r}{r^2} - \frac{2}{r^2}\frac{\partial U_\theta}{\partial \theta} \right) \hat{\boldsymbol{\epsilon}}_r + \left(-\frac{U_\theta}{r^2} + \frac{2}{r^2}\frac{\partial U_r}{\partial \theta} \right) \hat{\boldsymbol{\epsilon}}_\theta, \\
Q_G(\mathbf{U}, \mathbf{V}) &:= - \left\{ \left(U_x\frac{\partial}{\partial x} + U_r\frac{\partial}{\partial r} + \frac{U_\theta}{r}\frac{\partial}{\partial \theta} \right) \mathbf{V} + \left(-U_\theta \hat{\boldsymbol{\epsilon}}_r + U_r \hat{\boldsymbol{\epsilon}}_\theta \right) \frac{V_\theta}{r} \right\}, \\
G_G(f) &:= - \left(\frac{\partial f}{\partial x}\hat{\boldsymbol{\epsilon}}_x + \frac{\partial f}{\partial r}\hat{\boldsymbol{\epsilon}}_r + \frac{1}{r}\frac{\partial f}{\partial \theta}\hat{\boldsymbol{\epsilon}}_\theta \right).
\end{aligned}
$$

Here, $\hat{\boldsymbol{\epsilon}}_x$, $\hat{\boldsymbol{\epsilon}}_r$ and $\hat{\boldsymbol{\epsilon}}_\theta$ are respectively the unit vectors along the axial, radial and azimuthal directions.

Substituting the decomposition into base flow and fluctuations, one obtains

$$
\begin{aligned}
\frac{\partial \mathbf{u}}{\partial t} = &\frac{1}{Re}L_G\left(\mathbf{U}^b \right) + Q_G\left(\mathbf{U}^b, \mathbf{U}^b \right) + G_G\left(P^b \right) + \frac{1}{Re}L_G(\mathbf{u}) + Q_G\left(\mathbf{U}^b, \mathbf{u} \right) + Q_G\left(\mathbf{u}, \mathbf{U}^b \right) \\
&+ Q_G(\mathbf{u}, \mathbf{u}) + G_G(p).
\end{aligned}
$$

The azimuthal Fourier decomposition of the fluctuations are substituted in the above equation, followed by Galerkin projection onto the azimuthal Fourier basis. This yields

$$
\begin{aligned}
\frac{\partial \hat{\mathbf{u}}(m)}{\partial t} = &\,\delta_{m,0}\left\{ \frac{1}{Re}\hat{L}_G\left(\mathbf{U}^b \right) + \hat{Q}_G\left(\mathbf{U}^b, \mathbf{U}^b \right) + \hat{G}_G\left(P^b \right) \right\} + \frac{1}{Re}\hat{L}_G(\hat{\mathbf{u}}(m)) \\
&+ \hat{Q}_G\left(\mathbf{U}^b, \hat{\mathbf{u}}(m) \right) + \hat{Q}_G\left(\hat{\mathbf{u}}(m), \mathbf{U}^b \right) + \sum_{m'=m-M}^{M} \hat{Q}_G\left(\hat{\mathbf{u}}(m'), \hat{\mathbf{u}}(m-m') \right) + \hat{G}_G\left(\hat{p}(m) \right),
\end{aligned}
$$

where, for vector fields $\hat{\mathbf{u}}(m)$ and $\hat{\mathbf{v}}(m')$, and scalar field $\hat{f}(m)$, the functions are defined as

$$\hat{L}_{\mathrm{G}}\left(\hat{\mathbf{u}}(m)\right) := \left(\frac{\partial^2}{\partial x^2} + \frac{\partial^2}{\partial r^2} + \frac{1}{r}\frac{\partial}{\partial r} - \frac{m^2}{r^2}\right)\hat{\mathbf{u}}(m) - \frac{\hat{u}_r(m) + 2im\hat{u}_\theta(m)}{r^2}\hat{\boldsymbol{\epsilon}}_r$$
$$- \frac{\hat{u}_\theta(m) - 2im\hat{u}_r(m)}{r^2}\hat{\boldsymbol{\epsilon}}_\theta,$$

$$\hat{Q}_{\mathrm{G}}\left(\hat{\mathbf{u}}(m), \hat{\mathbf{v}}(m')\right) := -\left\{\left(\hat{u}_x(m)\frac{\partial}{\partial x} + \hat{u}_r(m)\frac{\partial}{\partial r} + \frac{im'\hat{u}_\theta(m)}{r}\right)\hat{\mathbf{v}}(m')\right.$$
$$\left. + \left(-\hat{u}_\theta(m)\hat{\boldsymbol{\epsilon}}_r + \hat{u}_r(m)\hat{\boldsymbol{\epsilon}}_\theta\right)\frac{\hat{v}_\theta(m')}{r}\right\},$$

$$\hat{G}_{\mathrm{G}}\left(\hat{f}(m)\right) := -\left(\frac{\partial}{\partial x}\hat{\boldsymbol{\epsilon}}_x + \frac{\partial}{\partial r}\hat{\boldsymbol{\epsilon}}_r + \frac{im}{r}\hat{\boldsymbol{\epsilon}}_\theta\right)\hat{f}(m).$$

Note that for the purposes of using the above functions with the base flow field as argument, the latter is treated as an axisymmetric mode $(m = 0)$.

Finally, substituting the Galerkin expansion of the velocity field fluctuations in the azimuthal Fourier domain using the POD basis, and performing a Galerkin projection onto the retained basis, one obtains the reduced-order model

$$\dot{\hat{\alpha}}^{(n)}(t; m) = \delta_{m,0}c_{\mathrm{G}}(n) + \sum_{n'=1}^{N_m} l_{\mathrm{G}}(n, n', m)\hat{\alpha}^{(n')}(t; m)$$
$$+ \sum_{m'=m-M}^{M} \sum_{n'=1}^{N_{m'}} \sum_{n'=1}^{N_{m-m'}} q_{\mathrm{G}}(n, n', n'', m, m')\hat{\alpha}^{(n')}(t; m')\hat{\alpha}^{(n'')}(t; m - m')$$
$$+ d_{\mathrm{G}}(t; n, m). \tag{5.49}$$

Here, the static coefficients are

$$c_{\mathrm{G}}(n) := \left\langle \frac{1}{Re}\hat{L}_{\mathrm{G}}(\mathbf{U}^b) + \hat{Q}_{\mathrm{G}}(\mathbf{U}^b, \mathbf{U}^b) + \hat{G}_{\mathrm{G}}(P^b) \,,\, \hat{\boldsymbol{\Phi}}^{(n)}(m = 0) \right\rangle, \tag{5.50a}$$

$$l_{\mathrm{G}}(n, n', m) := \frac{1}{Re}l_{\mathrm{G}}^{\mathrm{d}}(n, n', m) + l_{\mathrm{G}}^{\mathrm{c}}(n, n', m), \tag{5.50b}$$

$$l_{\mathrm{G}}^{\mathrm{d}}(n, n', m) := \left\langle \hat{L}_{\mathrm{G}}(\hat{\boldsymbol{\Phi}}^{(n')}(m)) \,,\, \hat{\boldsymbol{\Phi}}^{(n)}(m) \right\rangle, \tag{5.50c}$$

$$l_{\mathrm{G}}^{\mathrm{c}}(n, n', m) := \left\langle \hat{Q}_{\mathrm{G}}(\mathbf{U}^b, \hat{\boldsymbol{\Phi}}^{(n')}(m)) + \hat{Q}_{\mathrm{G}}(\hat{\boldsymbol{\Phi}}^{(n')}(m), \mathbf{U}^b) \,,\, \hat{\boldsymbol{\Phi}}^{(n)}(m) \right\rangle, \tag{5.50d}$$

$$q_{\mathrm{G}}(n, n', n'', m, m') := \left\langle \hat{Q}_{\mathrm{G}}(\hat{\boldsymbol{\Phi}}^{(n')}(m'), \hat{\boldsymbol{\Phi}}^{(n'')}(m - m')) \,,\, \hat{\boldsymbol{\Phi}}^{(n)}(m) \right\rangle. \tag{5.50e}$$

All these coefficients are real following the symmetry arguments presented earlier. The pressure enters the unsteady term as follows

$$d_{\mathrm{G}}(t; n, m) := \left\langle \hat{G}_{\mathrm{G}}\left(\hat{p}(t; m)\right) , \ \hat{\mathbf{\Phi}}^{(n)}(m) \right\rangle.$$

Since the flow is incompressible, the velocity field is divergence-free, and this term can be simplified using Gauss divergence theorem to obtain

$$d_{\mathrm{G}}(t; n, m) = -2\pi \left| \int_0^R \hat{p}(x, r, t; m) \hat{\Phi}_x^{(n)*}(x, r; m) r \mathrm{d}r \right|_{x=X_1}^{X_2}$$
$$- 2\pi R \int_{X_1}^{X_2} \hat{p}(x, R, t; m) \hat{\Phi}_r^{(n)*}(x, R; m) \mathrm{d}x. \tag{5.51}$$

The incompressibility of the flow can also be used to convert the second derivatives appearing in $l_{\mathrm{G}}^{\mathrm{d}}(n, n', m)$ into first derivatives using the Gauss divergence theorem.

$$l_{\mathrm{G}}^{\mathrm{d}}(n, n', m) = \int_0^R \left[\left| \frac{\partial \hat{\Phi}_i^{(n')}(m)}{\partial x} \hat{\Phi}_i^{(n)*}(m) \right|_{X_1}^{X_2} - \int_{X_1}^{X_2} \frac{\partial \hat{\Phi}_i^{(n')}(m)}{\partial x} \frac{\partial \hat{\Phi}_i^{(n)*}(m)}{\partial x} \mathrm{d}x \right] r \mathrm{d}r$$
$$+ \int_{X_1}^{X_2} \left[\left| r \frac{\partial \hat{\Phi}_i^{(n')}(m)}{\partial r} \hat{\Phi}_i^{(n)*}(m) \right|_R - \int_0^R \frac{\partial \hat{\Phi}_i^{(n')}(m)}{\partial r} \frac{\partial \hat{\Phi}_i^{(n)*}(m)}{\partial r} r \mathrm{d}r \right] \mathrm{d}x$$
$$+ \int_{X_1}^{X_2} \int_0^R \left[-m^2 \hat{\Phi}_i^{(n')}(m) - \left\{ \hat{\Phi}_r^{(n')}(m) + 2\mathrm{i}m \hat{\Phi}_\theta^{(n')}(m) \right\} \delta_{ir} \right.$$
$$\left. - \left\{ \hat{\Phi}_\theta^{(n')}(m) - 2\mathrm{i}m \hat{\Phi}_r^{(n')}(m) \right\} \delta_{i\theta} \right] \hat{\Phi}_i^{(n)*}(m) \frac{\mathrm{d}r \mathrm{d}x}{r}.$$

5.7.2 Particular Assumptions in Galerkin Projection

The main assumption of GP is the possibility of approximating the dynamics in the truncated basis. A specific assumption in the preceding derivation is also the incompressibility of the flow. Additional modeling approximations and assumptions are described here.

Base Flow Choice

Previously, the three main choices for the base flow have been mentioned briefly; these will be elaborated further here.

In applying the Reynolds decomposition to the Navier-Stokes equations, a dichotomy is noticed in the ROM literature regarding the appropriate mean field representation. One group has chosen the base field to be the steady mean field derived from empirical data by ensemble-averaging as well as averaging over any homogenous direction, if applicable (e.g., Deane et al., 1991; Rempfer and Fasel, 1994; Rajaee et al., 1994; Rowley et al., 2004; Caraballo et al., 2007). Another group has adopted a slowly time-varying mean field averaged over all homogenous directions, followed by a Boussinesq approximation to tie the mean field to the Reynolds stresses (e.g., Aubry et al., 1988; Zheng, 1990; Ukeiley et al., 2001; Noack et al., 2003, 2008; Luchtenburg et al., 2009). This is said to ensure bounded state trajectories by providing some feedback from the Reynolds stresses to the turbulence production mechanism (the gradient of the mean-field). For the turbulent axisymmetric jet, the large range of scales precludes an accurate approximation of the Reynolds stresses of the neglected scales, thereby prompting the adoption of a steady empirical mean field. In the free jet under consideration, the mean pressure field is atmospheric. The gradient vanishes for this constant field, and thus it does not contribute to the constant term in eqn (5.50).

The base flow can be set to the null field (e.g., Rempfer and Fasel, 1994; Barone et al., 2009). In this case, the first POD mode in the axisymmetric azimuthal mode $m = 0$ will be found to be the mean flow, since it is the common field among all snapshots and typically has the highest energy. Then, typically the corresponding modal coefficient is set to the constant $\sqrt{\Lambda^{(1)}(0)}$. In preliminary simulations of the resultant model for the flow field under consideration, it was found that fidelity is compromised in taking this route (compared to the first option described above). A possible reason for this is the large value of this one mode, which magnifies the inaccuracies that are already present due to the approximations.

The other possible reason is that the coefficient for the 'mean-flow-mode' is not strictly constant. Owing to these disadvantages, this route was not taken.

The base flow can be set to the steady solution the Navier-Stokes equation in eqn (5.48). This removes the constant term from the final equation set eqn (5.49). This is particularly beneficial for control law formulation, since typical control theory focuses on stabilizing the trivial solution of the associated ODEs. Note that the nonlinear set of ODEs typically does not have a unique equilibrium point, so that it is difficult to identify the state of the model to stabilize once the Galerkin projection has been performed as above. This route has been taken for wake-stabilization schemes in the literature (e.g., Luchtenburg et al., 2009; Noack et al., 2010; Tadmor et al., 2011). The steady solution of the low-Re DNS jet was computed and used in this manner, but the fidelity of the resulting ROM was found to be diminished compared to the first option above.

In summary, the base flow chosen in this work is the ensemble-averaged and azimuthal-averaged mean field. Such information is available for both numerical and experimental flow databases.

Modeling the Pressure Term

For the assumed incompressible flow under consideration, eqn (5.51) showed that the pressure term reduces to a surface integral over the boundary of the POD domain. Moreover, owing to the vanishing of velocity fluctuations (and hence, the eigenfunctions) at the outer radius of the POD domain, the second part of the expression is also negligible. Therefore, the pressure needs to be evaluated at the inflow and outflow cross-stream slices only. Even in this simplified form, the term cannot be directly evaluated from experimental data. In previous applications to similarly unbounded flows (Rajaee et al., 1994; Rempfer and Fasel, 1994), this term has been assumed to vanish altogether. Thus, before attempting to model

the term, the inaccuracy incurred by neglecting it altogether must be ascertained. The neglect of the pressure term would be shown to be allowable for the unforced flow. However, the actuation effect will be modeled with this term in the next chapter. It is noted here that Noack et al. (2005) showed that for cylinder wake flow simulations, it is most appropriate to retain the pressure term, and to solve for it in parallel using the pressure Poisson equation.

Eddy Viscosity Model

The eigenfunction-basis of the velocity is truncated in both the Fourier space as well as the POD space, keeping only the most energetic modes. The neglected modes have low energy and typically correspond to the smaller-scales of turbulence; this makes them important for dissipation. Since neglecting these modes generally has the effect of making the ROM overly energetic, it is common to model the effect of these neglected modes using an eddy-viscosity representation. Some researchers have incorporated a global eddy viscosity and treated it as a bifurcation parameter (Aubry et al., 1988; Zheng, 1990; Ukeiley et al., 2001). Others have computed empirical values of modal eddy viscosities by balancing energy or momentum among the retained modes (Cazemier et al., 1998; Couplet et al., 2003; Caraballo et al., 2007). Both these strategies amount to adding linear terms to the ROM, but the latter strategy removes the tuning parameter. A third route is the finite-time thermodynamics formulation of Noack et al. (2008). This has been shown to be useful for wake flows that are typically dominated by a few frequencies, so that several more modes can be retained to model the dynamics of the first few dissipation scales while still obtaining a low-dimensional description. The strategy was evaluated for the broadband turbulent flow under consideration, and found to be unsuitable. The empirical energy balance route is adopted here to model the eddy viscosity (Cazemier et al., 1998), because it was effective in the cavity tone control model developed at GDTL (Caraballo et al., 2007).

Moreover, the absence of tuning parameters in this eddy viscosity modeling scheme renders the implementation straightforward.

The linear term in the original ROM of eqn (5.49) was separated into a dissipative part and a convective part, and the eddy viscosity model augments the dissipative part as follows

$$
\begin{aligned}
\dot{\hat{\alpha}}^{(n)}(t;m) = {} & \delta_{m,0} c_G(n) + \sum_{n'=1}^{N_m} \left\{ \left(\frac{1}{Re} + \frac{\delta_{n,n'}}{Re_T{}^{(n)}(m)} \right) l_G^d(n,n',m) + l_G^c(n,n',m) \right\} \hat{\alpha}^{(n')}(t;m) \\
& + \sum_{m'=m-M}^{M} \sum_{n'=1}^{N_{m'}} \sum_{n'=1}^{N_{m-m'}} q_G(n,n',n'',m,m') \hat{\alpha}^{(n')}(t;m') \hat{\alpha}^{(n'')}(t;m-m') \\
& + d_G(t;n,m).
\end{aligned}
\tag{5.52}
$$

Subsequently, the modal eddy viscosity $Re_T{}^{(n)}(m)$ is uniquely determined by requiring that rate of change of the modal fluctuation energy vanish when averaged over the ensemble. That is,

$$
E\left[\frac{d}{dt} \left\{ \left| \hat{\alpha}^{(n)}(t;m) - E\left(\hat{\alpha}^{(n)}(t;m) \right) \right|^2 \right\} \right] = 0.
$$

The mean of the modal coefficients vanish if the mean flow is chosen as the base flow. With other base flows, the axisymmetric modes may have non-zero mean values. Moreover, the pressure term is also neglected per the preceding discussion. The modeled eddy viscosity should be non-negative to have the intended dissipative effect. Then, one obtains the following expression for the modal eddy viscosity

$$
\begin{aligned}
\frac{1}{Re_T{}^{(n)}(m)} = {} & \max\left[0, -\frac{1}{Re} - \frac{1}{l_G^d(n,n,m)\Lambda^{(n)}(m)} \left\{ l_G^c(n,n,m)\Lambda^{(n)}(m) \right. \right. \\
& \left. + \sum_{m'=m-M}^{M} \sum_{n'=1}^{N_{m'}} \sum_{n'=1}^{N_{m-m'}} q_G(n,n',n'',m,m') \right. \\
& \left. \left. \times E\left\{ \Re\left(\hat{\alpha}^{(n)*}(t;m) \hat{\alpha}^{(n')}(t;m') \hat{\alpha}^{(n'')}(t;m-m') \right) \right\} \right\} \right].
\end{aligned}
\tag{5.53}
$$

5.8 Galerkin Projection of the Compressible Governing Dynamics

The focus of this work is the development of a ROM for the jet employing an assumption of incompressibility. Thus the compressibility effects will not be addressed in great depth. Instead, standard techniques will be used directly from the literature to roughly assess the possible penalty incurred by neglecting compressibility effects.

The appropriate state vector to consider is $\mathbf{W} := (U_x, U_r, U_\theta, P, \Xi)^{\mathrm{T}}$ (Vigo, 1998). Here, the three components of velocity and pressure are readily recognized; the symbol Ξ denotes the specific volume, which is the reciprocal of density. This choice leads to a ROM that is a set of ODES's with quadratic polynomial nonlinearity. Note that the above state variables are normalized by the appropriate nozzle exit conditions, so that they are non-dimensional.

The governing dynamics are the mass, momentum and energy conservation equations, with momentum conservation being the Navier-Stokes equations. For a generic scalar q and a generic 3-D vector $\mathbf{v}$, the following vector calculus functions are defined.

$$L^D(\mathbf{v}) := \nabla \cdot \mathbf{v}$$

$$L^L(q) := \nabla^2 q$$

$$L^G(\mathbf{v}) := (\nabla \mathbf{v}) + (\nabla \mathbf{v})^{\mathrm{T}}$$

$$Q^C(\mathbf{v}, W) := (\mathbf{v} \cdot \nabla)W.$$

The functions are recognized as dilatation, Laplacian, symmetric gradient (of a vector), and convective acceleration functions respectively.

The components of a generic state vector are denoted as $\mathbf{q} := (q_x, q_r, q_\theta, q_p, q_\xi)^{\mathrm{T}}$, and its velocity subspace as $\mathbf{q}_u := (q_x, q_r, q_\theta)^{\mathrm{T}}$. Then, the governing equations can be compactly written in the following vector form (Batchelor, 1967; Schlichting, 1968; Gloerfelt, 2008)

$$\dot{\mathbf{W}} = \frac{1}{Re}Q^1(\mathbf{W}, \mathbf{W}) + Q^2(\mathbf{W}, \mathbf{W}). \tag{5.55}$$

Here,

$$Q^1\left(\mathbf{q}^{[1]},\mathbf{q}^{[2]}\right) := \begin{bmatrix} \left\{L^L\left(q_x^{[1]}\right) + \dfrac{1}{3}\dfrac{\partial L^D\left(\mathbf{q}_u^{[1]}\right)}{\partial x}\right\} q_\xi^{[2]} \\[2em] \left\{L^L\left(q_r^{[1]}\right) - \dfrac{q_r^{[1]}}{r^2} - \dfrac{2}{r^2}\dfrac{\partial q_\theta^{[1]}}{\partial \theta} + \dfrac{1}{3}\dfrac{\partial L^D\left(\mathbf{q}_u^{[1]}\right)}{\partial r}\right\} q_\xi^{[2]} \\[2em] \left\{L^L\left(q_\theta^{[1]}\right) - \dfrac{q_\theta^{[1]}}{r^2} + \dfrac{2}{r^2}\dfrac{\partial q_r^{[1]}}{\partial \theta} + \dfrac{1}{3r}\dfrac{\partial L^D\left(\mathbf{q}_u^{[1]}\right)}{\partial \theta}\right\} q_\xi^{[2]} \\[2em] \dfrac{\gamma}{\mathcal{P}}\left\{L^L\left(q_p^{[1]}\right) q_\xi^{[2]} + q_p^{[1]} L^L\left(q_\xi^{[2]}\right)\right\} \\ + (\gamma - 1)\left\{\tfrac{1}{2}L^G\left(\mathbf{q}_u^{[1]}\right):L^G\left(\mathbf{q}_u^{[2]}\right) - \tfrac{2}{3}L^D\left(\mathbf{q}_u^{[1]}\right)L^D\left(\mathbf{q}_u^{[2]}\right)\right\} \\[1.5em] 0 \end{bmatrix},$$

$$Q^2\left(\mathbf{q}^{[1]},\mathbf{q}^{[2]}\right) := -\begin{bmatrix} Q^C\left(\mathbf{q}_u^{[1]}, q_x^{[2]}\right) + q_\xi^{[1]}\dfrac{\partial q_p^{[2]}}{\partial x} \\[1.5em] Q^C\left(\mathbf{q}_u^{[1]}, q_r^{[2]}\right) - \dfrac{q_\theta^{[1]} q_\theta^{[2]}}{r} + q_\xi^{[1]}\dfrac{\partial q_p^{[2]}}{\partial r} \\[1.5em] Q^C\left(\mathbf{q}_u^{[1]}, q_\theta^{[2]}\right) + \dfrac{q_r^{[1]} q_\theta^{[2]}}{r} + q_\xi^{[1]}\dfrac{1}{r}\dfrac{\partial q_p^{[2]}}{\partial \theta} \\[1.5em] Q^C\left(\mathbf{q}_u^{[1]}, q_p^{[2]}\right) + \gamma q_p^{[1]} L^D\left(\mathbf{q}_u^{[2]}\right) \\[1em] Q^C\left(\mathbf{q}_u^{[1]}, q_\xi^{[2]}\right) - q_\xi^{[1]} L^D\left(\mathbf{q}_u^{[2]}\right) \end{bmatrix}.$$

Here, γ is the ratio of specific heats and $\mathcal{P}$ is the Prandtl number of the flow; both are assumed constant, as is the viscosity. The symbol : denotes the double dot product for two tensor quantities (Borisenko and Tarapov, 1968).

As in the incompressible case, the instantaneous flow state $\mathbf{W}$ is decomposed into a steady base flow $\mathbf{W}^b$ and the residual fluctuations $\mathbf{w}$. Then, the governing dynamics for the fluctuations are

$$\begin{aligned} \dot{\mathbf{w}} = &\left\{\frac{1}{Re}Q^1\left(\mathbf{W}^b,\mathbf{W}^b\right) + Q^2\left(\mathbf{W}^b,\mathbf{W}^b\right)\right\} \\ &+ \left[\frac{1}{Re}\left\{Q^1\left(\mathbf{W}^b,\mathbf{w}\right) + Q^1\left(\mathbf{w},\mathbf{W}^b\right)\right\} + \left\{Q^2\left(\mathbf{W}^b,\mathbf{w}\right) + Q^2\left(\mathbf{w},\mathbf{W}^b\right)\right\}\right] \\ &+ \left\{\frac{1}{Re}Q^1\left(\mathbf{w},\mathbf{w}\right) + Q^2\left(\mathbf{w},\mathbf{w}\right)\right\}. \end{aligned} \tag{5.57}$$

The subsequent azimuthal Fourier decomposition of the state vector fluctuations is standard:

$$\mathbf{w}(x, r, \theta, t) = \sum_{m=-M}^{M} \hat{\mathbf{w}}(x, r, t; m)\mathrm{e}^{im\theta}.$$

Here, M is the highest azimuthal mode retained. Applying this decomposition to eqn (5.57) followed by Galerkin projection on the Fourier azimuthal basis results in the following

$$
\begin{aligned}
\dot{\hat{\mathbf{w}}}(m) &= \delta_{m,0}\left\{\frac{1}{Re}Q^1\left(\mathbf{W}^b, \mathbf{W}^b\right) + Q^2\left(\mathbf{W}^b, \mathbf{W}^b\right)\right\} \\
&+ \frac{1}{Re}\left\{\hat{Q}^{\{1\}}\left(\mathbf{W}^b, \hat{\mathbf{w}}(m)\right) + \hat{Q}^{\{1\}}\left(\hat{\mathbf{w}}(m), \mathbf{W}^b\right)\right\} \\
&+ \left\{\hat{Q}^{\{2\}}\left(\mathbf{W}^b, \hat{\mathbf{w}}(m)\right) + \hat{Q}^{\{2\}}\left(\hat{\mathbf{w}}(m), \mathbf{W}^b\right)\right\} \\
&+ \sum_{m'=m-M}^{M}\left\{\frac{1}{Re}\hat{Q}^{\{1\}}\left(\hat{\mathbf{w}}(m'), \hat{\mathbf{w}}(m-m')\right) + \hat{Q}^{\{2\}}\left(\hat{\mathbf{w}}(m'), \hat{\mathbf{w}}(m-m')\right)\right\}.
\end{aligned}
$$

(5.58)

Here,

$$
\hat{Q}^{\{1\}}\left(\hat{\mathbf{q}}^{[1]}(m), \hat{\mathbf{q}}^{[2]}(m')\right)
$$

$$
:= \begin{bmatrix}
\left\{\hat{L}^l\left(\hat{q}_x^{[1]}(m)\right) + \frac{1}{3}\frac{\partial \hat{L}^d\left(\hat{\mathbf{q}}^{[1]}(m)\right)}{\partial x}\right\}\hat{q}_\xi^{[2]}(m') \\[2ex]
\left\{\hat{L}^l\left(\hat{q}_r^{[1]}(m)\right) - \frac{\hat{q}_r^{[1]}(m)}{r^2} - \frac{2im\hat{q}_\theta^{[1]}(m)}{r^2} + \frac{1}{3}\frac{\partial \hat{L}^d\left(\hat{\mathbf{q}}^{[1]}(m)\right)}{\partial r}\right\}\hat{q}_\xi^{[2]}(m') \\[2ex]
\left\{\hat{L}^l\left(\hat{q}_\theta^{[1]}(m)\right) - \frac{\hat{q}_\theta^{[1]}(m)}{r^2} + \frac{2im\hat{q}_r^{[1]}(m)}{r^2} + \frac{im\hat{L}^d\left(\hat{\mathbf{q}}^{[1]}(m)\right)}{3r}\right\}\hat{q}_\xi^{[2]}(m') \\[2ex]
\frac{\gamma}{\mathcal{P}}\left\{\hat{L}^l\left(\hat{q}_p^{[1]}(m)\right)\hat{q}_\xi^{[2]}(m') + \hat{q}_p^{[1]}(m)\hat{L}^l\left(\hat{q}_\xi^{[2]}(m')\right)\right\} \\
+ (\gamma-1)\left\{\frac{1}{2}\hat{L}^g\left(\hat{\mathbf{q}}^{[1]}(m)\right):\hat{L}^g\left(\hat{\mathbf{q}}^{[2]}(m')\right) - \frac{2}{3}\hat{L}^d\left(\hat{\mathbf{q}}^{[1]}(m)\right)\hat{L}^d\left(\hat{\mathbf{q}}^{[2]}(m')\right)\right\} \\[2ex]
0
\end{bmatrix},
$$

$$
\hat{Q}^{\{2\}}\left(\hat{\mathbf{q}}^{[1]}(m), \hat{\mathbf{q}}^{[2]}(m')\right)
$$

$$
:= - \begin{bmatrix}
\hat{Q}^c\left(\hat{\mathbf{q}}^{[1]}(m),\hat{q}_x^{[2]}(m')\right) + \hat{q}_\xi^{[1]}(m)\dfrac{\partial \hat{q}_p^{[2]}(m')}{\partial x} \\[2mm]
\hat{Q}^c\left(\hat{\mathbf{q}}^{[1]}(m),\hat{q}_r^{[2]}(m')\right) - \dfrac{\hat{q}_\theta^{[1]}(m)\hat{q}_\theta^{[2]}(m')}{r} + \hat{q}_\xi^{[1]}(m)\dfrac{\partial \hat{q}_p^{[2]}(m')}{\partial r} \\[2mm]
\hat{Q}^c\left(\hat{\mathbf{q}}^{[1]}(m),\hat{q}_\theta^{[2]}(m')\right) + \dfrac{\hat{q}_r^{[1]}(m)\hat{q}_\theta^{[2]}(m')}{r} + \hat{q}_\xi^{[1]}(m)\dfrac{\mathrm{i}m'}{r}\hat{q}_p^{[2]}(m') \\[2mm]
\hat{Q}^c\left(\hat{\mathbf{q}}^{[1]}(m),\hat{q}_p^{[2]}(m')\right) + \gamma\hat{q}_p^{[1]}(m)\hat{L}^d\left(\hat{\mathbf{q}}^{[2]}(m')\right) \\[2mm]
\hat{Q}^c\left(\hat{\mathbf{q}}^{[1]}(m),\hat{q}_\xi^{[2]}(m')\right) - \hat{q}_\xi^{[1]}(m)\hat{L}^d\left(\hat{\mathbf{q}}^{[2]}(m')\right)
\end{bmatrix},
$$

$$
\hat{L}^d\left(\hat{\mathbf{q}}(m)\right) := \frac{\partial \hat{q}_x(m)}{\partial x} + \frac{1}{r}\frac{\partial\{r\hat{q}_r(m)\}}{\partial r} + \frac{\mathrm{i}m}{r}\hat{q}_\theta(m),
$$

$$
\hat{L}^l\left(\hat{q}_i(m)\right) := \frac{\partial^2 \hat{q}_i(m)}{\partial x^2} + \frac{1}{r}\frac{\partial}{\partial r}\left\{r\frac{\partial \hat{q}_i(m)}{\partial r}\right\} - \frac{m^2}{r^2}\hat{q}_i(m),
$$

$$
\hat{L}^g\left(\hat{\mathbf{q}}(m)\right) := 2\frac{\partial \hat{q}_x(m)}{\partial x}\hat{\boldsymbol{\epsilon}}_x\otimes\hat{\boldsymbol{\epsilon}}_x + 2\frac{\partial \hat{q}_r(m)}{\partial r}\hat{\boldsymbol{\epsilon}}_r\otimes\hat{\boldsymbol{\epsilon}}_r + \frac{2}{r}\left(\mathrm{i}m\hat{q}_\theta(m)+\hat{q}_r(m)\right)\hat{\boldsymbol{\epsilon}}_\theta\otimes\hat{\boldsymbol{\epsilon}}_\theta
$$
$$
+ \left\{\frac{\partial \hat{q}_x(m)}{\partial r} + \frac{\partial \hat{q}_r(m)}{\partial x}\right\}\left(\hat{\boldsymbol{\epsilon}}_x\otimes\hat{\boldsymbol{\epsilon}}_r + \hat{\boldsymbol{\epsilon}}_r\otimes\hat{\boldsymbol{\epsilon}}_x\right)
$$
$$
+ \left\{\frac{\mathrm{i}m\hat{q}_x(m)}{r} + \frac{\partial \hat{q}_\theta(m)}{\partial x}\right\}\left(\hat{\boldsymbol{\epsilon}}_x\otimes\hat{\boldsymbol{\epsilon}}_\theta + \hat{\boldsymbol{\epsilon}}_\theta\otimes\hat{\boldsymbol{\epsilon}}_x\right)
$$
$$
+ \left\{\frac{1}{r}\left(\mathrm{i}m\hat{q}_r(m)-\hat{q}_\theta(m)\right) + \frac{\partial \hat{q}_\theta(m)}{\partial r}\right\}\left(\hat{\boldsymbol{\epsilon}}_r\otimes\hat{\boldsymbol{\epsilon}}_\theta + \hat{\boldsymbol{\epsilon}}_\theta\otimes\hat{\boldsymbol{\epsilon}}_r\right),
$$

$$
\hat{Q}^c\left(\hat{\mathbf{q}}^{[1]}(m),\hat{q}_i^{[2]}(m')\right) := \left\{\hat{q}_x^{[1]}(m)\frac{\partial}{\partial x} + \hat{q}_r^{[1]}(m)\frac{\partial}{\partial r} + \frac{\mathrm{i}m'}{r}\hat{q}_\theta^{[1]}(m)\right\}\hat{q}_i^{[2]}(m').
$$

The next step is the 2-D volumetric POD of the state fluctuations, which requires the specification of the inner product. Since the state variables are non-dimensionalized by the jet exit conditions which reflects the proper scaling laws, the inner product between two arbitrary states $\hat{\mathbf{w}}^{(1)}$ and $\hat{\mathbf{w}}^{(2)}$ is defined as (Iollo et al., 2000; Gloerfelt, 2008)

$$
\left\langle \hat{\mathbf{w}}^{(1)},\ \hat{\mathbf{w}}^{(2)}\right\rangle := \int_{x=X_1}^{X_2}\int_{r=0}^{R}\hat{\mathbf{w}}^{(2)*}\hat{\mathbf{w}}^{(1)}r\,\mathrm{d}r\,\mathrm{d}x.
$$

There is one other definition of the inner product in the literature (Lumley and Poje, 1997; Bourguet et al., 2011), which involves normalization of each state variable by its ensemble-averaged and domain-integrated variance. However, this may accord unphysical primacy to the thermodynamic variables vis-a-vis the velocity field in the POD, and hence is not pursued here.

The remaining POD follows directly from the previous presentation in the incompressible case. In particular, the POD of the state is formally written as

$$\hat{\mathbf{w}}(x, r, t; m) \approx \sum_{n=1}^{N_m} \hat{\alpha}^{(n)}(t; m) \hat{\mathbf{\Phi}}^{(n)}(x, r; m). \tag{5.60}$$

Here, $\hat{\mathbf{\Phi}}$ is the POD spatial eigenfunction and $\hat{\alpha}$ is the corresponding temporal coefficient. The notation is retained from the incompressible POD; any ambiguity may be resolved from the context.

The standard Galerkin projection of the above dynamic system onto the retained basis yields the set of ODEs with quadratic nonlinearity:

$$\dot{\hat{\alpha}}^{(n)}(m) = \delta_{m,0} \left\{ \frac{1}{Re} \tilde{C}_n^{[1]} + \tilde{C}_n^{[2]} \right\} + \sum_{n'=1}^{N_m} \left\{ \frac{1}{Re} \tilde{L}_{nn'}^{[1]}(m) + \tilde{L}_{nn'}^{[2]}(m) \right\} \hat{\alpha}^{(n')}(m)$$
$$+ \sum_{m'=m-M}^{M} \sum_{n'=1}^{N_{m'}} \sum_{n''=1}^{N_{m-m'}} \left\{ \frac{1}{Re} \tilde{Q}_{nn'n''}^{[1]}(m, m') + \tilde{Q}_{nn'n''}^{[2]}(m, m') \right\} \hat{\alpha}^{(n')}(m') \hat{\alpha}^{(n'')}(m - m'). \tag{5.61}$$

Here,

$$\tilde{C}_n^{[k]} := \left\langle \hat{Q}^{\{k\}}(\mathbf{W}^b, \mathbf{W}^b) \ , \ \hat{\mathbf{\Phi}}^{(n)}(m) \right\rangle,$$

$$\tilde{L}_{nn'}^{[k]}(m) := \left\langle \hat{Q}^{\{k\}}(\mathbf{W}^b, \hat{\mathbf{\Phi}}^{(n')}(m)) + \hat{Q}^{\{k\}}(\hat{\mathbf{\Phi}}^{(n')}(m), \mathbf{W}^b) \ , \ \hat{\mathbf{\Phi}}^{(n)}(m) \right\rangle,$$

$$\tilde{Q}_{nn'n''}^{[k]}(m, m') := \left\langle \hat{Q}^{\{k\}}(\hat{\mathbf{\Phi}}^{(n')}(m'), \hat{\mathbf{\Phi}}^{(n'')}(m - m')) \ , \ \hat{\mathbf{\Phi}}^{(n)}(m) \right\rangle.$$

The modal eddy viscosity can be introduced in a manner similar to the incompressible case. The choices of the base flow also follow from the preceding discussion of incompressible ROM.

5.9   Results and Discussion

The presentation and discussion of the results will be made in several logical steps, starting from the simplest case, and proceeding in increasing levels of complexity. This will allow the determination of the sources of errors in the modeling strategy.

1. The DNS jet database offers time- and space-resolved flow field information, and hence it directly serves as the empirical data underpinning the first reduced-order model developed here. The inaccuracy incurred by neglecting the pressure term and the compressibility effects are also analyzed with this database.

2. In the next step, the axial grid of the DNS database is down-sampled and then interpolated to mimic the reduced information available from experiments, and the model obtained is compared with the first ROM. This isolates the effect of grid resolution on modeling fidelity.

3. The unforced ILES database has similar information-content as the preceding database, and a ROM is derived from it at this point. Comparison of its behavior with the above models identifies Reynolds number effects on model behavior.

4. The experimental database has even poorer information content, since the flow field is not available simultaneously at the different axial locations, as supposed in the previous steps. So, a slice POD followed by SLSE is performed to reconstruct approximate snapshots from the DNS database, as would be possible from experimental data. The accuracy of this reconstruction is determined here. The ROM derived from this approximate database is also evaluated.

5. Similar data reduction and reconstruction is performed on the unforced ILES database to keep track of Reynolds number effects.

6. At this point, the experimental database is analyzed and modeled using the tools developed above to characterize its low-dimensional behavior.

Each of the above steps are covered in the subsequent sub-sections.

5.9.1 Model from Direct Numerical Simulation Database

In the semi-bounded jet flow under consideration, the choice of the domain size and location for the ROM is not obvious. Kastner (2007) performed extensive investigation of the effect of varying these parameters on the POD mode shapes educed from streamwise 2C-PIV data of the Mach 0.9 experimental jet. He reported that low-order POD modes had similar shapes as long as the axial window span accommodated the typical large-scale structures. Here, the ROM is developed for controlling the large-scale structures in the turbulent jet mixing layer near the end of the potential core. If the model domain is too short to accommodate the typical large-scale structures in their entirety, then their dynamics cannot be modeled correctly (Rajaee et al., 1994). The constraint at the other extreme is the necessity for the near-field pressure at the upstream location to be well-correlated to the velocity field on the cross-stream slice at the most downstream location for the success of the SLSE procedure. The need to focus the modeling effort near the end of the potential core has been elucidated in the introduction. The chosen cylindrical modeling domain extended from $X_1 = 7$ to $X_2 = 10$ along the axial direction; the radial extent was $R = 2$ (see Figure 5.5). The foregoing discussion, as well as the results of Kastner (2007), are used to justify this choice without further exploration.

Volumetric POD

The first step in the ROM development is the extraction of the low-dimensional kinematics through volumetric POD. There are 80 equally spaced azimuthal grid points, so that 41 distinct azimuthal modes can be resolved. The POD is performed on each of the azimuthal modes separately. In Section 2.5.1, the resolution of the uniform axial and radial grid has been mentioned to be $0.0625D$. Thus, with the POD domain defined as above,
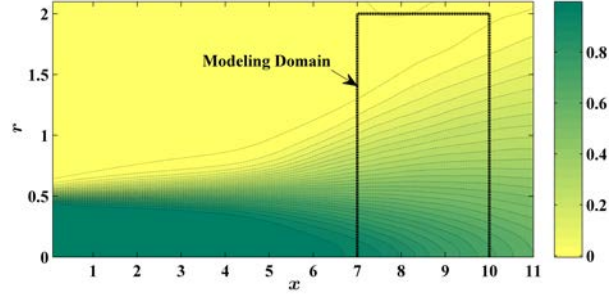
Figure 5.5: Contour of normalized mean axial velocity in DNS jet with cylindrical modeling domain indicated.

there are 49 axial and 32 radial grid points in it. Moreover, in the vector POD, all three velocity components are considered together. This makes for a 4704-dimensional eigenvalue problem for each azimuthal mode, which is beyond the capability of the desktop installation of MATLAB used for this work. Thus, the snapshot method must be used.

Recall that the number of measured snapshots selected must be augmented by an equal number of co-fields to incorporate the symmetries of the flow in the POD. Thus, to be a saving compared to the direct method, one can at most use 2351 snapshots in the snapshot method. The DNS database is time-resolved and its 2316 snapshots cover 164 flow time steps. For greater statistical significance, the snapshots retained in the ensemble are selected at random from the available database.

The convergence of the POD method with increasing number of snapshots retained (N_s) is shown in Figure 5.6(a); this graph is obtained in the following manner. The indicated number of snapshots is selected randomly from the database and their co-fields are appended to the ensemble. After performing the volumetric POD separately for each azimuthal mode, all the eigenvalues are gathered together and sorted in descending order. The cumulative sum is computed for the 100 most energetic modes in each case. Finally, the results are
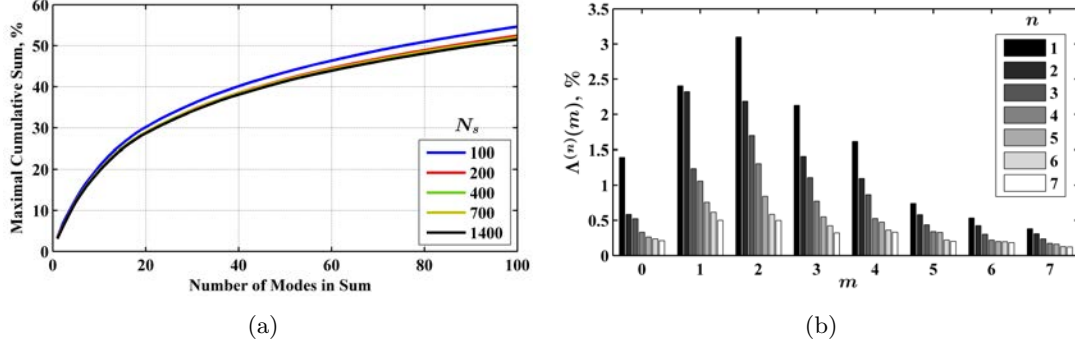
Figure 5.6: Eigenvalues of volumetric POD of DNS database. (a) Convergence of POD with increasing number of snapshots (N_s) retained. (b) Eigenspectrum for $N_s = 1400$.

normalized by the total energy over all modes. The latter is actually calculated directly from the turbulent kinetic energy, and is averaged over all the 2316 available snapshots. The results show that at least 200 snapshots should be retained, but anything beyond that does not really change the outcome. The high level of turbulence manifests itself in the poor overall convergence, with 40 modes resolving less than 40% of the energy.

The eigenspectrum obtained from the application of the volumetric vector POD to 1400 snapshots is presented in Figure 5.6(b), as a percentage of the total energy captured. For $m \neq 0$, the eigenvalues are doubled to account for the negative azimuthal modes too. The dominance of azimuthal modes 1 and 2 is to be expected in this axial domain from earlier slice POD's reported for cross-stream slices spanning this region (Jung et al., 2004; Tinney et al., 2008a). The steady decay in the azimuthal modal energy is useful for low-dimensional reconstruction.

Figure 5.7 presents some representative eigenfunctions from the POD. Following the arguments in eqn (5.30) only the non-trivial components of the eigenfunction are shown. In all the first three POD modes, the axisymmetric eigenfunctions have trivial azimuthal

126
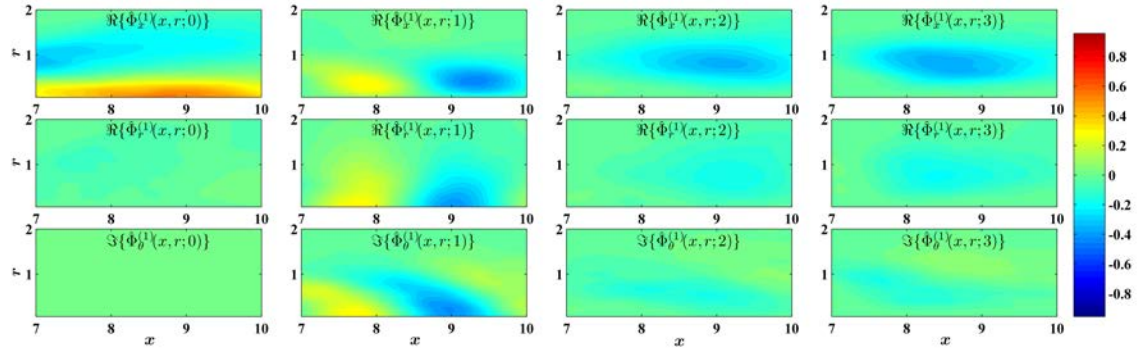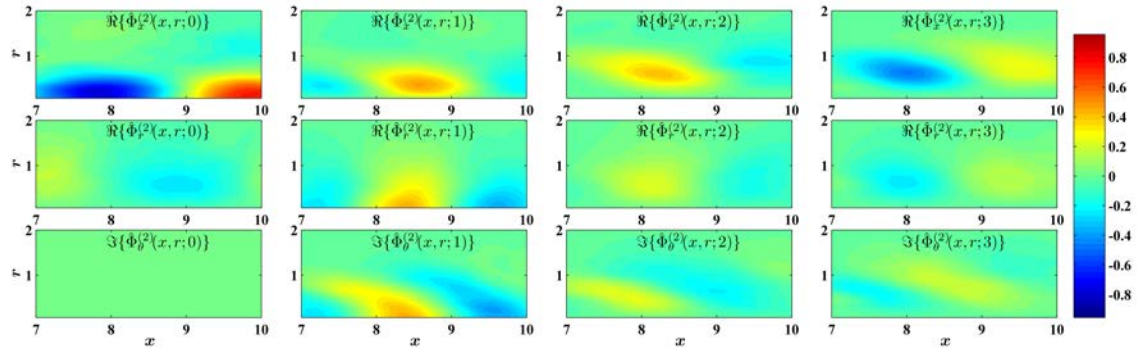
(a) POD mode 1
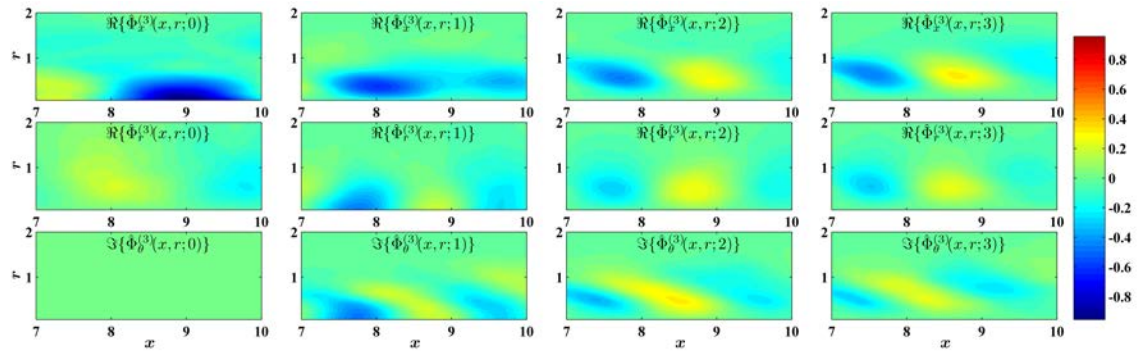
(b) POD mode 2

(c) POD mode 3

Figure 5.7: First few eigenfunctions from the volumetric POD of DNS database.

(a) POD mode 1   (b) POD mode 2
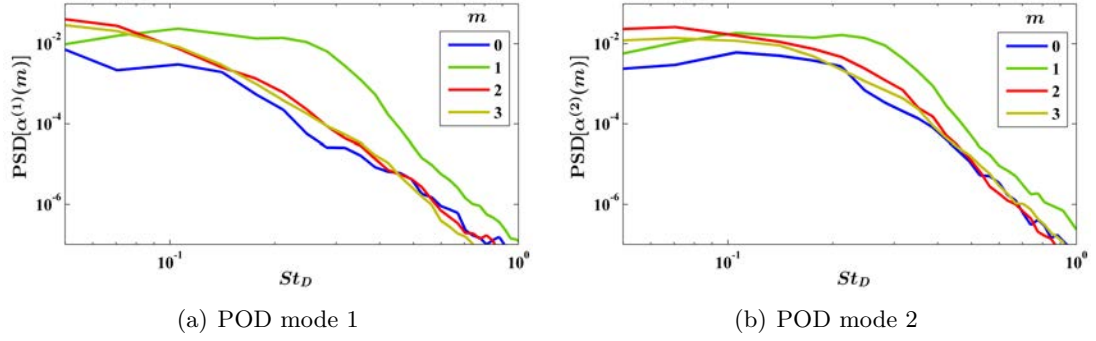
Figure 5.8: Power spectral densities of first few POD modal eigenfunctions from the volumetric POD of DNS database.

components (recall the discussion following eqn (5.30)). In fact, the non-trivial azimuthal component is not found till the 11th POD mode. Figure 5.8 depicts the power spectral densities of the first few POD modal coefficients. All these results are analyzed and discussed together next.

The axisymmetric mode is dominated by a shape that is reminiscent of the difference between the mean field and steady flow field. The steady flow field for this Reynolds number was found to have a long potential core. Thus compared to the mean flow, it has higher velocity on the centerline and lower velocity outside the lip-line. Such a mode has been termed the 'shift-mode' by Noack et al. (2010); and it arises explicitly with much higher energy when the steady flow is chosen as the base flow for the POD. The automatic incorporation of this mode in the POD is important for two reasons. In simulations of ROMs derived from this basis, this mode will have a slow time variation, which will mimic the inherent stabilizing feedback from the Reynolds stresses to the mean flow. Moreover, in forced jet models considered in Chapter 6, this mode will allow the mean flow of the simulation to change with forcing cases. The corresponding modal coefficient indeed has a

spectral peak at the lowest frequency resolved. The typical PSD of velocity on the centerline has a peak at the column mode for low speed jets (Petersen and Samet, 1988) and is much flatter for high speed jets (Tinney et al., 2006). Although the POD mode under discussion is dominated by a centerline structure, it has a very different PSD since it is behaving as the shift mode. The second and third axisymmetric POD modes essentially represent a traveling wave, as evident from their 90° phase shift (Holmes et al., 1996). The quadrature phase-relation between the axial and radial velocities is noteworthy since the associated structures signify a traveling vortex (Lau et al., 1972). The wavelength appears to be slightly longer than the axial extent of the domain. The shapes peak around the centerline. The spectrum of the 2nd POD coefficient also has a broadband peak away from the lowest frequency end, indicating a weak frequency preference.

The first two POD eigenvalues of $m = 1$ are paired, and the consequent traveling-wave-nature of the eigenfunctions (Holmes et al., 1996) are evident in Figure 5.7. The shapes are similar and are shifted by 90° with respect to each other. The axial component of the eigenfunctions is maximum around the lip-line whereas the radial and azimuthal components peak around the centerline. The wavelength appears to be $\sim 2.5D$. The PSD's of the corresponding coefficients have a broadband peak that is typically observed in the PSD of lip-line velocity measurements in high-speed jets (Tinney et al., 2006).

The 2nd and 3rd helical modes are dominated by large shapes with high axial velocity in the outside part of the shear layer. The spectra of the corresponding modal coefficients also demonstrate a low-frequency peak that is associated with the large size of the structures. The lower-energy modes have shapes similar to those found for the first helical mode. Their PSD's also have correspondingly broadband peaks. The peak frequencies are lower than for

the $m = 1$ modes, since the corresponding eigenfunctions peak in the outside part of the shear layer where frequencies are indeed lower (Jung et al., 2004).

If a flow is incompressible, then each of its velocity realizations are solenoidal. The vector POD eigenfunctions for such a flow, being linear combinations of these realizations (Rowley, 2002), inherit the solenoidal property also. Thus one way of assessing the incompressibility assumption for the present flow is to determine how close $\hat{\mathbf{\Phi}}^{(n)}(x, r; m)$ is to being solenoidal. The following metric is proposed for this purpose

$$
\hat{\mathcal{E}}_{sol}^{(n)}(m) := \frac{\displaystyle\int_{X_1}^{X_2} \int_0^R \left| \frac{\partial}{\partial x}\hat{\Phi}_x^{(n)}(m) + \frac{1}{r}\frac{\partial}{\partial r}\left\{r\hat{\Phi}_r^{(n)}(m)\right\} + \frac{m}{r}\hat{\Phi}_\theta^{(n)}(m) \right|^2 rdrdx}{\displaystyle\int_{X_1}^{X_2} \int_0^R \left[\left|\frac{\partial}{\partial x}\hat{\Phi}_x^{(n)}(m)\right|^2 + \left|\frac{1}{r}\frac{\partial}{\partial r}\left\{r\hat{\Phi}_r^{(n)}(m)\right\}\right|^2 + \left|\frac{m}{r}\hat{\Phi}_\theta^{(n)}(m)\right|^2 \right] rdrdx},
$$

(5.63)

where the dependencies on the spatial coordinates have been omitted. The numerator is the norm of the dilatation; the denominator is the sum of the norms of the individual components of the dilatation. The metric is evaluated for the eigenfunctions obtained above for $n \in [1, 12]$ and $m \in [0, 10]$. The maximum value of $\hat{\mathcal{E}}_{sol}$ is found to be 0.6%, thereby lending support to the incompressibility assumption.

Reduced-Order Model Simulation over a Short Time Horizon

The first derivatives of the eigenfunctions and mean velocities appearing in the coefficients of the ROMs are computed using 6th-order accurate finite differences. Higher order derivatives are not required in the model. The ROMs are simulated using MATLAB's `ode45`, which is a Runge-Kutta (4, 5) ODE solver with automatic step-size selection. The initial condition is taken directly from the DNS database; estimation strategies will be discussed in Chapter 7.

The simulation results are linearly interpolated on the time axis of the DNS database for direct comparison. For the purposes of feedback control, the ROM needs to predict the flow

over short periods, and a time horizon of 5 flow time steps is used in the results presented here, unless otherwise indicated. Simulations starting from 20 different initial conditions are performed to arrive at metrics for simulation fidelity. The first ROM considered ignores the pressure term (see eqn (5.51)).

Let the simulated fluctuating velocity be denoted by $\tilde{\mathbf{u}}(x, r, \theta, t)$, with $t \in [0, T_{\text{sim}}]$, T_{sim} being the time horizon of the simulation. The actual fluctuating velocity $\mathbf{u}(x, r, \theta, t)$ is also known at the same time instant t. Thus, with the underlying inner product defined as in eqn (5.13), the following simulation error metric is proposed

$$
\begin{aligned}
\mathcal{E}_{\text{sim}} &:= \frac{\dfrac{1}{T_{\text{sim}}} \displaystyle\int_{t=0}^{T_{\text{sim}}} ||\tilde{\mathbf{u}} - \mathbf{u}||^2 \mathrm{d}t}{\dfrac{1}{T_{\text{sim}}} \displaystyle\int_{t=0}^{T_{\text{sim}}} ||\mathbf{u}||^2 \mathrm{d}t} \\
&= 1 + \frac{\displaystyle\sum_{m=-M}^{M} \sum_{n=1}^{N_m} \frac{1}{T_{\text{sim}}} \int_{t=0}^{T_{\text{sim}}} \left\{ \left|\tilde{\hat{\alpha}}^{(n)}(m)\right|^2 - 2\Re\left(\tilde{\hat{\alpha}}^{(n)*}(m)\hat{\alpha}^{(n)}(m)\right) \right\} \mathrm{d}t}{\dfrac{1}{T_{\text{sim}}} \displaystyle\int_{t=0}^{T_{\text{sim}}} ||\mathbf{u}||^2 \mathrm{d}t}. \qquad (5.64)
\end{aligned}
$$

The second expression follows from the orthonormality of the eigenfunction basis. Here, the POD modal coefficients $\hat{\alpha}^{(n)}$ and $\tilde{\hat{\alpha}}^{(n)}$ correspond to velocities $\mathbf{u}$ and $\tilde{\mathbf{u}}$, respectively. The obvious functional dependencies have been omitted for notational convenience. This metric evidently compresses a lot of information, and is useful for a preliminary comparison of reduced-order models.

The fidelity of the ROM is not directly related to the number of most-energetic modes retained in the basis (Rempfer, 2000; Rowley, 2002; Caraballo et al., 2003; Ilak and Rowley, 2008). However, in the absence of any other information, it is still the best correlation to investigate. The eigenmodes are sorted as discussed for Figure 5.6(a), and increasing number of the most-energetic modes are retained in the assessment. Twenty initial conditions equally spaced over the available data record are used for simulations, and the reported
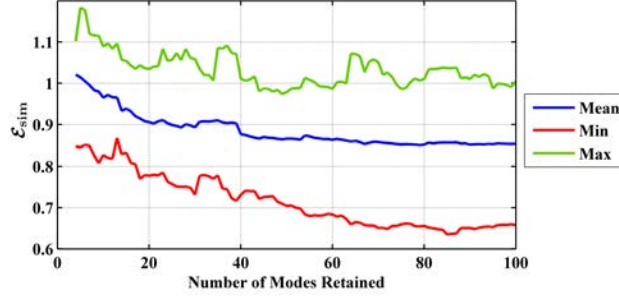
Figure 5.9: Simulation error for ROMs built from the original DNS database for various numbers of modes retained. The mean and range of errors across 20 different initial conditions are shown.

$\mathcal{E}_{\text{sim}}$ in Figure 5.9 is averaged over all of them. The range of simulation errors is also presented.

Several remarks on these results are in order:

- The simulation errors are quite large, demonstrating the inherent inaccuracies of low-dimensional modeling for this complex flow.

- The simulation error does not decrease monotonically with increasing size of the retained basis. In fact, an almost asymptotic behavior is noted beyond about 80 modes. Given this behavior, a 44-D basis is chosen for subsequent analysis. Its mean simulation error is 0.87.

- The initial condition is seen to have a large effect on the simulation error, as is to be expected for the short time horizon being analyzed.

- A large part of the error is due to the partial basis used. The contribution of this factor can be determined from Figure 5.6(a). The associated projection error is defined analogous to the simulation error in eqn (5.64), with $\tilde{\mathbf{u}}$ denoting the field reconstructed

132
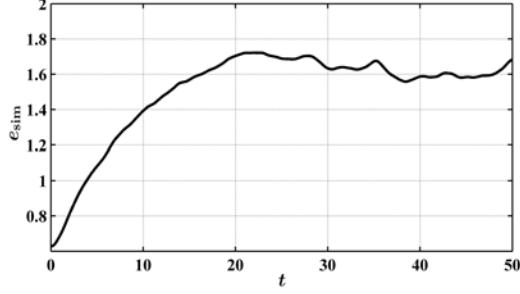
Figure 5.10: Temporal evolution of simulation error for the 44-D ROM built from the original DNS database, averaged over 10 initial conditions.

from the retained basis. For the 44-D basis, the projection error is 0.61 (i.e. it captures 39% of the flow energy).

The simulation error $\mathcal{E}_{\text{sim}}$ is a gross metric since it integrates the instantaneous errors. A more detailed metric that captures the temporal evolution of the error is defined as follows

$$e_{\text{sim}}(t) := \frac{||\tilde{\mathbf{u}}(\cdot, t) - \mathbf{u}(\cdot, t)||^2}{E\left\{||\mathbf{u}||^2\right\}}. \tag{5.65}$$

This metric is analyzed for the 44-D ROM in Figure 5.10 after averaging over 10 initial conditions. The initial error is the projection error owing to the truncated basis. The error is seen to grow monotonically initially, but stabilizes after about 20 time steps.

For more insight, the next analysis focuses on the behavior of the model on the projected basis; this removes the effect of the truncation errors. As indicated by eqn (5.64), two of the ingredients of the simulation error are the energies of the projection and simulation. The instantaneous energy of orthogonal projection onto the subspace S is defined as (see eqn (5.11))

$$\varepsilon(t) := ||\mathcal{P}_S \mathbf{u}(\cdot, t)||^2 = \sum_{m=-M}^{M} \sum_{n=1}^{N_m} \left|\hat{\alpha}^{(n)}(t; m)\right|^2. \tag{5.66}$$

133
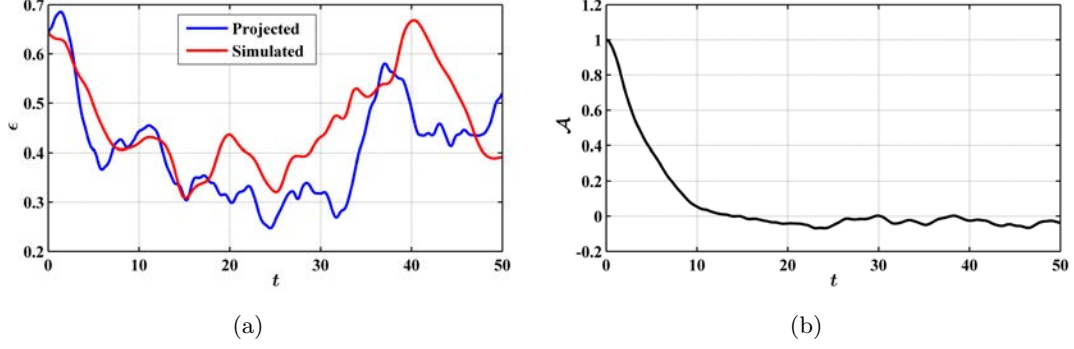
Figure 5.11: Temporal evolution of (a) instantaneous energies of projection and simulation, and (b) alignment of the two fields, for the 44-D ROM built from the original DNS database.

The instantaneous energy of simulation in the subspace S is defined analogously by replacing $\hat{\alpha}$ with $\tilde{\hat{\alpha}}$ in the above expression. The instantaneous energies of projection and simulation for the 44-D ROM are shown in Figure 5.11(a) for a particular initial condition. The simulation energy is seen to closely follow the projection energy.

The remaining ingredient of the simulation error is the alignment of the simulated and projected vector fields, defined as

$$
\begin{aligned}
\mathcal{A}(t) &:= \frac{\langle \mathcal{P}_S \mathbf{u}(\cdot, t) \, , \, \mathcal{P}_S \tilde{\mathbf{u}}(\cdot, t) \rangle}{||\mathcal{P}_S \mathbf{u}(\cdot, t)|| \, ||\mathcal{P}_S \tilde{\mathbf{u}}(\cdot, t)||} \\
&= \frac{\displaystyle\sum_{m=-M}^{M} \sum_{n=1}^{N_m} \tilde{\hat{\alpha}}^{(n)*}(t; m) \hat{\alpha}^{(n)}(t; m)}{\sqrt{\displaystyle\sum_{m=-M}^{M} \sum_{n=1}^{N_m} \left| \hat{\alpha}^{(n)}(t; m) \right|^2} \sqrt{\displaystyle\sum_{m=-M}^{M} \sum_{n=1}^{N_m} \left| \tilde{\hat{\alpha}}^{(n)}(t; m) \right|^2}}.
\end{aligned}
\tag{5.67}
$$

Figure 5.11(b) plots the alignment metric averaged over 10 different initial conditions. It demonstrates the degradation of alignment between the projected and simulated fields over time, owing to the modeling errors. However, the alignment is about 0.37 up to 5 flow time steps.

134
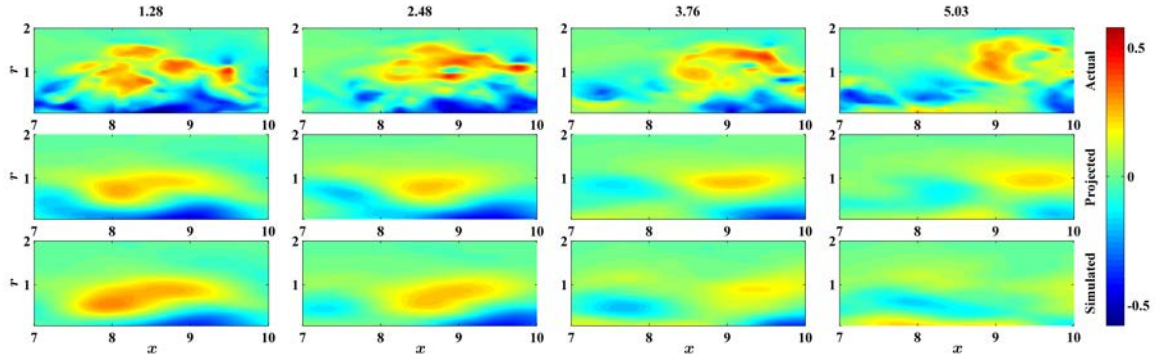
Figure 5.12: Snapshots of simulated axial velocity fluctuations on $\theta = 0$ plane with 44-D ROM built from the original DNS database. This is compared to the actual field as well as the projection of the actual field on the 44-D basis. The time of each snapshot from the initiation of simulation are shown atop each column.

Further intuition is provided by the representative simulation results shown in Figure 5.12 for a particular initial condition (the one used for Figure 5.11(a)). The 44-D basis captures the large-scale kinematics of the flow, and the ROM is seen to predict these kinematics quite well up to about 4 flow time steps.

Reduced-Order Model Simulation over Long Time Horizon

The long term stability characteristics of nonlinear ODEs cannot be predicted from the model structure directly. One has to simulate the model over long time horizons to numerically characterize the behavior. Although the long term stability of the ROM is not required for feedback control design, it would be beneficial for validating periodic actuation models subsequently. It is also of general interest for characterizing the essential dynamics of the flow being analyzed.

A limited investigation was performed to determine the long term behavior of the ROMs resulting from the present modeling strategy. The 44-D ROM discussed in the preceding article was found to have stable behavior over 5000 flow time steps of simulation, and this
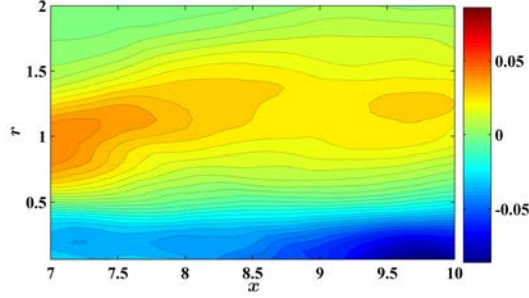
Figure 5.13: Error in mean axial velocity prediction from simulation of 44-D ROM from DNS database

is the main focus of analysis. Several initial conditions were simulated, and all of them showed virtually identical statistics, indicating that the simulated flow is converging to a stable attractor. As a counter-example, a 30-D ROM was found to be stable also, but the characteristic frequency spectrum were very different.

The ensemble-average flow field from the DNS database has been chosen as the base flow field for the ROM, so that the ensemble-average of the residual fluctuations should vanish. However, Figure 5.13 shows that the ensemble-average of the *simulated* fluctuations does not vanish. In fact, it represents a scaled version of the $m = 0$, $n = 1$ POD eigenfunction in Figure 5.7(a). In other words, the coefficient corresponding to the shift mode has a non-vanishing mean value in simulations. The truncation of the eigenfunction basis causes this modification of the mean location of the flow attractor in phase-space. The potential core is shortened and the mixing layer flares more.

Figure 5.14 presents the mean square of the fluctuating velocity fields (after subtraction of the mean value shown in Figure 5.13 for the simulated case). The decrease in fluctuations owing to truncation to the 44-D basis is per expectations. The simulation of the 44-D ROM is able to replicate the projected values of the fluctuation energy very closely. In fact, the

136
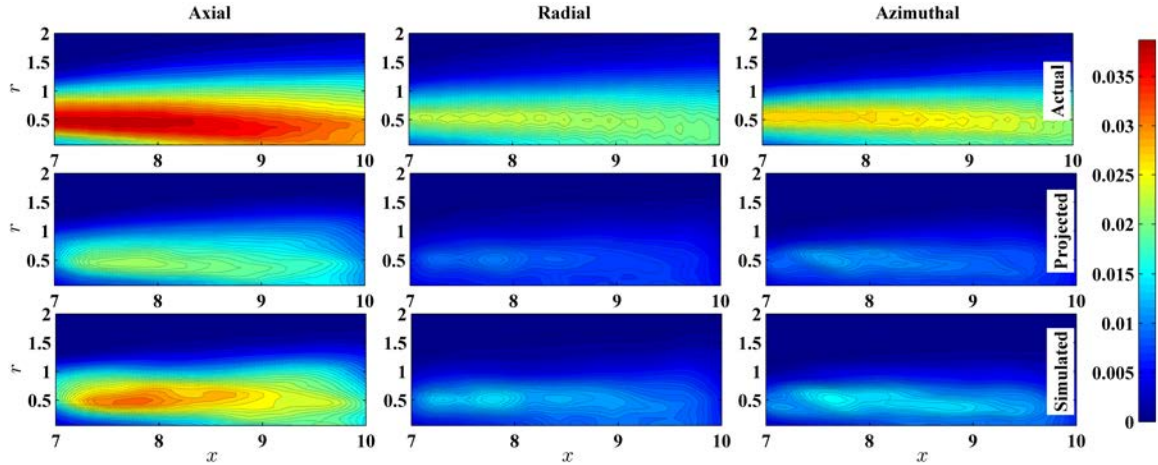
Figure 5.14: Mean square of fluctuating velocity fields from simulation of 44-D ROM compared to actual values in the DNS database, as well as those obtained by projecting the actual velocity fields onto the retained 44-D basis.

simulated energies are higher than those in the projection, and closer to the actual levels. This indicates correct reproduction of the dynamics.

Figure 5.15(a) presents the power spectral density of the simulated field at a salient point in the domain from the 44-D ROM. It is compared with the corresponding spectra from the projected field on the same 44-D basis and the actual field. The low frequency characteristics on this attractor are quite close to the actual dynamics. The high frequency roll-off is faster owing to the truncation of the basis.

As a counter-example, the simulation of the 30-D ROM is seen to have a very different behavior in Figure 5.15(b). Note that the spectrum of the projected field on the 30-D basis is not very different from that on the 44-D basis shown in Figure 5.15(a). However, some low-energy modes are obviously essential to the correct modeling of the dynamics of the flow.

(a) 44-D ROM   (b) 30-D ROM
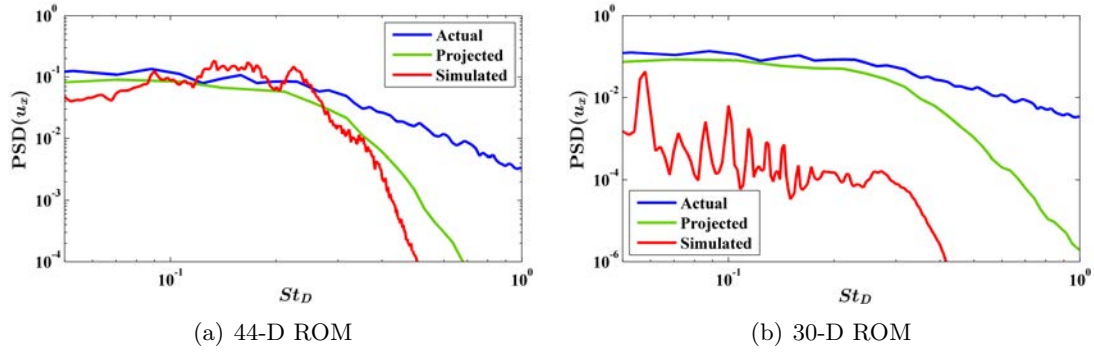
Figure 5.15: Power spectral density of axial velocity fluctuations at $x = 8.2$, $r = 0.5$ averaged over all azimuthal angles.
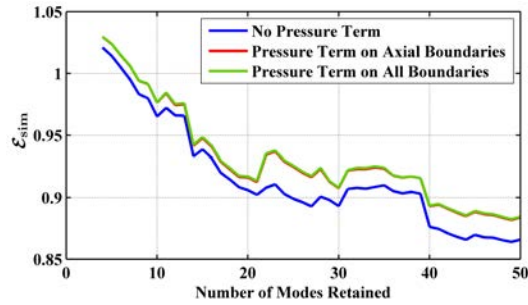
Figure 5.16: Effect of pressure term on simulation error of ROMs.

Significance of Pressure Term in ROM

The above computations had been made by neglecting the pressure term. The inaccuracy incurred thereof maybe assessed now, since the requisite pressure information is available in the DNS database. Two different approximations have been made in modeling the pressure term: neglecting the influence of the outer radial boundary, and neglecting the term altogether. Figure 5.16 compares the simulation error metric for all three cases. It is observed that the neglect of the pressure term results in trivial differences in fidelity. In

(a) Time-averaged simulation error metric

(b) Simulation error metric for 44-D model

(c) Alignment metric for 44-D model

(d) Power spectral densities as in Figure 5.15(a)
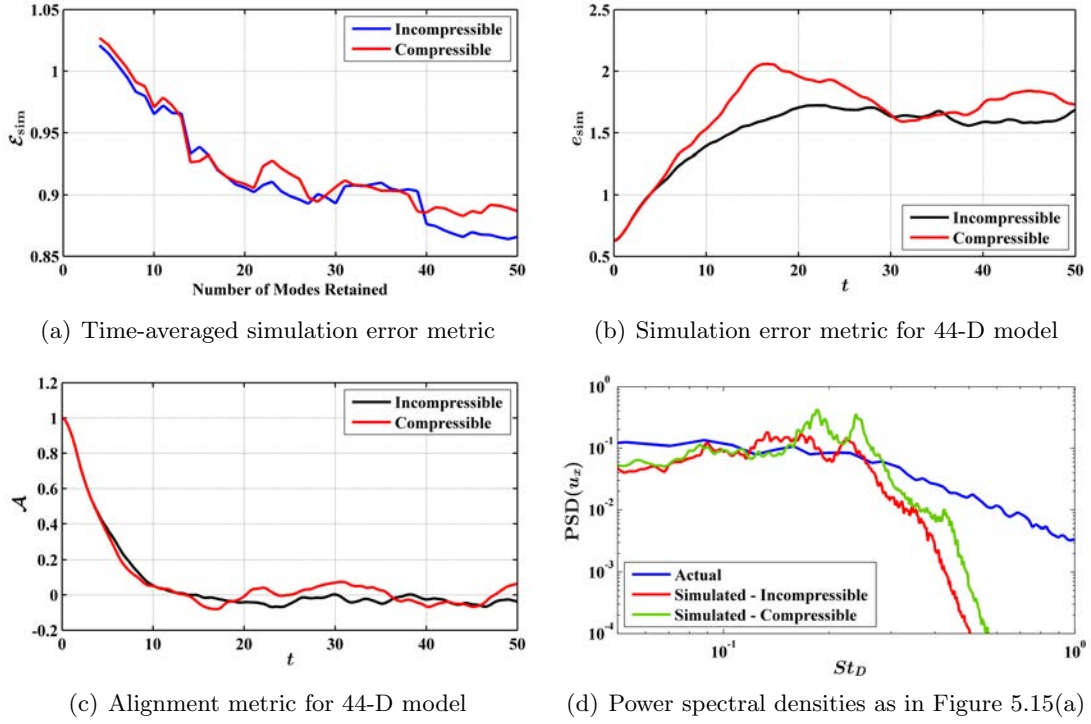
Figure 5.17: Compressibility effects on ROM accuracy in various metrics. The time-resolved metrics are averaged over 10 initial conditions.

fact, the inclusion of the pressure term appears to worsen the fidelity; the reason for this is not known. Finally, the influence of the outer radial boundary appears to be negligible indeed.

Compressibility Effects on ROM

The reduced-order modeling of the compressible dynamics has been described in Section 5.8. Following this strategy, the simulation error defined in eqn (5.64) is evaluated for increasing number of retained energetic modes. The results are compared with those for the ROM of the incompressible dynamics in Figure 5.17. The fidelity of the models are quite alike, thereby supporting the assumption of incompressibility.
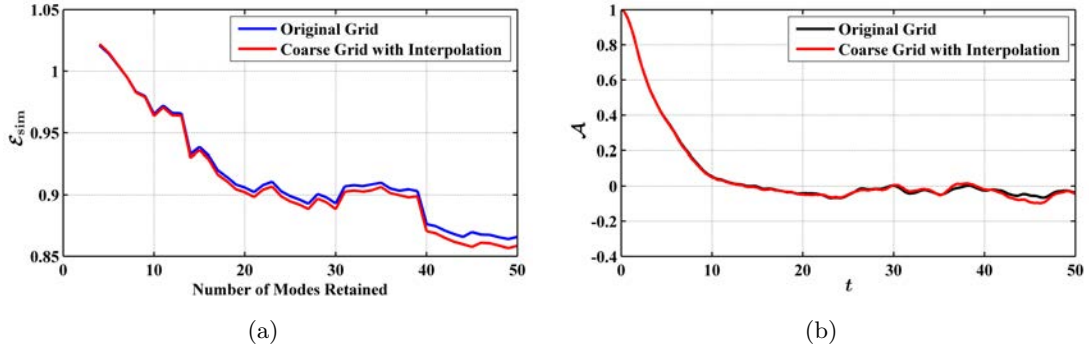
Figure 5.18: Grid resolution effects on ROM accuracy as measured by (a) simulation error metric, and (b) temporal evolution of alignment between simulated and projected fields for the 44-D ROM, averaged over 10 initial conditions.

5.9.2 Model from Direct Numerical Simulation with Coarse Axial Grid

The sensitivity of the ROM to the coarseness of the axial grid is investigated here. The model considered in the preceding section was built from a database where the axial grid resolution was $D/16$. Here, the fields are down-sampled by a factor of 4 (resolution is $D/4$ now), before cubic spline interpolation is used to approximate the data on the $D/16$ again. In essence, this smooths the spatial fluctuations of the flow fields. Although not shown here, the eigenspectrum and the most energetic eigenfunctions were essentially unchanged from the previous results shown in Figures 5.6(b) and 5.7. Figure 5.18 shows that the performance of the resulting model is indistinguishable from the corresponding model from the original DNS database.

5.9.3 Model from Implicit Large-Eddy Simulation with Coarse Axial Grid

In the foregoing discussion, the DNS database of the low Reynolds number Mach 0.9 jet was used to evaluate the reduced-order modeling strategy. Here, the implicit large-eddy simulation database of the high Reynolds number Mach 1.3 jet introduced in Section 2.5.2
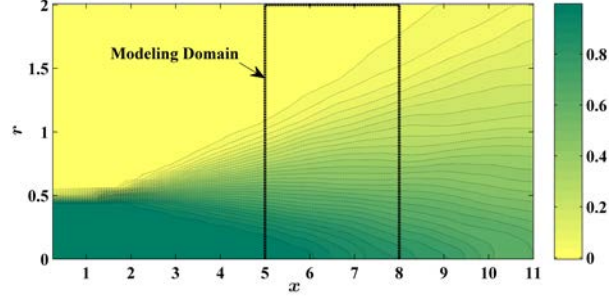
Figure 5.19: Contour of normalized mean axial velocity in ILES jet with cylindrical modeling domain indicated.

will be used as the test bench. Figure 5.19 shows the contours of normalized mean axial velocity from the unforced case of this database. Its potential core is seen to end around 6 jet diameters. Following the arguments presented in the case of the DNS database, the chosen cylindrical modeling domain for this database extended from $X_1 = 5$ to $X_2 = 8$ along the axial direction; the radial extent was $R = 2$ (see Figure 5.19). The investigation in the preceding article established that down-sampling does not materially affect the accuracy of the ROM. Thus, the ILES data was saved on a grid with axial resolution $\sim D/4$. As in the previous article, the flow fields were interpolated on to a grid with axial resolution $\sim D/16$ using cubic splines. Without this interpolation, the spatial derivatives required in the ROM could not be computed accurately, and consequently the performance in terms of the metrics introduced above was degraded.

The eigenvalues from the volumetric POD on this database are shown in Figure 5.20. The axial components of eigenfunctions of $n = 1$ to 3 and $m = 0$ to 3 are presented in Figure 5.21. The 2nd helical mode is the most energetic, as was found for the low-Re DNS database (see Figure 5.6(b)). However, a few important differences are observed in the eigensolutions, which are consequential for the reduced-order modeling. (a) The relatively large

141

(a) Eigenspectrum   (b) Cumulative Sum
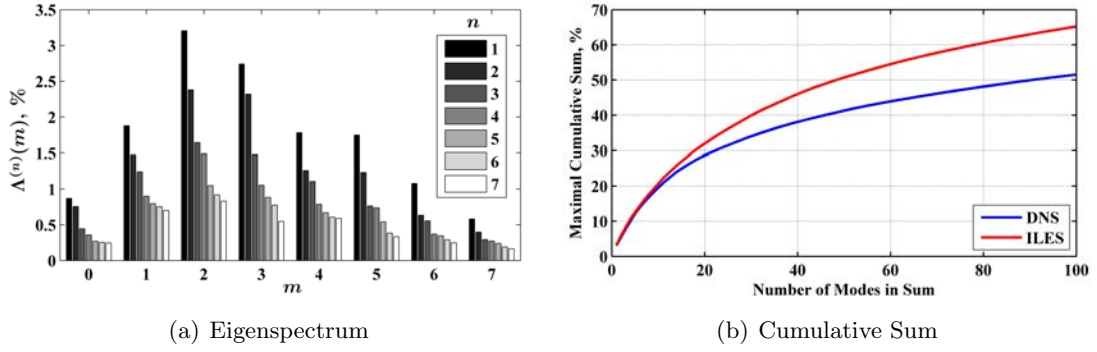
Figure 5.20: Eigenvalues of volumetric POD of ILES database..
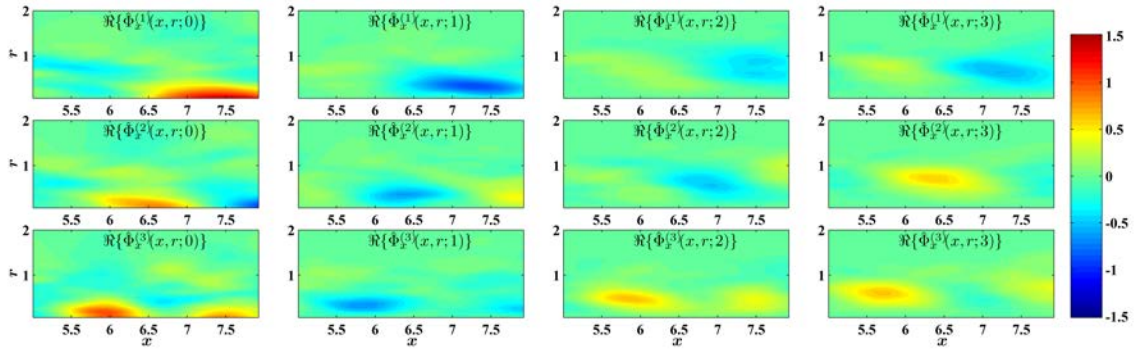
Figure 5.21: Axial components of the first 3 POD modes of azimuthal modes 0 to 3 from the volumetric POD of ILES database.

1st POD mode of $m = 0$ observed for the low-Re data in Figure 5.6(b) is absent. The shape of the 1st POD mode is also not representative of the 'shift-mode' found in Figure 5.7(a). As discussed in this context previously, the automatic inclusion of the 'shift-mode' is the most probable reason for the stability of the ROMs presented for the low-Re DNS database (see discussion in Noack et al. (2008) also). (b) The paired $m = 1$ modes found for the DNS database are also not observed here, testifying to the greater disorganization of the high-Re jet considered here. (c) The relative decay in energy of the higher azimuthal modes
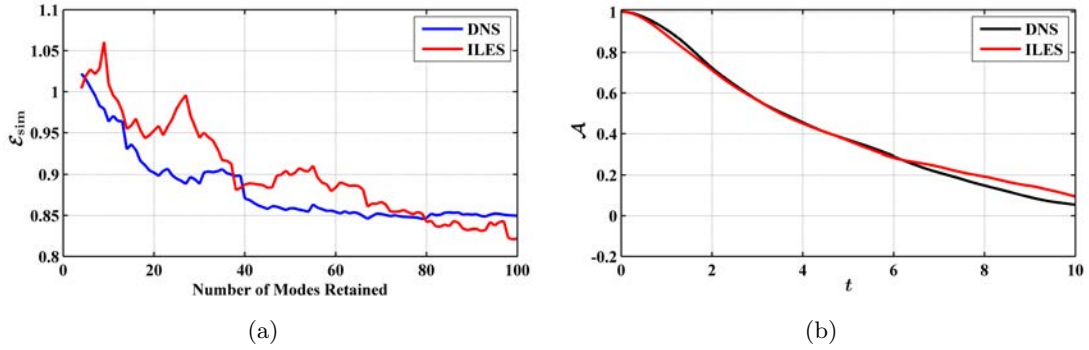
Figure 5.22: Accuracy of ROMs from ILES database compared to corresponding ones from DNS database. The measures are (a) simulation error metric, and (b) temporal evolution of alignment between simulated and projected fields for the 44-D ROM, averaged over 10 initial conditions.

is slower compared to the low-Re jet, which also substantiates the above argument. (d) The cumulative sum of the eigenvalues is seen to converge faster for the ILES in Figure 5.20(b) compared to the DNS database. This is counter-intuitive since increasing Reynolds number typically slows the convergence (Holmes et al., 1996). The probable reason for this is the small ILES dataset (2000 samples across 6.6 flow time steps) compared to the much larger DNS dataset (2316 samples but spread across about 160 flow time steps). Thus, there are not enough independent snapshots saved for the ILES database to represent the actual kinematics of the high-Re Mach 1.3 jet that it is simulating. This may not be too crucial, as the few modes that would be resolved in the ROM are probably well-resolved.

The overall short-time horizon performances of ROMs from the ILES are demonstrated by the plots of the simulation error metric in Figure 5.22(a). In this measure, the fidelity of the models cannot be clearly distinguished from those obtained with the DNS database. The performances are even more indistinguishable when comparing the alignment metric in Figure 5.22(b). The axial velocity fluctuations from simulations are shown in Figure 5.23
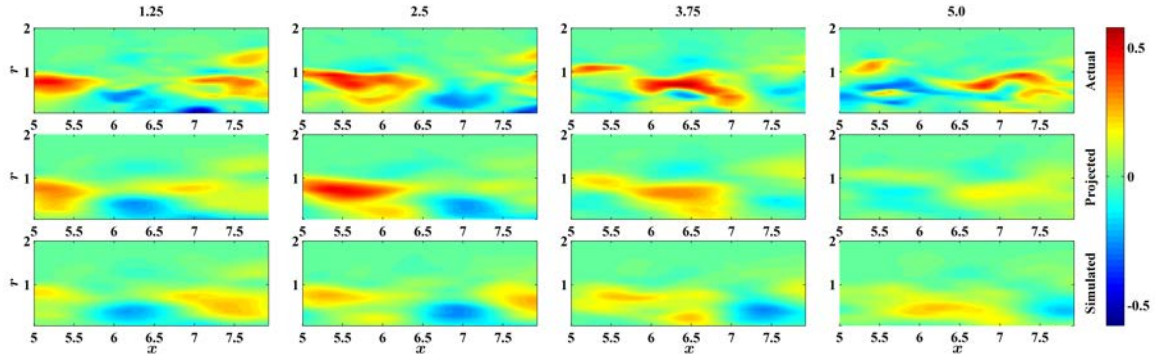
Figure 5.23: Snapshots of simulated axial velocity fluctuations on $\theta = 0$ plane with 44-D ROM built from the ILES database. This is compared to the actual field as well as the projection of the actual field on the 44-D basis. The time of each snapshot from the initiation of simulation are shown atop each column.

for better visual comparison. The fidelity of the simulation is seen to be quite good up to about 4 flow time steps, as in the case of the DNS in Figure 5.12. Thus, an increase in the Reynolds number by two orders of magnitude does not materially change the short-time horizon performance of the reduced-order modeling strategy introduced here.

An important behavior not revealed by the above presentation is the divergence of the simulation trajectories for this 44-D model after about 100 flow time steps. An 86-D model was also found to diverge. The primary cause of this is thought to be the absence of the shift mode from the POD basis, and not the increase in Reynolds number.

5.9.4 Model from Direct Numerical Simulation after Stochastic Estimation

Sensor Placement and Characterization

The stochastic estimation requires simultaneous sensing of the near-field pressure and the flow field on cross-stream slices intersecting the modeling domain. Thus, the sensors must necessarily be either upstream or downstream of the chosen modeling domain. The

144

(a) $x = 5$, various r (b) Sensors on a line at 5.6°
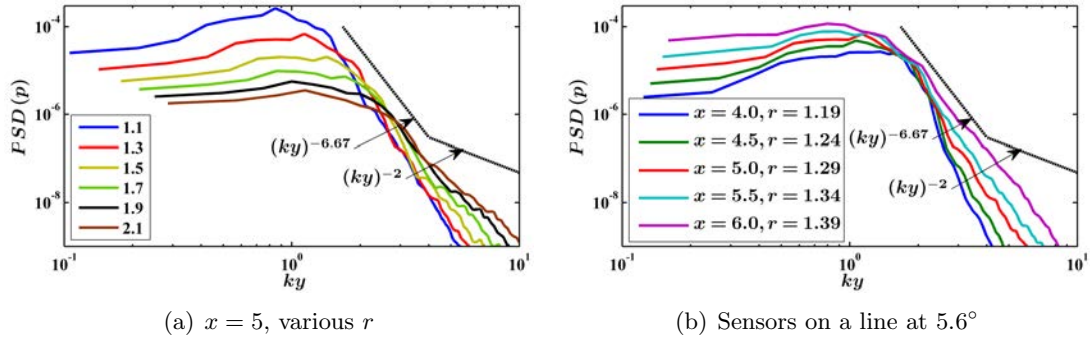
Figure 5.24: Wavenumber spectra of pressure from DNS database.

upstream configuration is preferred since the data acquired in this exercise would also be used for developing practical estimation strategies subsequently, which would require that the sensors be close to the nozzle exit.

The investigation of the hydrodynamic pressure field is pursued per the discussion of Section 3.3. Figure 5.24 shows the wavenumber spectral field of the DNS database. The acoustic signature ($(ky)^{-2}$ spectral decay) is missing from these spectra, but the focus here is on the hydrodynamic signature, which is well captured by the DNS. The collapse of the data is not as good as was observed for experiments (see Figure 3.2). The probable reason for this is the sub-optimal choice of the angle of the linear array. However, the present purpose requires the hydrodynamic signatures only, and the choice of sensor locations depicted in Figure 5.25 is useful.

The virtual pressure sensors are placed on a linear array between $x = 4$ and 6 at intervals of 0.5. The array makes an angle of 5.6° with the jet axis to parallel the outer edge of the shear layer, with the most upstream sensor located at $r = 1.2$. Alternatively, any or all of the sensors could be replaced by uniform azimuthal arrays of 80 sensors each (of the form shown in Figure 5.1). The precise locations of the sensors coincided with the nearest point

145
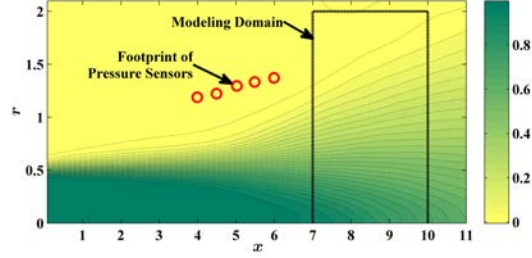
Figure 5.25: Contour plot of normalized mean axial velocity from DNS database in the background. Overlaid are the cross section of cylindrical modeling domain, and the footprints of pressure sensors (azimuthal array or linear array).
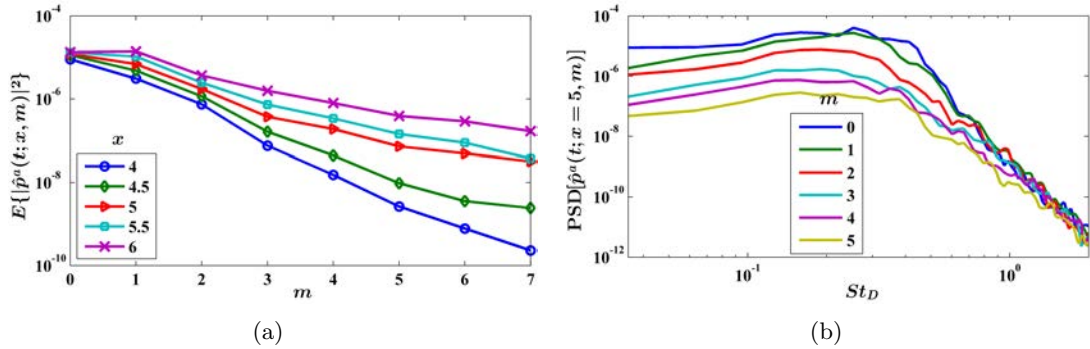
Figure 5.26: (a) Variance of near-field pressure measured at several axial stations, and (b) PSD of the pressure at $x = 5$, for the lower Fourier azimuthal modes.

on the non-uniform DNS grid. The results reported below were not altered when only 16 azimuthal points in the computational grid were 'instrumented' instead of all 80 of them, thereby attesting to the convergence of the low-order azimuthal modes.

The pressure signals measured at the above locations are characterized first. Figure 5.26(a) presents the energies in the various azimuthal modes of pressure measured on the ring arrays discussed above. The figure demonstrates the familiar low-dimensional character of the pressure field, as well as the downstream energy growth, that have been

observed by previous researchers (Ukeiley and Ponton, 2004; Hall et al., 2006; Jordan et al., 2005; Tinney et al., 2008b). The PSD of the various azimuthal modes of pressure measured at $x = 5$ are shown in Figure 5.26(b). These were computed with the Welch spectrogram technique using a window size of 400 samples, overlaps of 300 samples, and Hanning windowing (Oppenheim and Schafer, 1989). Similar pressure spectra were reported in Figure 3.4 for a ring array of pressure sensors placed at $x = 3$ and $r = 1$ in the experimental jet.

SLSE Reconstruction Fidelity

The application of 1-D slice-POD to the axisymmetric jet mixing layer is well established in the literature (Jung et al., 2004; Iqbal and Thomas, 2007; Tinney et al., 2008a). The present discussion proceeds to an investigation of the accuracy of reconstruction of the 3-D velocity field database using SLSE. The details of the implementation of the SLSE as well as the qualitative nature of the results follow Tinney et al. (2008b), and only a few particulars are mentioned here. The finite time Fourier transforms were implemented with $T = 56.8$ flow time steps and 87.5% overlap. In any estimation strategy evaluation, one should distinguish between a modeling and a validation dataset. However, the SLSE requires time records of sufficient length, and the numerical database did not have a very long record length. Thus, the modeling and validation are both performed on the entire DNS database. The cubic spline interpolation is kept out of this exercise for the time-being, to focus on the SLSE alone.

Using any of the methods described previously, one obtains the reconstructed fluctuating velocity field denoted by $\tilde{\mathbf{u}}(x, r, \theta, t)$, where $x \in \mathcal{X}_u$ is a coarse grid. The actual fluctuating velocity field $\mathbf{u}(x, r, \theta, t)$ at these locations is also known for the same time instant t. The

following reconstruction error metric is proposed:

$$\mathcal{E}_{\text{recon}} := \frac{E\left\{||\tilde{\mathbf{u}} - \mathbf{u}||^2\right\}}{E\left\{||\mathbf{u}||^2\right\}}. \tag{5.68}$$

The norm in the above expression is induced from the volumetric inner product defined in eqn (5.13), but the fields are evaluated on the coarse axial grid $x \in \mathcal{X}_u$. The definition is very similar to the simulation error metric proposed in eqn (5.64). The trapezoidal quadrature rule is used everywhere in the present work for implementing integration in a discretized domain. For a uniform grid, it accords half the weight to the end points as it does to the interior grid-points. For a very coarse grid (as for example, the coarse axial grids considered here), a better implementation is to accord the same weight to every grid-point. This amounts to extending the domain of integration by half the grid resolution on either end.

For converged statistics, the least-squares framework and the orthonormality of the eigenfunction basis afford $\mathcal{E}_{\text{recon}}$ to be computed directly from the cross-spectral tensors introduced in Section 5.5. For example, if the complementary SLSE is applied to reconstruct the *scalar* POD modal coefficients in the ranges $m \in [-M, M]$ and $n \in [1, N^1]$ respectively, then one obtains

$$\mathcal{E}_{\text{recon}} \approx 1 - \frac{\int_{x=X_1}^{X_2} \sum_{i \in \{x, r, \theta\}} \sum_{m=-M}^{M} \sum_{n=1}^{N^1} \int_{f=-\infty}^{\infty} \mathbf{S}_{p\gamma_i}^{(n)*}(x, m, f) \mathbf{S}_{pp}^{-1}(m, f) \mathbf{S}_{p\gamma_i}^{(n)}(x, m, f) \mathrm{d}f \mathrm{d}x}{E\left\{||\mathbf{u}||^2\right\}}. \tag{5.69}$$

The physical near-field pressure measurement rig has a limited resolution of the azimuthal direction, and hence only the first few azimuthal modes can be resolved. Moreover, the correlations are poorly converged for higher POD modes. Thus the SLSE reconstruction will be pursued in a limited region of the $M - N^1$ space. This means that the reconstructed velocity field may approach the projected velocity field, but cannot approach the actual
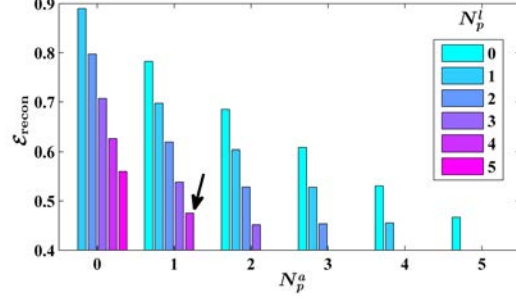
Figure 5.27: 'Best' configurations with given N_p^a & N_p^l based on the reconstruction errors.

velocity field. For 16 azimuthal pressure sensors, one can resolve at most $M = 7$. Moreover, with $N^1 = 9$, the projected velocity field captures 82% of the actual energy $E\left\{||\mathbf{u}||^2\right\}$. This imposes a lower limit of 0.18 on the reconstruction error metric that can be achieved when estimating these modes using SLSE.

In Figure 5.27, all possible pressure sensing configurations are compared. In this assay, the sets $\mathcal{X}_p^a$ and $\mathcal{X}_p^l$ are mutually exclusive and $0 < N_p^a + N_p^l \leq 5$; thus only the depicted combinations of N_p^a and N_p^l can be evaluated. For each combination, the plot denotes $(\arg\min_{\mathcal{X}_p^a, \mathcal{X}_p^l} \mathcal{E}_{\mathrm{recon}})$ computed from eqn (5.69) with $M = 7$ and $N^1 = 9$. Although the errors are quite large in general, it will be shown that the reconstructed database is still useful for the subsequent volumetric POD. One observes that beyond the first azimuthal ring array, each additional linear array location provides almost the same information as an additional azimuthal ring array. Keeping in mind the cost of implementation, the combination with $N_p^a = 1$ and $N_p^l = 4$ is chosen for further study. Approximately the same $\mathcal{E}_{\mathrm{recon}}$ (= 0.5) was obtained for all permutations in this case. Henceforth the configuration with $\mathcal{X}_p^a = \{5\}$ and $\mathcal{X}_p^l = \{4, 4.5, 5.5, 6\}$ is investigated exclusively. It is to be noted that

| | $\mathcal{E}_{\mathrm{recon}}$ | |
SLSE Method	Actual	Simplified
Individually for each radial location	0.72	0.49
Scalar POD in radial direction	0.62	0.50
Vector POD in radial direction	0.67	0.56

Table 5.1: Reconstruction error metric evaluated from the actual and simplified definitions for the three different SLSE methods.

this results in a significant improvement over the single azimuthal ring configuration used by Tinney et al. (2008b).

The preceding exploration of the most effective configuration was pursued with the simplification of $\mathcal{E}_{\mathrm{recon}}$ presented in eqn (5.69) since the computational load is much reduced. This analysis provided the basis for selecting one particular configuration. However, the simplification is strictly valid only for converged statistics. Hence, the next analysis in Table 5.1 focuses on the evaluation of $\mathcal{E}_{\mathrm{recon}}$ for this configuration using the definition in eqn (5.68). Three different ways of implementing SLSE were mentioned in Section 5.5, and all three are assessed.

The disparity between the actual and simplified $\mathcal{E}_{\mathrm{recon}}$ indicates the lack of statistical convergence. The discrepancy is worst when the velocity field at each radial location is estimated individually. This provides valuable justification for the preference of the complementary technique. Essentially, POD identifies the most correlated kinematics in the flow, so that convergence of the stochastic estimation is improved. The better performance of the scalar POD over vector POD is not surprising since the former has thrice as many curve-fitting parameters, corresponding to the three components of velocity. The scalar POD option will be investigated and used henceforth, unless otherwise mentioned.
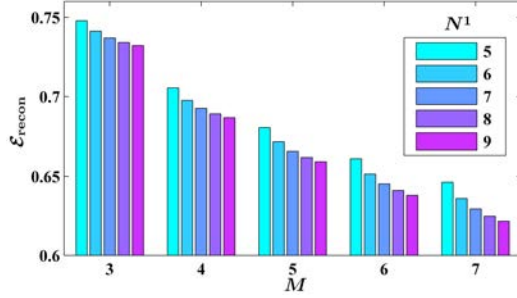
Figure 5.28: Improvement in $\mathcal{E}_{\mathrm{recon}}$ with increase in M & N^1.

The modeling and validation datasets were the same for evaluation of SLSE. Thus, it might appear strange that the actual and simplified reconstruction errors are different at all. If the underlying spectral correlations had been obtained by averaging over Fourier transforms of individual blocks centered on each datapoint, then these discrepancies would indeed vanish. However, it has been mentioned that the moving windows for the blocks have overlaps of 87.5% and the datapoints at the beginning and end of the record are not centered in any block, and these account for the discrepancies.

Figure 5.28 demonstrates the convergence of the reconstruction error in the $M - N^1$ space for the chosen configuration and scalar POD-SLSE combination. Here, the definition of eqn (5.68) is used. There are small but steady improvements of reconstruction fidelity with addition of 1-D POD modes even up to the 9th mode. This attests to the usefulness of the SLSE method and the chosen pressure sensing configuration in estimating the lower energetic kinematics.

The reconstruction error metric defined in eqn (5.68) integrates over all azimuthal modes and axial locations, and adds over all POD modes and velocity components. To get a more detailed insight into the reconstruction fidelity, the following local modal component-wise

(a) Local modal SLSE reconstruction error metric   (b) Reconstructed energy ratio for axial velocity
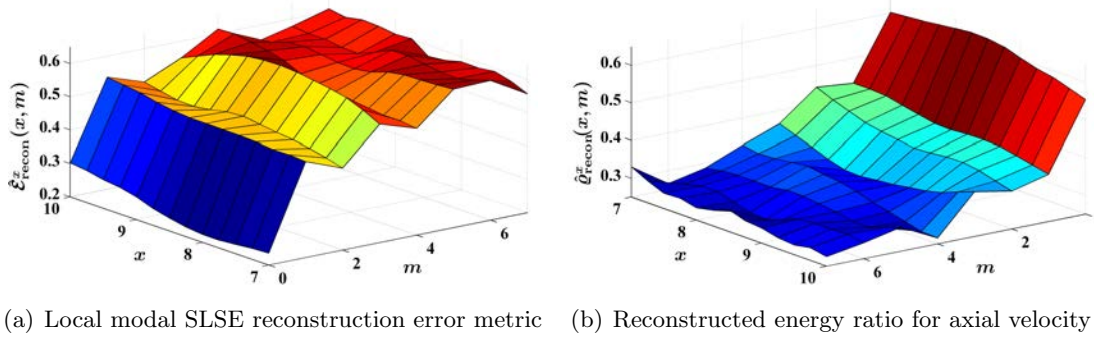
Figure 5.29: Assessment of fidelity of SLSE reconstruction for DNS database.

reconstruction error metric is proposed

$$
\hat{\mathcal{E}}^i_{\text{recon}}(x,m) := \frac{E\left\{\left|\left|\tilde{\hat{u}}_i(x,\cdot,\cdot;m) - \hat{u}_i(x,\cdot,\cdot;m)\right|\right|^2\right\}}{E\left\{||\hat{u}_i(x,\cdot,\cdot;m)||^2\right\}}.
\tag{5.70}
$$

Here, the norm is induced from the inner product introduced for the scalar 1-D slice POD in Section 5.4. Note that it still adds over all POD modes. The variation of this error metric for the axial component displayed in Figure 5.29(a) makes intuitive sense. Higher azimuthal modes correspond to smaller scales, for which the pressure and velocity become increasingly uncorrelated. The low turbulence in the DNS database is manifest in the relatively constant reconstruction errors at all axial slices with the pressure measured at the fixed upstream location. The error metric is observed to be lower than 0.65 over the parameter space. The metric is very similar for the other two components of velocity.

It is clear from the simplification presented in eqn (5.69) that the reconstruction error metric is an indicator of both the correlation between the reconstructed and actual velocity fields, as well as their relative energies. The latter aspect is studied in isolation now. For this, the local modal component-wise velocity field energy is defined using the norm induced

152

from the scalar 1-D slice inner product introduced in eqn (5.20):

$$\hat{\zeta}_i(x, m) := E\left\{||\hat{u}_i(x, \cdot, \cdot; m)||^2\right\} = 2\pi E\left\{\int_{r=0}^{R}|\hat{u}_i(x, r, \cdot; m)|^2 r\mathrm{d}r\right\}. \qquad (5.71)$$

When evaluated for the reconstructed velocity field $\tilde{\hat{u}}_i(x, \cdot, \cdot; m)$, the notation is $\tilde{\hat{\zeta}}_i(x, m)$. The ratio of the reconstructed energy to the actual energy is defined as the *reconstructed energy ratio*:

$$\hat{\varrho}_{\mathrm{recon}}^i(x, m) := \frac{\tilde{\hat{\zeta}}_i(x, m)}{\hat{\zeta}_i(x, m)} = \frac{E\left\{\left|\left|\tilde{\hat{u}}_i(x, \cdot, \cdot; m)\right|\right|^2\right\}}{E\left\{||\hat{u}_i(x, \cdot, \cdot; m)||^2\right\}}. \qquad (5.72)$$

Figure 5.29(b) depicts the reconstructed energy ratio evaluated for the axial component of the velocity in the DNS database. The conclusions are similar to those reached from Figure 5.29(a). The low turbulence in the DNS database is manifest in the relatively constant reconstructed energy ratios at all axial slices. The energy ratios do decrease with increasing azimuthal mode since the near-field pressure has a steeper roll-off in the azimuthal modal energy compared to the velocity field in the mixing layer. However, the ratio remains above 0.25 over the parameter space.

Tinney et al. (2008b) interpolated the 1-D slice POD eigenfunctions from the coarser measurement grid to the finer desired grid. Subsequent to this, the SLSE was performed for each axial location on the finer grid. The order of operations can be reversed. That is, the SLSE coefficients may be determined for each axial grid on the coarser grid. Once the field snapshots are reconstructed on the coarser grid in the azimuthal modal domain, they may be interpolated onto the finer grid, before the subsequent volumetric POD. The first advantage of this inversion of the order of operations is that the signs of the POD eigenfunctions do not need to be manipulated to make the interpolation consistent. Moreover, computational overhead is reduced since the SLSE is performed on the coarser grid. Finally, there is no detectable difference in the reconstruction fidelity between the two routes to interpolation.

153

(a) Cumulative Sums   (b) Eigenspectrum
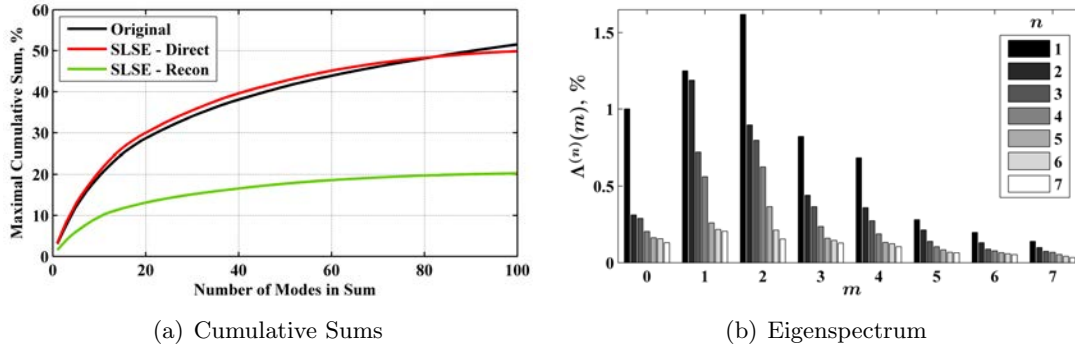
Figure 5.30: Modal energies from volumetric POD of the DNS-SLSE database expressed as percentages of the energy in the original database.

The new order of operations is chosen for implementation of SLSE reconstruction on the DNS database. It must be noted here that the original order of operations had to be used in experiments to implement a scaling transformation (see Section 5.9.6).

The application of SLSE to the scalar POD modal coefficients, in concert with the cubic spline interpolation, will be used to reconstruct a database of 3-D snapshots, and this will be referred to as the "chosen" SLSE database.

Volumetric POD on SLSE Database

The volumetric POD for the axisymmetric jet discussed in Section 5.6 is applied to the chosen SLSE database. The POD modal coefficients are obtained by projecting the flow field snapshots onto the SLSE-reconstructed POD basis. These flow field snapshots can be chosen in two ways: (*i*) from the original DNS database (referred to as 'SLSE-Direct'), or (*ii*) from the SLSE-reconstructed database (referred to as 'SLSE-Recon'). The first choice isolates the investigation of the effects of the SLSE POD basis on the model. However, only the second choice would be realizable in experiments.

The cumulative sum of the energies of the coefficients from the most-energetic POD modes are presented in Figure 5.30(a). The reconstruction errors in the SLSE database of approximate snapshots was demonstrated in Figure 5.29(a). However, the SLSE database is seen to contain almost the same empirical information as the original database; i.e. the SLSE is able to resolve the spatial *shapes* in the fields. This is concluded from Figure 5.30(a), which shows that the SLSE-Direct method and the original method capture almost the same amount of energy. In fact, the SLSE-Direct energies are slightly higher than the original energies which runs counter to the POD philosophy. This apparent contradiction is explained by recalling that the POD is the most efficient at capturing energies of a database, when only this database is given. In SLSE-Direct method, the empirical database is the SLSE database. The SLSE-Recon energies are about half the corresponding energies from the SLSE-Direct method. This reflects the inaccuracies in resolving the energies in the SLSE procedure.

The eigenspectrum from the volumetric POD is presented in Figure 5.30(b). This is also the spectrum of energies captured in the SLSE-Recon procedure. This is to be compared to the corresponding eigenspectrum presented for the original DNS database in Figure 5.6(b). Discounting for the disparity in the total energy captured as discussed above, the two eigenspectra are remarkably similar. The spectrum of energies captured in the SLSE-Direct procedure is not shown here since it is actually quite indistinguishable from Figure 5.6(b).

The axial components of the first few eigenfunctions from the SLSE database are examined in Figure 5.31. These are also found to be quite alike those displayed in Figure 5.7 for the original DNS database. Thus the SLSE procedure, when used with the appropriate near-field pressure sensing configuration, can generate a database of sufficient accuracy for identifying low-dimensional kinematics.
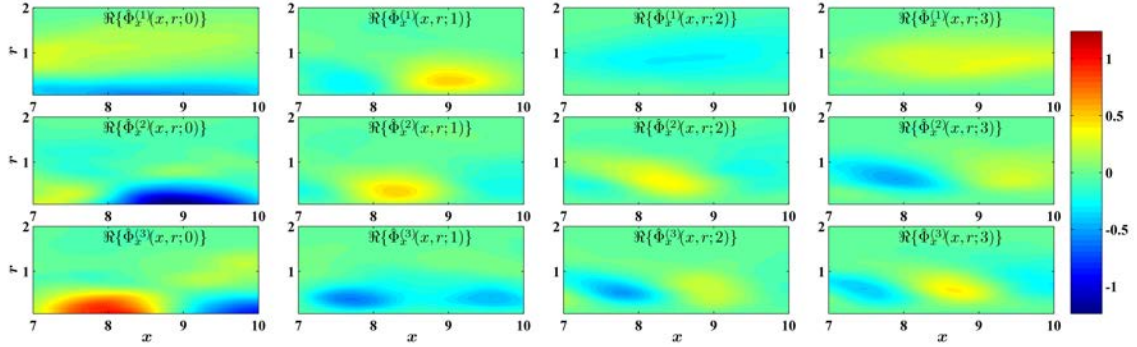
Figure 5.31: Axial components of first few eigenfunctions from the volumetric POD of SLSE-reconstructed DNS database.

Reduced-Order Model Simulation over a Short Time Horizon

The reduced-order modeling strategy introduced in Section 5.7 is applied to the chosen SLSE database. Once the POD has been completed, the SLSE database is not directly needed for determining the coefficients of the ROM. However, the eddy viscosity relies on the POD modal coefficients obtained by projecting the flow field snapshots onto the SLSE POD basis. The modal coefficients also serve as initial conditions for simulation. Thus both the choices of SLSE-Direct and SLSE-Recon are explored next.

Figure 5.32(a) shows the averaged simulation error metric over the first 5 flow time steps of simulation for various dimensions of retained bases. The performance of the SLSE-Direct method is seen to be quite similar to the original method, which was to be expected from the preceding paragraphs. The SLSE-Recon method results in poorer modeling accuracy. Moreover, the simulation error metric is observed to remain quite constant with increasing number of modes retained. To explore these behaviors in greater detail, the temporal evolution of the simulation error, averaged over 10 simulations from different initial conditions, is shown in Figure 5.32(b). The initial increase in inaccuracy is quite similar for the original

156

(a) Time-averaged simulation error metric (b) Simulation error metric for 44-D model

(c) Alignment metric for 44-D model
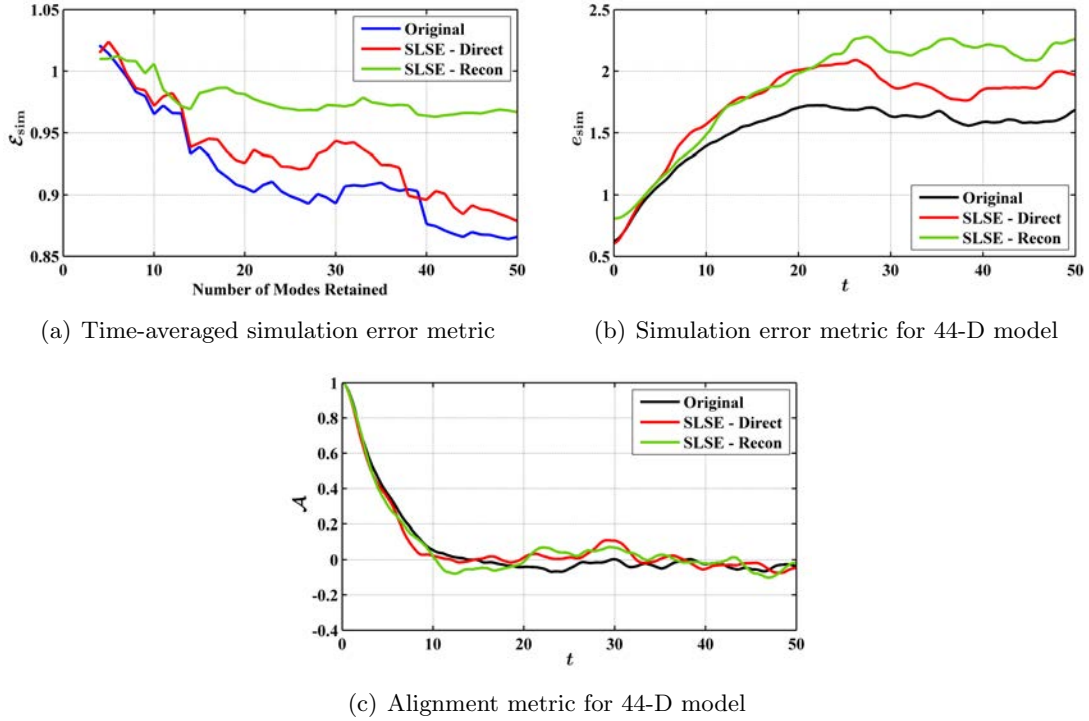
Figure 5.32: Accuracy of ROMs from SLSE-reconstructed DNS database compared to corresponding ones from the original DNS database. The measures are (a) simulation error metric, and (c) temporal evolution of alignment between simulated and projected fields for the 44-D ROM.

and SLSE-Direct methods, but the latter method results in larger errors in the longer term. The SLSE-Recon method starts with a greater error since the initial condition is estimated from the projection of the SLSE-reconstructed snapshots. However, the rate of increase of inaccuracy is no worse than with the other methods. This indicates that the biggest issue in SLSE-Recon is the inaccuracy in the determination of the initial condition of simulation.

The preceding findings are further substantiated in Figure 5.32(c) that shows the temporal evolution of the alignment between the simulated and projected fields, averaged over 10 simulations with different initial conditions. In this metric, the simulation fidelity of the three techniques cannot be distinguished.
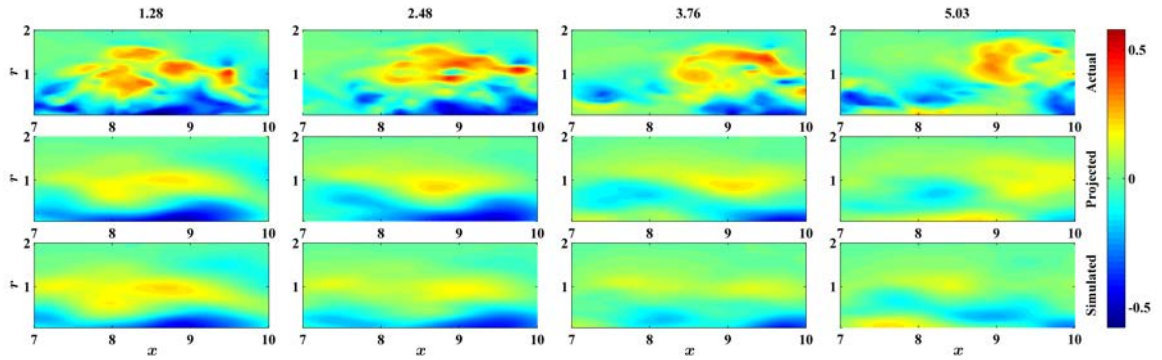
(a) SLSE-Direct
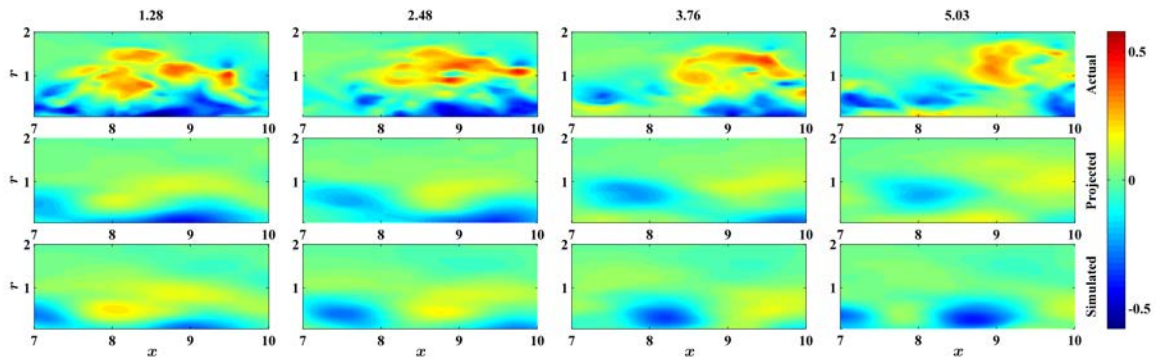
(b) SLSE-Recon

Figure 5.33: Snapshots of simulated fields with 44-D ROM built from SLSE of the DNS database using the SLSE-Direct and SLSE-Recon methods of determining the modal coefficients. The scheme of presentation follows from Figure 5.12.

An intuitive example is provided by the simulation snapshots of the 44-D model presented in Figure 5.33. The degradation in projection accuracy from SLSE-Direct to SLSE-Recon is quite evident. The closeness of the simulated and projected fields is also maintained longer in the SLSE-Direct method compared to the SLSE-Recon method. However, the very short term prediction ($\approx$ 2.5 flow time steps) of the two methods is somewhat similar in overall shape and location of structures, and this is important for the use of such ROMs in feedback control.

(a) SLSE-Direct	(b) SLSE-Recon
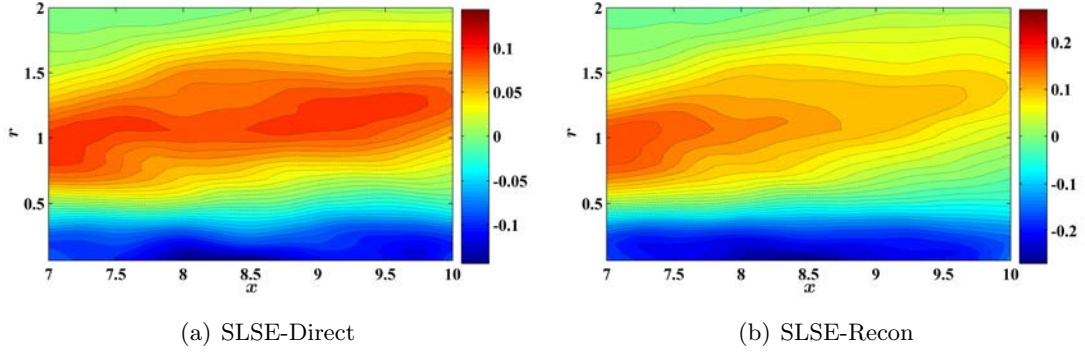
Figure 5.34: Error in mean axial velocity prediction from simulation of 44-D ROM built from SLSE of the DNS database.

Reduced-Order Model Simulation over Long Time Horizon

The preceding discussion focused on the short term simulation performance of the SLSE database. The simulated trajectories from both the SLSE-Direct and SLSE-Recon 44-D models remained bounded for at least 5000 flow time steps when simulated from many different initial conditions, thereby evidencing a stable attractor. One way of characterizing the attractor of the ROM is to plot the error in its predicted mean axial velocity field compared to that in the original DNS database, as shown in Figure 5.34. For comparison, refer to the corresponding plot in Figure 5.13 for the ROM obtained from the DNS database without SLSE reconstruction. The shape of the error contours still represent the shift mode. However, the error levels are seen to be approximately doubled and tripled in going to the SLSE-Direct and SLSE-Recon methods, respectively. Thus the progressive increase in short-term inaccuracies remarked in the preceding discussion are reflected here in greater discrepancies in the mean flow attractor locations.

Figure 5.35 presents the mean square of the fluctuating axial velocity fields (after subtraction of the mean value shown in Figure 5.34 for the simulated case). The actual field

159

(a) Actual   (b) SLSE reconstruction with $M = 7, N^1 = 9$

(c) Simulation of 44-D ROM with SLSE-Direct   (d) Simulation of 44-D ROM with SLSE-Recon
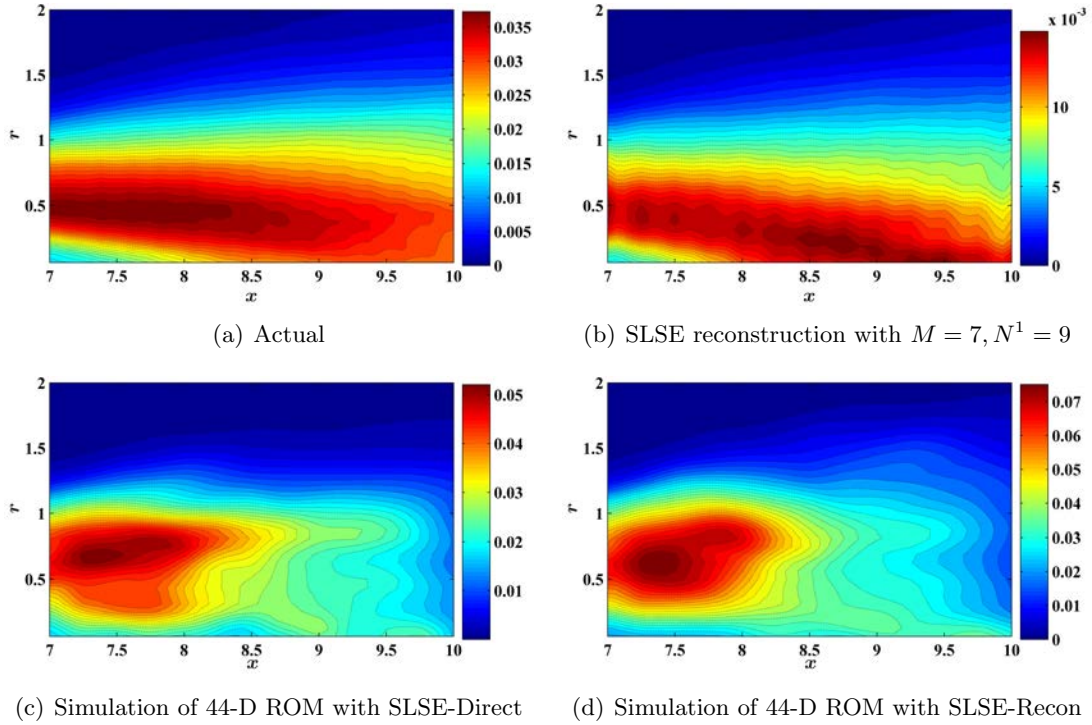
Figure 5.35: Mean square of fluctuating axial velocity fields from simulation of 44-D ROMs compared to actual values in the DNS database, as well as those obtained from SLSE reconstruction. Note the disparity in the color-scales.

from the DNS database is reproduced from Figure 5.14 for ease of comparison. The reconstructed energy ratio has been presented in Figure 5.29(b), so that the decrease in energy seen in the SLSE-reconstructed field in Figure 5.35(b) is unsurprising. However, the attractors of the 44-D ROM obtained by both the SLSE-Direct and SLSE-Recon methods have higher energies even compared to the actual values. The SLSE-Direct case is particularly interesting in this regard. The energy of the original flow field captured by the 44-D POD basis derived from the SLSE reconstruction was shown to be almost identical to the basis derived from the original database itself (see Figure 5.30(a)). This again shows that the amount of energy captured is not a good metric for simulation fidelity. It appears that
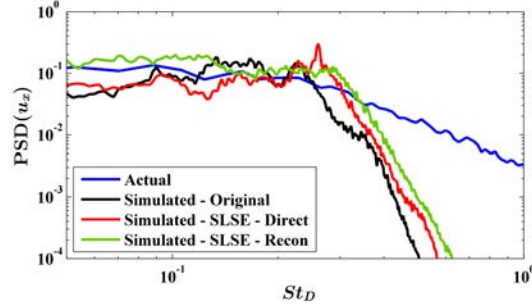
Figure 5.36: Representative power spectral densities from simulations of the 44-D ROMs built from SLSE of the DNS database. The particular details are as in Figure 5.15.

the SLSE skews the retained basis towards energy-producing instead of energy-dissipating structures so that the flow attractor ends up with greater energy. Moreover, the SLSE reconstructs the eigenfunction basis with greater fidelity at upstream locations, and this distorts the mean square velocity contours, as seen in Figure 5.35(c). The situation is worsened when SLSE-Recon method is used since now the eddy viscosities are also underestimated. In the subsequent discussion of ROMs derived from experiments where this issue is much magnified, an energy-scaling transformation is proposed.

Figure 5.36 displays the power spectral densities from a particular simulation. The three different methods of arriving at the ROM are seen to result in very similar spectral shapes. The discrepancies in amplitudes (much diminished in log-space plotting) are to be expected from the preceding discussion.

An earlier version of this work appeared in Sinha et al. (2010b) wherein a more compact pressure sensing arrangement (5 axial locations between $x = 5$ and $6D$) was used. The reconstruction and simulation fidelity was poorer than the results presented here with the more axially-extended configuration. The modifications in the configuration were made to
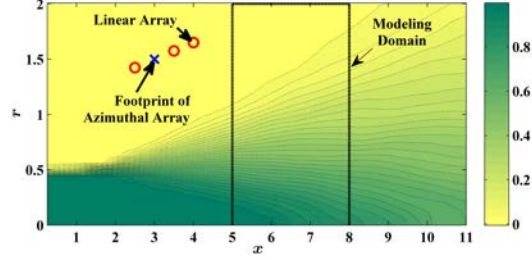
Figure 5.37: Contour plot of normalized mean axial velocity from ILES database in the background. Overlaid are the cross section of cylindrical modeling domain, the location of the linear array of pressure sensors, and the footprint of the azimuthal array.

mimic experimental realities since the axial spacing density of $0.25D$ for the linear array was unfeasible for the 0.0254 mm jet exit diameter.

5.9.5 Model from Large-Eddy Simulation after Stochastic Estimation

The effect of Reynolds number on the SLSE reconstruction and consequent ROM fidelity was explored using the ILES database. For this, the intent was to make the near-field pressure measurement configuration similar to the experimental setup described in the next article, which in turn was decided based on the numerical experiments on the DNS database discussed above. The pressure measurement configuration is shown in Figure 5.37. The azimuthal array had 20 sensors. The experiments had 16 sensors in the azimuthal array, but this was not a sub-multiple of the number of azimuthal grid-points (100) in the ILES database. The modeling domain was sliced by 15 cross-stream sections at about $0.25D$ intervals.

All reconstructions included azimuthal modes 0 through 7, and POD modes 1 through 9. The reconstruction error metric has been defined in eqn (5.68). It was evaluated to 0.62 for the SLSE performed on the ILES data. The simplified metric in eqn (5.69) was evaluated to 0.58, thereby attesting to the statistical convergence of the estimation procedure. Compared

162
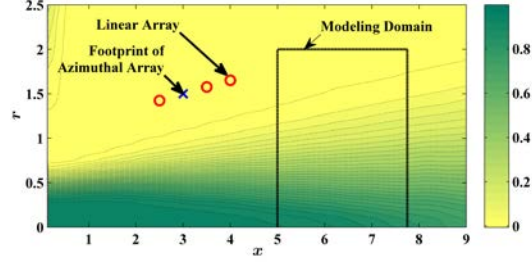
Figure 5.38: Contour plot of normalized mean axial velocity from experiments in the background. Overlaid are the cross section of cylindrical modeling domain, the location of the linear array of pressure sensors, and the footprint of the azimuthal array.

to the corresponding results for the DNS data, this represents a very similar character. Thus, the large difference in Reynolds number does not appear to affect the performance of the SLSE reconstruction.

Given the overall similarity of results from the SLSE performed on the DNS and ILES databases, the latter does not warrant any further investigation.

5.9.6   Model from Experiments

Revisiting the Setup

The contour plot of the mean axial velocity from experiments is shown in Figure 5.38. The potential core ends at around $x = 5.5$. Thus, following the preceding numerical experiments on the DNS database, the appropriate model domain is $x = 5$ to $7.75D$ as shown. The experimental setup has been detailed in Section 2.3.3.

The near-field pressure is sensed with microphones using the configuration shown in Figure 2.4(b) and described in Section 2.3.1; its footprint is visible in Figure 5.38. The 16-sensor azimuthal array is placed at $x = 3D$ with tips at $r = 1.5D$. The linear array makes an angle of $8.6°$ to the jet axis with sensors at $x = \{2.5, 3, 3.5, 4\}D$, the second sensor being common with the azimuthal array. The collapse of the wavenumber spectra from this

arrangement was shown in Figure 3.2(d), wherein it was concluded that the signature is dominated by hydrodynamic fluctuations.

The synchronization of PIV and pressure measurements is important for correctly obtaining the spectral correlations, and this has been discussed in Section 2.3.3. Each synchronous datapoint consists of simultaneous pressure timeseries on all 19 channels with a pair of closely-timed PIV snapshots in the middle of the timeseries. At least one thousand such datapoints were acquired for each of the 12 cross-stream locations where this synchronous data was taken.

SLSE Reconstruction Fidelity

The 1-D-slice POD results for a Mach 0.85 jet between $x/D = 3$ and 8 was reported by Tinney et al. (2008a). The results from the present experiments reproduced those data very well. Thus, the focus here is on the novel analysis, mainly the characterization of the reconstruction fidelity.

It is instructive to start with a qualitative intuition for the SLSE reconstruction. For the cross-stream slice at $x = 5.75D$, 1976 snapshots were collected instead of the usual 1000. This dataset was divided in two: one for modeling and the other for validation. Figure 5.39(a) presents the axial component of velocity fluctuations for a particular measured snapshot. The reconstruction from 1-D slice POD modes derived from the validation dataset itself is very faithful to the measured field (see Figure 5.39(b)). SLSE coefficients were derived from the validation dataset, and the corresponding reconstruction shown in Figure 5.39(c) captures the gross shape and rotational phase of some of the structures but under-predicts their amplitudes by a factor of about 4. POD modes and their SLSE coefficients were also derived from the modeling dataset, and these were used to estimate the

164
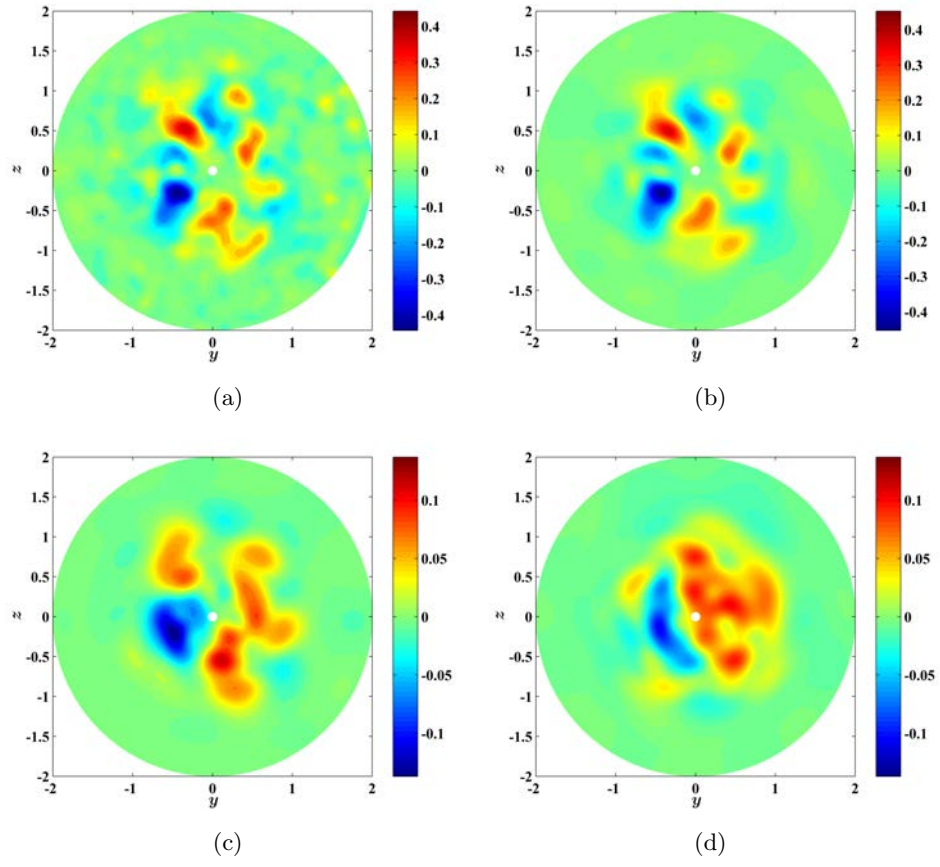
Figure 5.39: Snapshots taken from a validation dataset of the axial velocity fluctuations at $x = 5.75$ obtained from (a) PIV, (b) reconstruction from POD modes derived from the validation dataset, (c) reconstruction from SLSE of the above POD modes, and (d) reconstruction from SLSE of POD modes derived from a separate modeling dataset. All reconstructions include azimuthal modes 0 through 7, and POD modes 1 through 9. Note the disparity in the color-scales representing u_x/U_j.

(a) Local modal SLSE reconstruction error metric   (b) Reconstructed energy ratio for axial velocity
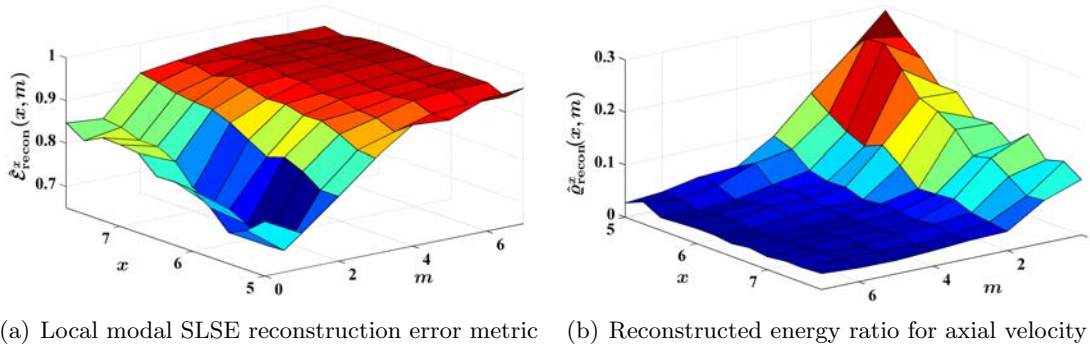
Figure 5.40: Assessment of fidelity of SLSE reconstruction for experimental database.

same snapshot in Figure 5.39(d). The disparities observed in comparing the last two sub-figures attest to the lack of full convergence of the SLSE procedure even with about 1000 datapoints. However, there are sufficient similarities in the results too. One feature that will be discussed later in greater detail is the dominance of an $m = 1$ structure Figure 5.39(d).

Apart from the slice at $x = 5.75D$, the dataset for all other slices consisted of 1000 datapoints. Thus, the modeling and validation of SLSE reconstruction were performed on the same dataset. All reconstructions included azimuthal modes 0 through 7, and POD modes 1 through 9. The reconstruction error metric has been defined in eqn (5.68). It was evaluated to 0.91 for the experimental dataset. This is much larger than the reconstruction errors of 0.62 evaluated for both the low-Re DNS database and the high-Re ILES database. The poorer performance of SLSE in experiments appears to be evidence of experimental uncertainty in computing the stochastic estimation coefficients.

To understand the source of this reconstruction error better, the local azimuthal modal component-wise error metric defined in eqn (5.70) is studied for the experimental database in Figure 5.40(a). Only the axial component is depicted, but the other components have

similar behavior. Comparison with the corresponding values for the DNS database presented in Figure 5.29(a) clearly shows that the inaccuracies are larger across all locations and azimuthal modes. It also appears that the errors are asymptoting to 1 both with increasing downstream distance and azimuthal mode. Figure 5.40(b) depicts the reconstructed energy ratio defined in eqn (5.72) evaluated for the axial component of the velocity in the experimental database. For comparison, refer to the corresponding results from the DNS database in Figure 5.29(b). The ratios are much diminished in experiments. The poorer pressure-velocity correlations are due to the higher turbulence as well as the greater uncertainties encountered in experimentation. The asymptoting of the error metric noticed at higher azimuthal modes and downstream locations in Figure 5.40(a) are also observed here for the experimental database.

The fluctuation energy from the empirical data enters into the reduced-order model through the computation of the eddy viscosity (see eqn (5.53)). Thus, an energy scaling technique is proposed here to improve the ROMs educed subsequently from experimental data by way of SLSE. Using the reconstructed energy ratio defined in eqn (5.72), the transformation is defined as

$$\tilde{\hat{u}}_i(x, \cdot, \cdot; m) \rightarrow \sqrt{\frac{1}{\hat{\varrho}^i_{\text{recon}}(x, m)}} \tilde{\hat{u}}_i(x, \cdot, \cdot; m). \tag{5.73}$$

This makes the azimuthal modal energies of the transformed database equal to their 'actual' values separately for each axial location and velocity component. In what follows, the original and transformed databases will be termed 'unscaled' and 'scaled', respectively.

The result of the scaling transformation, as well as the effect of cubic spline interpolation, are studied via contour plots of the mean square axial velocity fluctuations in Figure 5.41. The measured fluctuations from 3C-PIV are shown in Figure 5.41(a) to establish the baseline. If no scaling is applied to the SLSE reconstruction, then the levels are decreased by

167

(a) From 3C-PIV

(b) From unscaled SLSE reconstruction

(c) Scaling reconstruction before interpolating

(d) Interpolating reconstruction before scaling
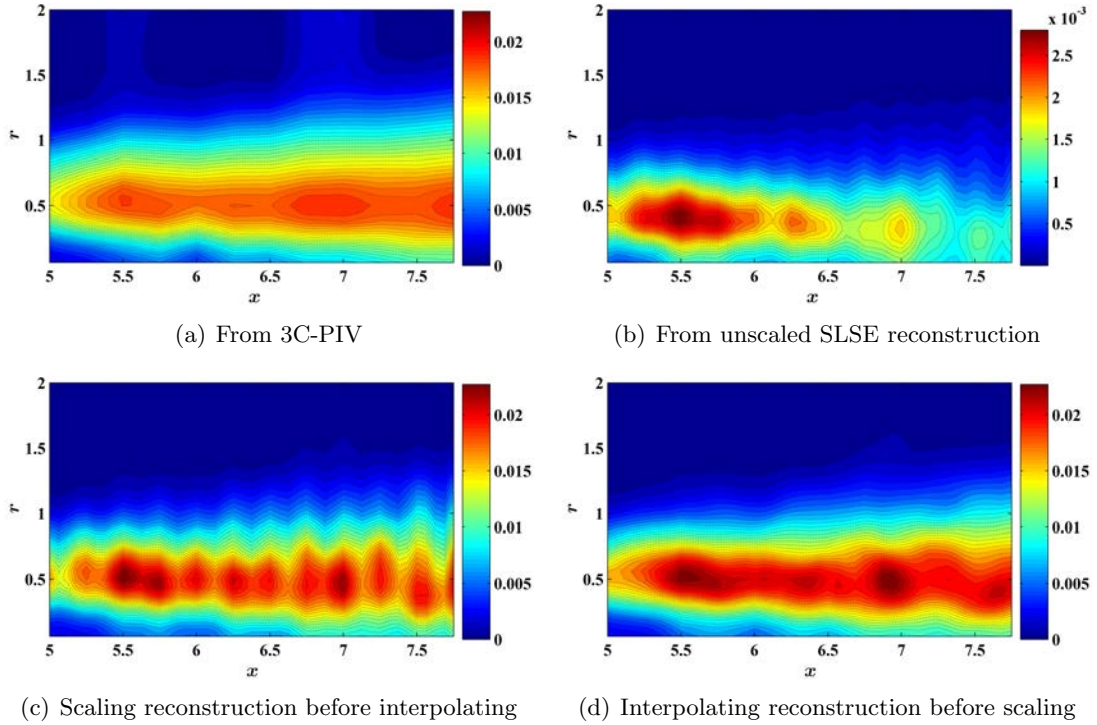
Figure 5.41: Mean square axial velocity reconstructed using different methods, compared to measurements in experiments. Note the disparity in the color-scales.

an order of magnitude, as seen in Figure 5.41(b). As expected from the reconstruction metrics displayed in Figure 5.40, the inaccuracies are much higher at downstream stations. Moreover, the low-speed side of the shear layer is preferentially de-energized relative to the high-speed side. The latter is dominated by the lower azimuthal modes (Tinney et al., 2008a), which are reconstructed better.

The scaling transformation performed on the SLSE reconstructed velocity fields is seen to restore the fluctuating energy to the actual value at the axial stations on the coarse grid. There are slight local over-predictions since the lower 1-D POD modes are being assigned the energy that the neglected higher modes have in the actual measurements. As in the DNS database, the desired axial grid resolution is $D/16$, and interpolation must

(a) Unscaled   (b) Scaled
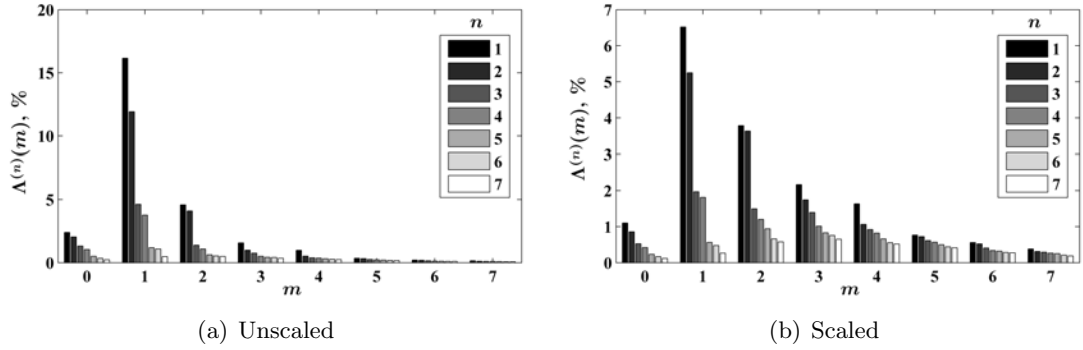
Figure 5.42: Eigenspectrum with volumetric POD of the SLSE-reconstructed experimental database.

be performed. The cubic spline interpolation results in smoothing of the field such that the fluctuation energy is reduced. Thus, if the interpolation is performed on the scaled reconstructions, then one ends up with the corrugated contours as shown in Figure 5.41(c). To avoid this, the order of operations must be inverted, with the more satisfactory result shown in Figure 5.41(d).

Volumetric POD on SLSE Database

The use of 16 sensors on the azimuthal array of near-field pressure sensors limits the resolution of azimuthal modes of the SLSE-reconstructed database to 7. Thus volumetric POD performed on this approximate database of snapshots can also resolve at most up to the 7th azimuthal mode.

The eigenspectrum from the volumetric POD performed on the unscaled database is presented in Figure 5.42(a). The eigenvalues are expressed as a percentage of the total resolved energy (limited to $M = 7$). The relatively high energy in $m = 1$ has already been anticipated from Figure 5.40. Comparison with the corresponding eigenspectrum from the DNS database shown in Figure 5.6(b) reveals other discrepancies. Firstly, the clear

separation of the 1st POD mode in $m = 0$ is no longer observed in experiments. This mode was the shift-mode that is thought to account for the stability of the ROMs educed from the DNS database. Secondly, the first POD modes in $m = 2$ and 3 were clearly dominant in the results from DNS, but this is not replicated in experiments. On the other hand, the similarity with the results from DNS is in the approximate equality of the first two POD modes in $m = 1$. The rapid diminution of contributions from the higher azimuthal modes was also observed in the DNS results.

The POD eigenspectrum from the scaled database is shown in Figure 5.42(b). The different azimuthal modes are of course scaled differently commensurate with their prior under-prediction. However, within a given azimuthal mode, the POD modal eigenspectrum remains quite similar.

The first few eigenfunctions of the axial component of velocity from the SLSE database are examined in Figure 5.43. The unscaled database was shown to be especially energy-deficient at downstream locations. A comparison of the two sub-figures demonstrate that the major effect of the scaling transformation on the eigenfunction shapes is the appearance of more large-scale structures at downstream locations in the lower POD modes. The shift mode is absent in the POD basis obtained from experiments. Moreover, the distinctive structures observed in the first POD modes of $m = 2$ and 3 in DNS (see Figure 5.7) are also absent. In fact, greater similarity is demonstrated with the results from the high-Re ILES database shown in Figure 5.21. In the latter case also, the shift mode was absent from $m = 0$ and the leading-energy structures in $m = 2$ and 3 were of comparable size.

Reduced-Order Model Simulation over a Short Time Horizon

The POD modal coefficients enter into the dynamical modeling process through the eddy viscosity computation (see eqn (5.53)). To capture the full statistics on the attractor one
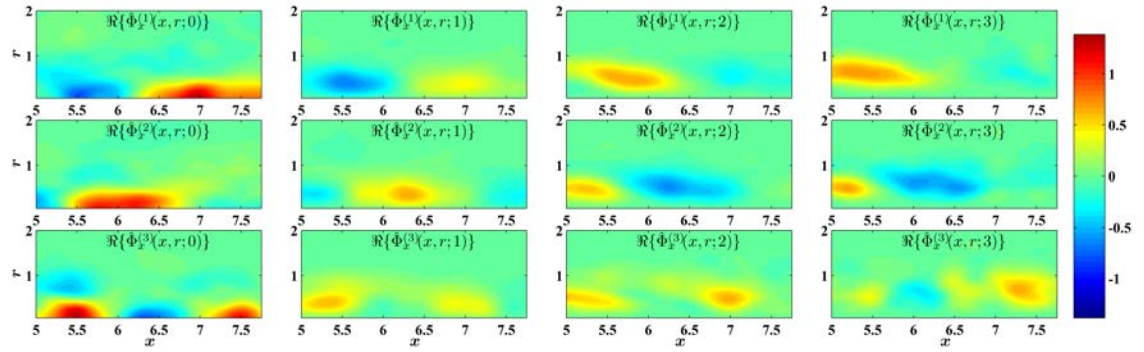
(a) Unscaled database
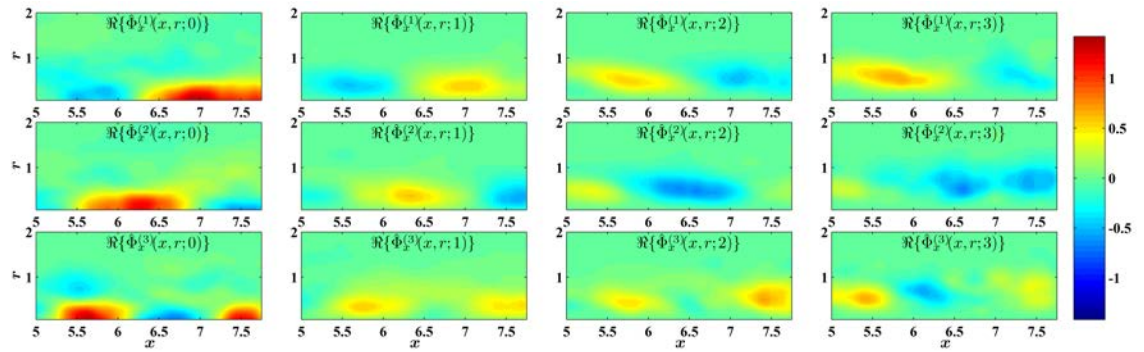
(b) Scaled database

Figure 5.43: Axial components of first few eigenfunctions from the volumetric POD of SLSE-reconstructed experimental database.
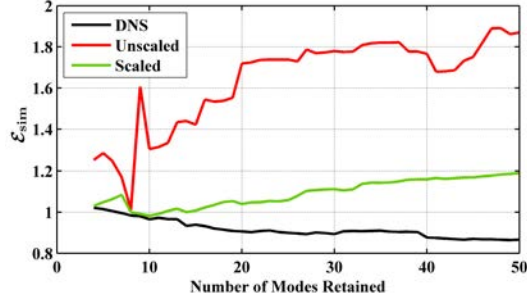
Figure 5.44: Simulation of ROMs from SLSE-reconstructed experimental database analyzed using the time-averaged simulation error metric.

should project the flow field at enough uncorrelated time instants. The experimental dataset is rich in this aspect, having thousands of uncorrelated time-series of pressure data measured on the near-field rig, each series spanning more than 400 flow time steps. However, as found in the investigation of this method for the DNS database, the projection coefficients from every reconstructed snapshot inherits the inaccuracies of the underlying SLSE technique. It will be demonstrated here that the estimation of the eddy viscosity is much improved by the scaling transformation presented in eqn (5.73).

The reduced-order modeling strategy proposed in Section 5.7 has been validated for the low-Re DNS database as well as the high-Re ILES database. The validation was made possible by the availability of the time-resolved volumetric flow field database. Such a validation database is not obtainable in experiments. In lieu of this, such a field will be estimated from the time-resolved pressure field. Basically, a moving window (in time) of pressure data is used along with SLSE to approximate the velocity field at the instant corresponding to the middle of each window. This field is projected onto the retained volumetric POD basis to obtain an approximation to the time-resolved modal coefficients. This is done separately for both the unscaled and scaled databases.

172

(a) Simulation energy ratio from unscaled data

(b) Simulation energy ratio from scaled data

(c) Simulation error metric from scaled data

(d) Alignment metric from scaled data
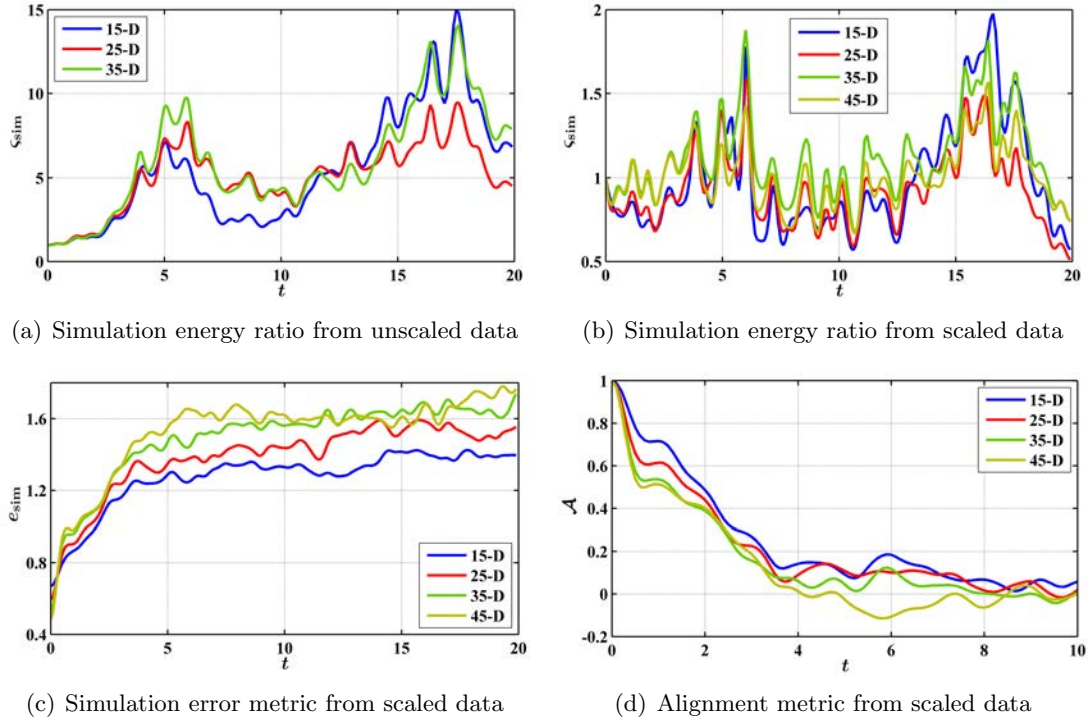
Figure 5.45: Time evolution of performance metrics for ROMs of various dimensions from SLSE performed on experimental data.

Figure 5.44 shows the simulation error metric per eqn (5.64) averaged over the first 5 flow time steps of simulations starting from 20 different initial conditions for various dimensions of retained bases. The performance of the models from the unscaled database is very poor. Much improvement is obtained by the scaling transformation. However, the errors increased steadily with the increase in the number of retained modes. This is due to erroneous approximation of the low energy modes. Models of different dimensions will be assessed below using the time evolution of different performance metrics.

The instantaneous energy of POD reconstruction has been defined in eqn (5.66). The ratio of the simulation energy to the projected energy, termed the simulated energy ratio,

is defined as

$$\varsigma_{\text{sim}}(t) := \frac{||\mathcal{P}_S \tilde{\mathbf{u}}(\cdot, t)||^2}{||\mathcal{P}_S \mathbf{u}(\cdot, t)||^2} = \frac{\displaystyle\sum_{m=-M}^{M} \sum_{n=1}^{N_m} \left| \tilde{\hat{\alpha}}^{(n)}(t; m) \right|^2}{\displaystyle\sum_{m=-M}^{M} \sum_{n=1}^{N_m} \left| \hat{\alpha}^{(n)}(t; m) \right|^2}. \tag{5.74}$$

The projected energy is used in the denominator instead of the actual energy, so that ROMs of different dimensions can be compared. The tilde indicates that the quantity is obtained from model simulation. In what follows, the time-evolving performance metrics, including the simulated energy ratio defined above, will be presented as an average over simulations from 10 different initial conditions.

The comparison of the simulated energy ratio in Figures 5.45(a) and 5.45(b) provides the explanation for the poor performance of the ROM from the unscaled database. The model is insufficiently dissipative owing to erroneous computation of the eddy viscosity. Moreover, the initial condition from the unscaled database has very low energy which is uncharacteristic for the attractor of the flow. This causes rapid growth of energy of the simulated trajectory. Figure 5.45(b) shows that with models from the scaled database, the energies of the simulated and projected fields remain similar. This figure also shows that there is no clear distinction between the simulated energy ratios obtained from the 4 models of very different dimensions. In the remainder, only the models from the scaled database will be considered.

Figure 5.45(c) depicts the time-evolution of the simulation error metric as defined in eqn (5.65). It clearly shows the steady degradation of simulation fidelity with increasing model dimension. The reason for this is the corresponding worsening of the alignment metric (see definition in eqn (5.67)) portrayed in Figure 5.45(d). The explanation for these trends can be found in the following consideration of the scaling transformation. Figure 5.45(b) has shown that the overall dynamics are not becoming more faithful with addition of modes

174
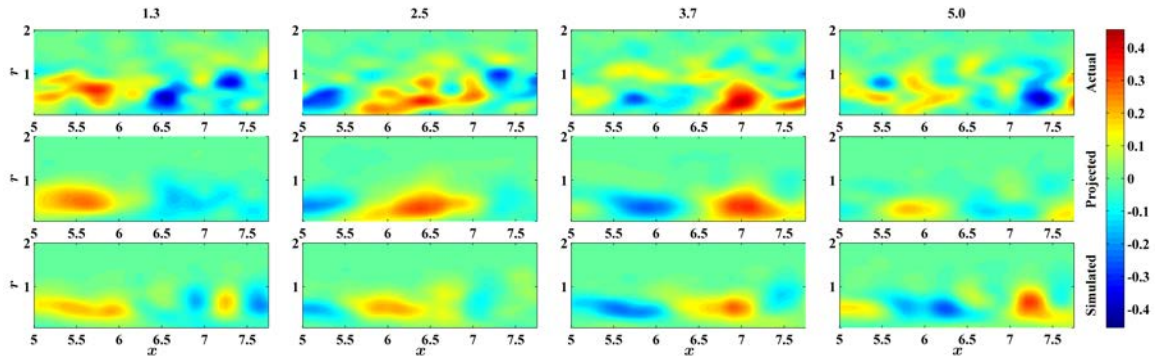
Figure 5.46: Snapshots of simulated fields with 25-D ROM built from the experimental database after energetic scaling. The scheme of presentation follows from Figure 5.12.

to the model. Thus, the energy scaling is most useful for correctly identifying the high-energy structures in the flow, but the technique becomes progressively ineffective in going to lower-energy structures. The small inaccuracies incurred in extracting kinematic features get magnified when their dynamics are being modeled.

Figure 5.46 illustrates the above discussion with representative snapshots from the simulation of the 25-D ROM from the scaled database. The simulated field replicates the projected field with sufficient accuracy up to about 4 flow time steps.

Reduced-Order Model Simulation over Intermediate Time Horizon

Figure 5.45(b) showed that the simulated energy remains close to the projected energy over the first 20 flow time steps after initiation of simulation for all the four models of different dimensions. This appears to suggest that the models have stable attractors. With more than 60 initial conditions tested, trajectories were found to become unbounded between 50 and 150 flow time steps, but not before that. For a given model dimension, the statistics obtained by averaging flow quantities simulated over the first 50 time steps were found to be quite similar for all initial conditions. This leads to the conclusion that there exists a

175

(a) 15-D ROM

(b) 25-D ROM

(c) 35-D ROM

(d) 45-D ROM
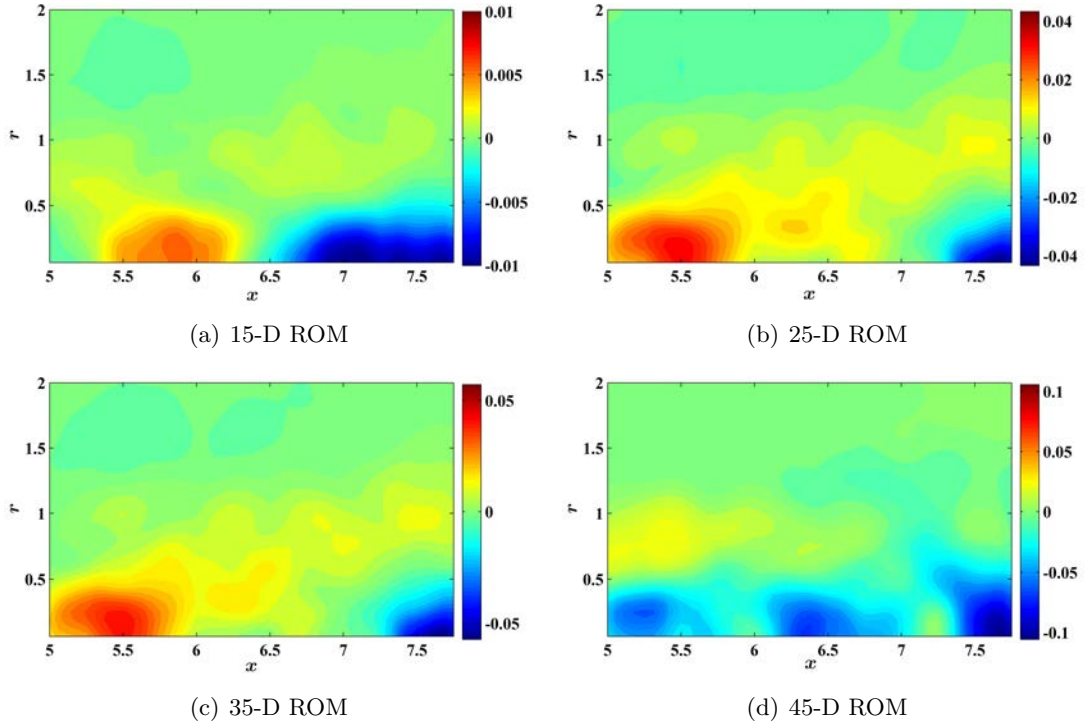
Figure 5.47: Error in mean axial velocity prediction from simulation of ROMs from scaled experimental database.

region in the state space of these models that is attractive to most but not all trajectories. In the following, the statistics that are presented were obtained by averaging over the first 50 flow time steps of simulation, as well as averaging over 20 different uncorrelated initial conditions.

Figure 5.47 shows the error in the predicted mean axial velocity from simulations of 4 different ROMs. First of all, it is noted that the error levels are quite comparable to those observed with a 44-D ROM derived from the DNS database (see Figure 5.13). There is a steady increase in error levels with increasing model dimension in Figure 5.47. The shape of the error mean field in the DNS simulation was identified as the shift mode. This is not discernible in the models from the experimental database here. The results for the 25-D and

(a) 15-D ROM

(b) 25-D ROM

(c) 35-D ROM

(d) 45-D ROM
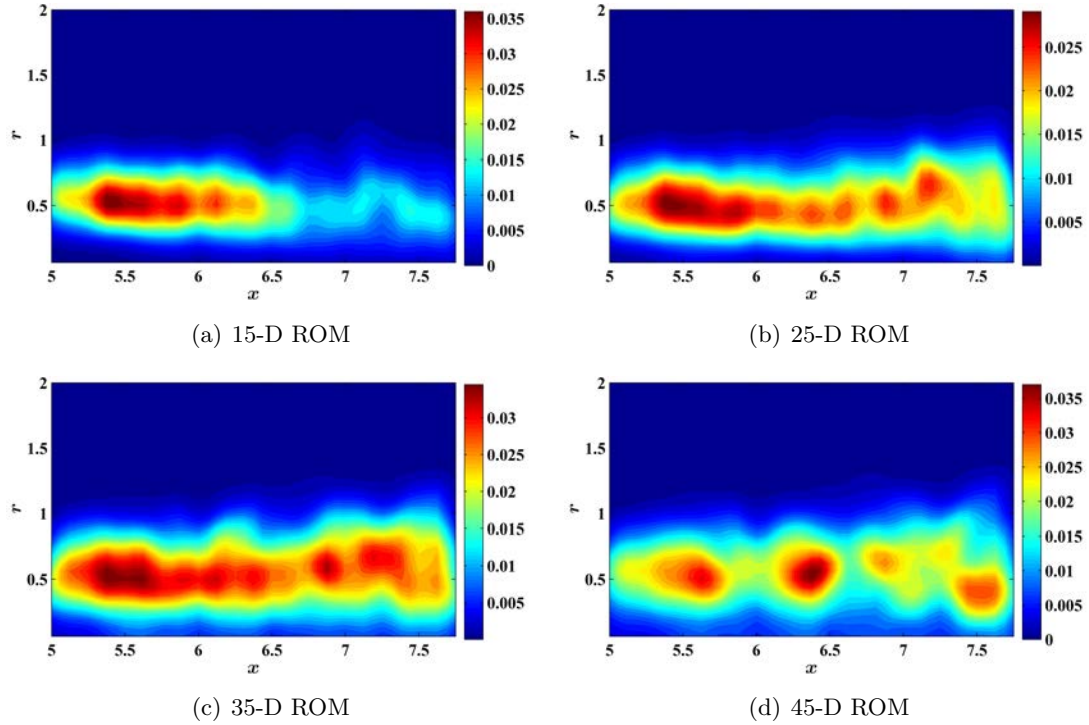
Figure 5.48: Mean square of axial velocity fluctuations from simulation of ROMs from scaled experimental database.

35-D ROMs are quite similar, and the contour plots display only two prominent localized error regions.

Figure 5.48 presents the mean square of the axial fluctuating velocity fields after subtraction of the respective mean values shown in Figure 5.47. For comparison, the reader is referred to the corresponding contour plot in Figure 5.41(c) that was obtained with the energy scaling transformation following the SLSE step. The 15-D model produces a contour plot that is quite different in both level and shape from the reference. The 45-D ROM also shows an unphysical distribution of fluctuation amplitudes. The 25-D and 35-D models replicate the reference plot quite closely, both in terms of fluctuation levels and contour shapes.

(a) 25-D ROM   (b) 35-D ROM
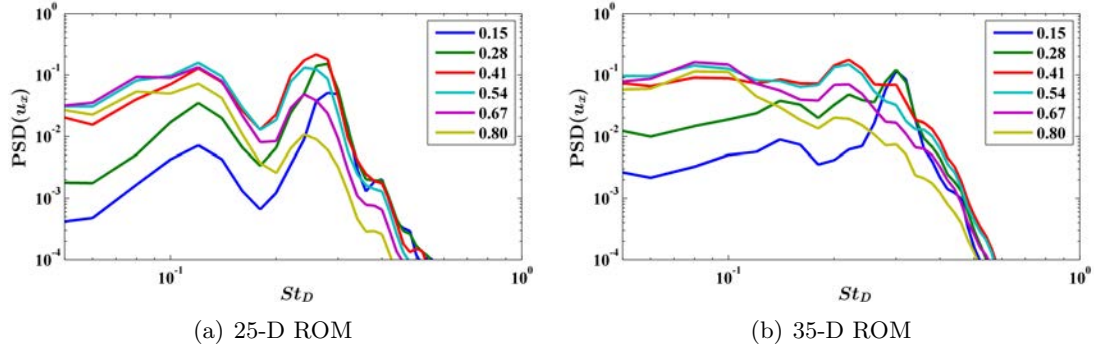
Figure 5.49: Power spectral density of axial velocity fluctuations at $x = 6$ and various r for ROMs of two different dimensions built from the scaled experimental database. The spectra were averaged over simulations from 20 different initial conditions. Each simulation was performed over 50 flow time steps.

The frequency domain character of the reduced-order model is important for reproducing the response of the jet to periodic excitation. The power spectral densities of the 25-D and 35-D models are studied in Figure 5.49. The spectral information for velocity in the mixing layer is not available from experiments at GDTL. However, the literature leads one to expect spectra quite similar to those observed for the DNS database presented in Figure 5.15 (Petersen and Samet, 1988; Citriniti and George, 2000; Jung et al., 2004; Tinney et al., 2006). From this point of view, the 35-D model is demonstrating more realistic frequency-domain behavior. The low-frequency parts of the spectra are flatter, indicating broadband turbulence. The shoulders for the high-frequency roll-offs are also less abrupt at all radial measurement locations.

A sharp peak around $St_D \approx 0.3$ is observed in the 25-D ROM at all the radial locations. Such a peak is also discernable in experiments at locations close the nozzle exit and near the centerline, and corresponds to the jet preferred mode (Petersen and Samet, 1988). However, such narrow-band behavior is not expected so far downstream of the nozzle exit,

and especially not on the lip-line. Moreover, the amplitude of the peak at the centerline is not expected to be higher than the broadband level at the lip-line (Tinney et al., 2006). This peak is much reduced at the high-speed side of the shear layer for the 35-D ROM, and is absent altogether at the other radial positions. Evidently, the inclusion of the lower energy modes in the 35-D model is improving the dynamical predictions owing to better replication of the nonlinearities inherent in the jet.

Finally, the expected overall radial variations in the spectra are replicated in both models. Namely, in moving radially outward, the spectral levels first increase and then decrease beyond the lip-line. Also, the shoulder-frequency starts off high near the centerline, but reduces in traversing outward.

The statistics presented above from the intermediate-time simulations of the reduced-order models obtained from experimental data are quite encouraging. They indicate that in spite of the many simplifying assumptions made in the derivation of the models, the essential dynamics of the jet are being captured with sufficient fidelity.

5.10   Conclusions

This chapter has presented a strategy for modeling high-speed and high Reynolds number flows in general, and the axisymmetric jet in particular. The development and implementation of the technique is motivated and guided by the end goal of obtaining a feedback-oriented model of the jet. However, in this chapter, the focus is on capturing the dynamics of the *unforced* jet with a model with the fewest degrees of freedom.

The two main pillars of the proposed modeling strategy are proper orthogonal decomposition (POD) and Galerkin projection (GP). The former is used for educing a low-dimensional description of the flow kinematics from empirical data, whereas the latter yields

a reduced-order model of the flow dynamics within the space of the above kinematics. Both these techniques are very well established and have been employed together for various flow configurations.

The novelty of the present work is the implementation of this POD–GP combination for a highly turbulent flow configuration that has been rarely addressed in the literature. The jet being modeled is nominally operated at Mach 0.9 and the Reynolds number is 6.7×10^5. The high Reynolds number of the jet considered means that a large range of flow scales are of dynamic importance, which makes system reduction very challenging. The demanding nature of the application necessitated much care in the implementation. In particular, symmetry considerations were crucial for efficiently capturing the inherent patterns in the flow. Moreover, a simple but robust formulation of the eddy-viscosity was selected from the literature that did not require any tuning parameters.

One of the main concerns in the present work was to ensure its applicability to an empirical database obtained in experiments, rather than from numerical simulation. A direct numerical simulation database was exploited extensively, but only insofar as to guide the modeling strategy development. A major limitation of present experimental techniques for high-speed flows is the infeasibility of obtaining thermodynamic (pressure, temperature) and velocity measurements simultaneously. It is shown in the text that this necessitates an assumption of incompressibility. One of the contributions of the present work is to demonstrate in numerical simulations that such an assumption is valid even in this high subsonic flow.

The results section has been divided into 6 parts to delineate the hierarchical progression of the model validation process. The beginning is made with time- and space-resolved DNS data of the Mach 0.9 but low Reynolds number jet. This allows careful analysis of the sources

of error in the modeling that is not possible with experimental data. This also allows a simulacrum of the experimental database to be generated by discarding information that would be unavailable from physical measurements. The model derived from this depleted database is then compared back to a family of models obtained directly from the DNS database. The comparison reveals that the essential dynamics of the jet are still captured with sufficient accuracy.

The denouement of the validation is the modeling of experimental data. The short-term predictive fidelity of the model is of paramount importance for feedback control. Extensive numerical simulations of reduced-order models were conducted to assure that this objective is met. The educed models were found to have unbounded trajectories after about 50 flow time steps from the initiation of simulation. This is not of immediate concern for feedback control. However, the flow statistics predicted in the intermediate term (up to 50 flow time steps) from the simulations of the ROMs were investigated in detail. The essential dynamics of the experimental jet were found to be reproduced well.

Chapter 6

Incorporating Actuation Effects in the Reduced-Order Model

6.1 Introduction

The previous chapters addressed the reduced-order modeling of an *unforced* axisymmetric jet. For the development of feedback laws, the model must have an explicit incorporation of the effect of actuation. Most control theories and all flow control applications in the literature are concerned with actuators whose effective *amplitudes* are to be determined in real time through feedback laws. However, the arc filament plasma actuators used in this work are radically different from such actuators since one has no control on their amplitude. The only actuation parameters that can be specified in real time are the frequency, the pulse width, and the relative phase within the actuator array. A phenomenological approach is proposed here to incorporate the effect of LAFPAs in the reduced-order model. But first, the flow control literature on incorporation of actuation effects is discussed briefly to provide the background.

Flow control actuators can be broadly divided into three categories based on the nature of their coupling with the flow; strategies for modeling them differ likewise. Actuators can produce a body force either in a local or a global manner. Since the body force appears as

an additive term in the Navier-Stokes equation, the incorporation of its amplitude in the reduced-order model is particularly straightforward (e.g. Rowley and Juttijudata, 2005; Ilak and Rowley, 2008; Tadmor et al., 2010). The alternating current dielectric barrier discharge plasma actuators generate such a body force (Corke et al., 2010).

The majority of actuators studied inject momentum into the flow at the boundary. Typical examples include zero net mass flux devices, steady or pulsed blowing and/or suction, and boundary movement (like cylinder rotation). There is no direct way to incorporate momentum-injection effects in a POD-Galerkin-based reduced-order dynamic model. The reason for this is that the boundary conditions enter into such a model indirectly through the information contained in the empirical snapshots, but the POD eigenfunctions themselves are defined over the whole flow domain. One way of addressing this issue is the sub-domain method of POD (Efe and Ozbay, 2004). The flow domain is divided into a main domain wherein the actuation does not have any direct effect, and one or more sub-domains near the boundaries where the momentum amplitude is a function of the actuation amplitude. A related technique is to separate the actuation effect through a weak formulation of the POD (Camphouse, 2005). Yet another approach is to posit that the flow field can be linearly decomposed into a subspace that does not change with forcing, and a different subspace consisting of 'actuation modes' modulated by the actuation amplitude (or a function thereof) (Caraballo et al., 2008; Kasnakoğlu et al., 2008; Andino et al., 2011). These techniques are collectively termed control-input separation methods, and they result in an explicit incorporation of the control term in the *kinematic* ansatz. Subsequent application of the Galerkin projection leads to the explicit inclusion of the actuation effect in the dynamic model. The above discussion focused on applications to nonlinear models.

The principle of superposition holds for linear flow models, and boundary actuation can be incorporated as an equivalent body force near the wall (Hogberg et al., 2003).

The third type of flow actuation is instability perturbation. Small amplitude fluctuations are seeded at a point of optimal receptivity in the flow. If the fluctuation frequency falls within the range for which the flow is unstable, then the perturbations are amplified by the flow itself, and develop into large scale structures. The goal of feedback control in this context is to manipulate these large scale structures through the real-time shaping of the relatively low-power actuation input, especially its frequency-domain characteristics. Clearly, the frequency of actuation is more important than the amplitude in this case, and the preceding techniques do not apply. Flow control research has not addressed the feedback-oriented modeling of this type of actuation effect till date. Apart from LAFPAs, nanosecond pulse-driven dielectric barrier discharge plasma actuators also fall in this category (Little et al., 2010; Rethmel et al., 2011). In fact, the body force and momentum injection devices can also be used in this manner, but then their feedback-oriented modeling runs into the issues described here.

The control-oriented ROMs in the preceding discussion are a system of ODEs (possibly nonlinear) of the form

$$\dot{\mathbf{y}} = F\left(\mathbf{y}\right) + G\left(\mathbf{y}, \gamma\right). \tag{6.1}$$

Here, $\mathbf{y}$ signifies the state vector, γ refers to the control input, F is called the drift vector field, and G is termed the input vector field. The literature on derivation of the input vector field has been discussed above; the next focus is on the drift vector field.

Ideally, in the absence of control, the dynamical model should revert to the model for the unforced flow, which implies that the drift vector field should be determined by Galerkin projection of the unforced flow data. This is the approach selected for the control-input

separation methods discussed above in reference to the modeling of momentum injection actuators. However, when controlled in closed-loop, the flow would typically operate away from the unforced flow regime. It is well known that in many flows, the most efficient functional basis for describing the unforced flow bears little resemblance to those best suited for reconstructing the forced flow. Moreover, feedback control may force the flow with parameters for which open-loop control data does not exist. Several techniques have been proposed to obtain a robust drift vector field that is suitable for modeling the actuated flow in closed-loop operation.

In the most widely applicable option, the flow is forced at various static parameter conditions covering the expected range of operation of the closed-loop flow. The empirical data from all these cases are merged with suitable relative weighting along with data from the unforced flow, and POD is performed on the entire database (Boree, 2003; Fogleman et al., 2004; Taylor and Glauser, 2004; Pinier et al., 2007; Caraballo et al., 2008). Subsequent application of Galerkin projection to this POD basis results in the desired drift vector field. Addition of data from the transient phase during the initiation and/or termination of actuation typically enriches the empirical database. In fact, this may be one way of automatically incorporating the shift mode discussed in Section 5.9.1 (see also Noack et al., 2010). In the extreme case, addition of flow field information measured with white-noise forcing has been found to produce very robust POD bases that can best span the operating regime of a closed-loop controlled flow (Caraballo et al., 2008). Note that the control-input separation methods rely on modeling the 'innovations' in the actuated flow data with respect to the unforced flow data, and hence such indiscriminate merging of databases is not allowed in those procedures.

For flows in the linear regime, a much more sophisticated and mathematically rigorous approach is to use the impulse response of the flow to perform a balanced POD (Rowley, 2005). This incorporates the observability and controllability criteria of the feedback control system in the modeling step. The balanced POD requires adjoint simulation data for implementation. The snapshot-based eigensystem realization algorithm was recently proposed to approximate the benefits of balanced POD without the necessity of adjoint simulations (Ma et al., 2011). This makes the technique applicable to time-resolved experimental data of linear flow systems. Such elegant solutions have not been found for flows in the nonlinear regime.

Yet another route that has been researched recently for flow control applications is the well-established concept of constrained nonlinear optimization. In this case, the structure of the model is derived from arguments as above, but the actual coefficients of the drift and input vector fields are *not* derived from Galerkin projection of the governing dynamics. Instead one uses the available empirical data to 'fit' the coefficients of these vector fields simultaneously (Cordier, 2011). There are several optional levels of complexity in posing the optimization problem, with consequent implementation difficulties and benefits. At a minimum, one needs snapshots of the acceleration field, which is difficult to obtain reliably from experiments, although some advances have been made for low-speed flows recently (Perret et al., 2006). At its most sophisticated, constrained optimization requires adjoint simulations, and the fidelity of the resulting models may be greatly improved in the process (Cordier, 2011). Unfortunately, none of these techniques are applicable to the experimental data of the high-speed jet flow under consideration.

This chapter is organized as follows. Section 6.2 discusses the question of obtaining the unactuated part of the dynamic model with applicability to the forced flow (i.e. the

drift vector field). The explicit incorporation of the forcing effect in the input vector field is addressed in Section 6.3. The proposed modeling strategy is validated in simulations in Section 6.4. Section 6.5 presents the conclusions drawn from this chapter.

6.2 Modeling the Unactuated Part of the Dynamics of a Forced Jet

6.2.1 Experimental Dataset

The experiments on the unforced flow and the ROMs derived from the resulting database have been discussed in Section 5.9.6. Additionally, six different forcing cases were tested. In the axisymmetric $m_F = 0$ mode, the jet was forced at St_{DF} of 0.25, 0.30, and 0.35. These are near the jet column mode, where the most enhancement of bulk-mixing has been previously observed (Samimy et al., 2007b; Kearney-Fischer et al., 2009). In the $m_F = 3$ mode, the jet was forced at St_{DF} of 1.5, 2.3, and 3.0. The largest reduction in far-field noise has been found to occur under these conditions (Samimy et al., 2007c). Although both these forcing groups will be discussed here, the deeper investigation would focus on the former group. This is because of the robust organized large scale structures that are generated by forcing around the jet column mode, which renders the reduced-order modeling somewhat more amenable.

Three-component PIV data were collected for each forcing case on cross-stream sections located at $x/D = \{5, 6, 7\}$. Note that the 3C-PIV for the unforced jet was performed on sections at every $0.25D$ intervals between 5 and $7.75D$. During all these measurements, the near-field pressure was acquired simultaneously in the configuration and procedure mentioned in Sections 2.3.1 and 5.9.6. Finally, the phase of actuation was recorded simultaneous with the pressure measurements and PIV snapshots per the discussion in Section 2.3.4. In addition to these simultaneous velocity and pressure measurements, 2C-PIV data are also available on a streamwise plane for a large number of forcing cases. The data from these

forcing cases are analyzed below, and this analysis contributes to the derivation of the drift vector field.

In systems with periodic forcing, the response can be analyzed using the triple decomposition (Reynolds and Hussain, 1972). Any instantaneous signal W can be represented as

$$W = \overline{W} + \overleftarrow{W} + w. \tag{6.2}$$

Here, $\overline{W}$ is the time- or ensemble-average, as first introduced for the pressure signal in eqn (3.1) and then again for the velocity field in eqn (5.2). The *phase-average* $\overleftarrow{W}$ is obtained by averaging the residuum (instantaneous signal minus the ensemble-average) over a large ensemble of time-instances corresponding to the same phase of the reference periodic forcing. The final remainder w is then the fluctuations or *turbulent motion* (Reynolds and Hussain, 1972). In the axisymmetric jet, the ensemble-average is augmented by an azimuthal average (see eqns (3.1) and (5.2)). For forcing in a particular azimuthal mode m_F, the phase-averaging can also be augmented by extracting only the azimuthal mode $m = m_F$ from the residuum (whenever the data exist to do so), and this will be adopted in the present work.

Forcing the jet with $St_{DF} = 0.3$ and $m_F = 0$ has been known to generate robust and organized axisymmetric structures (Samimy et al., 2007b; Kearney-Fischer et al., 2009). In Figure 6.1, phase-averaged fields from the two different PIV experiments performed are compared. For the 3C-PIV experiments, phase-locking was not performed. However, a binning operation was performed on the actuation phase corresponding to each snapshot to educe phase-averaged velocity fields for eight equally-spaced phases. The close match of the fields shown here lends credence to this phase-averaging procedure. Additionally, the fields agree closely with the results presented in Kearney-Fischer et al. (2009), where a correlation-based conditional-averaging technique (Konstantinidis et al., 2005) was used
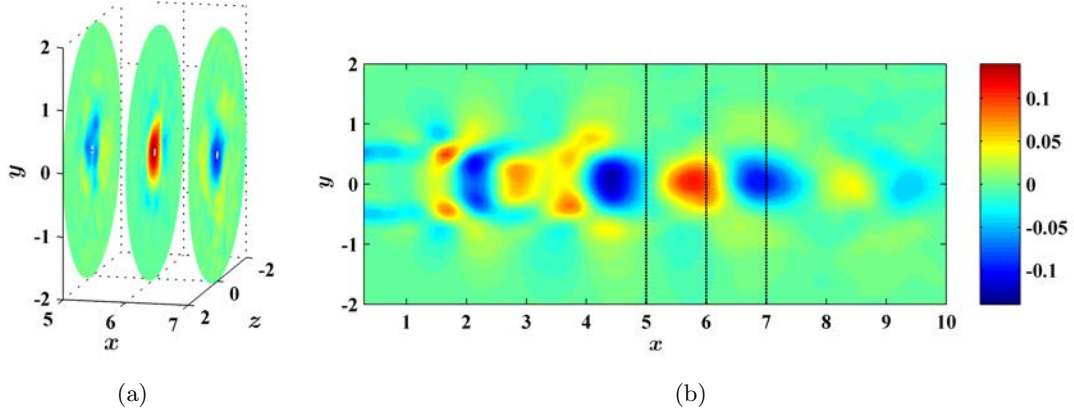
Figure 6.1: Comparison of u_x averaged at $45°$ phase of actuation with $St_{DF} = 0.3$ and $m_F = 0$ from (a) 3C-PIV on discrete cross-stream slices, and (b) phase-locked 2C-PIV on meridional plane. The color scale is same for both sub-figures, and is normalized by U_j.

to determine an approximately phase-averaged velocity field for the present forcing case. Under these forcing conditions, the length of the potential core was previously reported as $\sim 5D$ (Kearney-Fischer et al., 2009). The wavelength in the vicinity of the potential core end is observed to be $\sim 2.4D$ which, with the known St_{DF} of 0.3, gives a convective velocity of $0.72U_j$. This matches well with the value of convective velocity for axisymmetric structures reported for the *unforced* Mach 0.85 jet (Tinney et al., 2008b).

6.2.2 Forcing Effects on Mean Flow

The base flow field for the POD/Galerkin models of unforced jets considered in Chapter 5 has been the respective ensemble-averaged flow fields. One of the primary effects of forcing the jet with LAFPAs is the modification of the mean flow (Samimy et al., 2007b; Kim et al., 2009a; Kearney-Fischer et al., 2009). This change must be understood and accounted for in the base flow field for the correct modeling of the drift vector field.

The contour plot of the mean axial velocity from the unforced jet has been presented in Figure 5.38. In Figure 6.2, the mean axial velocity field from the unforced jet is subtracted

(a) $m_F = 0$, $St_{DF} = 0.3$ (b) $m_F = 3$, $St_{DF} = 1.8$
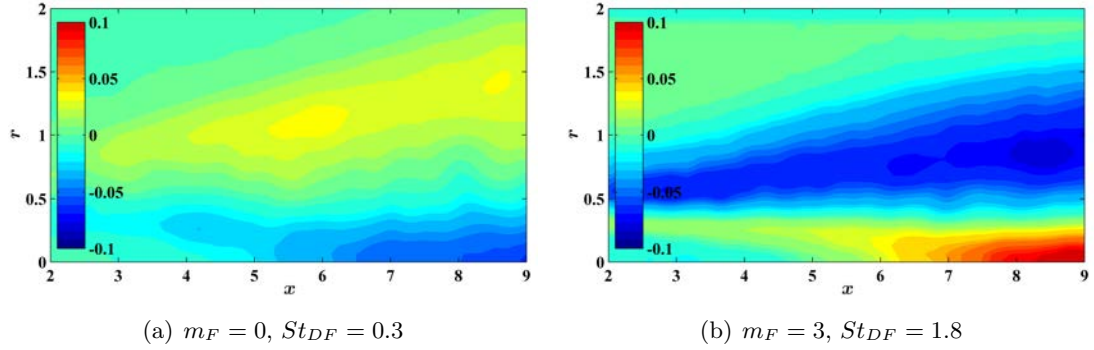
Figure 6.2: Contours of the difference in mean axial velocity fields of forced cases over the unforced.

from that obtained with two typical forcing cases. Forcing near the jet column mode reduces the length of the potential core and flares the mixing layer, as demonstrated in Figure 6.2(a). Figure 6.2(b) shows that forcing at the much higher Strouhal number has the opposite effect. Such characteristics have been reported in jet centerline Mach number and jet half-width plots for plasma actuation (Samimy et al., 2007b; Kim et al., 2009a; Kearney-Fischer et al., 2009).

The two forcing conditions considered in Figure 6.2 are representative of the two different regimes in which the closed-loop flow is expected to operate. As such, the differential flow fields represent the main change when forcing is initiated or terminated. The low-dimensional functional basis of the flow must be able to resolve these changes so that the dynamical model obtained by Galerkin projection on this basis can accurately predict the associated transients. Note that these constitute a type of shift mode as discussed by Noack et al. (2010).

If the mean flow field changed linearly with forcing frequency, then the shift mode represented by Figure 6.2(a) would have been sufficient to characterize the transient dynamics

(a) Case of $St_{DF} = 0.3$ minus $St_{DF} = 0.25$ (b) Case of $St_{DF} = 0.3$ minus $St_{DF} = 0.35$
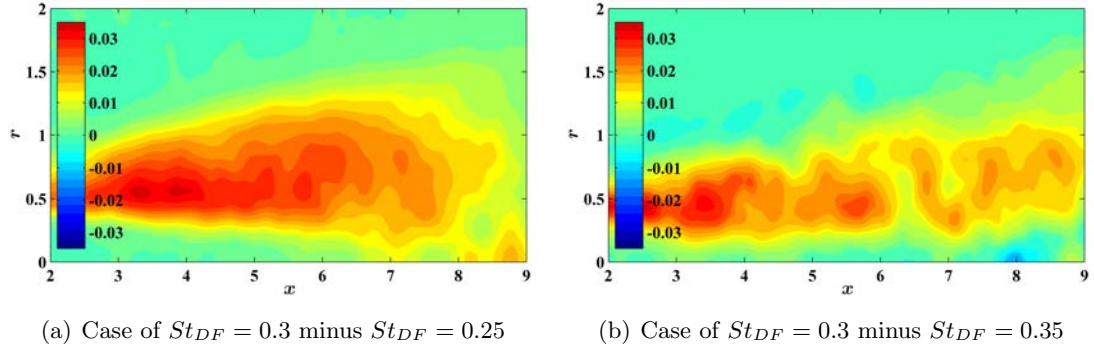
Figure 6.3: Contours of the mean axial velocity fields of two different forced cases subtracted from the case of forcing with $St_{DF} = 0.3$. All flows were forced at the axisymmetric mode.

in close-loop operation near the jet column mode. However, previous research with LAF-PAs has shown that the bulk mixing enhancement is optimum in a narrow range of forcing frequencies around the jet column mode, thereby evidencing strong nonlinearities (Samimy et al., 2007b; Kim et al., 2009a; Kearney-Fischer et al., 2009). This sensitive response has also been discussed in the context of near-field pressure fluctuations in Section 3.4.

Figure 6.3 displays the changes in the axial mean velocity field in the vicinity of the forcing parameter of $m_F = 0$ and $St_{DF} = 0.3$. The results demonstrate that changes in the centerline velocity are small in this forcing parameter space, and the main change is in the width of the shear layer. These sub-figures also show that the $St_{DF} = 0.3$ case results in greater mixing compared to both lower ($St_{DF} = 0.25$) and higher ($St_{DF} = 0.35$) forcing Strouhal numbers. Moreover, the changes in the width of the shear layer are not quite symmetric around this forcing optimal forcing parameter.

The closed-loop controlled flow would primarily operate in the range of forcing parameters depicted in Figure 6.3 when the control objective is bulk mixing enhancement. Thus, the ROM for computing feedback laws for this performance goal should be developed from

a functional basis that can resolve the mean flow field changes shown. These differential fields then represent the more pertinent shift modes for modeling bulk mixing enhancement, rather than the one depicted in Figure 6.2(a).

6.2.3 Forcing Effects on Velocity Fluctuations

The effect of forcing with LAFPAs on jet centerline and lip-line turbulent kinetic energy has been extensively investigated (Samimy et al., 2007b; Kim et al., 2009a; Kearney-Fischer et al., 2009). The experimental database in the present work consists of 3C-PIV information on cross-stream slices, which has not been explored previously. Owing to the axisymmetry of the jet, it is natural to study the velocity field in its Fourier azimuthal domain, instead of the physical azimuthal domain.

The energy in the mth azimuthal mode of the ith velocity component at the cross-stream slice location x is defined using the norm induced from the scalar inner product introduced in eqn (5.20):

$$\hat{\zeta}_i(x, m) := 2\pi E\left\{ \int_{r=0}^{R} |\hat{u}_i(x, r, t; m)|^2 r\mathrm{d}r \right\}. \tag{6.3}$$

This quantity was defined in eqn (5.71) previously to assess SLSE reconstruction fidelity. The energies in the most pertinent azimuthal modes are shown in Figure 6.4. The growth of total energy in this axial range, as well as the distribution of energies in the various azimuthal modes for the different components of velocity in the unforced jet, agree with previous results (Zheng and Glauser, 1990; Jung et al., 2004; Iqbal and Thomas, 2007; Tinney et al., 2008a,b; Kearney-Fischer et al., 2009).

It is observed in Figure 6.4 that when the forcing frequency is near the jet column mode (i.e. with $St_{DF} = 0.3$), all azimuthal modes are energized equitably even though the forcing azimuthal mode is axisymmetric. One consequence of the present discrete actuation method is that the excitation energy itself leaks into azimuthal modes other than the one intended.

(a) Axial component

(b) Radial component

(c) Azimuthal component
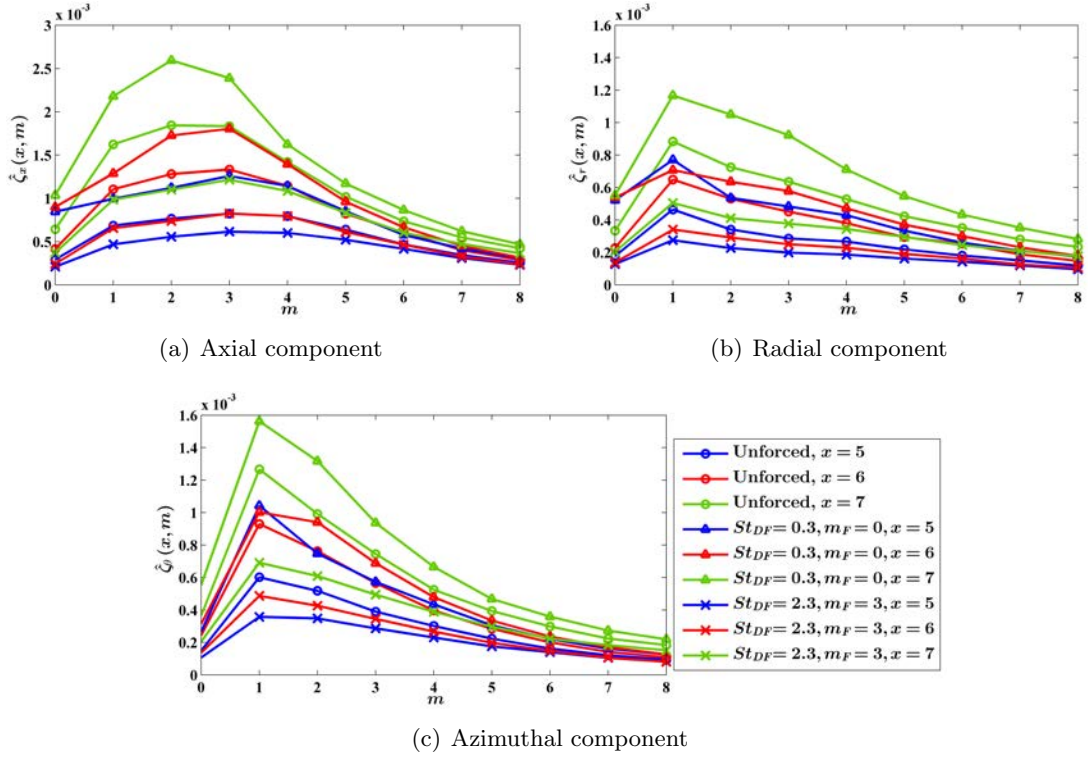
Figure 6.4: Azimuthal modal composition of the three components of the velocity field. The forcing parameters and measurement locations are indicated in the legend. Note that the ordinate scales are disparate.

However, this effect was determined to be small in simple simulations of the rectangular trigger signals that control the LAFPAs. A more probable explanation is the nonlinear amplifying behavior of the jet which couples the energies between different azimuthal modes. Such nonlinearity is also captured by a quadratic interaction term in the reduced-order model described subsequently. For forcing at the much higher Strouhal number $St_{DF} = 2.3$ and $m_F = 3$, the modal energies are found to decrease at all azimuthal modes and at all measurement locations tested. This was expected from the reduction in the turbulent kinetic energy observed previously with these forcing parameters (Kim et al., 2009a). However,

the novel result is that forcing does not significantly affect the *relative* azimuthal modal composition of the velocity field.

One-dimensional slice POD was discussed in Section 5.4 to study the low-dimensional structure of the flow in the radial direction. This is also the preliminary step in obtaining an approximate database of volumetric snapshots of the flow through spectral linear stochastic estimation (see Section 5.5). The focus here is on understanding the change in the low-dimensional structure of the flow with forcing. For this, the relative effectiveness of two different POD bases of the same dimension will be assessed. Consider a subspace S_{unforced} consisting of the first N^1 1-D scalar slice POD eigenfunctions of each of the Fourier azimuthal modes from 0 to M derived from snapshots of the unforced jet database at several cross-stream sections. Consider another subspace S_{self} of the same dimension and derived from snapshots obtained in similar experiments, but for a particular forcing condition. For reconstructing the flow field from the same forcing condition, the 'self' basis S_{self} optimally captures the energy. So, to assess the change in low-dimensional structure of the flow with forcing, the above reconstructed energy will be compared to that obtained by using S_{unforced}.

The instantaneous energy of orthogonal projection of an arbitrary fluctuating velocity field $\mathbf{u}(x, \cdot, \cdot, t)$ onto the 1-D scalar slice POD subspace S at x is related to the corresponding POD modal coefficients using the discussion in Section 5.4:

$$\varepsilon_S(x,t) := ||\mathcal{P}_S\mathbf{u}(x,\cdot,\cdot,t)||^2 = \sum_{i\in\{x,r,\theta\}} \sum_{m=-M}^{M} \sum_{n=1}^{N^1} \left|\hat{\gamma}_i^{(n)}(t;x,m)\right|^2.$$

The total flow energy at axial location x and time instant t is also defined using the norm introduced in Section 5.4:

$$\varepsilon(x,t) := ||\mathbf{u}(x,\cdot,\cdot,t)||^2.$$
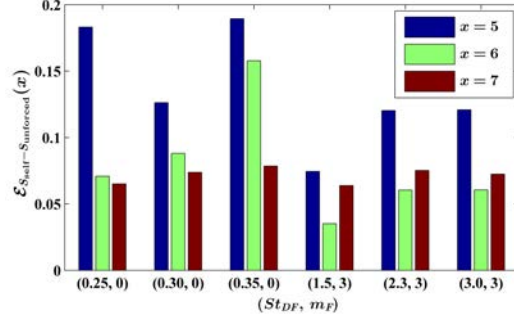
Figure 6.5: Normalized reconstructed energy discrepancy indicating modification of low-dimensional structure of flow under various forcing conditions.

Then, the energetic discrepancy discussed above, normalized by the total flow energy, is defined as

$$\mathcal{E}_{S_{\text{self}}-S_{\text{unforced}}}(x) := \frac{E\left\{\varepsilon_{S_{\text{self}}}(x,t)\right\} - E\left\{\varepsilon_{S_{\text{unforced}}}(x,t)\right\}}{E\left\{\varepsilon(x,t)\right\}}. \tag{6.4}$$

The energetic discrepancy metric is computed with $M = 7$ and $N^1 = 9$. The results are presented in Figure 6.5. One can readily conclude that the POD basis educed from the unforced flow is reasonable for a low-dimensional representation of the forced flows as well. This observation is crucial for justifying the later use of the ROM derived from the unforced jet database as the base for incorporating actuation effects.

6.2.4 Forcing Effects on Reconstruction of Volumetric Snapshots

Volumetric snapshots of the forced flow field are needed to determine the empirical functional basis of the kinematics. In Chapter 5, spectral linear stochastic estimation has been shown to be useful in approximating such snapshots from time-resolved near-field pressure data and pre-computed spectral pressure-velocity cross-correlations.

The effect of forcing on the near-field pressure has been investigated in Section 3.4, but the measurement location was slightly different there. Figure 6.6 depicts the modification
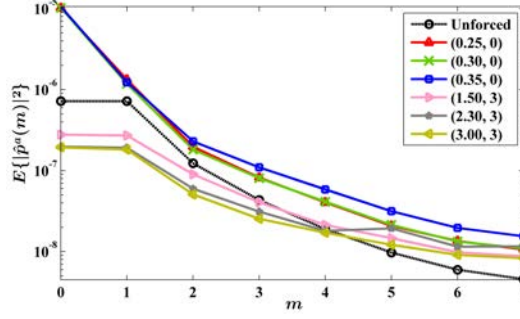
Figure 6.6: Effect of forcing on azimuthal modal composition of the near-field pressure at $x/D = 3$, $r/D = 1.5$. In the legend, the forcing cases are signified by (St_{DF}, m_F).

in measured azimuthal modal energies at different forcing conditions with the present measurement setup. Forcing in the axisymmetric mode with frequencies near the jet column mode is found to preferentially amplify the axisymmetric mode of pressure. Forcing in the third helical mode at much higher frequencies is seen to attenuate the azimuthal modes of pressure that were originally more energetic, resulting in a more equitable distribution of energy. This change in the azimuthal modal composition of the pressure is evidently different from the effect of forcing on the velocity field. This difference implies that the pressure-velocity correlations may be altered by forcing.

The differences in the effect of forcing at $St_{DF} = 0.3$ and $m_F = 0$ on the velocity and pressure fields have been presented in Figures 6.4 and 6.6, respectively. Figure 6.7(a) presents the axial component of velocity fluctuations for a particular measured snapshot under these forcing conditions. Note that even with axisymmetric forcing, no axisymmetric structure can be distinguished at this instant. The SLSE coefficients were determined using the database of 1000 such snapshots with simultaneous pressure measurements. The reconstruction of the same snapshot using the associated pressure record and these estimation coefficients is presented in Figure 6.7(b). Owing to the strong axisymmetry of the

196
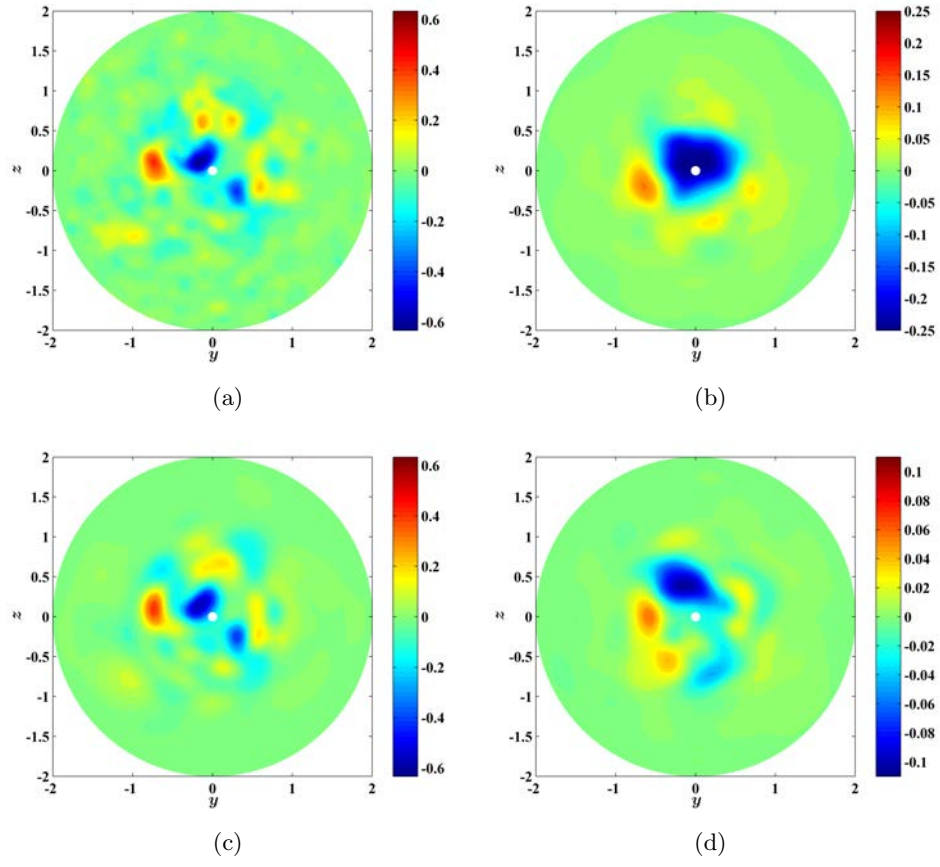
Figure 6.7: Snapshot of the axial velocity fluctuations at $x = 5$ with forcing at $St_{DF} = 0.3$ and $m_F = 0$, obtained from (a) PIV, (b) reconstruction from SLSE of POD modes derived from the same forced dataset, (c) reconstruction from POD modes derived from unforced dataset, and (d) reconstruction from SLSE of the above POD modes. All reconstructions include azimuthal modes 0 through 7, and POD modes 1 through 9. Note the disparity in the color-scales representing u_x/U_j.

	Forcing Case						
Database	Unforced	(0.25, 0)	(0.3, 0)	(0.35, 0)	(1.5, 3)	(2.3, 3)	(3.0, 3)
Self	0.91	0.93	0.98	0.97	0.93	0.93	0.93
Unforced	0.91	0.99	0.99	1.00	1.06	1.14	1.15

Table 6.1: The reconstruction error for SLSE applied to experimental data. The modeling database is either the same forcing case or the unforced case. The particular forcing case is denoted by the pair $(St_{DF}, \; m_F)$.

pressure field (as noted in Figure 6.6), a strongly axisymmetric velocity field is erroneously estimated. The POD eigenfunctions educed from the unforced dataset have also been used to reconstruct the same snapshot in Figure 6.7(c). The appropriateness of this operation was remarked in the discussion regarding Figure 6.5, and can be observed here again. Finally, the SLSE coefficients educed from the unforced dataset have been used in conjunction with the pressure recorded simultaneous with the snapshot under consideration, and the resulting reconstruction is shown in Figure 6.7(d). Although the amplitudes of structures are under-predicted, their shapes are captured much better in comparison to Figure 6.7(b).

The reconstruction error metric $\mathcal{E}_{\mathrm{recon}}$ defined in eqn (5.68) allows a quantitative assessment of the effectiveness of SLSE. It is evaluated for the various forcing conditions considered here and the results are presented in Table 6.1. These were obtained with $\mathcal{X}_u = \{5, 6, 7\}$ and the first 9 POD modes were retained for each of the azimuthal modes from 0 to 7. The reconstruction of the unforced database was discussed in Section 5.9.6, and is repeated here for comparison. Considering the first row of the table, the reconstruction errors are seen to be quite large. Experimental uncertainty in computing the stochastic estimation coefficients was cited as a possible reason for this poor fidelity in Section 5.9.6. Considering the second row of the table, it is apparent that the SLSE coefficients educed from the

unforced database is leading to greater errors in reconstructing the velocity fields in the forced cases. The discrepancy is less at the lower forcing frequencies near the jet column mode. In fact, it is negligible for the forcing case of $St_{DF} = 0.3$, $m_F = 0$ considered in Figure 6.7, reinforcing the conclusions drawn thereof. However, the discrepancy increases at the higher forcing frequencies. Previous research has established that forcing the jet with LAFPAs at these high forcing Strouhal numbers and higher helical modes results in smaller structures, and hence a higher-dimensionality of kinematics (Kastner et al., 2009b; Kim et al., 2009a; Samimy et al., 2010). On the other hand, the near-field pressure signature filters out the effect of the smaller scales (George et al., 1984). Such disparity in behavior of the pressure and velocity fields may explain the inaccuracies in reconstruction of the jet forced with higher forcing Strouhal numbers and $m_F = 3$ using SLSE coefficients derived from the unforced jet. In the remaining chapter, the focus will remain on forcing cases around the jet column mode.

6.2.5 Modeling Drift Vector Field for Forcing Near the Jet Column Mode

The particular characteristics of the LAFPAs, as well as the experimental database at hand, leave only two options for modeling the drift vector field. The first route is to directly use the drift vector field determined from the unforced database; this has been investigated in Section 5.9.6. Otherwise, one may employ the technique of merging empirical databases from various forcing cases, as discussed in the introduction. The latter option will be evaluated here.

The results presented in Table 6.1 support the use of the spectral linear stochastic estimation coefficients derived from the unforced jet to approximate volumetric snapshots of the jet forced near the column mode. In Section 6.2.2, it was shown that the mean flow field changes significantly with forcing near the jet column mode. The parameter set of

$St_{DF} = 0.3$ and $m_F = 0$ represents the typical forcing case in this regime, and its mean flow is chosen as the base flow for POD. Before appending to the merged database, the snapshots from the different forcing cases (as well as from the unforced case) must be modified such that they represent deviations from this base flow instead of from their respective mean flows. Note that this step automatically incorporates into the database the mean field differences displayed in Figures 6.2(a) and 6.3.

An energy-based scaling transformation was proposed in Section 5.9.6 for the approximate database of the unforced jet to address the large difference in energies of the SLSE-reconstruction velocity field and the 3C-PIV measured field. With this technique, the energies in the two fields were equalized individually in each azimuthal mode at all axial stations and in every velocity component. The SLSE coefficients determined in Section 5.9.6 are re-used here, so that the same scale factors are applied to the reconstructions of the snapshots of the forced jet too.

The number of independent snapshots to use from each forcing case in the merged database is a critical question. Since POD performs an energy-based ranking of flow features, incorporating more snapshots from a particular forcing case would skew the POD mode ranking towards structures that are more prevalent with this forcing. Unfortunately, there is no empirical guide to this choice. Hence, the database is created from equal number of uncorrelated snapshots (350 each) reconstructed for the four cases — unforced, and forcing with St_{DF} of 0.25, 0.3, and 0.35. The forcing is always axisymmetric.

Figure 6.8 displays the POD eigenspectrum of this merged database. Comparison with the corresponding plot for the unforced jet database in Figure 5.42(b) reveals several differences. The major difference is the relatively higher energy in $m = 0$ due to forcing at this azimuthal mode. Within $m = 0$, the POD modal eigenspectrum in Figure 6.8 also depicts
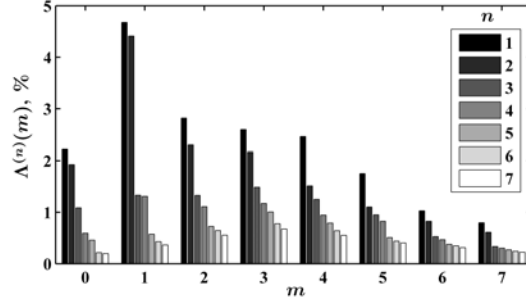
Figure 6.8: Eigenspectrum from volumetric POD performed on the merged database for various forcing cases near the jet column mode, as well as the unforced case.
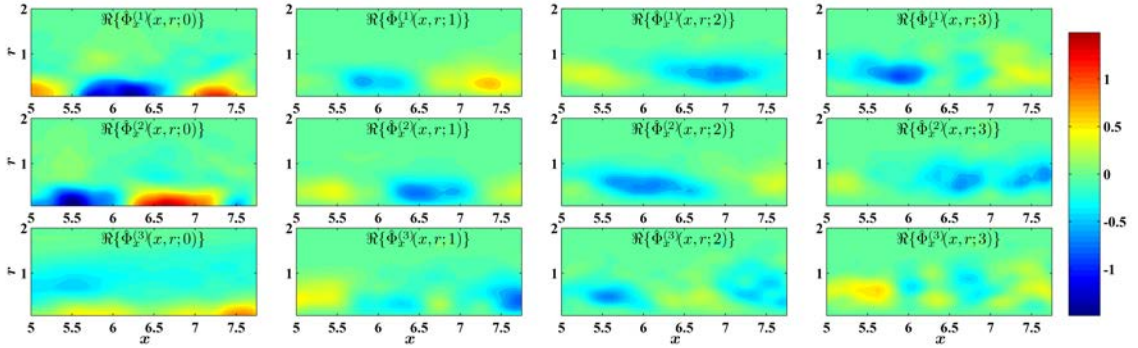
Figure 6.9: Axial components of first few eigenfunctions from the volumetric POD performed on the merged database for various forcing cases near the jet column mode, as well as the unforced case.

a clear separation of energies between the first 3 POD modes and all the remaining. In $m = 1$, the pairing of the first two POD modes is observed again, indicating a potential traveling wave structure. Unlike the spectrum for the unforced database in Figure 5.42(b), all the azimuthal modes from 1 to 4 display high and comparable energy. Note that the same energy scaling transformation is applied as in the unforced jet, so that this broader azimuthal modal spectrum is indicative of the actual behavior in the merged database.

(a) Initial condition from unforced case   (b) Initial condition from $St_{DF} = 0.3$
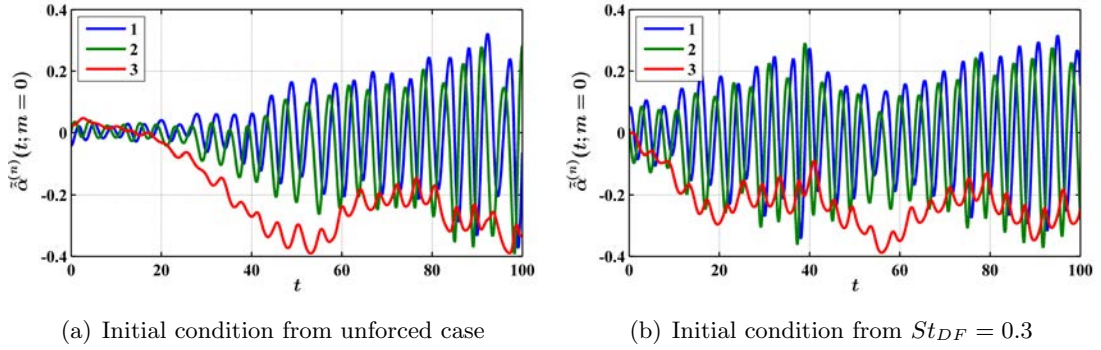
Figure 6.10: Trajectories of the first 3 POD modes in $m = 0$ from simulations of the 35-D ROM derived from the merged database starting.

The axial components of the first few POD eigenfunctions are depicted in Figure 6.9. The first 2 POD eigenfunctions in $m = 0$ are similar to those observed for the unforced jet in Figure 5.43. This pair represents the natural traveling wave pattern in the jet corresponding to the jet column mode. Forcing around this frequency amplifies these structures thereby causing their relative energy to increase (see Figure 6.8) while keeping the shape unchanged. The third POD eigenfunction in $m = 0$ represents the part of the shift mode discussed above that is orthonormal to the first two eigenfunctions. The POD eigenfunctions in the higher azimuthal modes are quite similar in the merged and unforced databases.

The drift vector field can be derived from the eigenfunction basis of the merged database using the Galerkin projection discussed in Chapter 5. A full evaluation of the suitability of the resulting ROM for modeling the dynamics of the forced jet must await the design of the input vector field pursued in the next section. Here, the 35-D unforced model (just the drift vector field) is simulated with several different initial conditions. Very similar behavior was observed for many different initial conditions from the unforced jet, and for

several different model dimensions. The results from two representative initial conditions are shown in Figure 6.10.

Figure 6.10(a) presents the trajectories of the first 3 POD modes in $m = 0$ starting from an initial condition corresponding to the unforced jet. The initial energy in these modes is low, but by about 50 flow time steps there has been an order of magnitude increase in the amplitude of oscillations. The first and second POD modes indeed oscillate approximately $90°$ out-of-phase representing a traveling wave. The third mode has the expected behavior of a shift mode (Noack et al., 2008); it has a slowly modulated mean value with smaller fluctuations superimposed. Such oscillations were typically found to persist for at least 400 flow times steps starting from many initial conditions, before the trajectories became unbounded. However, this is not the expected behavior in the unforced jet, which should not display any correlated oscillations. Moreover, the energy of simulations is quite different from the energy of the projected modal coefficients from the unforced jet.

Figure 6.10(b) presents the results of simulation from an initial condition chosen from the SLSE-reconstructed database of forcing at $St_{DF} = 0.3$ and $m_F = 0$. The initial energy in the first 2 POD modes in $m = 0$ is higher than in the unforced case, and saturation is reached earlier. But the character of the oscillations are quite identical to those observed in the unforced jet simulations, both in terms of amplitude and frequency. Very similar mode trajectories were obtained when the initial conditions were chosen from the two other forcing cases included in the merged database, viz. $St_{DF} = 0.25$ and $St_{DF} = 0.35$.

It must be re-iterated that these simulations are without periodic forcing, so that the observed periodic oscillations are not physical. The reason for this behavior is postulated here. The snapshots included in the merged database displayed strong oscillations, which were captured well in the POD basis (see Figures 6.8 and 6.9). Compared to the functional

basis investigated for the unforced jet in Section 5.9.6, the other distinctive feature of the basis from the merged database is the presence of the shift mode. One of the ways of modeling the dynamics of the shift mode has been laid out in the theory of finite time thermodynamics (Noack et al., 2008). There, the mean-field deformation represented by the slow dynamics of the shift mode have been directly linked in a feedback mechanism to the dissipative Reynolds stresses associated with the neglected scales. The spectral linear stochastic estimation involved in approximating the snapshots in the database can only reconstruct the largest scales with reliability. This suggests a possible cause for the unphysical limit cycle behavior of the shift mode in Figure 6.10. Thus, for the purposes of Galerkin projection, the merging of databases prior to POD that necessarily incorporates shift modes into the eigenfunction basis, is incompatible with SLSE reconstruction of the individual databases.

As reported in Section 5.9.6, the ROM (i.e. the drift vector field) derived from the SLSE-reconstructed database of the unforced jet is able to predict the dynamics in both the short and intermediate terms. For the remainder of this chapter, this drift vector field will be adopted exclusively for the forced jet too, and the idea of merging databases will be abandoned.

6.3   Modeling the Actuated Part of the Dynamics of a Forced Jet

In the jet under consideration, the modeling domain chosen is downstream of the actuator location (see Figure 6.11). So the actuation is neither a body force nor a boundary force term that can be prescribed directly. In fact, the effect of actuation is modulated by the intervening axial length of the mixing layer of the jet before reaching the model domain through convection. The dynamical reduced-order model has been discussed in Chapter 5,
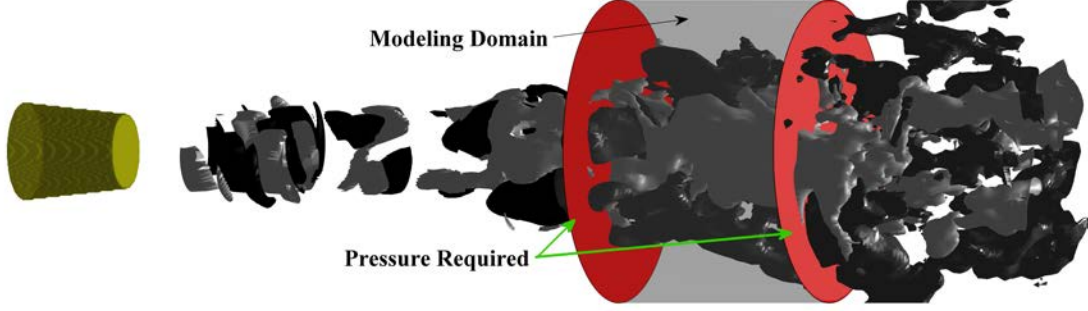
Figure 6.11: Schematic of jet modeling domain indicating regions where the pressure is to be specified.

and it is reproduced below for convenience of discussion:

$$
\begin{aligned}
\dot{\hat{\alpha}}^{(n)}(t;m) = {} & \delta_{m,0} c_{\mathrm{G}}(n) + \sum_{n'=1}^{N_m} l_{\mathrm{G}}(n,n',m)\hat{\alpha}^{(n')}(t;m) \\
& + \sum_{m'=m-M}^{M} \sum_{n'=1}^{N_{m'}} \sum_{n'=1}^{N_{m-m'}} q_{\mathrm{G}}(n,n',n'',m,m')\hat{\alpha}^{(n')}(t;m')\hat{\alpha}^{(n'')}(t;m-m') \\
& \underbrace{-2\pi \left| \int_0^R \hat{p}(x,r,t;m)\hat{\Phi}_x^{(n)*}(x,r;m) r \mathrm{d}r \right|_{x=X_1}^{X_2}}_{\text{Input vector field}}.
\end{aligned}
\tag{6.5}
$$

Careful inspection of the model reveals that the only entry point of actuation effects is the pressure term. The schlieren image in Figure 2.3(b) demonstrated the generation of compression waves with each actuation pulse. Thus, it is proposed to model the input vector field by specifying the pressure field at all times at the inflow and outflow boundaries of the modeled domain (see Figure 6.11).

The periodicity of the pressure field is identical to the forcing period. However, beyond this fact, not much can be specified regarding the pressure fluctuations from first principles. In particular, the amplitude and radial shape of the compression waves need to be determined. Also, the phase relation between the actuator firing at the nozzle exit and

(4) (3) (2) (1)

Entrainment
region

$+u_x$ $-u_r$ $-u_x$ $+u_r$

$-p$ $+p$ $-p$

Mixing
region

Pattern
convected

$-p$ $+p$ $-p$

Potential
core

$-u_x$ $-u_r$ $+u_x$ $+u_r$
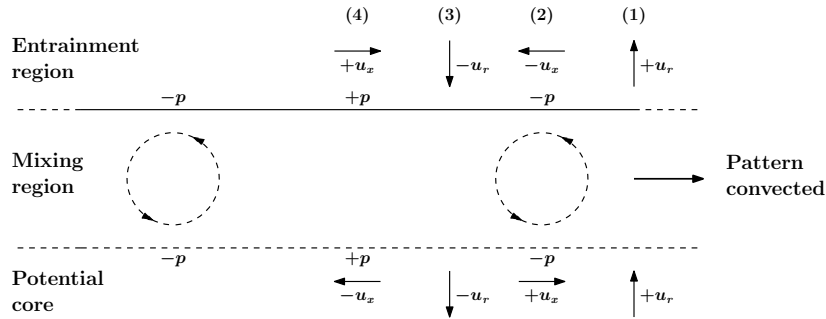
Figure 6.12: Vortex model of pressure-velocity relationship in a jet adapted from Lau et al. (1972).

the pressure fluctuations at the model boundaries remains to be characterized. Such information is not readily available from experiments. However, from experiments, one has knowledge of the fluctuating velocity field over forcing cycles. To utilize this information in determining the pressure field, the vortex model proposed by Lau et al. (Lau et al., 1972; Lau and Fisher, 1975) will be invoked in the following development. The ILES database of the forced jet introduced in Section 2.5.2 will also be used in this effort.

6.3.1 Vortex model of Lau et al.

The pressure field in an incompressible flow is related to the *global* velocity field through Poisson's equation. However, the solution of this equation requires precise knowledge of the boundary conditions, which is not available for experimental data.

Lau et al. (Lau et al., 1972) proposed a very simple, elegant and intuitive relation between the *local* pressure and velocity fields in the jet. Figure 6.12 is adapted from their work and explains the original vortex model succinctly; a brief description follows. The mixing layer of the jet is supposed to consist of large-scale coherent structures convecting downstream. The original vortex model addressed the core and entrainment regions only

(see Figure 6.12). Consider an observer at station (1) relative to the vortex street. The radial velocity fluctuations are positive in both the core and entrainment regions whereas the pressure and axial velocity fluctuations should vanish. Thus, the latter quantities are in quadrature with the radial velocity. When the observer is at station (2), the radial component should vanish at both the core and entrainment regions, whereas the pressure fluctuations should reach its most negative value in both regions. The axial velocity fluctuations would be positive in the core and negative in the entrainment region. Thus pressure and axial velocity fluctuations are in phase in the entrainment region, whereas they are in anti-phase in the potential core. On the other hand, pressure fluctuations are in quadrature with and lead the radial velocity fluctuations in both regions. The axial and radial velocity fluctuations are in quadrature in both regions, with the former lagging the latter in the core and leading in the entrainment region. The phase of the velocity fluctuations with respect to the actuation pulses are known from 3C-PIV data acquired simultaneous with the actuation signal, as discussed in the context of Figure 6.1(a). The vortex model supplies the crucial phase relation between pressure and velocity fluctuations in the jet, for the eventual modeling of the input vector field.

Lau et al. (1972) noted that this simple model predicts that there should be no Reynolds stresses in the mixing region, contrary to experimental findings. Subsequently, Lau and Fisher (1975) proposed a refinement of the earlier model, wherein viscosity was implicitly invoked to argue for a non-linear interaction that leads to a positive Reynolds stress in the mixing layer.

The validating experimental results presented in Lau et al. (1972) were obtained with a 2 inch nozzle run at Reynolds numbers between 1×10^5 and 3×10^5 (speeds ranged from 31 to 92 m/s). The first question to be answered here is whether this simple model can be
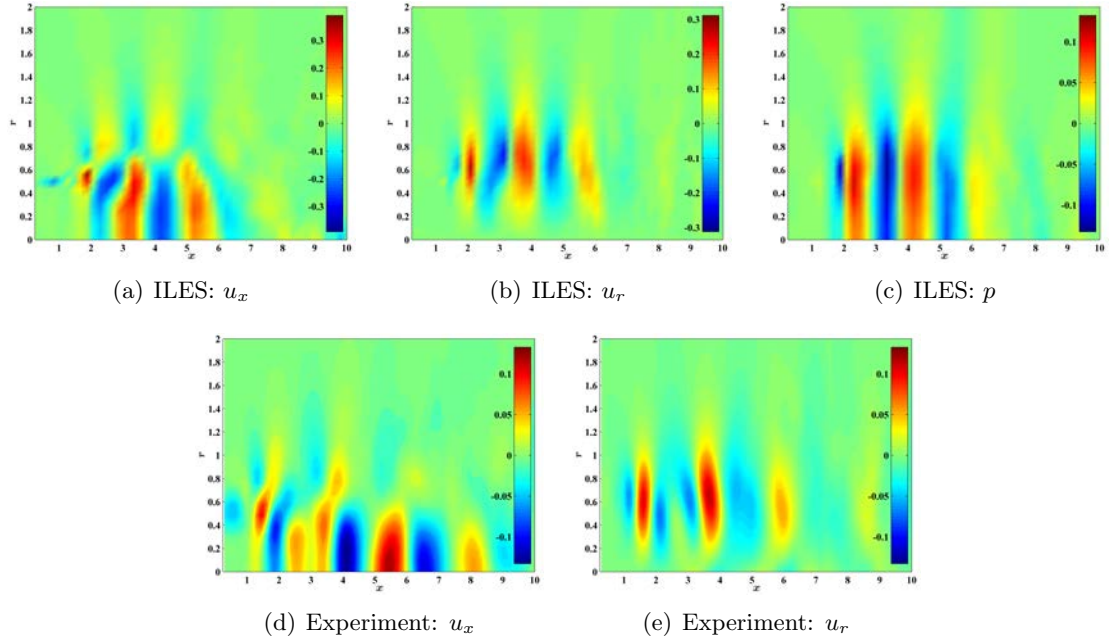
Figure 6.13: Phase-averaged contours of pressure and velocity fluctuations from two databases for $m_F = 0$ and $St_{DF} = 0.3$. Note the disparity in the color-scales.

useful at higher speeds. To this end, the temporal correlations of pressure and velocity are investigated for the ILES database of the forced jet (Mach 1.3 and $Re = 1.1 \times 10^6$). The end goal is to extend the results to an experimental database of Mach 0.9 and $Re = 0.67 \times 10^6$ for which only velocity data exists.

To focus attention on the relevant statistics, it is pertinent to first discuss the similarity of the ILES results with open-loop forcing experiments. Forcing the jet in the axisymmetric mode with frequency near the column mode has been found to produce very robust and organized structures. Figure 6.13 shows the available phase-averaged fields with $m_F = 0$ and $St_{DF} = 0.3$ from both the ILES database and 2C-PIV experiments, invoking the triple decomposition introduced in eqn (6.2). The first focus is on the axial velocity fluctuations from the ILES and experimental databases in Figures 6.13(a) and 6.13(d). Several remarks

are in order: (*a*) The amplitude of the fluctuations in the ILES database are about thrice those obtained from experiments. Recall that these are normalized by the jet exit velocity. (*b*) The shapes of the structures are similar over the axial domain up to $x \approx 5.5$. The similarities include the extents, geometries, and relative strengths of the structures. The induced velocity field is also seen to affect the potential core similarly. (*c*) Further downstream, there is a very quick drop in the strength of the structures from the ILES database. However, the experimental database shows large and strong structures spanning the jet centerline up to $x \approx 8.5$.

The remarks made for the axial velocity fluctuations hold for the radial velocity fluctuations in the most part (see Figures 6.13(b) and 6.13(e)). There is a similar discrepancy in the amplitude of the fluctuations. The upstream structures display similarities, but there are some discrepancies in the structures spacing and relative shapes and sizes. However, the characteristics at $x = 5$ are rather similar. Moreover, the drop off in structure strength further downstream is similar in the two databases for the radial component of velocity.

The phase-locked pressure fluctuations from the ILES database are presented in Figure 6.13(c). Recall that for the purpose of ROM development, the interest is in the radial distribution of pressure at $x = 5$ and $x = 8$, the inflow and outflow boundaries of the domain spanning the end of the potential core. Pressure fluctuations are negligible at the outflow boundary. This is of immediate practical importance since one can safely ignore the anomalies in the correlations in the ILES database that appeared at downstream stations, as discussed above. At the inflow boundary, the pressure fluctuations are strong, and appear as plane wavefronts covering the radial domain from the centerline to about one jet diameter. Further out radially, the wavefronts still appear flat, but the amplitude is diminished. This is the behavior that one wants to replicate for an approximate pressure

209

field for the experimental database. The foregoing discussion serves as the background for the following considerations of the correlations pertaining to the vortex model.

The tool to study the pressure-velocity relationship is the single-point normalized temporal cross-correlation. The single-point temporal cross-correlation between the fluctuations of any two flow variables α and β is defined as

$$\Pi_{\alpha\beta}(x, r, t') := E\left\{\frac{1}{2\pi} \int_{-\pi}^{\pi} \alpha(x, r, \theta, t + t')\beta(x, r, \theta, t)\mathrm{d}\theta\right\}, \qquad (6.6)$$

wherein the axisymmetry and stationarity of the jet are implicitly invoked. The corresponding normalized quantity is

$$\mathcal{C}_{\alpha\beta}(x, r, t') := \frac{\Pi_{\alpha\beta}(x, r, t')}{\{\Pi_{\alpha\alpha}(x, r, 0)\Pi_{\beta\beta}(x, r, 0)\}^{1/2}}. \qquad (6.7)$$

For proper comparison of results, the radial coordinate must be converted to the radial similarity variable (see Fleury et al. (2008) and references therein):

$$\eta(x, r) := \frac{r - r_{1/2}(x)}{\delta_\theta(x)}, \qquad (6.8)$$

where $r_{1/2}$ is the jet half-width at half-maximum mean axial velocity $\overline{U}_x(x, r = 0)$ and δ_θ is the shear layer momentum thickness, both evaluated at a particular axial station x. Additionally, the time separation variable, t', will be normalized by the local flow time scale to obtain

$$\tau(x) := \frac{t'\overline{U}_x(x, r = 0)}{\delta_\theta(x)}. \qquad (6.9)$$

Figure 6.14 shows the temporal velocity-pressure correlations at $x = 5$ in the ILES database for the case of forcing with $m_F = 0$ and $St_{DF} = 0.3$. Although the vortex model of Lau et al. (Lau et al., 1972; Lau and Fisher, 1975) was validated for an unforced jet, the results presented here show that the model can explain the behavior of this forced high Reynolds number jet remarkably well. The predicted phase relations as well as the

(a) $\mathcal{C}_{u_x u_r}(x, \eta, \tau)$ (b) $\mathcal{C}_{u_x p}(x, \eta, \tau)$ (c) $\mathcal{C}_{u_r p}(x, \eta, \tau)$
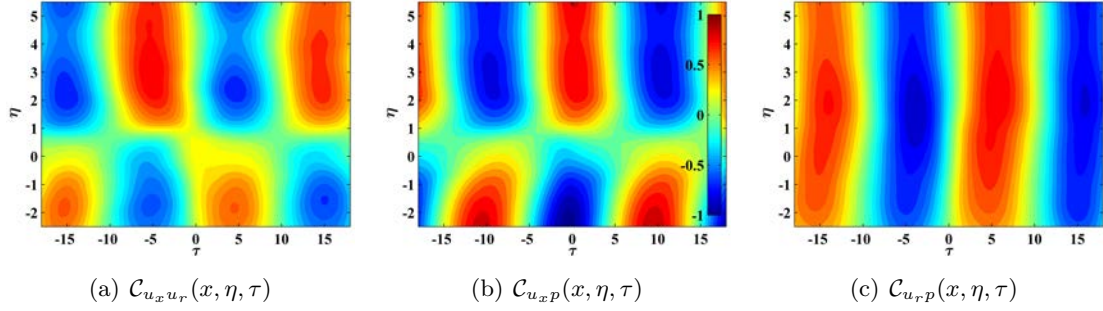
Figure 6.14: Contours of velocity-pressure correlations at $x = 5$ from the ILES database for forcing with $m_F = 0$ and $St_{DF} = 0.3$. The common color-scale is shown in the middle figure.

radial variations of the correlations follow the vortex model closely. The periodicity of the correlations are the result of the creation of robust repetitive structures due to the forcing. Figure 6.13 indicated that at this axial station coherent fluctuations span the potential core, and the core-type behavior is seen in the correlations here over a significant radial extent too. This is signaled by the anti-correlation of axial velocity with pressure, as explained in Figure 6.12. Schlieren images in experiments of this forcing case have confirmed the existence of such strong ring-like structures in the mixing layer that induce corresponding coherence in the potential core (Kearney-Fischer et al., 2011a).

6.3.2   Predicting the model inflow pressure in experiments

The success of the vortex model documented above prompts the following modeling of the inflow pressure for the ROM of experimental data. Essentially, the velocity fluctuation levels and phase in the experiments will be used to predict the pressure fluctuations at the inflow boundary of the ROM by exploiting the velocity-pressure relation observed in the ILES database.

For experimental data, axial-to-radial velocity correlations with varying time-separations are not directly possible at present since time-resolved PIV is unfeasible at the flow time scales and domain sizes of interest. While this is strictly true for the unforced jet, an approximation may be made for the case of the forced jet. The forcing signal provides a readily identifiable phase relation in the data. The steps for obtaining the correlations of interest is described next.

1. Recall that the open-loop forcing experiments are performed at a fixed frequency and azimuthal mode. Three-component PIV data are acquired on cross-stream slices (3 slices in as many separate runs) at ~ 2 Hz, which makes the consecutive snapshots uncorrelated. However, the phase of actuation is also acquired simultaneous with the PIV snapshots.

2. The sequence of snapshots are sorted in ascending order of their respective actuation phase. Next, the critical assumption is made that the structure organization due to forcing renders this sequence of snapshots into an approximation for a time-resolved velocity field.

3. The above sequence is linearly interpolated onto a uniform phase space covering one forcing period. Three repetitions of the sequence are concatenated to exploit its periodicity in increasing the statistical significance of the ensuing correlation. This is the required approximation of the time-resolved three-component velocity field at a particular axial location, for all radial and azimuthal coordinates.

4. It is assumed that the azimuthal Fourier mode of velocities corresponding to the forcing azimuthal mode are organized, so that this low-dimensional velocity field (at an arbitrary but fixed reference azimuthal angle) is extracted for each field.

(a) $x = 5$ (b) $x = 6$ (c) $x = 7$
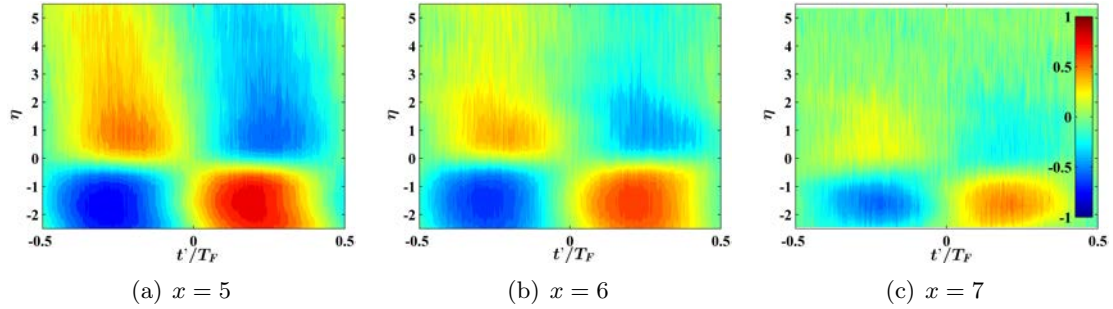
Figure 6.15: Contours of $\mathcal{C}_{u_x u_r}(x, \eta, \tau)$ from experiments with forcing at $m_F = 0$ and $St_{DF} = 0.3$.

5. The final correlation step implements the formula presented earlier, with the omission of the integration over the azimuthal domain. The determination of the Fourier azimuthal mode of the velocity corresponding to the forcing azimuthal mode has already incorporated this integration implicitly.

The open-loop experimental data for the forcing case of $m_F = 0$ and $St_{DF} = 0.3$ is investigated with the technique detailed above. The non-dimensionalized forcing period T_F is the reciprocal of St_{DF}. The results at three cross-stream slices in the axial domain of interest are presented in Figure 6.15. Comparison of Figure 6.15(a) with the corresponding results from the ILES database in Figure 6.14(a) reveals remarkable similarity in all aspects, including the strength and phase relations of correlations as well as the radial variation. This attests to the usefulness of forcing with LAFPA for educing time-resolved statistics in high-speed jets.

On further study of Figure 6.15, one notices very similar shapes of the correlation contours and phase relations, but a decrease of correlation levels in moving downstream. Also, there is a slight shift in the radial location of the changeover from lag to lead of the axial velocity fluctuations vis-a-vis the radial counterpart. The potential core ends at

213

$x \approx 5D$ for this forcing case (Kearney-Fischer et al., 2009). However, the core-like behavior is seen to persist up to $x = 7$ at the least. This has also been indicated by the phase-locked velocity fluctuations presented in Figures 6.13(d) and 6.13(e). The shift in the η of the changeover may be partially explained by the fact that the radial similarity variable does not account for the collapse of the potential core. However, the overall agreement of the velocity correlations obtained from the experimental and ILES databases with the vortex model of Lau et al. motivates the following modeling of the requisite pressure field.

The vortex model relates the approximate pressure, $\tilde{p}$, to the two-component velocity field at each point in the flow individually without assuming any spatial filtering:

$$\tilde{p}(x,r,\theta,t) = \frac{1}{T_1 + T_2} \int_{-T_1}^{T_2} L_x^*(\tau; x, r) u_x(x, r, \theta, t + \tau) \mathrm{d}\tau$$
$$+ \frac{1}{T_3 + T_4} \int_{-T_3}^{T_4} L_r^*(\tau; x, r) u_r(x, r, \theta, t + \tau) \mathrm{d}\tau. \qquad (6.10)$$

This basically means that the pressure at any time t at a particular location is approximately determined by the behavior of the axial and radial velocities at that point over a window of time spanning t. The time constants T_1, T_2, T_3 and T_4 are left unspecified for now. The axisymmetry assumption removes the dependency of the model coefficients L_x and L_r on the azimuthal coordinate. It is expected that the model coefficients should vanish at large $|\tau|$. The asterisk refers to the complex conjugate, which is superfluous for the real quantities in the above expression, but are important in the following development.

The present objective is to predict the pressure in a forced jet. The following modifications are made to the above model for application to the problem at hand.

- The real-time velocity field information is required by the above model for predicting the pressure. This is not directly available. One could use the near-field pressure measurements to estimate this. However, such a strategy would make the control

214

term somewhat self-referential. Instead, one needs to know the control term directly as a function of the actuation parameters, viz. frequency and phase. This means that the pressure approximated from the above model must be periodic, which in turn implies that one must extract the periodic part of the velocity field required by the model. This also means that the limits of time integration in eqn (6.10) may be set as $T_1 = T_2 = 0$ and $T_3 = T_4 = T_F$.

- The jet is forced at a particular azimuthal mode during any given run. It is assumed that the pressure field in the forced jet is also organized so that it can be fully represented by the same azimuthal mode. The linearity of the above model means that one needs to consider only the velocity field in the forced azimuthal mode. The azimuthal organization of the pressure field has been confirmed in experiments with schlieren imaging (Hahn et al., 2011) as well as in large-eddy simulations (Gaitonde, 2011).

- The radial coordinate will be normalized as in eqn (6.8) so that the results from the numerical simulations may be carried over to predict the pressure field in experiments.

The resulting model is

$$\tilde{\hat{p}}(x, \eta, t; m_F) = \frac{1}{T_F} \int_0^{T_F} L_x^*(\tau; x, \eta) \hat{u}_x(x, \eta, t + \tau; m_F) \mathrm{d}\tau$$

$$+ \frac{1}{T_F} \int_0^{T_F} L_r^*(\tau; x, \eta) \hat{u}_r(x, \eta, t + \tau; m_F) \mathrm{d}\tau. \qquad (6.11)$$

Consider the forcing of the jet using plasma actuators with time period T_F. The temporal direction is rendered approximately periodic by this forcing, so that any generic flow variable $w(t)$ may lend itself to the temporal Fourier transform denoted by $w(t) \overset{\mathcal{F}_f}{\mapsto} \breve{w}(k/T_F)$; $\breve{w}(k/T_F) := (1/T_F) \int_0^{T_F} w(t) \mathrm{e}^{-2\pi \mathrm{i} k t/T_F} \mathrm{d}t$. Here k is the frequency mode. The inverse Fourier transform will be denoted by $\breve{w}(k/T_F) \overset{\mathcal{F}_t}{\mapsto} w(t)$; $w(t) = \sum_{k=-\infty}^{\infty} \breve{w}(k/T_F) \mathrm{e}^{2\pi \mathrm{i} k t/T_F}$.

To exploit the periodicity in the flow, one takes the temporal Fourier transform of the pressure prediction model in eqn (6.11) to obtain for any k

$$\check{\tilde{p}}\left(x, \eta; m_F, \frac{k}{T_F}\right) = \check{L}_x^*\left(x, \eta, \frac{k}{T_F}\right) \check{\tilde{u}}_x\left(x, \eta; m_F, \frac{k}{T_F}\right) + \check{L}_r^*\left(x, \eta, \frac{k}{T_F}\right) \check{\tilde{u}}_r\left(x, \eta; m_F, \frac{k}{T_F}\right).$$
(6.12)

The pressure term required in the ROM is then recovered from the above estimate as

$$\hat{p}(x, r, t; m) \approx \delta_{m, m_F} \sum_{k=-K}^{K} \check{\tilde{p}}\left(x, r; m_F, \frac{k}{T_F}\right) \mathrm{e}^{2\pi \mathrm{i} k t / T_F},$$
(6.13)

where, K is the highest multiple of the fundamental forcing frequency retained through the temporal Fourier transform.

The above pressure approximation model is recognized as a straightforward spectral linear stochastic estimation problem (Tinney et al., 2006). The model coefficients are determined from the following set of linear equations involving the spectral correlations obtained from the ILES database

$$\left[\begin{array}{c} \check{L}_x(x, \eta, k/T_F) \\ \check{L}_r(x, \eta, k/T_F) \end{array} \right] = \left[\begin{array}{cc} S_{u_x u_x}(x, \eta, k/T_F) & S_{u_x u_r}(x, \eta, k/T_F) \\ S_{u_r u_x}(x, \eta, k/T_F) & S_{u_r u_r}(x, \eta, k/T_F) \end{array} \right]^{-1} \left[\begin{array}{c} S_{u_x p}(x, \eta, k/T_F) \\ S_{u_r p}(x, \eta, k/T_F) \end{array} \right],$$
(6.14)

where, the spectral cross-correlations have the general definition

$$S_{\alpha\beta}(x, \eta, k/T_F) := \frac{1}{T_F} \int_0^{T_F} \Pi_{\alpha\beta}(x, \eta, t') \mathrm{e}^{-2\pi \mathrm{i} k t' / T_F} \mathrm{d}t',$$
(6.15)

where, the cross-correlation in the physical domain is defined in eqn (6.6).

The strategy for obtaining an approximation of the time-resolved velocity field from experiments in the forced jet has been outlined at the beginning of this sub-section. A temporal Fourier transform is performed on this approximate field to determine its frequency content. The periodic pressure field on the $x = 5$ cross-section in the axisymmetric mode is estimated using the first harmonic $K = 1$ in Figure 6.16(a). Using the second harmonic

(a) Estimation from experiments with $K = 1$

(b) Estimation from experiments with $K = 2$

(c) Directly from ILES database
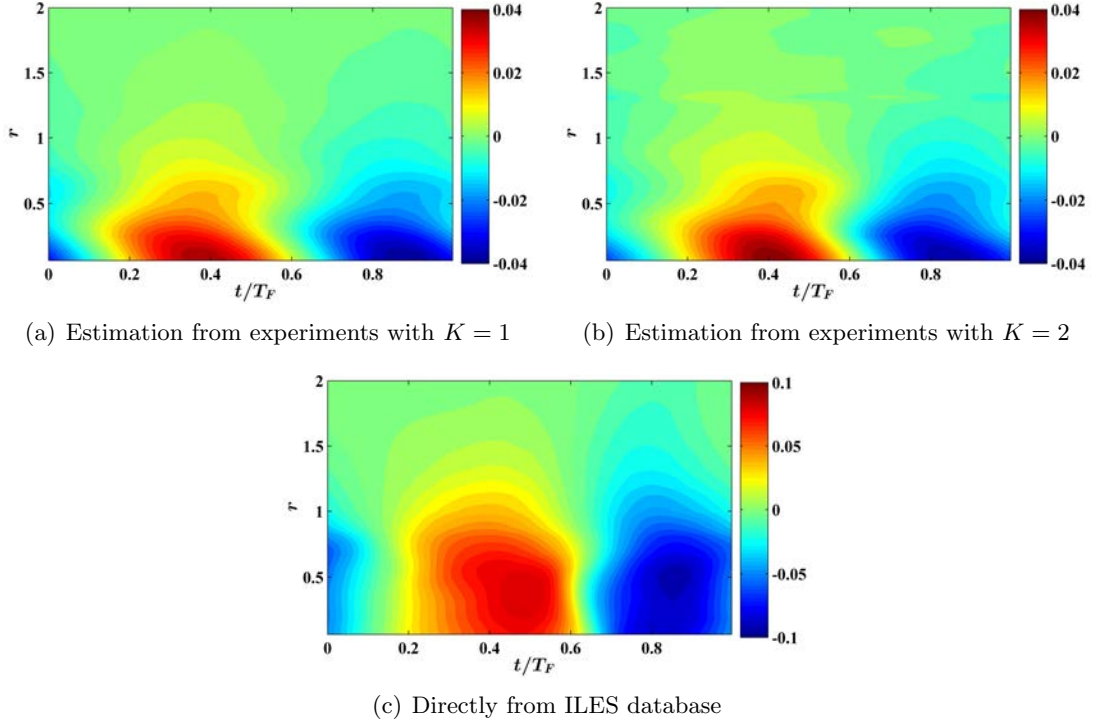
Figure 6.16: Phase variation of axisymmetric mode of pressure fluctuations for forcing with $m_F = 0$ and $St_{DF} = 0.3$ at $x = 5$. Note the disparity in the color-scales.

additionally does not appear to result in any significant change in Figure 6.16(b), so that in the remainder of this work only the first harmonic will be retained. Figure 6.16(c) shows the corresponding pressure field obtained directly from the ILES database for comparison. The phase of pressure fluctuations in this last contour plot should be ignored. The exact radial variation of the predicted pressure fluctuations from experiments is seen to be different from that found in the ILES. This is a consequence of minor differences in the respective velocity fields presented in Figure 6.13. The amplitudes observed in experiments are about 2.5 times smaller than those seen in the ILES database, but this is to be expected from the corresponding differences in the respective velocity fields used for prediction (see Figure 6.13).

(a) Estimation from experiments   (b) Directly from ILES
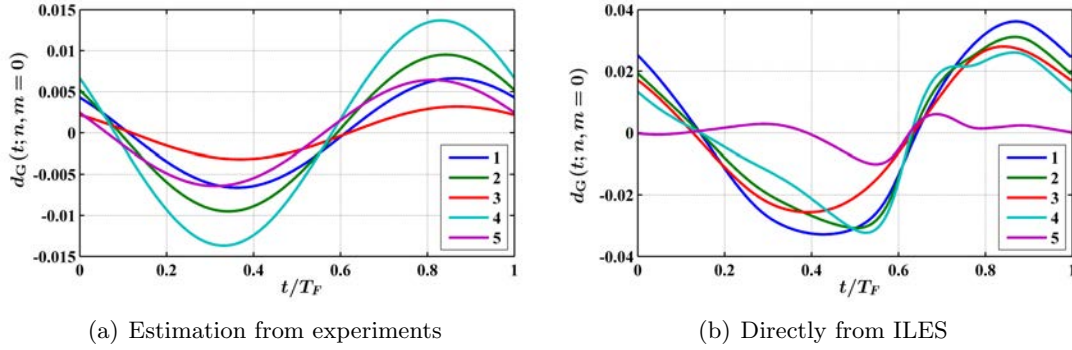
Figure 6.17: Periodic input vector field for forcing the dynamics of the first 5 POD modes in the axisymmetric mode.

With this approximate knowledge of the pressure variations over a forcing cycle, one can readily formulate a periodic form of the pressure term in eqn (6.5). Figure 6.17 shows the periodic input vector fields obtained from the estimated pressure fields in experiments as well as directly from the ILES database. Apart from the scaling of the overall amplitudes by a factor of 2.5, as mentioned above, there are also notable differences in the frequency content as well as the relative amplitudes of the forcing terms for the different modes. The proposed design of the input vector field depicted in Figure 6.17(a) will be evaluated next. In analyzing the results thereof, the possible effects of including the richer frequency content displayed in Figure 6.17(b) would be discussed.

Although the input vector field was estimated for a particular forcing frequency ($St_{DF} = 0.3$) in the axisymmetric mode, it may be valid for a range of the forcing parameters in a neighborhood in the parameter space (i.e. around the jet column mode). Also, since Lau's vortex model describes a *local* relationship between the velocity and pressure fluctuations, the preceding procedure can be readily applied for forcing in non-axisymmetric modes too.

218

6.4 Validating the Model of the Forced Jet

It has been discussed in the introduction to this chapter that the LAFPAs excite jet instabilities through small-amplitude perturbations wherein the most important aspect is the frequency. As such, the short-term simulations of the ROM of the forced jet cannot display the effect of forcing compared to the unforced jet. Moreover, it was mentioned in Section 5.9.6 that the models of the unforced ROM display bounded trajectories till at least 50 flow time steps after initiation of simulation, but the trajectories diverge some time there-after. Thus, the investigation of forcing effects here focuses solely on the intermediate-term statistical measures. To ensure that transients do not skew the statistics, the simulations are run for 30 flow time steps, and the data from the last 10 flow time steps are used in the computations. Converged statistics are obtained by averaging over 20 simulations starting from different initial conditions. Some statistics were obtained with averaging over and ensemble of 30 simulations, but no changes were observed.

The pressure variations that incorporate the effect of forcing in the ROM have been deduced from experimental and ILES data from jets forced at $St_{DF} = 0.3$. Here, the validity of this modeling approach is assessed. In addition, the same pressure distribution is specified at other frequencies near the jet column mode, and the simulation results are investigated to judge the robustness of the actuated model. All numerical experiments are performed with a 35-D ROM derived from experimental data. Extensive numerical simulation results were presented in Section 5.9.6 to demonstrate that this model is quite faithful to the experimental jet in the intermediate term of simulation.

The triple decomposition described in eqn (6.2) is the tool of choice for studying the effect of periodic forcing on the flow. The change in the mean axial velocity contours with forcing will be discussed here. The phase-averaged fields will be presented subsequently.

(a) $St_{DF} = 0.3$ from experiment

(b) $St_{DF} = 0.25$ from simulation

(c) $St_{DF} = 0.3$ from simulation

(d) $St_{DF} = 0.35$ from simulation
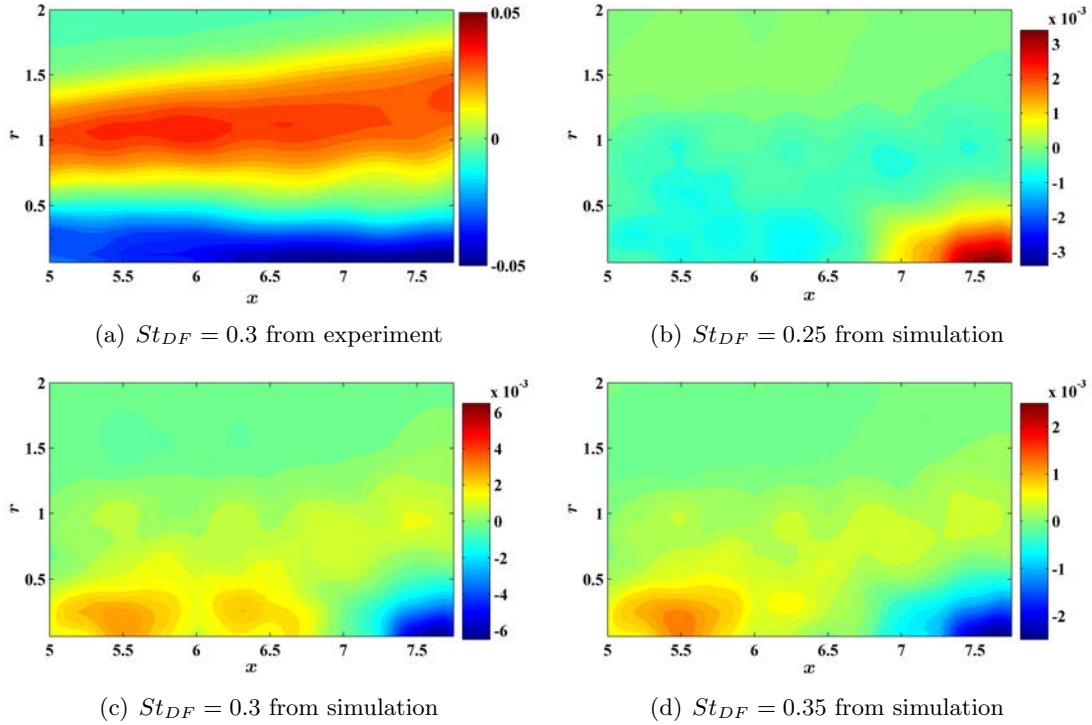
Figure 6.18: Change in mean axial velocity with forcing in $m_F = 0$ from experiments and from the 35-D ROM. Note the disparity in the color-scales.

Figure 6.18(a) depicts the change in the mean value with forcing at $St_{DF} = 0.3$ measured in 2C-PIV experiments. This is a zoomed-in version of Figure 6.2(a) with a new color-scale. The 35-D ROM is forced with three different Strouhal numbers near the jet column mode, and the change in the mean axial velocity compared to the results for the unforced jet simulations (presented in Figure 5.47(c)) are shown in Figures 6.18(b)–6.18(d). The characteristics that are expected from the experimental results are not observed in simulations. The amplitudes of change are an order of magnitude lower, and the profiles appear quite unphysical. Issues in accurate prediction of the mean velocity have been noted for models of the unforced jet derived from the DNS database as well (see Figure 5.13).

(a) $St_{DF} = 0.3$ from experiment

(b) $St_{DF} = 0.2$ from simulation

(c) $St_{DF} = 0.3$ from simulation

(d) $St_{DF} = 0.4$ from simulation
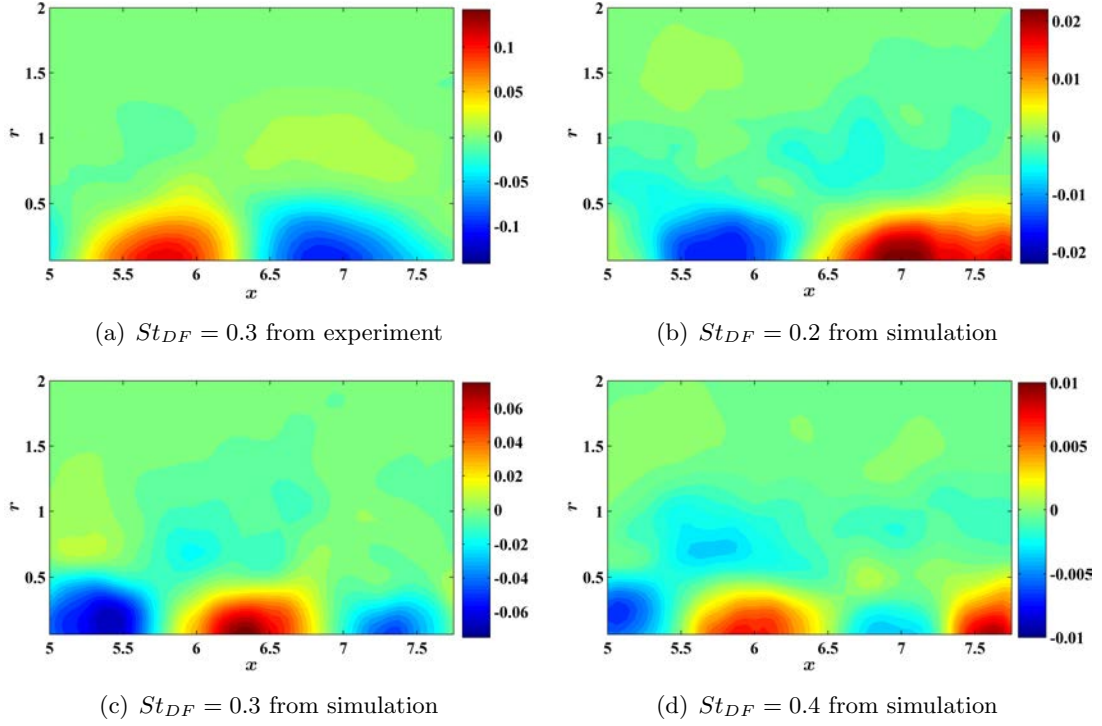
Figure 6.19: Phase-averaged axial velocity with forcing in $m_F = 0$ from experiments and from the 35-D ROM. Note the disparity in the color-scales.

The next consideration is of the phase-averaged axial velocity. Since the focus is on the observable wavelength and wave shape in the phase-averaged velocity profiles, the actual phase is arbitrary. The result from phase-locked 2C-PIV experiments with $St_{DF} = 0.3$ is shown in Figure 6.19(a) for comparison. This is a zoomed-in version of Figure 6.1(b). The corresponding simulation of the 35-D ROM in Figure 6.19(c) demonstrates good similarity, both in the shapes of the undulations as well as in their spacing. The amplitudes from the model simulation are somewhat lower than those observed in experiments. The model was also forced at $St_{DF} = 0.2$ and $St_{DF} = 0.4$, and the resulting phase-averaged axial velocities are presented in Figures 6.19(b) and 6.19(d), respectively. With increasing forcing frequency, the wavelength is expected to decrease linearly since convective velocity

(a) $St_{DF} = 0.3$ from experiment   (b) $St_{DF} = 0.25$ from simulation

(c) $St_{DF} = 0.3$ from simulation   (d) $St_{DF} = 0.35$ from simulation
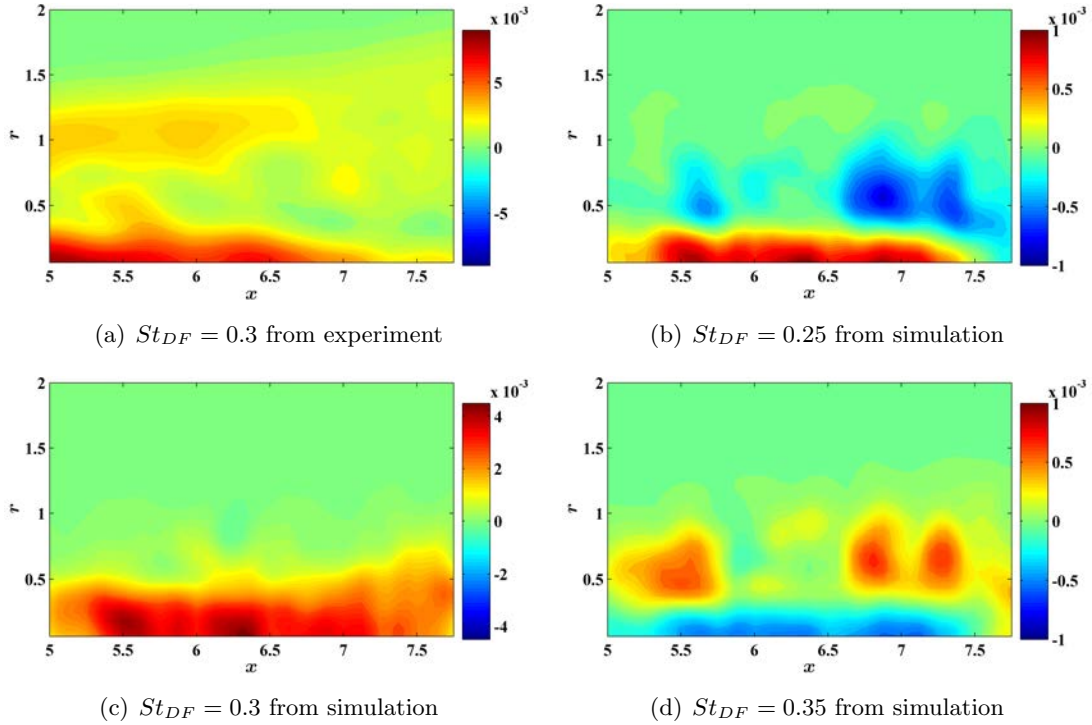
Figure 6.20: Change in mean squared axial velocity with forcing in $m_F = 0$ from experiments and from the 35-D ROM. Note the disparity in the color-scales.

is approximately constant, and this trend is certainly replicated by the model. In fact, the forcing frequencies depicted here were chosen to span a larger range than in Figure 6.18 to highlight this trend. The other pattern that is even more interesting is the change in the amplitudes of the structures with variation in the forcing frequency. With forcing at the side frequencies, the fluctuation levels are much diminished compared to forcing at the center frequency of $St_{DF} = 0.3$. In going from $St_{DF} = 0.2$ to $St_{DF} = 0.3$ to $St_{DF} = 0.4$, the amplitude increases three-fold and then decreases six-fold. The significance of this trend will be discussed subsequently.

The final consideration in the validation is the change in mean square axial velocity fluctuations with forcing. The experimental result with $St_{DF} = 0.3$ is presented in Figure 6.20(a). It shows the increase in fluctuations near the jet centerline that is characteristic of the shortened potential core. The major part of the shear layer itself does not display much change in fluctuation amplitude with this forcing. However, the flaring of the shear layer is indicated by an increase in turbulence in the entrainment region. This result is best replicated by forcing the 35-D ROM at the same frequency (see Figure 6.20(c)). The fluctuation levels are quite comparable. The increase in fluctuation levels is concentrated near the centerline. However, the flaring of the shear layer is not captured by the model simulation. Forcing the model at $St_{DF} = 0.25$ is shown in Figure 6.20(b) to have a much smaller effect. Moreover, there is decrease in turbulence in the downstream part of the shear layer itself. Figure 6.20(d) demonstrates that forcing the model at $St_{DF} = 0.35$ inverts the effect, which is a much more rapid effect than is observed in experiments (Kastner et al., 2009b).

The power spectral density of model simulations has been studied in Chapter 5. Such a study is not possible for the forced jet model. In avoiding the transients, the data from any one simulation is only available over 10 flow time steps, as mentioned at the outset of this section. The spectral resolution with this data will be $St_D = 0.1$ which is too coarse to discern forcing effects.

Considering all the results presented in this section, one can conclude that the jet forced with LAFPAs is modeled reasonably well by the proposed compression-wave-based concept. The behavior of the 35-D model when forced with $St_{DF} = 0.3$ is quite close to those observed in experiments. Note that this is in spite of the fact that the drift vector field is obtained from a database of the unforced jet. The behavior of the simulated model at the side forcing

223

frequencies of $St_{DF} = 0.25$ and $St_{DF} = 0.35$ are not as accurately modeled. The phase-averaged velocity fields show the correct structures. But the mean square axial velocity fluctuation patterns change very sharply with forcing frequency. This is a crucial nonlinear response of the jet to forcing near the column mode, but the model appears to be more sensitive than the actual jet. A sharp maximum has also been observed in near-field pressure fluctuations presented in Figure 3.6. In Chapter 4 this peak has been linked to optimal bulk mixing enhancement, which is one of the main goals of jet control.

6.5   Conclusions

This chapter began with a detailed study of the effects of forcing on the velocity field of the axisymmetric jet. The modification of the near-field pressure with actuation has already been discussed in Chapter 3. The particular focus here was the modification of the pressure–velocity correlations, which enter into the approximation of the velocity field snapshots based on the spectral linear stochastic estimation. It was shown that the estimation coefficients obtained from experiments with the unforced jet are suitable even for the jet forced around the column mode. The same cannot be said for the jet forced in the shear layer mode where the Strouhal numbers are an order of magnitude higher; recall that this actuation regime has been found to be useful for noise mitigation. The focus of modeling here was on forcing near the jet column mode. Further discussion regarding the modeling of the actuation effects in the shear layer mode appears in Section 8.2.

A very general dynamical model of a forced system is one that can be separated into a drift vector field that predicts the behavior in the absence of forcing, and a superimposed input vector field that incorporates the actuation effects. Several techniques have been proposed in the literature on flow control for designing the drift vector field. One of these

that can be evaluated with the experimental data at hand is the idea of merging databases of snapshots from various forcing conditions prior to the determination of the low-dimensional kinematics. A straightforward Galerkin projection can be applied subsequently to arrive at the drift vector field. This method was implemented with data from several forcing cases near the jet column mode, along with the database from the unforced jet. The procedure automatically incorporates the appropriate shift modes that encode the kinematic directions along which the flow mean field changes with actuation. However, the trajectories from such a model were found to settle into a limit cycle behavior within about 50 flow time steps from the initiation of simulation even in the absence of external forcing. This failure of the model has been attributed to the inability of stochastic estimation to accurately reconstruct the energy dissipating scales that are essential for obtaining the proper dynamics of the shift modes. This defect may be alleviated if numerical simulation data is available for the particular jet operating conditions and forcing parameters. In the absence of this information, the drift vector field educed from the unforced jet database in Chapter 5 was used directly in the forced jet model. In Chapter 5 it was shown that the models that avoid the stochastic estimation step are more faithful to the dynamics of the unforced jet.

A novel method for designing the input vector field to incorporate the effect of plasma actuation on the jet is proposed here. The idea arose from the observation of compression waves that are generated with each plasma pulsation. The reduced-order model of the jet derived in Chapter 5 in fact has a ready-made pressure-based forcing term. This term was found to be negligible for the unforced jet. However, in this chapter, it is demonstrated that this term can be fashioned as the input vector field.

The forcing term requires the pressure field to be specified at all times on the boundaries of the cylindrical modeling domain spanning the end of the potential core. This information

is not available from experiments. However, the simple but effective vortex-based model of the jet shear layer proposed by Lau et al. (1972) was shown to be useful in this situation. Its predictions were first verified for the high-speed and and high-Reynolds number experimental jet under consideration, as well as for the implicit LES jet database. Subsequently, the information from the two databases was brought together using spectral linear stochastic estimation to obtain an approximation of the requisite pressure field. The pressure variation on the inflow boundary was estimated as a pure sine wave at each radial location. However, at any instant the phase was not uniform in the radial direction.

The proposed technique of incorporating the actuation effects was assessed in simulations of the 35-D ROM that was designed and investigated in Section 5.9.6. Several different forcing frequencies near the jet column mode (from $St_{DF} = 0.2$ to 0.4) were evaluated. The simulated trajectories were found to possess repeatable statistics in the intermediate term, from 20 to 30 flow time steps after initiation of simulation. The model was able to replicate the essential nonlinear dynamics of the jet around the column mode. The ROM displayed a sharp increase in turbulent fluctuation amplitudes at $St_{DF} = 0.3$. The phase-averaged axial velocity field contour plots also resembled experimental observations.

The jet response is highly nonlinear near the column mode. Near-field pressure fluctuations as well as far-field acoustics show a sharp increase near $St_{DF} = 0.3$. The jet centerline Mach number decay and turbulent kinetic energy increase also have their maxima at this forcing frequency. However, the response of the model is even more sensitive than the actual jet. This is a minor shortcoming of the proposed model.

In looking for solutions to the above issue, one possible route would be to model the periodic variation of the specified pressure field in a non-sinusoid manner. This would incorporate more frequency content in the forcing term, the proper shaping of which may

lead to more realistic behavior of the model. The other solution would be to improve the modeling of the drift vector field, as mentioned above.

Chapter 7

Real-time Flow State Estimation

A large part of the contents of this chapter has been accepted for publication in Sinha et al. (2011).

7.1   Introduction

Feedback control of a system requires real-time observation of the state of the system, which is rarely feasible. Instead, one typically must resort to estimating the state from a related *output* variable that can be measured. To control an incompressible jet, its instantaneous velocity field must be available to the controller. Real-time measurement of the velocity in a high-speed jet is not feasible. However, as discussed in Chapter 3, this velocity field is strongly correlated with the pressure in the irrotational near-field of the jet. The latter can be acquired in real-time relatively non-intrusively, and being a scalar variable it is also easier to measure (Tinney et al., 2008b). Thus, a more practical feedback control system would measure the pressure in the irrotational near-field in real-time, and use it to estimate the velocity.

State estimation for closed-loop control is essentially a filtering operation. As such, it may be divided into the following categories based on the memory requirement.

(*a*) The *zero-memory*, or single-time, variant involves using the measured output at each instant to directly estimate the state at that particular instant. This is the original form of stochastic estimation (SE), in which the state-output relation is determined by curve-fitting.

(*b*) The *limited-memory* estimation employs a finite backward-extended time history of outputs to approximate the state at any instant. This is the finite impulse response (FIR) filter, or the multi-time SE.

(*c*) In the *infinite-memory* variant, the entire history of outputs measured up to a point in time is used for the recursive estimation of the state at that time; this is the infinite impulse response (IIR) filter. The linear time-invariant filter (LTIF) and Kalman filter (KF) are popular members of this category.

The brief background of stochastic estimation (SE) provided in Section 5.5 is expanded here to set the stage for its discussion. The research in SE started with *linear* SE (LSE) in the areas of isotropic turbulence (Adrian and Moin, 1988), boundary layer (Guezennec, 1989), and axisymmetric jet shear layer (Cole et al., 1992). In these works, the instantaneous velocity at various locations in the flow were approximated as separate linear functions of the velocities measured at the same instant at only a few locations. In a parallel development, higher-order SE, including quadratic SE (QSE), were implemented for isotropic turbulence (Adrian, 1979; Tung and Adrian, 1980), and the boundary layer (Guezennec, 1989). These studies generally concluded that, compared to LSE, the marginal improvements in accuracy of estimation with higher-order SE did not warrant the added complications of computing the higher-order statistical moments.

Numerous researchers have advanced the original technique of SE in several significant directions. Instead of using measurements of the spatially-sparse velocity field itself to estimate a spatially-denser velocity field, measurements of other relevant flow quantities, viz. pressure and wall shear stress, have been used (Picard and Delville, 2000; Naguib et al., 2001; Murray and Ukeiley, 2003; Boree, 2003; Taylor and Glauser, 2004; Tinney et al., 2006; Caraballo et al., 2007; Pinier et al., 2007; Kastner et al., 2009a). This modification typically reduces the complexity of experiments since time-resolved velocity measurements are difficult and intrusive. As the solution of Poisson's equation indicates, the pressure field is related to the global velocity field. This implies that pressure-velocity correlations are strong across greater distances compared to velocity-velocity correlations. In the investigations where surface pressure was used in the estimation, significant improvements in accuracy were observed with QSE compared to LSE (Naguib et al., 2001; Murray and Ukeiley, 2003; Caraballo et al., 2007; Pinier et al., 2007). For the application to the turbulent boundary layer, this outcome was shown to indicate the comparable relevance of the mean-turbulent and turbulent-turbulent pressure source terms (Naguib et al., 2001). In the cavity flow configuration, it was posited that the higher order terms were necessary since the linear model becomes less accurate when the measurement location is far away from the estimation location (Murray and Ukeiley, 2003).

Another development of SE is its coupling with POD to obtain a *low-dimensional* estimate of the flow kinematics. In the classical version of the *complementary* technique, the velocity field obtained through LSE was further filtered using POD (Bonnet et al., 1994; Ewing and Citriniti, 1999). In the *modified complementary* SE, first the POD modal coefficients of the velocity field were estimated using a different flow variable, say the pressure

or wall shear stress, followed by a POD reconstruction of the velocity field from these estimates (Picard and Delville, 2000; Boree, 2003; Taylor and Glauser, 2004; Caraballo et al., 2007; Murray and Ukeiley, 2007; Pinier et al., 2007; Tinney et al., 2008b). The concept was later extended by decomposing both the measured field and the field to be estimated into their respective low-dimensional spatial modes, be they Fourier and/or POD, before linking the corresponding modal coefficients through stochastic estimation (Tinney et al., 2008b; Baars et al., 2010). The successive modifications were implemented to take advantage of the implicit spatial filtering and the increased correlations between the low-dimensional quantities, while reducing computations.

The above discussion focused on the single-time version of SE. In *single-time-delay* SE, a delayed version of the measurement is used to estimate the field at any given time (Guezennec, 1989; Naguib et al., 2001). This is useful where the time scales of the measurement and estimate are alike, but a fixed pre-determined convective delay has to be considered. On the other hand, *multi-time* SE uses measurements over a finite moving window stretching back in time for estimating the present state (Caraballo et al., 2007; Durgesh and Naughton, 2010). This accounts for convection effects in the flow, while also taking advantage of the temporal persistence of the large-scale structures being estimated. Although the accuracy of estimation first improves with the size of the time window, the fidelity actually degrades quite rapidly beyond a certain size (Durgesh and Naughton, 2010). Thinking from the perspective of polynomial curve-fitting, this may be explained by the over-determination of the fit of a high-degree polynomial in the absence of enough independent realizations. In real-time estimation, the number of delays in discrete time that can be considered is typically limited by hardware constraints.

Extending the concept of multi-time SE to the limit of theoretically infinite time, one arrives at the *spectral* variant of SE, which was the focus of Section 5.5. This technique may be implemented for statistically stationary flows where the correlation is computed in the temporal Fourier domain (Ewing and Citriniti, 1999; Tinney et al., 2006, 2008b; Baars et al., 2010). The spectral SE is especially useful whenever the spectral features of the measured and estimated variables are disparate, and/or significant time delays exist between them (Tinney et al., 2006). In practical implementations, one is typically limited to a finite time window, but this has to be long enough for satisfactory resolution of the frequency content. Moreover, its non-recursive nature and the necessity of computing the temporal Fourier transform, restrict the spectral SE to offline estimation applications.

The preceding discussion highlights the need for a recursive filtering technique that would address the dynamics of the flow while avoiding the hardware constraints of limited memory. This is the essence of an IIR filter like the Kalman filter (Kalman, 1960; Jazwinski, 1970; Anderson and Moore, 2005). However, unlike SE, IIR filters need a model of the flow dynamics. For the axisymmetric jet under consideration, the reduced-order modeling strategy presented in Chapter 5 fulfills this requirement. One of the advantages of a model-based filter over a stochastic estimator is the inherent noise-filtering properties of the former (Bewley and Protas, 2004). In essence, by incorporating some predictive knowledge of the system, model-based filters may separate the noise from the signal. On the other hand, stochastic estimators typically pass through the unfiltered measurement noise to the state estimate. A different model-based technique is adjoint-based model predictive estimation (Bewley and Protas, 2004). Typically, this strategy is quite computation-intensive, and hence may not be as suitable for real-time control implementation as an IIR filter.

Owing to the need for a reduced-order model of the flow dynamics, implementing a model-based state estimation is a challenge. Estimation of narrow-band frequency fluid dynamics has been reported by several investigators (Pastoor et al., 2008; Ahuja and Rowley, 2010; Wiederhold et al., 2010). These typically focus on a few states, and the benefits of dynamic estimation over stochastic estimation are easily demonstrated. In two recent contributions to the field of broad-band fluid dynamic estimation, the use of Kalman filters has been proposed to estimate the full state of a channel flow, given spatially-resolved measurements of the two-component wall shear stress and wall pressure everywhere on the surfaces (Hoepffner et al., 2005; Chevalier et al., 2006). Previously, it had been shown that a theoretically complete information of the flow can be deduced from this set of measurements (Bewley and Protas, 2004). Such comprehensive measurements are rarely feasible in unbounded flows, and one has to settle for far greater approximations. The present work proposes effective strategies in such a challenging situation.

The first implementation of LSE for the axisymmetric jet (Picard and Delville, 2000) employed a linear array of near-field microphones to estimate the axial and radial velocities in the shear layer. For computing the requisite pressure-velocity correlations the velocities were measured using hot-wires. In a subsequent effort, a similar microphone setup was used but the velocity was measured using 2C-PIV in a meridional plane (Kastner et al., 2009a). This work demonstrated that QSE substantially improves the estimation of the turbulent kinetic energy. The next development in this area was to employ an azimuthal ring array of sensors in the near-field simultaneously with laser Doppler anemometry in the shear layer (Tinney et al., 2006). This research also introduced the technique of spectral LSE. In a recent contribution, the pressure was measured on a similar azimuthal ring array and the velocity was measured on multiple cross-stream slices with 3C-PIV (Tinney et al., 2008b).

In this effort, both the pressure and velocity fields were reduced to their low-dimensional azimuthal Fourier modes and the velocity was additionally represented using POD, before SLSE was applied. The present work builds on these techniques, but with a focus on real-time state estimation. The two main contributions of this article are the development of a Kalman filter for infinite-memory estimation and the formulation of QSE in the Fourier azimuthal domain, both in the context of an axisymmetric jet shear layer.

The dynamic estimation strategies require a dynamic model of the plant. For the axisymmetric jet, such a model was developed in Chapter 5. The expression for the model was presented in eqn (5.49). In Chapter 6, the time-dependent external pressure term $d_\mathrm{G}(t; n, m)$ was used to incorporate the effect of actuation. For the state-estimation problem, this represents a quantity that is known a priori. Hence, it may be ignored in the assessment of the estimation strategies. Then, the relevant model is

$$\dot{\hat{\alpha}}^{(n)}(t; m) = \delta_{m,0} c_\mathrm{G}(n) + \sum_{n'=1}^{N_m} l_\mathrm{G}(n, n', m)\hat{\alpha}^{(n')}(t; m)$$
$$+ \sum_{m'=m-M}^{M} \sum_{n'=1}^{N_{m'}} \sum_{n'=1}^{N_{m-m'}} q_\mathrm{G}(n, n', n'', m, m')\hat{\alpha}^{(n')}(t; m')\hat{\alpha}^{(n'')}(t; m - m'). \quad (7.1)$$

Recall that although the POD modal coefficients are in the complex domain, the model coefficients above are real. It is clear that the POD modal coefficients constitute the state to be estimated in real time.

Since the feedback control will be implemented in discrete time, the continuous dynamics must be converted to a sampled dynamical system; the sampling period is denoted by T_s. The sampled version of the state of the ROM is denoted by $\hat{\alpha}_k^{(n)}(m) \equiv \hat{\alpha}^{(n)}(t = kT_s; m)$, where $k \in \mathbb{N}$, the set of natural numbers. For each individual azimuthal mode, the state vector is defined as

$$\boldsymbol{\hat{\alpha}}_k(m) := \left[\begin{array}{ccc} \hat{\alpha}_k^{(1)}(m) & \cdots & \hat{\alpha}_k^{(N_m)}(m) \end{array} \right]^\mathrm{T}. \quad (7.2)$$

234
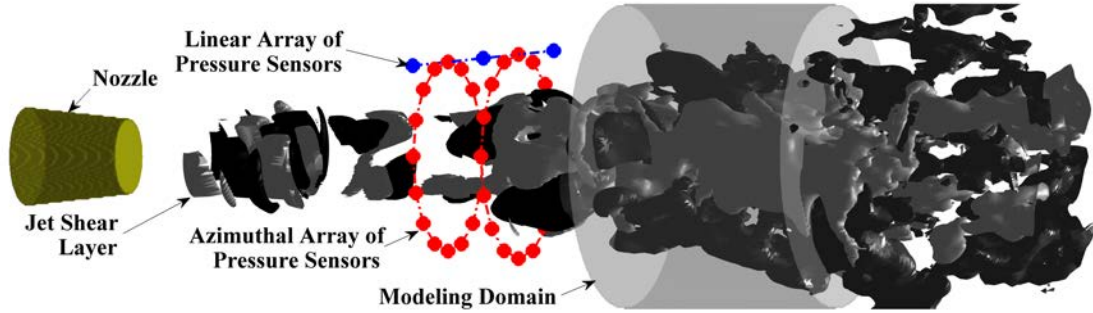
Figure 7.1: Near pressure field measurement schematic.

The DNS database provided by (Freund, 2001) has been discussed in Section 2.5; it would serve as the test-bed for evaluating the various estimation strategies. The appropriate T_s for the implementation is then the periodicity with which data were saved in the DNS database.

7.2 Estimator Modeling Preliminaries

For a practical implementation of real-time estimation for a jet, the pressure sensors must be located near the nozzle exit. However, the velocity field is to be estimated in a domain that is further downstream in the vicinity of the end of the potential core. The setup is identical to the configuration presented in Section 5.5, and is reproduced in Figure 7.1 for ease of discussion. Owing to convection, the estimate from such a configuration would lead the actual velocity field in time. This is very useful for feedback control. The ensuing formulation considers a unique value of the time-lead represented by $N_c T_s$. A method is proposed for determining the actual value of N_c in Section 7.5.

Two main approaches are taken for real-time estimation of the model state. In the first approach, single-time-delay modified complementary stochastic estimation is used to directly estimate the POD modal coefficients as a function of the pressure measured in the

irrotational near-field, the time-separation being $N_c T_s$. Both linear and quadratic SE are evaluated. This procedure does not utilize the known dynamics of the jet as captured by the model of eqn (7.1). Alternatively, a Kalman filter is implemented that uses the derived ROM of the jet, as well as a static *output equation* that expresses the near-field pressure at any instant of time t as a linear function of the POD modal coefficients at time $t + N_c T_s$. It is not trivial to obtain the said output equation from first principles. One option is to extend the incompressibility assumption made in the derivation of the ROM to argue for the approximate validity of Poisson's equation for pressure, which may then be explicitly solved in real-time (Noack et al., 2005). A novel contribution of the present work is to employ stochastic estimation to derive this equation from empirical data. Note that this represents the inverse of the SE problem for state estimation.

The continuous-time domain notation for the measurement configuration has been presented in Section 5.5; here, a discrete-time domain notation is preferred for implementation. The mth azimuthal Fourier mode of the pressure fluctuation signal at time t computed from an azimuthal array located at $x \in \mathcal{X}_p^a$ has been denoted as $\hat{p}^a(t; x, m)$. In discrete time, the notation is $\hat{p}_k^a(x, m) \equiv \hat{p}^a(t = kT_s; x, m)$. The pressure fluctuation signal at time t on the linear array at location $x \in \mathcal{X}_p^l$ has been denoted as $p^l(t; x)$. In discrete time, the notation is $p_k^l(x) \equiv p^l(t = kT_s; x)$. Using this notation, the following output vectors are defined

$$\hat{\mathbf{p}}_k^a(m) := \left[\hat{p}_k^a(x_1, m) \ \cdots \ \hat{p}_k^a(x_{N_p^a}, m) \right]^{\mathrm{T}}, \tag{7.3a}$$

$$\mathbf{p}_k^l := \left[p_k^l(x_1) \ \cdots \ p_k^a(x_{N_p^l}) \right]^{\mathrm{T}}. \tag{7.3b}$$

Remark 1. *Since the jet is axisymmetric, the statistics should be independent of the direction of measurement of the azimuthal coordinate. In Chapter 5, this property was invoked*

to show that, given any realization identified by the set

$$\left\{ \{\hat{\boldsymbol{\alpha}}(m)\}_{m=0}^{M}, \{\hat{\mathbf{p}}^a(m)\}_{m=0}^{M}, \mathbf{p}^l \right\},$$

one can extend *the database by appending another realization that is characterized by*

$$\left\{ \{\hat{\boldsymbol{\alpha}}^*(m)\}_{m=0}^{M}, \{\hat{\mathbf{p}}^{a*}(m)\}_{m=0}^{M}, \mathbf{p}^l \right\}.$$

Following this reasoning, one can conclude that any order of statistical moment involving these quantities would be real, although the individual quantities are complex.

Remark 2. *Using the above property along with the properties of the Fourier transform, one may derive the following*

$$E\left\{ \hat{p}_k^{a,r}(x,m)\hat{p}_k^{a,r}(x',m) \right\} = E\left\{ \hat{p}_k^{a,i}(x,m)\hat{p}_k^{a,i}(x',m) \right\}, \quad m \neq 0, \tag{7.4a}$$

$$E\left\{ \hat{p}_k^{a,r}(x,m)\hat{p}_k^{a,i}(x',m) \right\} = 0, \tag{7.4b}$$

$$\hat{p}_k^a(x,-m) = \hat{p}_k^{a*}(x,m). \tag{7.4c}$$

Remark 3. *Consider K arbitrary scalar fields in the azimuthal Fourier domain $\hat{w}^1(m_1)$ to $\hat{w}^K(m_K)$. Then, their cumulative spectrum satisfies the relation*

$$E\left\{ \hat{w}^1(m_1) \times \cdots \times \hat{w}^K(m_K) \right\} = \hat{\Pi}_{w^1, \cdots, w^K}(m_1, \cdots, m_K)\, \delta_{m_1 + \cdots + m_K, 0}.$$

In the above, $\hat{\Pi}$ is the azimuthal Fourier transform of the corresponding cumulative correlation in the physical domain. In particular, this means that $\hat{w}^K(m_K)$ is only correlated to certain products of azimuthal modes of the remaining variables.

7.3 Stochastic Estimation

7.3.1 Linear Stochastic Estimation

Denote the linear stochastic estimate of $\hat{\boldsymbol{\alpha}}_k(m)$ given the measurement at time instant k' by $\tilde{\hat{\boldsymbol{\alpha}}}_{\text{LSE},k\backslash k'}(m)$. Note that the estimate implicitly depends on the choice of $\mathcal{X}_p^a$ and

$\mathcal{X}_p^l$, the set of axial locations defining the measurement configuration. The following linear model is posited for the LSE with time-separation due to convection

$$\tilde{\hat{\boldsymbol{\alpha}}}_{\text{LSE},k+N_c\backslash k}(m) = \mathbf{L}_{\text{LSE}}^{a*}(m, N_c)\hat{\mathbf{p}}_k^a(m) + \mathbf{L}_{\text{LSE}}^{l*}(m, N_c)\mathbf{p}_k^l, \tag{7.5}$$

where $\mathbf{L}_{\text{LSE}}^a(m, N_c) \in \mathbb{R}^{N_p^a \times N_m}$ and $\mathbf{L}_{\text{LSE}}^l(m, N_c) \in \mathbb{R}^{N_p^l \times N_m}$ represent the families of LSE parameter matrices. Although these parameters are complex in general, it will be shown soon that the axisymmetry of the present problem renders them real. Remark 3 is invoked to argue for the decoupling of the estimation problems for each azimuthal Fourier mode. The asterisk signifies complex conjugate transpose.

Linear stochastic estimation proceeds by defining the mean square estimation error

$$e_{\text{LSE}}(m, n) := E\left\{\left|\tilde{\hat{\alpha}}_{\text{LSE},k+N_c\backslash k}^{(n)}(m) - \hat{\alpha}_{k+N_c}^{(n)}(m)\right|^2\right\}$$

for each $m - n$ pair, which is quadratic in the respective estimation parameters. The optimal parameter matrix is located at the unique global minimum of the error surface; the expression is

$$\begin{bmatrix} \mathbf{L}_{\text{LSE}}^a(m, N_c) \\ \mathbf{L}_{\text{LSE}}^l(m, N_c) \end{bmatrix} = \begin{bmatrix} E\left\{\hat{\mathbf{p}}_k^a(m)\hat{\mathbf{p}}_k^{a*}(m)\right\} & E\left\{\hat{\mathbf{p}}_k^a(m)\mathbf{p}_k^{l*}\right\} \\ E\left\{\mathbf{p}_k^l\hat{\mathbf{p}}_k^{a*}(m)\right\} & E\left\{\mathbf{p}_k^l\mathbf{p}_k^{l*}\right\} \end{bmatrix}^{-1} \begin{bmatrix} E\left\{\hat{\mathbf{p}}_k^a(m)\hat{\alpha}_{k+N_c}^*(m)\right\} \\ E\left\{\mathbf{p}_k^l\hat{\alpha}_{k+N_c}^*(m)\right\} \end{bmatrix}. \tag{7.6}$$

Following Remark 1, the estimation parameters can be concluded to be real.

With reference to the above formulation, consider how the correlations involving a particular linear array sensor would be modified if it were supplanted by an azimuthal array at the same axial location. Invoking the orthonormality of the Fourier basis, one obtains

$$E\left\{p_k^l(x)\hat{\boldsymbol{\alpha}}_{k'}^*(m)\right\} = E\left\{\sum_{m'=-\infty}^{\infty} \hat{p}_k^a(x, m')\text{e}^{\text{i}m'(\theta=0)}\hat{\boldsymbol{\alpha}}_{k'}^*(m)\right\} = E\left\{\hat{p}_k^a(x, m)\hat{\boldsymbol{\alpha}}_{k'}^*(m)\right\}, \tag{7.7a}$$

$$E\left\{p_k^l(x)\hat{\mathbf{p}}_k^{a*}(m)\right\} = E\left\{\hat{p}_k^a(x, m)\hat{\mathbf{p}}_k^{a*}(m)\right\}, \tag{7.7b}$$

$$E\left\{p_k^l(x)p_k^l(x')\right\} = \sum_{m=-\infty}^{\infty} E\left\{\hat{p}_k^a(x, m)\hat{p}_k^{a*}(x', m)\right\}. \tag{7.7c}$$

The above analysis shows that, except for $E\left\{\mathbf{p}_k^l \mathbf{p}_k^{l*}\right\}$, all the other terms appearing in eqn (7.6) are unchanged if an azimuthal ring array of sensors is used in place of the single sensor on the linear array at the same axial location. This explains the logic behind a configuration consisting of a combination of linear and azimuthal arrays of sensors, instead of the more expensive arrangement consisting of multiple azimuthal arrays.

7.3.2 Quadratic Stochastic Estimation

Denote the quadratic stochastic estimate of $\hat{\alpha}_k^{(n)}(m)$ given the measurement at time instant k' by $\tilde{\hat{\alpha}}_{\mathrm{QSE},k\backslash k'}^{(n)}(m)$. Then the following quadratic model is posited for the QSE with time-separation due to convection

$$
\begin{aligned}
\tilde{\hat{\alpha}}_{\mathrm{QSE},k+N_c\backslash k}^{(n)}(m) = {} & \delta_{m,0}c_{\mathrm{QSE}}(n,N_c) + \sum_{s=1}^{N_p^a} l_{\mathrm{QSE}}^a(s,m,n,N_c)\hat{p}_k^a(x_s,m) \\
& + \sum_{s=1}^{N_p^l} l_{\mathrm{QSE}}^l(s,m,n,N_c)p_k^l(x_s) + \sum_{s,s'=1}^{N_p^l} q_{\mathrm{QSE}}^{ll}(s,s',m,n,N_c)p_k^l(x_s)p_k^l(x_{s'}) \\
& + \sum_{m'=m-M}^{M}\sum_{s,s'=1}^{N_p^a} q_{\mathrm{QSE}}^{aa}(s,s',m',m-m',n,N_c)\hat{p}_k^a(x_s,m')\hat{p}_k^a(x_{s'},m-m') \\
& + \sum_{m'=-M}^{M}\sum_{s=1}^{N_p^a}\sum_{s'=1}^{N_p^l} q_{\mathrm{QSE}}^{al}(s,s',m',m,n,N_c)\hat{p}_k^a(x_s,m')p_k^l(x_{s'}). \qquad (7.8)
\end{aligned}
$$

Remark 3 dictates the particular azimuthal modes of pressure retained in the above expression, and the estimation parameters can be shown to be real by appealing to Remark 1. The constant term addresses the fact that some of the quadratic terms do not vanish in ensemble averaging of the above equation.

A review of the literature did not reveal any exposition of the implementation of QSE for multi-point measurements in a Fourier modal domain. Thus a sketch of the procedure is provided here.

Implementing stochastic estimation consists of three main steps: identifying the product terms to retain among all possible combinations, simplifying the model so that the set of 'regressors' is linearly independent, and determining the set of multiplicative parameters so that the model optimally fits the given dataset. For QSE in the Fourier domain, the model proposed in eqn (7.8) already addressed the first issue by reference to Remark 3. The second step will be discussed next.

The model proposed in eqn (7.8) has different quadratic parameters multiplying product terms that differ only in the order of multiplication. Such terms are not independent, and thus the least-mean-squares problem becomes ill-posed if one tries to determine the associated parameters as distinct entities. A related issue is that all the estimation parameters are known a priori to be real following arguments made in Remark 1. Thus, for $m = 0$, to avoid redundancies, one formulates the following estimator:

$$
\tilde{\hat{\alpha}}^{(n)}_{\mathrm{QSE},k+N_c\setminus k}(0) = c_{\mathrm{QSE}}(n, N_c) + \sum_{s=1}^{N_p^a} l^a_{\mathrm{QSE}}(s,0,n,N_c)\hat{p}^a_k(x_s,0) + \sum_{s=1}^{N_p^l} l^l_{\mathrm{QSE}}(s,0,n,N_c)p^l_k(x_s)
$$

$$
+ \sum_{m'=0}^{M}\sum_{s=1}^{N_p^a}\sum_{s'=1}^{s} \overrightarrow{q}^{aa}_{\mathrm{QSE}}(s,s',m',-m',n,N_c)\Re\left\{\hat{p}^a_k(x_s,m')\hat{p}^{a*}_k(x_{s'},m')\right\}
$$

$$
+ \sum_{s=1}^{N_p^l}\sum_{s'=1}^{s} \overrightarrow{q}^{ll}_{\mathrm{QSE}}(s,s',0,n,N_c)p^l_k(x_s)p^l_k(x_{s'})
$$

$$
+ \sum_{m'=0}^{M}\sum_{s=1}^{N_p^a}\sum_{s'=1}^{N_p^l} \overrightarrow{q}^{al}_{\mathrm{QSE}}(s,s',m',0,n,N_c)\Re\left\{\hat{p}^a_k(x_s,m')\right\}p^l_k(x_{s'}).
$$

For $m \neq 0$, the redundancies are removed thus:

$$
\tilde{\hat{\alpha}}^{(n)}_{\mathrm{QSE},k+N_c\setminus k}(m) = \sum_{s=1}^{N_p^a} l^a_{\mathrm{QSE}}(s,m,n,N_c)\hat{p}^a_k(x_s,m) + \sum_{s=1}^{N_p^l} l^l_{\mathrm{QSE}}(s,m,n,N_c)p^l_k(x_s)
$$

$$
+ \sum_{m'=m-M}^{\lfloor m/2 \rfloor}\sum_{s=1}^{N_p^a} \overrightarrow{q}^{aa}_{\mathrm{QSE}}(s,s,m',m-m',n,N_c)\hat{p}^a_k(x_s,m')\hat{p}^a_k(x_s,m-m')
$$

$$
+ \sum_{m'=m-M}^{M}\sum_{s=2}^{N_p^a}\sum_{s'=1}^{s-1} \overrightarrow{q}^{aa}_{\mathrm{QSE}}(s,s',m',m-m',n,N_c)\hat{p}^a_k(x_s,m')\hat{p}^a_k(x_{s'},m-m')
$$

$$+ \sum_{s=1}^{N_p^l} \sum_{s'=1}^{s} \overrightarrow{q}_{\text{QSE}}^{ll}(s, s', m, n, N_c) p_k^l(x_s) p_k^l(x_{s'})$$

$$+ \sum_{m'=-M}^{M} \sum_{s=1}^{N_p^a} \sum_{s'=1}^{N_p^l} q_{\text{QSE}}^{al}(s, s', m', m, n, N_c) \hat{p}_k^a(x_s, m') p_k^l(x_{s'}), \quad m \in [1, M].$$

Here, $\lfloor \cdot \rfloor$ denotes the `floor` function.

As in all stochastic estimators, QSE proceeds by defining the mean square estimation error. It is immediate from the above formulations that the QSE model is linear in the estimation parameters, so that the mean-square error surface is a paraboloid in the parameter space. From this stage on, the problem becomes indistinguishable from an LSE, and the solution is well-known; see for example Ljung (1999).

The estimation parameters appearing in eqn (7.8) can be retrieved from the ones determined above using the following equations. However, it must be understood that those parameters that appear on the right hand side of the equations below but not in the above equations, are identically zero.

$$q_{\text{QSE}}^{aa}(s, s', m', m - m', n, N_c)$$

$$= \frac{0.5}{1 + \delta_{m,0}} \left\{ \overrightarrow{q}_{\text{QSE}}^{aa}(s, s', m', m - m', n, N_c) + \overrightarrow{q}_{\text{QSE}}^{aa}(s', s, m', m - m', n, N_c) \right\}$$

$$+ 0.25 \left\{ \overrightarrow{q}_{\text{QSE}}^{aa}(s, s', m - m', m', n, N_c) + \overrightarrow{q}_{\text{QSE}}^{aa}(s', s, m - m', m', n, N_c) \right\},$$

$$q_{\text{QSE}}^{ll}(s, s', m, n, N_c) = 0.5 \left\{ \overrightarrow{q}_{\text{QSE}}^{ll}(s, s', m, n, N_c) + \overrightarrow{q}_{\text{QSE}}^{ll}(s', s, m, n, N_c) \right\},$$

$$q_{\text{QSE}}^{al}(s, s', m', 0, n, N_c) = 0.5 \left\{ \overrightarrow{q}_{\text{QSE}}^{al}(s, s', m', 0, n, N_c) + \overrightarrow{q}_{\text{QSE}}^{al}(s, s', -m', 0, n, N_c) \right\}.$$

7.4 Infinite Impulse Response Filtering

An infinite-impulse response filter uses the predictive capability of a dynamical model of the flow to systematically reduce pass-through of measurement noise to the state estimate. For linear models, the Kalman filter (KF) is the optimal filter, so that the linearized version

of the ROM presented in eqn (7.1) is a good starting point. The KF is time-varying so that one has to perform the computations for the filter gains in real-time. Since the gains do not depend on the actual measurements, one can also pre-compute them to reduce processor overhead, with a commensurate increase in memory requirement. If the filter is stable, then the gains reach steady state. Using the steady state gains in a linear time-invariant filter (LTIF) may be a viable alternative to the KF. For nonlinear models, such as the ROM in eqn (7.1), the extended Kalman filter (EKF) is an ad hoc extension of the KF that is known to be sub-optimal. All the three filters mentioned above are well-established (Anderson and Moore, 2005), and they are implemented in this work. It must be mentioned here that EKF is not the only IIR filter available for nonlinear models. However, the alternatives such as unscented KF, iterated EKF, and particle filter, are even more computation-intensive, and thus deemed unsuitable for the present application.

7.4.1 Kalman Filter

The typical control task involves stabilizing the equilibrium point of a system. The trivial solution of the ROM in eqn (7.1) is typically not an equilibrium point of the full Navier-Stokes equation, since the mean flow is not the steady solution. Moreover, the attractor of the controlled flow is not evident a priori. Thus the state about which one should linearize the ROM is not obvious. The unforced flow is being estimated here, and it remains close to the mean flow. This is further substantiated by the fact that the constant term in the ROM turns out to be quite small. Thus, for the purpose of assessing the fidelity of dynamic estimation, the appropriate linearization involves simply neglecting the constant and quadratic terms of the vector field. Note that this decouples the dynamics of the individual azimuthal modes.

Previously it has been pointed out that the filter needs to be implemented in a sampled-data system. Then, the following linearized model is obtained

$$\hat{\boldsymbol{\alpha}}_{k+1}(m) = \mathbf{L}_{\mathrm{G}}(m)\hat{\boldsymbol{\alpha}}_k(m) + \boldsymbol{\psi}_{\mathrm{KF},k}(m). \tag{7.9}$$

Here, $\mathbf{L}_{\mathrm{G}}(m) = \exp\left(\mathbf{L}_{\mathrm{G}}^{\mathrm{C}}(m)T_s\right) \in \mathbb{R}^{N_m \times N_m}$, with $\left\{\mathbf{L}_{\mathrm{G}}^{\mathrm{C}}(m)\right\}_{n,n'} := l_{\mathrm{G}}(n, n', m)$ from eqn (7.1) (Franklin et al., 1990). As is common in filtering, the uncertainties introduced by the modeling approximations, including the linearization, are addressed by the family of additive noise sequences $\boldsymbol{\psi}_{\mathrm{KF},k}(m) \in \mathbb{C}^{N_m}$, which are assumed to be stationary independent random processes (white noise) with identically zero mean and constant covariance matrices

$$E\left\{\boldsymbol{\psi}_{\mathrm{KF},k}(m)\boldsymbol{\psi}_{\mathrm{KF},k'}^*(m')\right\} =: \boldsymbol{\Psi}_{\mathrm{KF}}(m)\delta_{k,k'}\delta_{m,m'}. \tag{7.10}$$

The symmetric matrices $\boldsymbol{\Psi}_{\mathrm{KF}}$ are real following Remark 1.

Apart from the dynamical model presented above, the KF also assumes a linear static map linking the measured output to the state. The following set of output equations specifies the measured pressure as a linear function of the POD modal coefficients with the time-separation discussed previously

$$\hat{\mathbf{p}}_k^a(m) = \mathbf{L}_{\mathrm{KF}}^{a*}(m, N_c)\hat{\boldsymbol{\alpha}}_{k+N_c}(m) + \boldsymbol{\xi}_{\mathrm{KF},k}^a(m, N_c), \tag{7.11a}$$

$$\mathbf{p}_k^l = \sum_{m=0}^{M} \mathbf{L}_{\mathrm{KF}}^{l*}(m, N_c)\hat{\boldsymbol{\alpha}}_{k+N_c}^r(m) + \boldsymbol{\xi}_{\mathrm{KF},k}^l(N_c). \tag{7.11b}$$

The linear operators are $\mathbf{L}_{\mathrm{KF}}^a(m, N_c) \in \mathbb{R}^{N_m \times N_p^a}$ and $\mathbf{L}_{\mathrm{KF}}^l(m, N_c) \in \mathbb{R}^{N_m \times N_p^l}$; more will be said about these subsequently. The decoupling of the azimuthal Fourier modes in the first equation follows from Remark 3. The imaginary parts of the POD modal coefficients are absent from the second equation following the arguments made in Remark 1. The measurement uncertainties are modeled by the families of additive sequences $\boldsymbol{\xi}_{\mathrm{KF}}^a \in \mathbb{C}^{N_p^a}$ and $\boldsymbol{\xi}_{\mathrm{KF}}^l \in \mathbb{R}^{N_p^l}$ that are independent random processes (white noise) with identically zero

means and constant covariance matrices

$$E\left\{\boldsymbol{\xi}^a_{\mathrm{KF},k}(m,N_c)\boldsymbol{\xi}^{a*}_{\mathrm{KF},k'}(m',N_c)\right\} =: \boldsymbol{\Xi}^{aa}_{\mathrm{KF}}(m,N_c)\delta_{k,k'}\delta_{m,m'}, \tag{7.12a}$$

$$E\left\{\boldsymbol{\xi}^l_{\mathrm{KF},k}(N_c)\boldsymbol{\xi}^{l*}_{\mathrm{KF},k'}(N_c)\right\} =: \boldsymbol{\Xi}^{ll}_{\mathrm{KF}}(N_c)\delta_{k,k'}, \tag{7.12b}$$

$$E\left\{\boldsymbol{\xi}^a_{\mathrm{KF},k}(m,N_c)\boldsymbol{\xi}^{l*}_{\mathrm{KF},k'}(N_c)\right\} =: \boldsymbol{\Xi}^{al}_{\mathrm{KF}}(m,N_c)\delta_{k,k'}. \tag{7.12c}$$

The covariance matrices are real following Remark 1. Additionally, it is commonplace to assume that the state uncertainties appearing in eqn (7.9) are not correlated with the measurement uncertainties; i.e.,

$$E\left\{\boldsymbol{\psi}_{\mathrm{KF},k}(m)\boldsymbol{\xi}^{a*}_{\mathrm{KF},k'}(m',N_c)\right\} \equiv \mathbf{0}, \tag{7.13a}$$

$$E\left\{\boldsymbol{\psi}_{\mathrm{KF},k}(m)\boldsymbol{\xi}^{l*}_{\mathrm{KF},k'}(N_c)\right\} \equiv \mathbf{0}. \tag{7.13b}$$

It has been mentioned earlier that the parameter matrices $\mathbf{L}^a_{\mathrm{KF}}$ and $\mathbf{L}^l_{\mathrm{KF}}$ would be determined using stochastic estimation. Appealing to the orthogonality of the POD modal coefficients from eqn (5.24), the LSE yields

$$\mathbf{L}^a_{\mathrm{KF}}(m,N_c) = \begin{bmatrix} \dfrac{E\left\{\hat{\alpha}^{(1)}_{k+N_c}(m)\hat{\mathbf{p}}^{a*}_k(m)\right\}}{\Lambda^{(1)}(m)} \\ \vdots \\ \dfrac{E\left\{\hat{\alpha}^{(N_m)}_{k+N_c}(m)\hat{\mathbf{p}}^{a*}_k(m)\right\}}{\Lambda^{(N_m)}(m)} \end{bmatrix}, \quad \mathbf{L}^l_{\mathrm{KF}}(m,N_c) = \begin{bmatrix} \dfrac{2E\left\{\hat{\alpha}^{(1),r}_{k+N_c}(m)\mathbf{p}^{l*}_k\right\}}{(1+\delta_{m,0})\Lambda^{(1)}(m)} \\ \vdots \\ \dfrac{2E\left\{\hat{\alpha}^{(N_m),r}_{k+N_c}(m)\mathbf{p}^{l*}_k\right\}}{(1+\delta_{m,0})\Lambda^{(N_m)}(m)} \end{bmatrix}. \tag{7.14}$$

The parameter matrices are real following Remark 1.

Now, as in Section 7.3.1, consider what happens when an azimuthal array of sensors is used in place of a single sensor on the linear array at the same axial location. Using arguments that are similar to those presented in eqn (7.7a), along with those made in Remark 2, one can show that

$$E\left\{\hat{\alpha}^{(n),r}_{k+N_c}(m)p^{l*}_k(x)\right\} = E\left\{\hat{\alpha}^{(n)}_{k+N_c}(m)\hat{p}^{a*}_k(x,m)\right\}. \tag{7.15}$$

This provides a simple relation between the relevant model parameters in eqn (7.14).

The output equation, eqn (7.11b), requires partitioning the state vector into real and imaginary parts. It also couples all the azimuthal Fourier modes from the perspective of the filter. In view of this, the accent $(\breve{\cdot})$ is used to indicate the new real quantity formed by assembling all the corresponding complex quantities in the azimuthal Fourier domain, as follows

$$\breve{\boldsymbol{\alpha}} := \left[\{\hat{\boldsymbol{\alpha}}(0)\}^{\mathrm{T}} \ \{\hat{\boldsymbol{\alpha}}^r(1)\}^{\mathrm{T}} \ \cdots \ \{\hat{\boldsymbol{\alpha}}^r(M)\}^{\mathrm{T}} \ \{\hat{\boldsymbol{\alpha}}^i(1)\}^{\mathrm{T}} \ \cdots \ \{\hat{\boldsymbol{\alpha}}^i(M)\}^{\mathrm{T}} \right]^{\mathrm{T}}, \tag{7.16a}$$

$$\breve{\mathbf{p}} := \left[\{\hat{\mathbf{p}}^a(0)\}^{\mathrm{T}} \ \{\hat{\mathbf{p}}^{a,r}(1)\}^{\mathrm{T}} \ \cdots \ \{\hat{\mathbf{p}}^{a,r}(M)\}^{\mathrm{T}} \ \{\hat{\mathbf{p}}^{a,i}(1)\}^{\mathrm{T}} \ \cdots \ \{\hat{\mathbf{p}}^{a,i}(M)\}^{\mathrm{T}} \ \left\{\mathbf{p}^l\right\}^{\mathrm{T}} \right]^{\mathrm{T}},$$
$$\tag{7.16b}$$

$$\breve{\boldsymbol{\psi}}_{\mathrm{KF}} := \left[\{\boldsymbol{\psi}_{\mathrm{KF}}(0)\}^{\mathrm{T}} \ \{\boldsymbol{\psi}_{\mathrm{KF}}^r(1)\}^{\mathrm{T}} \ \cdots \ \{\boldsymbol{\psi}_{\mathrm{KF}}^r(M)\}^{\mathrm{T}} \ \{\boldsymbol{\psi}_{\mathrm{KF}}^i(1)\}^{\mathrm{T}} \ \cdots \ \{\boldsymbol{\psi}_{\mathrm{KF}}^i(M)\}^{\mathrm{T}} \right]^{\mathrm{T}},$$
$$\tag{7.16c}$$

$$\breve{\boldsymbol{\xi}}_{\mathrm{KF}} := \left[\{\boldsymbol{\xi}_{\mathrm{KF}}^a(0)\}^{\mathrm{T}} \ \{\boldsymbol{\xi}_{\mathrm{KF}}^{a,r}(1)\}^{\mathrm{T}} \ \cdots \ \{\boldsymbol{\xi}_{\mathrm{KF}}^{a,r}(M)\}^{\mathrm{T}} \ \left\{\boldsymbol{\xi}_{\mathrm{KF}}^{a,i}(1)\right\}^{\mathrm{T}} \ \cdots \ \left\{\boldsymbol{\xi}_{\mathrm{KF}}^{a,i}(M)\right\}^{\mathrm{T}} \ \left\{\boldsymbol{\xi}_{\mathrm{KF}}^l\right\}^{\mathrm{T}} \right]^{\mathrm{T}}.$$
$$\tag{7.16d}$$

In the above, the time index k as well as the functional dependence on N_c have been omitted for notational convenience. The superscripts r and i respectively denote the real and imaginary parts of a complex quantity.

Since $\mathbf{L}_{\mathrm{G}}(m)$ in eqn (7.9) is real for all m, the new state transition matrix is the block-diagonal concatenation

$$\breve{\mathbf{L}}_{\mathrm{G}} := \mathrm{diag}\left([\mathbf{L}_{\mathrm{G}}(0) \ \mathbf{L}_{\mathrm{G}}(1) \ \cdots \ \mathbf{L}_{\mathrm{G}}(M) \ \mathbf{L}_{\mathrm{G}}(1) \ \cdots \ \mathbf{L}_{\mathrm{G}}(M)] \right).$$

The form of the new output matrix follows from the modal output matrices in eqn (7.11); omitting the functional dependence on N_c for notational convenience, one obtains

$$
\check{\mathbf{L}}_{\mathrm{KF}} := \begin{bmatrix}
\mathbf{L}_{\mathrm{KF}}^a(0) & 0 & \cdots & 0 & 0 & \cdots & 0 & \mathbf{L}_{\mathrm{KF}}^l(0) \\
0 & \mathbf{L}_{\mathrm{KF}}^a(1) & \cdots & 0 & 0 & \cdots & 0 & \mathbf{L}_{\mathrm{KF}}^l(1) \\
\vdots & \vdots & \ddots & \vdots & \vdots & \ddots & \vdots & \vdots \\
0 & 0 & \cdots & \mathbf{L}_{\mathrm{KF}}^a(M) & 0 & \cdots & 0 & \mathbf{L}_{\mathrm{KF}}^l(M) \\
0 & 0 & \cdots & 0 & \mathbf{L}_{\mathrm{KF}}^a(1) & \cdots & 0 & 0 \\
\vdots & \vdots & \ddots & \vdots & \vdots & \ddots & \vdots & \vdots \\
0 & 0 & \cdots & 0 & 0 & \cdots & \mathbf{L}_{\mathrm{KF}}^a(M) & 0
\end{bmatrix}.
$$

The new state uncertainty sequence remains a zero-mean independent random process, and its covariance can be derived from eqns (5.24) and (7.10)

$$
E\left\{\check{\boldsymbol{\psi}}_{\mathrm{KF},k}\check{\boldsymbol{\psi}}_{\mathrm{KF},k'}^*\right\} =: \check{\boldsymbol{\Psi}}_{\mathrm{KF}}\delta_{k,k'}
$$

$$
= \mathrm{diag}\left(\begin{bmatrix}\boldsymbol{\Psi}_{\mathrm{KF}}(0) & \tfrac{1}{2}\boldsymbol{\Psi}_{\mathrm{KF}}(1) & \cdots & \tfrac{1}{2}\boldsymbol{\Psi}_{\mathrm{KF}}(M) & \tfrac{1}{2}\boldsymbol{\Psi}_{\mathrm{KF}}(1) & \cdots & \tfrac{1}{2}\boldsymbol{\Psi}_{\mathrm{KF}}(M)\end{bmatrix}\right)\delta_{k,k'}.
$$

The new measurement uncertainty sequence also remains a zero-mean independent random process, and its covariance can be derived from Remark 2 and eqn (7.12)

$$
E\left\{\check{\boldsymbol{\xi}}_{\mathrm{KF},k}(N_c)\check{\boldsymbol{\xi}}_{\mathrm{KF},k'}^*(N_c)\right\} =: \check{\boldsymbol{\Xi}}_{\mathrm{KF}}(N_c)\delta_{k,k'}
$$

$$
= \begin{bmatrix}
\boldsymbol{\Xi}_{\mathrm{KF}}^{aa}(0) & 0 & \cdots & \cdots & \cdots & \cdots & 0 & \boldsymbol{\Xi}_{\mathrm{KF}}^{al}(0) \\
0 & \tfrac{1}{2}\boldsymbol{\Xi}_{\mathrm{KF}}^{aa}(1) & \cdots & 0 & \cdots & \cdots & 0 & \boldsymbol{\Xi}_{\mathrm{KF}}^{al}(1) \\
\vdots & \vdots & \ddots & \vdots & \vdots & \ddots & \vdots & \vdots \\
0 & 0 & \cdots & \tfrac{1}{2}\boldsymbol{\Xi}_{\mathrm{KF}}^{aa}(M) & 0 & \cdots & 0 & \boldsymbol{\Xi}_{\mathrm{KF}}^{al}(M) \\
0 & \cdots & \cdots & 0 & \tfrac{1}{2}\boldsymbol{\Xi}_{\mathrm{KF}}^{aa}(1) & \cdots & 0 & 0 \\
\vdots & \vdots & \ddots & \vdots & \vdots & \ddots & \vdots & \vdots \\
0 & 0 & \cdots & 0 & 0 & \cdots & \tfrac{1}{2}\boldsymbol{\Xi}_{\mathrm{KF}}^{aa}(M) & 0 \\
\boldsymbol{\Xi}_{\mathrm{KF}}^{al*}(0) & \boldsymbol{\Xi}_{\mathrm{KF}}^{al*}(1) & \cdots & \boldsymbol{\Xi}_{\mathrm{KF}}^{al*}(M) & 0 & \cdots & 0 & \boldsymbol{\Xi}_{\mathrm{KF}}^{ll}
\end{bmatrix}\delta_{k,k'}.
$$

From eqn (7.13), one obtains

$$
E\left\{\check{\boldsymbol{\psi}}_{\mathrm{KF},k}\check{\boldsymbol{\xi}}_{\mathrm{KF},k'}^*(N_c)\right\} = \mathbf{0}.
$$

Then, the model becomes

$$
\check{\boldsymbol{\alpha}}_{k+1} = \check{\mathbf{L}}_{\mathrm{G}}\check{\boldsymbol{\alpha}}_k + \check{\boldsymbol{\psi}}_{\mathrm{KF},k}, \tag{7.17a}
$$

246

$$\breve{\mathbf{p}}_k = \breve{\mathbf{L}}_{\mathrm{KF}}^{\mathrm{T}}(N_c)\breve{\boldsymbol{\alpha}}_{k+N_c} + \breve{\boldsymbol{\xi}}_{\mathrm{KF},k}(N_c). \tag{7.17b}$$

Denote the Kalman filter estimate of $\breve{\boldsymbol{\alpha}}_k$ given all measurements up to and including instant k' by $\tilde{\breve{\boldsymbol{\alpha}}}_{\mathrm{KF},k/k'}$. Note the difference from the corresponding notation for single-time SE. Let $\boldsymbol{\Theta}_{\mathrm{KF},k/k'}$ be the auto-covariance of the estimation error at k given the measurements up to k', i.e.

$$\boldsymbol{\Theta}_{\mathrm{KF},k/k'} := E\left[\left\{\tilde{\breve{\boldsymbol{\alpha}}}_{\mathrm{KF},k/k'} - \breve{\boldsymbol{\alpha}}_k\right\}\left\{\tilde{\breve{\boldsymbol{\alpha}}}_{\mathrm{KF},k/k'} - \breve{\boldsymbol{\alpha}}_k\right\}^*\right].$$

Then, the following relations specify the Kalman Filter (Anderson and Moore, 2005)

$$\mathbf{K}_{\mathrm{KF},k}(N_c) = \boldsymbol{\Theta}_{\mathrm{KF},k+N_c/k-1}\breve{\mathbf{L}}_{\mathrm{KF}}(N_c)\left(\breve{\mathbf{L}}_{\mathrm{KF}}^{\mathrm{T}}(N_c)\boldsymbol{\Theta}_{\mathrm{KF},k+N_c/k-1}\breve{\mathbf{L}}_{\mathrm{KF}}(N_c) + \breve{\boldsymbol{\Xi}}_{\mathrm{KF}}(N_c)\right)^{-1},$$
$$\tag{7.18a}$$

$$\tilde{\breve{\boldsymbol{\alpha}}}_{\mathrm{KF},k+N_c/k} = \tilde{\breve{\boldsymbol{\alpha}}}_{\mathrm{KF},k+N_c/k-1} + \mathbf{K}_{\mathrm{KF},k}(N_c)\left(\breve{\mathbf{p}}_k - \breve{\mathbf{L}}_{\mathrm{KF}}^{\mathrm{T}}(N_c)\tilde{\breve{\boldsymbol{\alpha}}}_{\mathrm{KF},k+N_c/k-1}\right), \tag{7.18b}$$

$$\boldsymbol{\Theta}_{\mathrm{KF},k+N_c/k} = \boldsymbol{\Theta}_{\mathrm{KF},k+N_c/k-1} - \mathbf{K}_{\mathrm{KF},k}(N_c)\breve{\mathbf{L}}_{\mathrm{KF}}^{\mathrm{T}}(N_c)\boldsymbol{\Theta}_{\mathrm{KF},k+N_c/k-1}, \tag{7.18c}$$

$$\tilde{\breve{\boldsymbol{\alpha}}}_{\mathrm{KF},k+N_c+1/k} = \breve{\mathbf{L}}_{\mathrm{G}}\tilde{\breve{\boldsymbol{\alpha}}}_{\mathrm{KF},k+N_c/k}, \tag{7.18d}$$

$$\boldsymbol{\Theta}_{\mathrm{KF},k+N_c+1/k} = \breve{\mathbf{L}}_{\mathrm{G}}\boldsymbol{\Theta}_{\mathrm{KF},k+N_c/k}\breve{\mathbf{L}}_{\mathrm{G}}^{\mathrm{T}} + \breve{\boldsymbol{\Psi}}_{\mathrm{KF}}, \tag{7.18e}$$

$$\tilde{\breve{\boldsymbol{\alpha}}}_{\mathrm{KF},k'/-1} = \mathbf{0}, \ k' \in [0, N_c], \tag{7.18f}$$

$$\boldsymbol{\Theta}_{\mathrm{KF},k'/-1} = \mathrm{diag}\left(\Lambda^{(1)}(0) \ \cdots \ \Lambda^{(N_0)}(0) \ \frac{\Lambda^{(1)}(1)}{2} \ \cdots \ \frac{\Lambda^{(N_1)}(1)}{2} \ \cdots \ \frac{\Lambda^{(1)}(M)}{2} \ \cdots \ \frac{\Lambda^{(N_M)}(M)}{2} \right.$$
$$\left. \frac{\Lambda^{(1)}(1)}{2} \ \cdots \ \frac{\Lambda^{(N_1)}(1)}{2} \ \cdots \ \frac{\Lambda^{(1)}(M)}{2} \ \cdots \ \frac{\Lambda^{(N_M)}(M)}{2}\right), \ k' \in [0, N_c]. \tag{7.18g}$$

The first equation defines the time-varying Kalman gain, the next two define the measurement-updates of the state and its error covariance, and the fourth and fifth equations establish their respective time-updates. The sixth equation sets the initial condition for the state estimate to the zero vector, in the absence of any other information. Then, the initial condition for the error covariance in the last equation becomes equal to the covariance of the state vector itself; its form is derived from eqn (5.24).

7.4.2 Linear Time-Invariant Filter

The state dynamics and output equations in eqn (7.17) are time-invariant, but the state model may not have a stable equilibrium. Then, the Kalman filter will be asymptotically stable if (*a*) the pair $[\check{\mathbf{L}}_{\mathrm{G}}, \ \check{\mathbf{L}}_{\mathrm{KF}}^{\mathrm{T}}(N_c)]$ is completely detectable, *and* (*b*) the pair $[\check{\mathbf{L}}_{\mathrm{G}}, \ \check{\mathbf{\Psi}}_1]$ is stabilizable for any $\check{\mathbf{\Psi}}_1$ such that $\check{\mathbf{\Psi}}_1 \check{\mathbf{\Psi}}_1^{\mathrm{T}} = \check{\mathbf{\Psi}}_{\mathrm{KF}}$ (see Anderson and Moore (2005)). The stationary (or steady-state) error-covariance matrix $\mathbf{\Theta}_{\mathrm{LTIF}}(N_c)$ is obtained as the solution of the following discrete-time algebraic Riccati equation

$$\mathbf{\Theta}_{\mathrm{LTIF}}(N_c) = \check{\mathbf{L}}_{\mathrm{G}}\mathbf{\Theta}_{\mathrm{LTIF}}(N_c)\check{\mathbf{L}}_{\mathrm{G}}^{\mathrm{T}} - \check{\mathbf{L}}_{\mathrm{G}}\mathbf{\Theta}_{\mathrm{LTIF}}(N_c)\check{\mathbf{L}}_{\mathrm{KF}}(N_c)$$
$$\times \left(\check{\mathbf{L}}_{\mathrm{KF}}^{\mathrm{T}}(N_c)\mathbf{\Theta}_{\mathrm{LTIF}}(N_c)\check{\mathbf{L}}_{\mathrm{KF}}(N_c) + \check{\mathbf{\Xi}}_{\mathrm{KF}}(N_c) \right)^{-1} \check{\mathbf{L}}_{\mathrm{KF}}^{\mathrm{T}}(N_c)\mathbf{\Theta}_{\mathrm{LTIF}}(N_c)\check{\mathbf{L}}_{\mathrm{G}}^{\mathrm{T}} + \check{\mathbf{\Psi}}_{\mathrm{KF}}. \quad (7.19)$$

The stationary Kalman gain matrix is obtained by inserting $\mathbf{\Theta}_{\mathrm{LTIF}}(N_c)$ in eqn (7.18a). Use of a stationary gain reduces the original time-varying KF to the linear time-invariant filter (LTIF). Then, the only expressions to be evaluated in real-time are eqns (7.18b) and (7.18d), which makes the LTIF comparable in complexity to the LSE model in eqn (7.5).

7.4.3 Extended Kalman Filter

The conversion of the continuous ODE with quadratic nonlinearity in eqn (7.1) to an equivalent difference equation for a sampled data system is not obvious. The approach taken here treats the linear part as if the quadratic part were absent, so that the linear part of the difference equation is identical to that in eqn (7.9). Subsequently, the quadratic part is determined as if the state derivative were approximated by a first-order forward difference scheme. The resultant state model is the following set of difference equations with quadratic nonlinearity

$$\hat{\alpha}_{k+1}^{(n)}(m) = \delta_{m,0}c_{\mathrm{G}}(n) + \mathbf{l}_{\mathrm{G}}(n,m)\hat{\boldsymbol{\alpha}}_k(m)$$

$$+ \sum_{m'=m-M}^{M} \{\hat{\boldsymbol{\alpha}}_k(m')\}^{\mathrm{T}} \mathbf{Q}_{\mathrm{G}}(n, m, m')\hat{\boldsymbol{\alpha}}_k(m - m') + \psi_{\mathrm{EKF},k}^{(n)}(m). \qquad (7.20)$$

Here, $\mathbf{l}_{\mathrm{G}}(n, m)$ is the nth row of $\mathbf{L}_{\mathrm{G}}(m)$ introduced in eqn (7.9), and $\{\mathbf{Q}_{\mathrm{G}}(n, m, m')\}_{n', n''} = T_s q_{\mathrm{G}}(n, n', n'', m, m')$ from eqn (7.1). The state uncertainty sequences ψ_{EKF} are modeled in a manner akin to the KF; the details are omitted for brevity.

For the EKF, the output equations are also assumed to be quadratic. Then, the arguments in Remark 3, along with the time-separation discussed previously, yield the following model

$$\hat{p}_k^a(x_s, m) = \delta_{m,0} c_{\mathrm{EKF}}^a(s, N_c) + \sum_{n=1}^{N_m} l_{\mathrm{EKF}}^a(n, m, s, N_c)\hat{\alpha}_{k+N_c}^{(n)}(m)$$

$$+ \sum_{m'=m-M}^{M} \sum_{n'=1}^{N_{m'}} \sum_{n''=1}^{N_{m-m'}} q_{\mathrm{EKF}}^a(n', n'', m', m - m', s, N_c)\hat{\alpha}_{k+N_c}^{(n')}(m')\hat{\alpha}_{k+N_c}^{(n'')}(m - m')$$

$$+ \xi_{\mathrm{EKF},k}^a(m, x_s, N_c), \qquad (7.21\mathrm{a})$$

$$p_k^l(x_s) = c_{\mathrm{EKF}}^l(s, N_c) + \sum_{m'=-M}^{M} \sum_{n'=1}^{N_{m'}} l_{\mathrm{EKF}}^l(n', m', s, N_c)\hat{\alpha}_{k+N_c}^{(n')}(m')$$

$$+ \sum_{m',m''=-M}^{M} \sum_{n'=1}^{N_{m'}} \sum_{n''=1}^{N_{m''}} q_{\mathrm{EKF}}^l(n', n'', m', m'', s, N_c)\hat{\alpha}_{k+N_c}^{(n')}(m')\hat{\alpha}_{k+N_c}^{(n'')}(m'')$$

$$+ \xi_{\mathrm{EKF},k}^l(x_s, N_c). \qquad (7.21\mathrm{b})$$

The determination of the family of measurement uncertainty sequences ξ_{EKF}^a and ξ_{EKF}^l follows the developments for KF. The model in eqn (7.21a) can be seen as a special case of the model structure introduced in eqn (7.8); the procedure to determine its parameters using QSE is presented in Section 7.3.2. The model in eqn (7.21b) can also be analyzed in a similar manner to determine its parameters using QSE. All the parameters of both models are real from arguments in Remark 1.

Following the procedure used for KF, the above models can be reduced to the standard form in the real domain. Subsequent to this, the theory of EKF (Anderson and Moore, 2005) can be applied directly; the details are omitted.
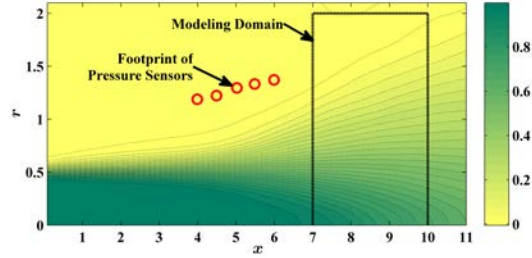
Figure 7.2: Contour plot of normalized mean axial velocity from DNS database in the background. Overlaid are the cross section of cylindrical modeling domain, and the footprints of pressure sensors (azimuthal array or linear array).

7.5   Results

The DNS database created by Freund (2001) has been discussed in Section 2.5. It was utilized extensively for validating the reduced-order modeling strategy in Chapter 5. It would again serve as the test-bench for validating and assessing the relative merits of the estimation strategies presented here. The main benefit of this well-established numerical database is the availability of time-resolved and space-resolved flow field data for the Mach 0.9 albeit low-Re jet. Figure 7.2 is reproduced from Figure 5.25 and depicts the modeling domain as well as the virtual sensor locations for performing the spectral linear stochastic estimation. These sensor locations will be re-used for real-time estimation for the reasons discussed in Section 5.9.4.

The temporal order of the snapshots was randomized before dividing them equally into two mutually exclusive sets. The various estimation models discussed in this chapter were built using the statistics computed from the first set (the *training set*). The fidelity of each estimation strategy was then tested using the second set (the *validation set*). While this division into training and validation datasets is ideal for stochastic estimation, the simulation of the IIR filters require the entire time-history of the output, so that the distinction is

250

not as well-defined. The IIR filter models were developed solely from the training set, but they were simulated using the time-resolved pressure from the entire database. Finally, the samples corresponding to the validation dataset were selected to evaluate the performance.

The reduced-order models discussed in Chapters 5 and 6 were always created by retaining the most energetic modes available for a given model dimension. The only model that will be discussed here is a 30-D model that retains the first 5 POD modes in each of the azimuthal modes from 0 to 5; i.e. $M = 5$ and $N_m = 5$ for all $m \in [0, M]$. This makes the coding of the estimation strategy much easier, and the energy captured is 33% instead of 34% that would be retained with optimal selection. The attempt in the following assays would be to estimate these 30 modes as well as possible.

To compare the overall performance of the various state estimators, the following modal estimation error metric is established

$$\eta(n, m, N_c) := \sqrt{\frac{E\left\{\left|\tilde{\hat{\alpha}}^{(n)}_{k+N_c/k}(m) - \hat{\alpha}^{(n)}_{k+N_c}(m)\right|^2\right\}}{\sqrt{E\left\{\left|\tilde{\hat{\alpha}}^{(n)}_{k+N_c/k}(m)\right|^2\right\} E\left\{\left|\hat{\alpha}^{(n)}_k(m)\right|^2\right\}}}}. \quad (7.22)$$

The metric implicitly depends on the choice of the pressure measurement configuration characterized by $\mathcal{X}^a_p$ and $\mathcal{X}^l_p$, as well as the estimation strategy. In fact, the particular estimation strategy is omitted from the subscript for generality. Moreover, the notation appears specific to infinite memory filters, but is also applicable to single-time stochastic estimators.

A value of η close to 0 indicates high fidelity. The metric will have a moderate value if the instantaneous estimation is not accurate, but the variance of the state $\hat{\alpha}$ is well-replicated by the estimate. On the other hand, η will become large whenever the variance of the estimate is significantly disparate from that of the state.

The above error metric differs from the ones considered for evaluating the performance of SLSE reconstruction in eqn (5.68), and of reduced-order model simulation in eqn (5.64). Those earlier metrics represented the ratio of the square of the norm of the field errors to that of the actual field. The numerator of the metric proposed in eqn (7.22) also represents the field error in estimation, but the error is with respect to the projected field, since the actual field is not the target for estimation. Also, the norm is used instead of the square of the norm. The main difference, however, is in the denominator, which is now the square root of the product of the norms of the projected field and its estimation.

The modification in the performance measuring approach was necessitated by the nature of errors encountered in estimation. In many cases, it will be seen that the LSE results in very small estimated energy. In this case, the earlier approaches would have yielded an error value close to 1. Other estimation strategies, e.g. the LTIF, typically predict the energy much more faithfully, which should be reflected in an improved performance measure. However, low correlations between the projected and estimated fields may still result in error values close to or exceeding 1. The metric proposed in eqn (7.22) accounts for both fidelity in energy prediction as well as correlation between the estimate and the projection.

A more concise but less informative metric is the following global estimation error metric

$$\breve{\eta}(N_c) := \sqrt{\frac{\sum\limits_{m=-M}^{M} \sum\limits_{n=1}^{N_m} E\left\{\left|\tilde{\hat{\alpha}}_{k+N_c/k}^{(n)}(m) - \hat{\alpha}_{k+N_c}^{(n)}(m)\right|^2\right\}}{\sqrt{\sum\limits_{m=-M}^{M} \sum\limits_{n=1}^{N_m} E\left\{\left|\tilde{\hat{\alpha}}_{k+N_c/k}^{(n)}(m)\right|^2\right\} \sum\limits_{m=-M}^{M} \sum\limits_{n=1}^{N_m} E\left\{\left|\hat{\alpha}_{k}^{(n)}(m)\right|^2\right\}}}}. \tag{7.23}$$

Owing to the orthonormality of the POD and azimuthal Fourier bases, the above metric actually represents the estimation error of the physical velocity field.
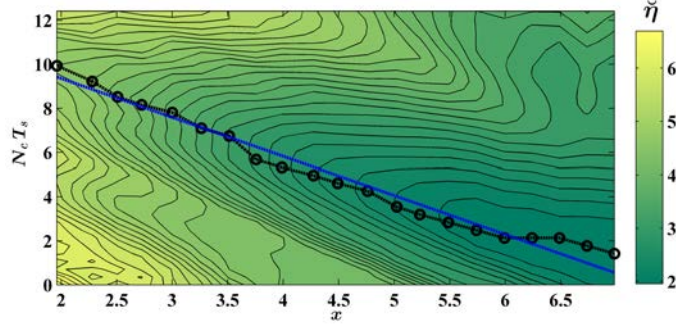
Figure 7.3: Estimation error using LSE for various axial locations of the sole azimuthal array of pressure sensors, and time-separations. The markers trace the bottom of the 'error valley', and the straight line is best-fit through them.

The convection inherent in the jet results in the pressure signal leading the POD modal coefficient by the time separation that is denoted herein by $N_c T_s$. Although the pressure measurement is localized, the POD modal coefficient is non-local. So N_c cannot be directly obtained from the convective velocity of the jet. The approach taken here uses LSE in conjunction with a single azimuthal ring array of sensors to determine the N_c that minimizes $\breve{\eta}$. Figure 7.3 shows that the curve tracing the bottom of the 'error valley' for each axial location is very well approximated by a line with slope -1.75 and x-intercept of 7.3. Due to the implicit normalizations, the negative reciprocal of the slope signifies the ratio of the convective velocity to the jet exit velocity, which is close to the value of 0.6 reported for the DNS database (Freund, 2001). The x-intercept signifies the apparent 'centroid' of the modeling domain (from $x = 7$ to 10), as represented by its POD basis. The pressure sensing configuration that is chosen for further investigation is centered on $x = 5$ (see Figure 7.2), for which the optimal N_c turns out to be 55. This corresponds to a lead of 3.9 flow time steps, and is used in all further analyses reported below unless otherwise mentioned. It is worth noting that in similar assays using QSE and LTIF, the same optimal N_c was found.
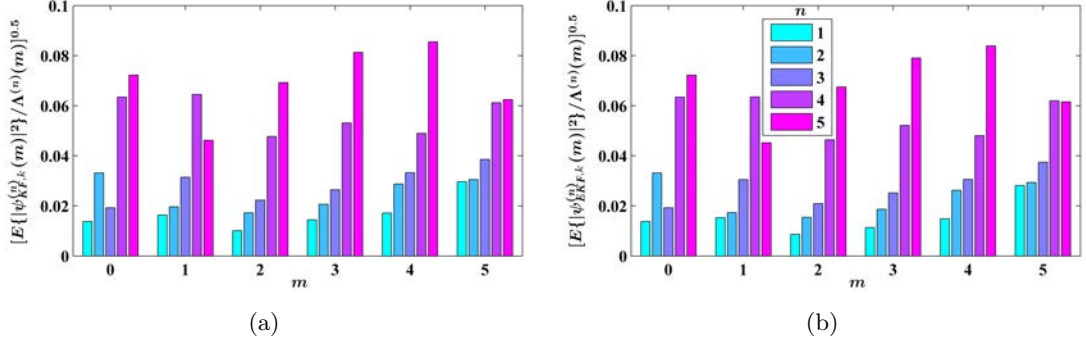
Figure 7.4: Normalized standard deviations of state uncertainty sequences for (a) KF, and (b) EKF.

The coefficients of the ROM presented in eqn (7.1) have been determined during the developments pursued in Chapter 5. Thus, the linear or quadratic state transition operators appearing in eqns (7.17a) and (7.20) can be computed. The DNS database is time-resolved so that realizations of the respective modeling uncertainty sequences $\breve{\psi}_{\mathrm{KF}}$ and $\breve{\psi}_{\mathrm{EKF}}$ are directly available. Then, using the white-noise assumption, the corresponding state uncertainty covariances $\breve{\Psi}_{\mathrm{KF}}$ and $\breve{\Psi}_{\mathrm{EKF}}$ can be ascertained empirically by ensemble-averaging. For this step, each snapshot k had to be paired with the corresponding $k+1$ snapshot; there were 575 such pairs in the training dataset, which was enough for convergence. It must be noted here that the requisite time-resolved empirical velocity database may be educed from experiments with the modeling strategy adopted in Chapter 5.

The diagonal terms of the covariance matrices are shown in Figure 7.4; the off-diagonal terms were found to be substantially smaller by comparison. It is interesting to note that although the quadratic terms are known to be crucial for the correct simulation of the ROM (Holmes et al., 1996), they do not have much effect on the modeling uncertainty.

(a) Azimuthal array of sensors at $x = 5$ (b) Linear array sensor at $x = 6$
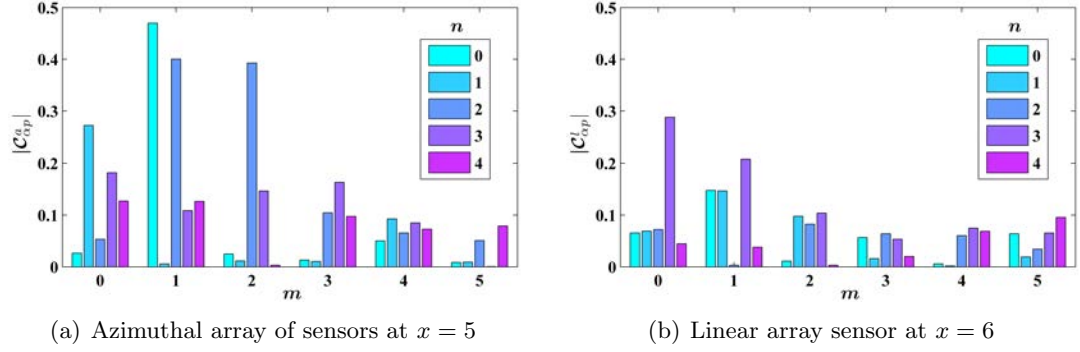
Figure 7.5: Representative normalized 2nd order correlations of POD modal coefficients with pressure.

The next focus is on the linear output relation for the Kalman filter appearing in eqn (7.11). Recall from eqn (7.14) that the model coefficients are to be determined by an application of LSE to the empirical data. This warrants a study of the following set of normalized cross-correlation coefficients

$$
\mathcal{C}_{\alpha p}^{a}(n, m, x, N_c) := \frac{E\left\{\hat{\alpha}_{k+N_c}^{(n)}(m)\hat{p}_k^{a*}(x, m)\right\}}{\sqrt{E\left\{\left|\hat{\alpha}_k^{(n)}(m)\right|^2\right\} E\left\{\left|\hat{p}_k^{a}(x, m)\right|^2\right\}}}, \tag{7.24a}
$$

$$
\mathcal{C}_{\alpha p}^{l}(n, m, x, N_c) := \frac{E\left\{\hat{\alpha}_{k+N_c}^{(n)}(m)p_k^{l}(x)\right\}}{\sqrt{E\left\{\left|\hat{\alpha}_k^{(n)}(m)\right|^2\right\} E\left\{\left|p_k^{l}(x)\right|^2\right\}}}. \tag{7.24b}
$$

The cross-correlation coefficients are real following Remark 1, and their mutual relationship has been established in eqn (7.7). The above statistics are also relevant to the direct LSE model in eqns (7.5) and (7.6), which are the dual of the KF output relations.

The convergence of the above statistics was assessed for the DNS database. In particular, the correlation coefficients were evaluated from the training dataset, as well as from the full database, and the differences were found to be insignificant. Figure 7.5 presents the absolute values of $\mathcal{C}_{\alpha p}^{a}$ and $\mathcal{C}_{\alpha p}^{l}$ for selected axial locations of the pressure sensors. This should be

255

analyzed from two perspectives. In determining the accuracy of the KF output relation, eqn (7.11a), for a particular $x - m$ combination, one is seeking a high correlation level for any n. Similarly, eqn (7.11b) will be accurate for a particular axial location if the correlation level is high for any $m - n$ combination. From this perspective, the linear output equations appear to be feasible. However, the ultimate goal is to estimate the model states from the pressure, so that one is seeking high correlation levels for all states. From this perspective, one can conclude that direct LSE would perform poorly if used with a single azimuthal ring array, although additional measurements from the linear array sensors should improve the accuracy of estimation. Since the KF uses an approximate knowledge of the dynamic coupling of the different states in addition to the static output relation, it may be expected to perform better even with the single ring array of sensors.

A similar study can be made of the third order moments involved in the direct QSE in eqn (7.8), as well as the QSE that determines the quadratic output equation for the EKF in eqn (7.21). The relevant normalized correlation coefficients are

$$
\mathcal{C}^a_{\alpha\alpha p}(n, n', m, m', x, N_c) := \frac{E\left\{\hat{\alpha}^{(n)}_{k+N_c}(m')\hat{\alpha}^{(n')}_{k+N_c}(m - m')\hat{p}^{a*}_k(x, m)\right\}}{\sqrt{E\left\{\left|\hat{\alpha}^{(n)}_k(m')\right|^2\right\} E\left\{\left|\hat{\alpha}^{(n')}_k(m - m')\right|^2\right\} E\left\{\left|\hat{p}^a_k(x, m)\right|^2\right\}}},
$$

$$(7.25a)$$

$$
\mathcal{C}^l_{\alpha\alpha p}(n, n', m, m', x, N_c) := \frac{E\left\{\hat{\alpha}^{(n)}_{k+N_c}(m)\hat{\alpha}^{(n')}_{k+N_c}(m')\hat{p}^l_k(x)\right\}}{\sqrt{E\left\{\left|\hat{\alpha}^{(n)}_k(m)\right|^2\right\} E\left\{\left|\hat{\alpha}^{(n')}_k(m')\right|^2\right\} E\left\{\left|\hat{p}^l_k(x)\right|^2\right\}}}.
$$

$$(7.25b)$$

These statistics are real following Remark 1.

Figure 7.6 presents the absolute values of some of the above 3rd order normalized cross-correlation coefficients. These are not insignificant compared to the second order moments shown in Figure 7.5. Thus, a quadratic model can be expected to be more accurate than a

(a) $n = 1, n' = 1$ with azimuthal array at $x = 5$ (b) $n = 1, n' = 1$ with single sensor at $x = 6$
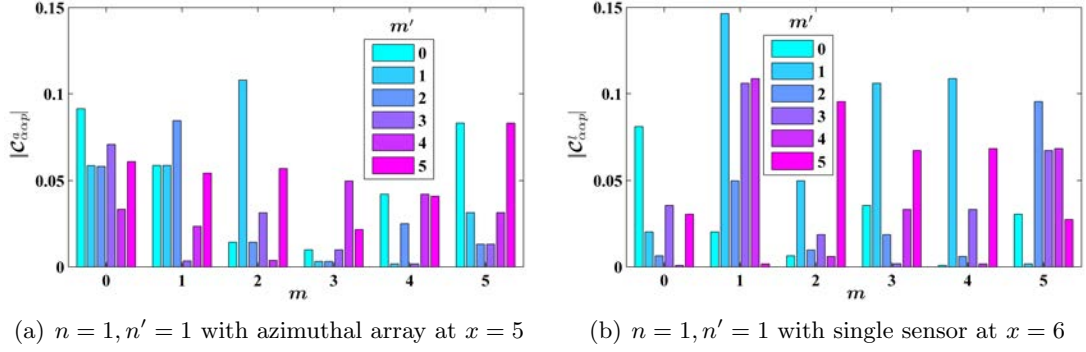
Figure 7.6: Representative normalized 3rd order correlations of POD modal coefficients with pressure.

linear one. It must be noted that these third order statistics were not well-converged, the consequences of which will be discussed further later.

The training dataset that was used to determine the coefficients of the output eqns (7.11) and (7.21) through stochastic estimation, was re-used to obtain a realization of the set of corresponding measurement uncertainty sequences ξ_{KF}^a, ξ_{KF}^l, ξ_{EKF}^a, and ξ_{EKF}^l. Then, with the white-noise assumption, the respective measurement uncertainty covariances $\breve{\Xi}_{\mathrm{KF}}$ and $\breve{\Xi}_{\mathrm{EKF}}$ were ascertained empirically by ensemble-averaging. As an aside, note that for converged statistics, the KF model affords the following simplifications

$$
\frac{E\left\{\left|\xi_{\mathrm{KF},k}^a(x, m, N_c)\right|^2\right\}}{E\left\{\left|\hat{p}_k^a(x, m)\right|^2\right\}} = 1 - \sum_{n=1}^{N_m} \left|\mathcal{C}_{\alpha p}^a(n, m, x, N_c)\right|^2,
$$

$$
\frac{E\left\{\left|\xi_{\mathrm{KF},k}^l(x, N_c)\right|^2\right\}}{E\left\{\left|p_k^l(x)\right|^2\right\}} = 1 - \sum_{m=-M}^{M} \sum_{n=1}^{N_m} \left|\mathcal{C}_{\alpha p}^l(n, m, x, N_c)\right|^2.
$$

This arises due to the least-squares formulation for determining the estimation parameters as well as the orthonormality of the POD and Fourier bases.
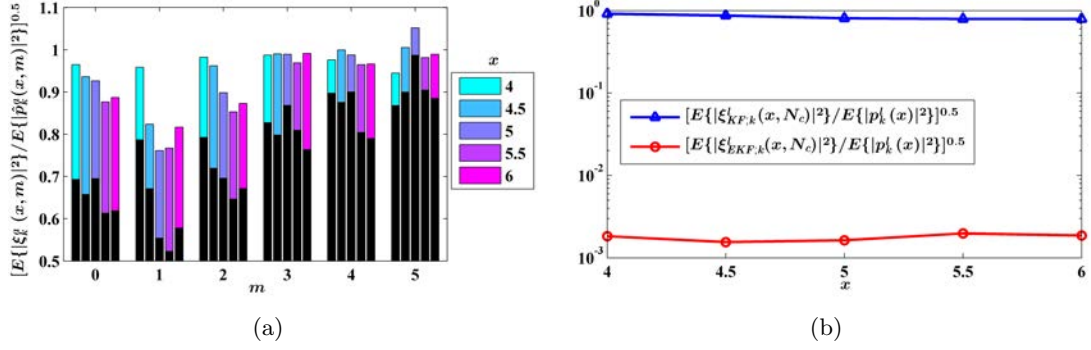
Figure 7.7: Normalized standard deviations of measurement uncertainties in KF and EKF models for pressure measured on (a) the azimuthal array, and (b) the linear array. In (a), the colored bars indicate the values for KF, whereas the overlaid black bars represent the corresponding values for EKF.

The diagonal terms of the covariance matrices are shown in Figure 7.7. Unlike the state uncertainty covariances presented in Figure 7.4, the measurement uncertainty covariances are substantially reduced in going from a linear expression to a quadratic one. In assessing these results, it must be borne in mind that the linear output equation for the azimuthal modal pressure measured on a ring array has 5 parameters to fit the empirical dataset of 1131 snapshots. On the other hand, the corresponding quadratic output equation has anywhere from 80 (for $m = 5$) to 146 (for $m = 0$) independent parameters. For the linear array measurements, the linear model has 30 degrees of freedom, whereas the quadratic model has 821. Thus, although the EKF is in principle more accurate than the KF, this profusion of model parameters for the EKF would make it prohibitively expensive for real-time implementation. The large number of model parameters also complicates their determination owing to poor convergence of the third order statistics involved. Recalling that the convective time-separation $N_c T_s$ was optimized for the azimuthal array of pressure sensors at

		Method				
No.	Configuration	LSE	QSE	KF	LTIF	EKF
1	$\mathcal{X}_p^a = \emptyset$, $\mathcal{X}_p^l = \{4, 4.5, 5, 5.5, 6\}$	2.52	1.81	1.34	—	1.42
2	$\mathcal{X}_p^a = \{5\}$, $\mathcal{X}_p^l = \emptyset$	2.26	1.88	1.38	1.38	1.43
3	$\mathcal{X}_p^a = \{5\}$, $\mathcal{X}_p^l = \{6\}$	2.16	1.64	1.35	1.35	1.50
4	$\mathcal{X}_p^a = \{5\}$, $\mathcal{X}_p^l = \{4.5, 5.5\}$	2.11	1.51	1.33	1.33	1.42
5	$\mathcal{X}_p^a = \{5\}$, $\mathcal{X}_p^l = \{4, 4.5, 5.5, 6\}$	2.03	1.32	1.32	1.32	1.37
6	$\mathcal{X}_p^a = \{6\}$, $\mathcal{X}_p^l = \{4, 4.5, 5, 5.5\}$	2.00	1.31	1.74	1.93	1.34
7	$\mathcal{X}_p^a = \{4, 4.5, 5, 5.5, 6\}$, $\mathcal{X}_p^l = \emptyset$	1.60	—	1.33	1.32	1.18

Table 7.1: The global estimation error for all strategies in several measurement configurations.

$x = 5$, it is noteworthy that the output uncertainties are not necessarily minimum at this location.

Recall that at each of the 5 axial locations considered herein, one could either place a ring array of pressure sensors or a single sensor that belongs to the linear array. All the 242 possible permutations and combinations of measurement configurations were analyzed with each of the estimation strategies presented herein. Table 7.1 presents the global estimation errors evaluated using the validation dataset for the most pertinent and interesting configurations. Based on these results, the following remarks are in order.

- First, the blanks in the table will be explained. In the case of QSE with 5 ring arrays, the covariance matrix of the 96-dimensional regressor for $m = 0$ was close to singularity so that the estimation parameters could not be determined reliably. This shows that the 5 ring arrays are unable to provide enough independent information. In the case of LTIF with 5 linear array sensors, the detectability criterion mentioned in Section 7.4.2 was not satisfied so that the discrete-time algebraic Riccati equation did not have a finite solution. Since the filter stability conditions are sufficient but

not necessary, it is not surprising that the KF still gave good results in this case. The filter stability criteria were satisfied in all configurations involving at least one ring array.

- With the above caveat, the performance of the LTIF is seen to be indistinguishable from that of the KF, as long as the ring array is placed at the axial location for which the convective time separation was optimized (i.e. $x = 5$). Later it will be shown that the equality of the error metric for KF and LTIF is not an artifact of averaging the error over a large number of realizations.

- The linear IIR filters display only a slight improvement when a linear array of sensors is included in the configuration, and the number of such sensors is seen to be inconsequential. This indicates that the use of the ROM is rendering the additional measurements somewhat redundant.

- To analyze the degradation of performance of the linear IIR filters in going from case #5 to #6, the convective time separation $N_c T_s$ was re-optimized for $x = 6$. The new value of $N_c = 33$ (see Figure 7.3), when used with configuration #6, yielded $\breve{\eta} = 1.31$ for both KF and LTIF, and $\breve{\eta} = 1.28$ for QSE.

- Linear IIR filtering matches or outperforms QSE while having substantially reduced real-time computational overhead.

- The worst performance in all configurations is found with LSE, while QSE represents a large improvement over LSE.

- The LSE and QSE continue to show significant performance improvements with increasing numbers of measurements.

- The EKF does not necessarily represent an improvement in performance over the KF. This is most likely a result of improper tuning of the uncertainty covariances resulting from the over-fitting of the training dataset, as mentioned before. It is also apparent in the inconsistent improvement of fidelity of the EKF with increasing measurement locations. However, the EKF also demonstrates the best performance in the table, viz. in the configuration with 5 ring arrays.

From the point of view of estimation accuracy and feasibility of implementation, the measurement configuration $\mathcal{X}_p^a = \{5\}$, $\mathcal{X}_p^l = \{4, 4.5, 5.5, 6\}$ is selected for further study based on the above discussion. To gain a more intuitive understanding of the behavior of the various estimators in this setup, the trajectories of two estimated states are shown in Figure 7.8. The following comments are based on these results.

- In Figure 5.8, the 1st POD modal coefficients for $m = 0$ and 1 were shown to have different peak-frequencies. This disparity is reflected well in Figure 7.8. On the other hand, all the azimuthal modes of pressure demonstrated similar spectral shape in Figure 5.26(b). This shape was replicated by the $m = 1, n = 1$ POD modal coefficient in Figure 5.8. In multi-point LSE performed in the physical domain, the estimated quantity, irrespective of its true spectrum, will have the same spectral shape as the measured quantity (Tinney et al., 2006). The same argument can be extended to multi-point LSE performed in a spatial Fourier domain when all the independent measurements have similar spectral shapes, as is the present case. This explains the frequency mismatch of the LSE trajectory for $m = 0$, when compared with the true trajectory. It also explains the matching of frequencies and consequent improved estimation in the $m = 1$ case. The state trajectories estimated by the linear IIR
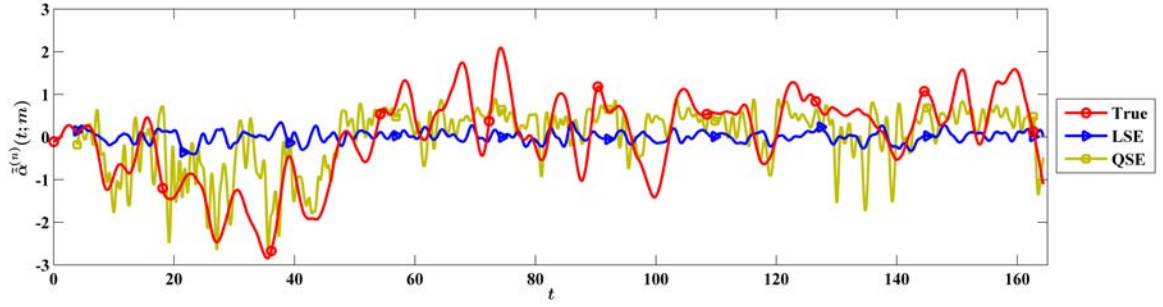
(a) SE's for $m = 0, n = 1$
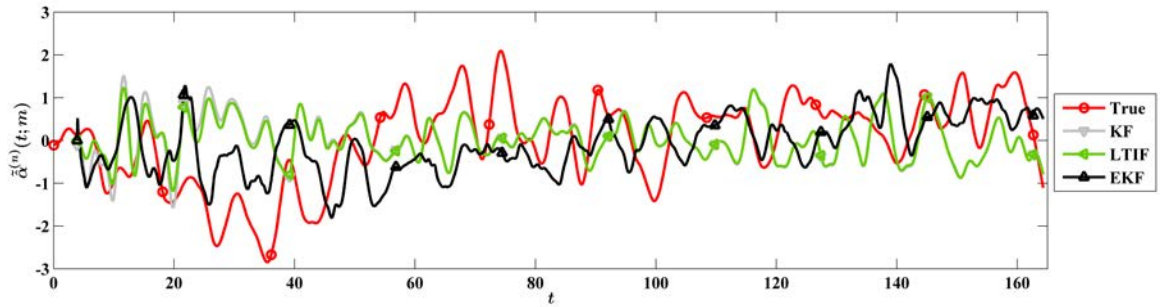
(b) IIR's for $m = 0, n = 1$
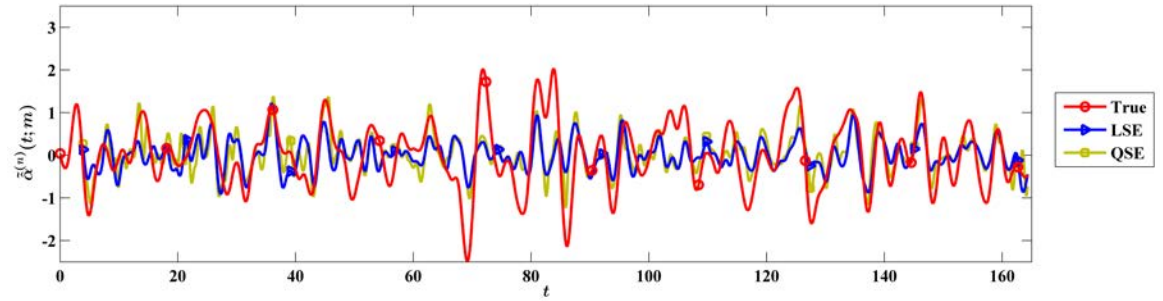
(c) SE's for $m = 1, n = 1$, real part
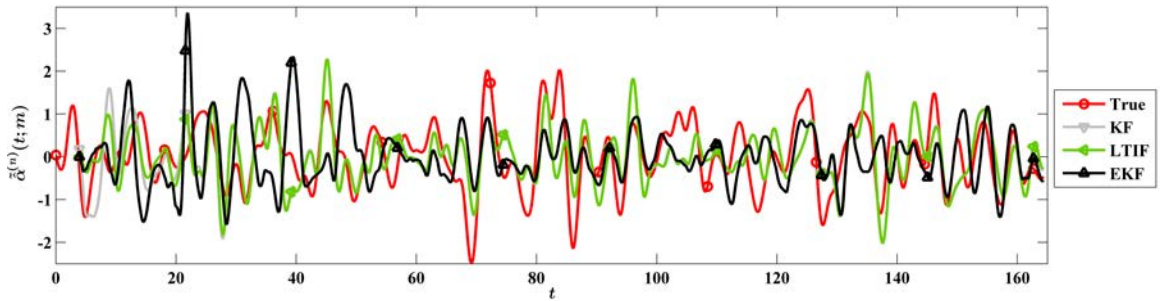
(d) IIR's for $m = 1, n = 1$, real part

Figure 7.8: Trajectories of selected states estimated with various strategies in the $\mathcal{X}_p^a = \{5\}$, $\mathcal{X}_p^l = \{4, 4.5, 5.5, 6\}$ configuration. Each state is normalized by its standard deviation.

filters have improved frequency matching for both modes owing to their reliance on the ROM, which approximately captures the true frequency content of the state.

- The KF gains were found to reach steady-state within ≈ 25 flow time steps, and this is borne out by the quick coalescence of the trajectories estimated with KF and LTIF. Moreover, one filter cannot be said to be more accurate than the other during the period that they produced different estimates.

- The fidelity of KF and EKF cannot be distinguished, in spite of the order-of-magnitude increase in computational complexity in the latter.

- The LSE essentially gives a null result for $m = 0$, which could have been anticipated from the low value of the corresponding correlation coefficient presented in Figure 7.5(a). The LTIF demonstrates superior fidelity while using the same correlation, since it additionally exploits the knowledge of the dynamic coupling of the states.

- Compared to LSE, use of QSE significantly improves the estimation performance in the instance of $m = 0$, with an attendant increase in computational cost. However, in the $m = 1$ case, QSE does not demonstrate any obvious improvement over LSE.

The foregoing discussion makes it apparent that the LTIF stands out from the other strategies in terms of estimation accuracy combined with feasibility of real-time implementation. To make this determination more conclusive, a final detailed comparison is made with QSE. The discussion based on Figure 7.8 gave some insight, but it was somewhat anecdotal since only two of the 30 states were considered. For quantitative analysis, the modal estimation error metric η defined in eqn (7.22) was evaluated using the validation dataset. The results are presented in Figure 7.9. Recalling the modal energy spectrum
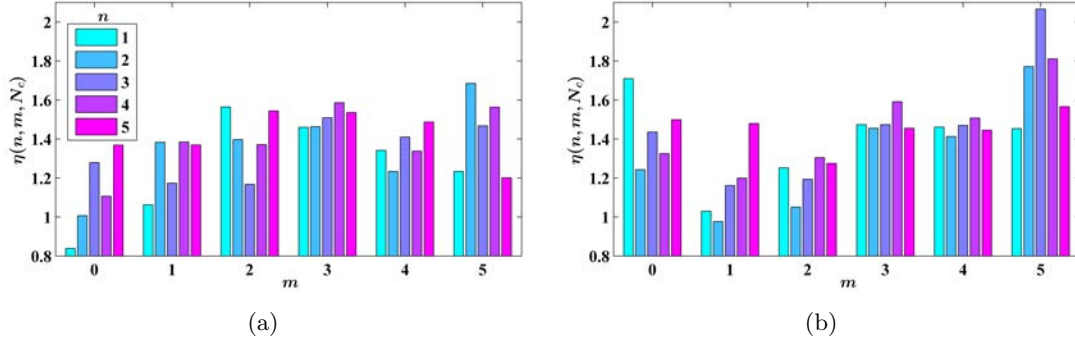
Figure 7.9: The modal estimation errors in the configuration $\mathcal{X}_p^a = \{5\}$, $\mathcal{X}_p^l = \{4, 4.5, 5.5, 6\}$ using (a) QSE, and (b) LTIF.

presented in Figure 5.8, it is observed that LTIF generally displays greater accuracy for the more energetic modes. The same cannot be said of QSE. However, the two strategies yield an overall similarity of error levels that could be anticipated from Table 7.1.

In the introduction, mention was made of multi-time SE as an intermediate between single-time SE and IIR filtering. So it is pertinent to query if multi-time LSE can be as effective as LTIF. Multi-time QSE need not be considered because single-time QSE itself poses real-time processing challenges. A multi-time LSE was implemented for the measurement configuration $\mathcal{X}_p^a = \{5\}$, $\mathcal{X}_p^l = \{4, 4.5, 5.5, 6\}$, with the same convective time-separation as before. It must be noted that owing to the moving window scheme, the training dataset was made up of the 1st half of the database and the validation dataset comprised of the 2nd half. It was found that a moving window stretching back in time by 25 samples yielded $\breve{\eta} = 1.62$, whereas the best result ($\breve{\eta} = 1.30$) was obtained with a window of 120 samples. The existence of an optimal window size has been demonstrated before (Durgesh and Naughton, 2010). Evidently, the memory requirements of any effective multi-time LSE strategy would render it infeasible for real-time estimation.

7.6   Conclusions

As in many engineering problems, real-time state estimation for feedback flow control poses an essential dilemma between simplicity and performance. Single-time linear and quadratic stochastic estimators have long been the preferred strategy due to their simplicity. At heart, these are essentially curve-fitting techniques that do not exploit any available knowledge of the flow dynamics. Multi-time stochastic estimators do incorporate some notion of the dynamics, but at the cost of increased memory overhead. A major shortcoming of stochastic estimators is that they pass measurement noise unfiltered to the state estimate. Moreover, some flow states may not have a direct static relation with the measured output, but may only be observable indirectly through coupled dynamics.

In some cases a linear time-invariant reduced-order model of the flow dynamics may be at hand. Then a linear time-invariant infinite-memory filter may yield an improved estimation with minimal increase in runtime complexity over the single-time linear stochastic estimator. The two shortcomings of stochastic estimators mentioned above may both be mitigated by this technique. The infinite memory of the filter is the result of a recursive update strategy for the state estimate that requires only the previous estimate to be actually held in memory. A time-invariant filter may suffer from large transients in state estimation error, which may be addressed by a linear time-varying Kalman filter. The latter is significantly more complex since the estimator feedback gains must be computed by matrix inversion at every time step. If a nonlinear dynamic model and/or measurement model is available, then an extended Kalman filter may be implemented. However, the increased amount of computation necessitated at every time step may overwhelm hardware capabilities in case of most high-speed flows of interest. Moreover, the increasing complexity may even lead to a degradation of fidelity if the filter is not tuned properly.

In this chapter, all the above estimation strategies were implemented and assessed using a well-established direct numerical simulation database of a high-speed low Reynolds number axisymmetric jet. The reduced-order model of the dynamics of the unforced jet has been developed in Chapter 5, and this is used in dynamic state estimation here. In closed-loop operation, the forcing effect is known a priori, and hence can be disregarded for assessing estimation strategies.

The pressure in the irrotational near-field has long been surmised to be an ideal measurement for estimating the state of the shear layer in real-time. For practical implementation, the pressure sensors should be close to the nozzle exit, upstream of the modeling domain. In the axisymmetric jet, it is meaningful to employ an azimuthal ring array of such sensors in a cross-sectional plane, or a linear array in meridional plane. In this chapter, various permutations and combinations of such arrays were located upstream of the end of the potential core.

An effective configuration was found with a ring array in the middle and two sensors on either side of it forming a uniform linear array over the above axial range. Compared to a single ring array, the above arrangement improved the estimation accuracy to a greater or lesser extent depending on the strategy used. The convective time-separation between the upstream measurement and the downstream velocity field to be estimated was addressed by making the estimator predictive; this is a significant benefit for feedback control. Another novel approach introduced in this article is to derive the measurement equation for the dynamic estimator using single-time stochastic estimation.

Single-time linear stochastic estimation was found to be quite unsuitable for the present application, since some states of the model are not linearly related to the pressure signal. Quadratic stochastic estimation yielded significant improvements in accuracy, bearing

testimony to the essential nonlinearity in the pressure-velocity coupling. The estimation accuracy of the linear time-invariant filter was indistinguishable from the linear time-varying Kalman filter. The former showed better or equivalent fidelity compared to the quadratic stochastic estimator, thereby demonstrating the distinct benefit to be accrued in moving to a dynamic model-based estimation strategy. It is to be emphasized that the linear time-invariant filter is similar in complexity to the linear stochastic estimator, and considerably less resource-intensive than the quadratic stochastic estimator. The extended Kalman filter is significantly more complicated, but it actually under-performed the linear filters, possibly owing to insufficient tuning.

Chapter 8

Conclusions and Future Work

Fluid flows are ubiquitous in most engineering systems so that even small improvements in terms of effectiveness, efficiency, quietness, etc., represent large gains of practical importance. Active control of flows constitutes one of the major endeavors of fluid engineers at present. Paralleling the development of the necessary actuators and characterization of their open-loop behavior, is the incorporation of the flow system in a feedback loop for robustness of practical operation. Localized arc filament plasma actuators have demonstrated significant potential in controlling high-speed and high Reynolds number jets in open-loop when deployed in an azimuthal array around the periphery of the nozzle lip. Instead of the more common amplitude manipulation approach, this actuation system only allows specification of the forcing frequency, pulse width, and the azimuthal Fourier mode of actuation. The present research develops the tools for implementing feedback for this flow control system. The particular jet considered here is a Mach 0.9 axisymmetric configuration with Reynolds number of 6.7×10^5 based on the nozzle exit diameter and conditions.

8.1 Discussion of Results

Accurate but non-intrusive sensing of the effect of forcing is a cornerstone of any feedback system. The high level of turbulence in the jet coupled with the low energy ratio of

the plasma actuators to the main flow make real-time sensing a challenge. Observing the pressure fluctuations in the near irrotational field has been proposed as a viable candidate (Tinney et al., 2008b). Thus the research here begins by performing a detailed characterization of the near-field pressure of the unforced jet, followed by an extensive open-loop forcing parameter sweep. The behavior of the near-field pressure fluctuations is found to parallel the observations in the far-field acoustics reported earlier for the plasma actuation (Samimy et al., 2007c). Forcing at frequencies near the jet column mode results in significant amplification of fluctuations in both fields. This has been associated with the generation of robust and organized large-scale structures in the jet shear layer that cause considerable enhancement of bulk mixing (Samimy et al., 2007b). Forcing at frequencies that are an order of magnitude higher leads to appreciable reduction in pressure fluctuations in the near-field that mirrors the noise mitigation observed in the far-field. The frequencies fall within the range that leads to maximum jet initial growth rate, thereby limiting significant dynamics of structures to a shorter region close to the nozzle exit (Samimy et al., 2010).

The preliminary feedback control system that was developed and implemented for the jet was model-free online optimization. Two gradient-free algorithms were adapted from the existing literature on offline optimization with significant modifications for use in a real-time feedback loop. The two different goals were either maximizing bulk mixing or minimizing far-field noise. Initiated from an arbitrary forcing frequency in a broad range, feedback control was able to optimize the frequency by sensing the intended extremization of the near-field pressure fluctuations. Since the jet dynamics were not incorporated in the feedback algorithm, the online optimization required a relatively long time, viz. $\sim 10^5$ flow time steps, corresponding to about 1 second for the laboratory jet under consideration.

The slowness of the model-free controllers motivated the exploration of reduced-order models of the jet dynamics that are required for designing dynamical feedback laws. Such models also afford an investigation into the essential physics of the flow system by simplifying the governing Navier-Stokes equations using empirical flow data. A cylindrical domain spanning the end of the potential core was isolated for dynamical modeling owing to its importance in both bulk mixing and far-field noise radiation. A proper orthogonal decomposition/Galerkin projection strategy was adopted to devise the model for the unforced jet from experimental data. One of the contributions of this research was to systematically exploit the symmetries of the flow and the governing equations for increasing the robustness of the model. Another demonstration was of the effectiveness of a simple eddy viscosity formulation proposed by Cazemier et al. (1998), to account for the effect of the neglected scales in the model without recourse to any tuning parameter. An additional novelty of this work was a demonstration of the applicability of this technique to experimental databases which have much lower information-content compared to numerical databases. For this part, the recent technique proposed by Tinney et al. (2008b) was adapted. This uses spectral linear stochastic estimation to reconstruct volumetric snapshots of the jet flow from time-resolved near-field pressure measurements coupled with pre-computed pressure-velocity correlations.

Prior to the application on experimental data, extensive validation was performed on existing numerical simulation databases of a low Reynolds number Mach 0.9 jet (Freund, 2001) and a high Reynolds number Mach 1.3 jet (Gaitonde, 2011). The purpose was to guide the modeling strategy as well as to identify the sources of modeling errors. A 44-dimensional model was developed from the direct numerical simulation database of the low Reynolds number Mach 0.9 jet and evaluated for fidelity with respect to the original database. The model demonstrated reliable predictions in the short term, which is essential

for feedback law design. The simulated trajectories also remained bounded up to 5000 flow time steps from initiation of simulation (which was the maximum tested). The statistics from such long-term simulations displayed acceptable similarity with those computed from the database directly. Subsequently, a 35-dimensional model was demonstrated to capture the most important dynamical aspects of the jet under experimental investigation. The short-term prediction accuracy was shown to be acceptable for the purpose of feedback control. The statistics from intermediate-term simulations also displayed good agreement with experimental observations. However, the simulated trajectories from the models were found to become unbounded beyond about 50 flow time steps from initiation of simulation.

The effect of periodic plasma actuation was subsequently incorporated into the reduced-order model. The proposed procedure was based on the observation of compression waves that are generated at every plasma actuation. Thus the forcing term modeled the periodic pressure fluctuations on the boundaries of the modeling domain. To obtain this pressure information for the experimental jet, use was made of an existing simple but effective vortex-based local static model of the pressure-velocity relationship in the jet (Lau et al., 1972), along with a numerical simulation database of the forced high Reynolds number Mach 1.3 jet, and the spectral linear stochastic estimation technique. The resulting model was able to predict quite reasonably the nonlinear response of the jet to forcing near the column mode. Phase-averaged velocity field from simulations with different forcing frequencies displayed the expected structure patterns. The modifications of the second-order statistics under forcing also demonstrated significant similarity with experimental observations. However, the sensitivity of the response was found to be sharper than expected.

It was discussed at the outset that the near-field pressure constitutes an appropriate measurement for real-time observation of the flow state. Various estimation strategies were

adapted and assessed using the direct numerical simulation database of the jet. The most common strategy in the flow control literature is stochastic estimation, which functions as a static filter. The reduced-order dynamical model developed above may be used to implement a dynamic filter which is not only more accurate but also more robust to noise. These attributes were indeed demonstrated for a linear time-invariant filter which is yet no more processor-intensive than a linear stochastic estimator.

8.2 Directions for the Future

One of the major questions left unanswered in the present work is the appropriate modeling strategy for the jet forced in the shear layer mode for noise mitigation. Actuation at the associated high Strouhal numbers results in lesser organization in the jet shear layer, which is thought to cause noise reduction. However, this lack of detectable large-scale structures also makes the reduced-order modeling more challenging. Potentially, many more modes must be retained to ensure all the dynamically-significant features have been accounted for. An attendant difficulty is the comparative ineffectiveness of the stochastic estimation that is used to approximate volumetric snapshots of the flow field from experimental data. This is because the underlying pressure-velocity correlations become weaker with forcing in this mode. A possible solution is to use numerical simulations of the jet forced in the vicinity of the shear layer mode to obtain the requisite empirical data, in which case the stochastic estimation step may be avoided. Such data is not at hand for the Mach 0.9 jet. However, for the Mach 1.3 jet, (Gaitonde, 2011) has performed implicit large-eddy simulations of the high Reynolds number jet forced over a large range of frequencies and azimuthal modes, which may be exploited.

The practical goal of jet control is either bulk mixing enhancement, or far-field noise mitigation in the context of this research. With the dynamical model in hand as derived in this work, one is first faced with the problem of specifying the performance objective in terms of the model states. Once this is addressed, a suitable feedback law must be designed.

Consider the case of noise mitigation. It has been shown by numerous researchers that the jet is a very inefficient generator of noise (e.g. Jordan and Gervais, 2008). While this is very beneficial in terms of noise pollution levels, it complicates the determination of an effective functional of the flow field to characterize the acoustics. Mere reduction of fluctuation intensity in the flow field is probably too coarse an objective. Some ideas are offered by the recent works of (Cavalieri et al., 2011; Papamoschou, 2011) which model the noise sources as wavepackets. Such an ansatz offers the possibility of real-time identification of the radiating part of the flow fluctuations, for subsequent control. A related idea proposed by Schlegel et al. (2009) is the most-observable-decomposition technique to model the dynamics of just those structures in the jet flow field that are relevant for noise production. However, this requires numerical simulation data linking the flow field to the far-field. In case these techniques remain infeasible for practical application, one can still resort to attempting a reduction of the fluctuations in the most energetic model states in real-time. The analogous formulation in control theory is the typical objective of stabilization of an equilibrium point or limit cycle. A sophisticated hierarchy of linear and nonlinear control techniques exist to address this problem. Of course, forcing cannot make the jet steady, but in striving for this goal, one can obtain reduction in the fluctuations. Similar strategies have been successfully implemented for reducing cavity tones (Samimy et al., 2007a; Caraballo et al., 2008), ameliorating optical path fluctuations in the flow over a turret (Seidel et al., 2010; Andino et al., 2011), delaying separation over a high-lift airfoil (Pinier et al., 2007),

etc. These prior applications employed amplitude-control actuators. The challenge in the case of plasma actuators is their sole reliance on frequency control.

Considering the goal of bulk mixing enhancement, an even more non-standard control objective is encountered in which one is trying to *increase* flow field fluctuations. It has been discussed that the requisite forcing around the jet column mode generates robust and organized large-scale structures. Their quasi-periodicity may be exploited to estimate the fluctuation amplitude at any instant from the instantaneous phase of the two modal coefficients that encode the traveling-wave behavior. Similar ideas have been employed in most of the publications cited in the previous paragraph which were aimed at reducing the flow oscillations. The performance objective in this application can be formulated as the real-time maximization of the amplitude of fluctuations. The typical feedback controllers are designed to force in anti-phase to the dominant oscillations in the system to diminish them. The goal of enhancing fluctuations may be theoretically achieved by simply switching the sign on the control signal determined from the standard algorithms. However, for plasma actuators, one again encounters the problem of lack of direct control on the forcing amplitude.

A recurring theme in the preceding paragraphs is the ultimate hurdle posed by the frequency-modulation control paradigm of the plasma actuators in both applications. Controller design techniques for such an actuator have not received much research attention in the flow control community. A related practical issue is the very high frequencies involved in the control applications under consideration, especially in a laboratory setting. For the 0.0254 mm diameter laboratory jet operated at Mach 0.9, bulk mixing is optimized around 3.5 kHz and noise reduction is maximum around 30 kHz. The dSpace 1103 DSP board used for rapid prototyping of control algorithms in the laboratory has a clock rate of 50 kHz.

This imposes a stringent constraint for practical control implementation and validation in experiments. Consequently, the two applications of bulk mixing enhancement and noise attenuation may require different strategies as discussed below. Note that in full-scale jets, the typical frequencies are much reduced in real terms, so that the above constraint may not be as severe.

The typical optimal forcing frequency for bulk mixing is an order-of-magnitude smaller than the achievable controller update rate. This implies that sub-forcing-period control may be possible for this application. That is, a typical forcing period may be resolved well enough by the controller so that the control signal can be manipulated within the same period. In this case, the feedback algorithm may be posed as a frequency modulation control problem (Gelig and Churilov, 1998). Then, one may attempt a phase-locking of the plasma actuators to the phase of the dominant oscillations as discussed above.

For noise attenuation in the laboratory-scale jet, the optimal frequency range is comparable to the dSpace clock rate, thereby precluding a sub-forcing-period control strategy for this application. Averaging theory (Chow and Mallet-Paret, 1977; Sanders et al., 2007) may be a promising approach in this situation. Averaging has been mostly used as a stability analysis tool once a control law has been chosen (Kasnakoğlu and Serrani, 2007; Almer and Jonsson, 2009). It is not quite clear as to its utility in the actual control *design* stage for a discontinuous system.

Bibliography

R. J. Adrian. On the role of conditional averages in turbulence theory. In *Turbulence in Liquids; Proc. 4th Biennal Symp. Missouri, USA (A77-40426 18-34), Princeton, NJ*, pages 323–332. Science Press, 1977.

R. J. Adrian. Conditional eddies in isotropic turbulence. *Physics of Fluids*, 22(11):2065–2070, 1979.

R. J. Adrian. Stochastic estimation of conditional structure: a review. *Applied Scientific Research*, 53:291–303, 1994.

R. J. Adrian and P. Moin. Stochastic estimation of organized turbulent structure: homogeneous shear flow. *Journal of Fluid Mechanics*, 190:531–559, 1988.

K. K. Ahuja and D. F. Blakney. Tone excited jets, Part IV: Acoustic measurements. *Journal of Sound and Vibration*, 102:93–117, 1985.

S. Ahuja and C. R. Rowley. Feedback control of unstable steady states of flow past a flat plate using reduced-order estimators. *Journal of Fluid Mechanics*, 645:447–478, 2010.

S. Almer and U. Jonsson. Harmonic analysis of pulse-width modulated systems. *Automatica*, 45:851–862, 2009.

B. D. O. Anderson and J. B. Moore. *Optimal Filtering.* Dover, New York, 2005.

J. D. Anderson. *Modern Compressible Flow: With Historical Perspective.* McGraw Hill, 3 edition, 2003.

M. Y. Andino, R. D. Wallace, M. N. Glauser, R. C. Camphouse, R. F. Schmit, and J. Myatt. Boundary feedback flow control: proportional control with potential application to aero-optics. *AIAA Journal*, 49(1):32–40, 2011.

A. C. Antoulas. *Approximation of large-scale dynamical systems.* Cambridge University Press, 2005.

K. B. Ariyur and M. Krstić. *Real time optimization by extremum seeking control.* Wiley Interscience, Hoboken, NJ, 2003.

R. E. A. Arndt, D. F. Long, and M. N. Glauser. The proper orthogonal decomposition of pressure fluctuations surrounding a turbulent jet. *Journal of Fluid Mechanics*, 340(1): 1–33, 1997.

N. Aubry, P. Holmes, J. L. Lumley, and E. Stone. The dynamics of coherent structures in the wall region of a turbulent boundary layer. *Journal of Fluid Mechanics*, 192:115–173, 1988.

W. Baars, C. E. Tinney, and E. J. Powers. POD based spectral higher-order stochastic estimation. In *48th AIAA Aerospace Sciences Meeting, AIAA Paper 2010-1292*, 2010.

C. T. H. Baker. *The numerical treatment of integral equations.* Clarendon, 1977.

M. F. Barone, I. Kalashnikova, D. J. Segalman, and H. K. Thornquist. Stable Galerkin reduced order models for linearized compressible flow. *Journal of Computational Physics*, 228:1932–1946, 2009.

R. R. Barton and J. S. Ivey. Nelder-mead simplex modifications for simulation optimization. *Management Science*, 42(7):954–973, 1996.

G. K. Batchelor. *An Introduction to Fluid Dynamics*. Cambridge University Press, 1967.

J.-F. Beaudoin, O. Cadot, J.-L. Aider, and J.-E. Wesfreid. Bluff-body drag reduction by extremum-seeking control. *Journal of Fluids and Structures*, 22(6-7):973–978, 2006.

D. W. Bechert and E. Pfizenmaier. On the amplification of broad band jet noise by a pure tone excitation. *Journal of Sound and Vibration*, 43(3):581–587, 1975.

R. Becker, R. King, R. Petz, and W. Nitsche. Adaptive closed-loop separation control on a high-lift configuration using extremum seeking. *AIAA Journal*, 45(6):1382–1392, 2007.

J. S. Bendat and A. G. Piersol. *Engineering Applications of Correlation and Spectral Analysis*. John Wiley, 3rd edition, 2000.

G. Berkooz, P. Holmes, and J. Lumley. The proper orthogonal decomposition in the analysis of turbulent flows. *Annual Review of Fluid Mechanics*, 25(1):539–575, 1993.

T. R. Bewley and S. Liu. Optimal and robust control and estimation of linear paths to transition. *Journal of Fluid Mechanics*, 365:305–349, 1998.

T. R. Bewley and B. Protas. Skin friction and pressure: the "footprints" of turbulence. *Physica D*, 196(1-2):28–44, 2004.

D. J. Bodony and S. K. Lele. On using large-eddy simulation for the prediction of noise from cold and heated turbulent jets. *Physics of Fluids*, 17:085103, 2005.

J.-P. Bonnet, D. R. Cole, J. Delville, M. N. Glauser, and L. S. Ukeiley. Stochastic estimation and proper orthogonal decomposition: Complementary techniques for identifying structure. *Experiments in Fluids*, 17(5):307–314, 1994.

J. Boree. Extended proper orthogonal decomposition: A tool to analyse correlated events in turbulent flows. *Experiments in Fluids*, 35(2):188–192, 2003. ISSN 07234864.

A. I. Borisenko and I. E. Tarapov. *Vector and tensor analysis with applications*. Dover Publication Inc., 1968.

R. Bourguet, M. Braza, and A. Dervieux. Reduced-order modeling of transonic flows around an airfoil submitted to small deformations. *Journal of Computational Physics*, 230:159–184, 2011.

G. L. Brown and A. Roshko. On density effects and large structure in turbulent mixing layers. *Journal of Fluid Mechanics*, 64(4):775–816, 1974.

R. C. Camphouse. Boundary feedback control using proper orthogonal decomposition models. *Journal of Guidance, Control, and Dynamics*, 28(5):931–938, 2005.

R. Camussi and G. Guj. Experimental analysis of intermittent coherent structures in the near field of a high Re turbulent jet flow. *Physics of Fluids*, 11(2):423–431, 1999.

E. Caraballo, M. Samimy, and J. DeBonis. Low dimensional modeling of flow for closed-loop flow control. In *41st AIAA Aerospace Sciences Meeting and Exhibit, AIAA Paper 2003-0059*, 2003.

E. Caraballo, J. Little, M. Debiasi, and M. Samimy. Development and implementation of an experimental-based reduced-order model for feedback control of subsonic cavity flows. *ASME Journal of Fluids Enginnering*, 129(7):813–824, 2007.

279

E. Caraballo, C. Kasnakoğlu, A. Serrani, and M. Samimy. Control input separation methods for reduced-order model-based feedback flow control. *AIAA Journal*, 46(9):2306–2322, 2008.

A. V. G. Cavalieri, G. Daviller, P. Comte, P. Jordan, G. Tadmor, and Y. Gervais. Using LES to explore sound-source mechanisms in jets. *Procedia Engineering*, 6:104–113, 2010.

A. V. G. Cavalieri, P. Jordan, A. Agarwal, and Y. Gervais. Jittering wave-packet models for subsonic jet noise. *Journal of Sound and Vibration*, 330(18-19):4474–4492, 2011.

W. Cazemier, R. W. C. P. Verstappen, and A. E. P. Veldman. Proper orthogonal decomposition and low-dimensional models for driven cavity flows. *Physics of Fluids*, 10(7): 1685–1699, 1998.

M. Chevalier, J. Hoepffner, T. R. Bewley, and D. S. Henningson. State estimation in wall-bounded flow systems. Part 2. Turbulent flows. *Journal of Fluid Mechanics*, 552:167–187, 2006.

S. N. Chow and J. Mallet-Paret. Integral averaging and bifurcation. *Journal of Differential Equations*, 26(1):112–159, 1977.

J. H. Citriniti and W. K. George. Reconstruction of the global velocity field in the axisymmetric mixing layer utilizing the proper orthogonal decomposition. *Journal of Fluid Mechanics*, 418:137–166, 2000.

J. Cohen and I. Wygnanski. The evolution of instabilities in the axisymmetric jet. Part 1. The linear growth of disturbances near the nozzle. *Journal of Fluid Mechanics*, 176(1): 191–219, 1987.

F. Coiffet, P. Jordan, J. Delville, Y. Gervais, and F. Ricaud. Coherent structures in subsonic jets: a quasi-irrotational source mechanism? *International Journal of Aeroacoustics*, 5 (1):67–89, 2006.

D. R. Cole, M. N. Glauser, and Y. G. Guezennec. An application of the stochastic estimation to the jet mixing layer. *Physics of Fluids*, 4(1):192–194, 1992.

S. S. Collis, R. D. Joslin, A. Seifert, and V. Theofilis. Issues in active flow control: theory, control, simulation, and experiment. *Prog. Aerosp. Sci.*, 40:237–289, 2004.

L. Cordier. Flow control and constrained optimization methods. In B. R. Noack, M. Morzynski, and G. Tadmor, editors, *Reduced-Order Modelling for Flow Control*, volume 528 of *CISM International Centre for Mechanical Sciences*. Springer, 2011.

T. C. Corke, F. Shakib, and H. M. Nagib. Mode selection and resonant phase locking in unstable axisymmetric jets. *Journal of Fluid Mechanics*, 223(1):253–311, 1991.

T. C. Corke, C. L. Enloe, and S. P. Wilkinson. Dielectric barrier discharge plasma actuators for flow control. *Annu. Rev. Fluid Mech.*, 42:505–529, 2010.

M. Couplet, P. Sagaut, and C. Basdevant. Intermodal energy transfers in a proper orthogonal decomposition-Galerkin representation of a turbulent separated flow. *Journal of Fluid Mechanics*, 491:275–284, 2003.

D. G. Crighton. Jet noise and the effects of jet forcing vol. 136, 1981, pp. 340-362. In J. Jiminez, editor, *The Role of Coherent Structures in Modeling Turbulence and Mixing*, volume 136 of *Lecture Notes in Physics*, pages 340–362. Springer, 1981.

S. Crow and F. Champagne. Orderly structure in jet turbulence. *Journal of Fluid Mechanics*, 48(3):547–591, 1971.

A. E. Deane, I. G. Kevrekidis, G. E. Karniadakis, and S. C. Orszag. Low-dimensional models for complex geometry flows: Application to grooved channels and circular cylinders. *Physics of Fluids A*, 3(10):2337–2354, 1991.

C. DeBoor. *A Practical Guide to Splines*. Springer-Verlag, New York, 1978.

A. Debussche, T. Dubois, and R. Temam. The nonlinear Galerkin method: A multiscale method applied to the simulation of homogeneous turbulent flows. *Theoretical and Computational Fluid Dynamics*, 7(4):279–315, 1995.

J. Delville, L. S. Ukeiley, L. Cordier, J.-P. Bonnet, and M. N. Glauser. Examination of large-scale structures in a turbulent plane mixing layer. Part 1. Proper orthogonal decomposition. *Journal of Fluid Mechanics*, 391(1):91–122, 1999.

J. E. Dennis and V. J. Torczon. Direct search methods on parallel machines. *SIAM J. Optim.*, 1(4):448–474, 1991.

V. Durgesh and J. W. Naughton. Multi-time-delay LSE-POD complementary approach applied to unsteady high-Reynolds-number near wake flow. *Experiments in Fluids*, 49(3): 571–583, 2010.

M. O. Efe and H. Ozbay. Low dimensional modelling and dirichlet boundary controller design for burger's equation. *Int. J. of Control*, 77(10):895–906, 2004.

M. O. Efe, M. Debiasi, P. Yan, H. Ozbay, and M. Samimy. Neural network-based modelling of subsonic cavity flows. *International Journal of Systems Science*, 39(2):105–117, 2008.

R. Everson, L. Sirovich, and K. R. Sreenivasan. Wavelet analysis of the turbulent jet. *Physics Letters A*, 145(6-7):314–322, 1990.

D. Ewing and J. H. Citriniti. Examination of a LSE/POD complementary technique using single and multi-time information in the axisymmetric shear layer. In J.N. Sorensen, E.J. Hopfinger, and N. Aubry, editors, *Proceedings of the IUTAM Symposium on simulation and identification of organized structures in flows, Lyngby, Denmark, 25-29 May 1997*, pages 375–384. Kluwer Academic Press, 1999.

V. Fleury, C. Bailly, E. Jondeau, M. Michard, and D. Juve. Spacetime correlations in two subsonic jets using dual particle image velocimetry measurements. *AIAA Journal*, 46 (10):2498–2509, 2008.

M. Fogleman, J. Lumley, D. Rempfer, and D. Haworth. Application of the proper orthogonal decomposition to datasets of internal combustion engine flows. *Journal of Turbulence*, 5 (23):1–18, 2004.

G. F. Franklin, J. D. Powell, and M. L. Workman. *Digital Control of Dynamic Systems*. Addison-Wesley, 1990.

J. B. Freund. Noise sources in a low-Reynolds-number turbulent jet at Mach 0.9. *Journal of Fluid Mechanics*, 438(1):277–305, 2001.

H. V. Fuchs. Space correlations of the fluctuating pressure in subsonic turbulent jets. *Journal of Sound and Vibration*, 23(1):77–99, 1972.

D. V. Gaitonde. Simulation-based analysis of the near field in a supersonic jet controlled by plasma actuators. In *49th AIAA Aerospace Sciences Meeting, AIAA Paper 2011-23*, 2011.

D. V. Gaitonde and M. Samimy. Coherent structures in plasma-actuator controlled supersonic jets: Axisymmetric and mixed azimuthal modes. Submitted to Physics of Fluids.

283

D. V. Gaitonde and M. Samimy. Effect of plasma-based azimuthal mode excitation on supersonic jet flow. In *5th AIAA Flow Control Conference, AIAA Paper 2010-4416*, 2010.

S. Gamard, W. K. George, D. Jung, and S. Woodward. Application of a slice proper orthogonal decomposition to the far field of an axisymmetric turbulent jet. *Physics of Fluids*, 14(7):2515–2522, 2002.

A. K. Gelig and A. N. Churilov. *Stability and oscillations of nonlinear pulse-modulated systems*. Birkhauser, Boston, 1998.

W. K. George. Insight into the dynamics of coherent structures from a proper orthogonal decomposition. In *Proc. Symp. on Near Wall Turbulence, Dubrovnik, Yugoslavia*, 1988.

W. K. George, P. D. Beuther, and R. E. A. Arndt. Pressure spectra in turbulent free shear flows. *Journal of Fluid Mechanics*, 148(1):155–191, 1984.

M. N. Glauser, S. J. Leib, and W. K. George. Coherent structures in the axisymmetric jet mixing layer. In *Proc. Fifth Int. Symp. Turbulent Shear Flows, Ithaca, USA*, 1985.

M. N. Glauser, X. Zheng, and C. R. Doering. The dynamics of organized structures in the axisymmetric jet mixing layer. In M. Lesieur and O. Metais, editors, *Turbulence and coherent structures*, pages 253–265. Kluwer, 1989.

X. Gloerfelt. Compressible proper orthogonal decomposition/Galerkin reduced-order model of self-sustained oscillations in a cavity. *Physics of Fluids*, 20:115105, 2008.

Y. G. Guezennec. Stochastic estimation of coherent structures in turbulent boundary layers. *Physics of Fluids*, 1(6):1054–1060, 1989.

E. J. Gutmark and C.-M. Ho. Preferred modes and the spreading rates of jets. *Physics of Fluids*, 26(10):2932–2938, 1983.

E. J. Gutmark, K. C. Schadow, and K. H. Yu. Mixing enhancement in supersonic free shear flows. *Annual Review of Fluid Mechanics*, 27(1):375–417, 1995. ISSN 00664189.

C. Hahn, M. Kearney-Fischer, and M. Samimy. Effects of ring groove and duty cycle on plasma actuator performance in high speed jets. In *49th AIAA Aerospace Sciences Meeting, AIAA Paper 2011-977*, 2011.

J. Hall, J. Pinier, A. M. Hall, and M. N. Glauser. Two-point correlations of the near and far-field pressure in a transonic jet. In *Proceedings of the Fluids Engineering Summer Meeting, Miami, Fl*, number FEDSM2006-98458. ASME, 2006.

J. W. Hall, A. M. Hall, J. T. Pinier, and M. N. Glauser. Cross-spectral analysis of the pressure in a Mach 0.85 turbulent jet. *AIAA Journal*, 47(1):54–59, 2009.

M. Harper-Bourne. On modelling the hydrodynamic field of high-speed jets. In *10th AIAA/CEAS Aeroacoustics Conference, AIAA Paper 2004-2830*, 2004.

N. Heinz, R King, F. Haucke, and W. Nitsche. Robust closed-loop control on a 2D-high-lift-device. *Int. J. of Flow Control*, 2(2):91–108, 2010.

L. Henning, M. Pastoor, B. R. Noack, R. King, and G. Tadmor. Feedback control applied to the bluff body wake. In R. King, editor, *Active Flow Control*, pages 369–390. Springer-Verlag, 2007.

J. Hoepffner, M. Chevalier, T. R. Bewley, and D. S. Henningson. State estimation in wall-bounded flow systems. Part 1. Perturbed laminar flows. *Journal of Fluid Mechanics*, 534: 263–294, 2005.

M. Hogberg, T. R. Bewley, and D. S. Henningson. Linear feedback control and estimation of transition in plane channel flow. *Journal of Fluid Mechanics*, 481:149175, 2003.

P. Holmes, J. Lumley, and G. Berkooz. *Turbulence, Coherent Structures, Dynamical Systems and Symmetry*. Cambridge University Press, New York, 1996.

R. Hooke and T. A. Jeeves. Direct search solution of numerical and statistical problems. *Journal of the Association of Computing Machinery*, 8:212–229, 1961.

A. K. M. F. Hussain and K. B. M. Q. Zaman. The 'preferred mode' of the axisymmetric jet. *Journal of Fluid Mechanics*, 110(1):39–71, 1981.

M. Ilak and C. R. Rowley. Modeling of transitional channel flow using balanced proper orthogonal decomposition. *Physics of Fluids*, 20:034103, 2008.

A. Iollo, S. Lanteri, and J.-A. Desideri. Stability properties of POD-Galerkin approximations for the compressible navierstokes equations. *Theoretical and Computational Fluid Dynamics*, 13(6):377–396, 2000.

M. O. Iqbal and F. O. Thomas. Coherent structure in a turbulent jet via a vector implementation of the proper orthogonal decomposition. *Journal of Fluid Mechanics*, 571: 281–326, 2007. ISSN 0022-1120.

A. H. Jazwinski. *Stochastic processes and filtering theory*. Academic Press, Inc., 1970.

P. Jordan and Y. Gervais. Subsonic jet aeroacoustics: associating experiment, modelling and simulation. *Experiments in Fluids*, 44(1):1–21, 2008.

P. Jordan, C. E. Tinney, J. Delville, F. Coiffet, M. N. Glauser, and A. M. Hall. Low-dimensional signatures of the sound production mechanisms in subsonic jets: Towards

their identification and control. In *35th AIAA Fluid Dynamics Conference and Exhibit, AIAA Paper 2005-4647*, 2005.

D. H. Jung, S. Gamard, and W. K. George. Downstream evolution of the most energetic modes in a turbulent axisymmetric jet at high Reynolds number. Part 1. The near-field region. *Journal of Fluid Mechanics*, 514:173–204, 2004.

R. E. Kalman. A new approach to linear filtering and prediction problems. *J. Basic Eng., Trans. ASME, Series D*, 82(1):35–45, 1960.

C. Kasnakoğlu and A. Serrani. Analysis and nonlinear control of Galerkin models using averaging and center manifold theory. In *American Control Conference*, 2007.

C. Kasnakoğlu, A. Serrani, and M. O. Efe. Control input separation by actuation mode expansion for flow control problems. *International Journal of Control*, 81(9):1475–1492, 2008.

J. Kastner. *Far-field Radiated Noise Mechanisms in High Reynolds Number and High-Speed Jets*. PhD thesis, The Ohio State University, 2007.

J. Kastner, M. Samimy, J. Hileman, and J. B. Freund. Comparison of noise mechanisms in high and low Reynolds number high-speed jets. *AIAA Journal*, 44(10):2251–2258, 2006.

J. Kastner, C. Harris, J. Mignee, and E. J. Gutmark. Linear stochastic estimation of the flowfield from a bypass ratio 8 nozzle configuration. In *47th AIAA Aerospace Sciences Meeting, AIAA Paper 2009-72*, 2009a.

J. Kastner, J.-H. Kim, and M. Samimy. A study of the correlation of large-scale structure dynamics and far-field radiated noise in an excited Mach 0.9 jet. *International Journal of Aeroacoustics*, 8(3):231–259, 2009b.

287

J. Kastner, D. Cuppoletti, B. Malla, and E. Gutmark. Simultaneous measurement of flow fluctuations and near-field pressure in a subsonic jet. In *48th AIAA Aerospace Sciences Meeting, AIAA Paper 2010-1217*, 2010.

M. Kearney-Fischer, J.-H. Kim, and M. Samimy. Control of a high Reynolds number Mach 0.9 heated jet using plasma actuators. *Physics of Fluids*, 21(9):095101, 2009.

M. Kearney-Fischer, J.-H. Kim, and M. Samimy. A study of mach wave radiation using active control. *Journal of Fluid Mechanics*, 681:261–292, 2011a.

M. Kearney-Fischer, J.-H. Kim, and M. Samimy. Noise control of a high Reynolds number high speed heated jet using plasma actuators. *International Journal of Aeroacoustics*, 10 (5-6):635–658, 2011b.

C. W. Kerechanin, M. Samimy, and J.-H. Kim. Effects of nozzle trailing edges on acoustic field of supersonic rectangular jet. *AIAA Journal*, 39(6):1065–1070, 2001.

H. Kesten. Accelerated stochastic approximation. *The Annals of Mathematical Statistics*, 29(1):41–59, 1958.

J. Kiefer and J. Wolfowitz. Stochastic estimation of the maximum of a regression function. *The Annals of Mathematical Statistics*, 23(3):462–466, 1952.

J. Kim and T. R. Bewley. A linear systems approach to flow control. *Annu. Rev. Fluid Mech.*, 39:383–417, 2007.

J.-H. Kim, J. Kastner, and M. Samimy. Active control of a high Reynolds number Mach 0.9 axisymmetric jet. *AIAA Journal*, 47(1):116–128, 2009a.

J.-H. Kim, M. Nishihara, I. Adamovich, M. Samimy, S. V. Gorbatov, and F. V. Pliavaka. Development of localized arc filament RF plasma actuators for high-speed and high Reynolds number flow control. *Experiments in Fluids*, 49:497–511, 2010.

K. Kim, C. Kasnakoğlu, A. Serrani, and M. Samimy. Extremum-seeking control of subsonic cavity flow. *AIAA Journal*, 47(1):195–205, 2009b.

E. Konstantinidis, S. Balabani, and M. Yianneskis. Conditional averaging of PIV plane wake data using a cross-correlation approach. *Experiments in Fluids*, 39:38–47, 2005.

J. C. Lagarias, J. A. Reeds, M. H. Wright, and P. E. Wright. Convergence properties of the Nelder-Mead simplex algorithm in low dimensions. *SIAM J. Optim.*, 9(1):112–147, 1998.

J. C. Lau and M. J. Fisher. The vortex-street structure of 'turbulent' jets. Part 1. *Journal of Fluid Mechanics*, 67(2):299–337, 1975.

J. C. Lau, M. J. Fisher, and H. V. Fuchs. The intrinsic structure of turbulent jets. *Journal of Sound and Vibration*, 22(4):379–406, 1972.

R. M. Lewis, V. J. Torczon, and M. W. Trosset. Direct search methods: then and now. *Journal of Computational and Applied Mathematics*, 124:191–207, 2000.

J. Little, K. Takashima, M. Nishihara, I. Adamovich, and M. Samimy. High lift airfoil leading edge separation control with nanosecond pulse driven DBD plasma actuators. In *5th AIAA Flow Control Conference, AIAA Paper 2010-4256*, 2010.

L. Ljung. *System Identification - Theory for the user*. Prentice Hall, 1999.

D. M. Luchtenburg, B. Gunther, B. R. Noack, R. King, and G. Tadmor. A generalized mean-field model of the natural and high-frequency actuated flow around a high-lift configuration. *Journal of Fluid Mechanics*, 623:283–316, 2009.

J. L. Lumley. The structure of inhomogeneous turbulent flows. In A. M. Yaglom and V. I. Tatarsky, editors, *Atm. Turb. and Radio Wave Prop.*, pages 166–178. Nauka, Moscow, 1967.

J. L. Lumley and A. Poje. Low-dimensional models for flows with density fluctuations. *Physics of Fluids*, 9(7):2023–2031, 1997.

Z. Ma, S. Ahuja, and C. W. Rowley. Reduced-order models for control of fluids using the eigensystem realization algorithm. *Theoretical and Computational Fluid Dynamics*, 25 (1-4):233–247, 2011.

M. Marion and R. Temam. Nonlinear Galerkin methods. *SIAM J. Numer. Anal.*, 2005(5): 1139–1157, 1989.

A. Michalke. On spatially growing instabilities in an inviscid shear layer. *Journal of Fluid Mechanics*, 23(3):521–544, 1965.

A. Michalke and H. V. Fuchs. On turbulence and noise of an axisymmetric shear flow. *Journal of Fluid Mechanics*, 70(1):179–205, 1975.

P. Moin and R. D. Moser. Characteristic-eddy decomposition of turbulence in a channel. *Journal of Fluid Mechanics*, 200:471–509, 1989.

C. J. Moore. The role of shear-layer instability waves in jet exhaust noise. *Journal of Fluid Mechanics*, 80(2):321–367, 1977.

N. E. Murray and L. S. Ukeiley. Estimation of the flowfield from surface pressure measurements in an open cavity. *AIAA Journal*, 41(5):969–972, 2003.

N. E. Murray and L. S. Ukeiley. Modified quadratic stochastic estimation of resonating subsonic cavity flow. *Journal of Turbulence*, 8(53):1–23, 2007.

A. M. Naguib, C. E. Wark, and O. Juckenhofel. Stochastic estimation and flow sources associated with surface pressure events in a turbulent boundary layer. *Physics of Fluids*, 13(9):2611–2626, 2001.

J. A. Nelder and R. Mead. A simplex method for function minimization. *The Computer Journal*, 7(4):308–313, 1965.

B. R. Noack, K. Afanasiev, M. Morzynski, G. Tadmor, and F. Thiele. A hierarchy of low-dimensional models for the transient and post-transient cylinder wake. *Journal of Fluid Mechanics*, 497:335–363, 2003.

B. R. Noack, P. Papas, and P. Monkewitz. The need for a pressure-term representation in empirical Galerkin models of incompressible shear flows. *Journal of Fluid Mechanics*, 523:339–365, 2005.

B. R. Noack, M. Schlegel, B. Ahlborn, G. Mutschke, M. Morzynski, P. Comte, and G. Tadmor. A finite time thermodynamics of unsteady fluid flows. *Journal of Non-equilibrium Thermodynamics*, 33:103–148, 2008.

B. R. Noack, M. Schlegel, M. Morzynski, and G. Tadmor. System reduction strategy for Galerkin models of fluid flows. *Int. J. Numer. Meth. Fluids*, 63:231–248, 2010.

A. V. Oppenheim and R. W. Schafer. *Discrete-Time Signal Processing*. Prentice-Hall, Englewood Cliffs, NJ, 1989.

D. Papamoschou. Wavepacket modeling of the jet noise source. In *17th AIAA/CEAS Aeroacoustics Conference, AIAA Paper 2011-2835*, 2011.

M. Pastoor, L. Henning, B. R. Noack, R. King, and G. Tadmor. Feedback shear layer control for bluff body drag reduction. *Journal of Fluid Mechanics*, 608:161–196, 2008.

L. Perret, E. Collin, and J. Delville. Polynomial identification of POD based low-order dynamical system. *Journal of Turbulence*, 7(17):1–15, 2006.

R. A. Petersen and M. M. Samet. On the preferred mode of jet instability. *Journal of Fluid Mechanics*, 194:153–173, 1988.

C. Picard and J. Delville. Pressure velocity coupling in a subsonic round jet. *International Journal of Heat and Fluid Flow*, 21(3):359–364, 2000.

J. T. Pinier, J. M. Ausseur, M. N. Glauser, and H. Higuchi. Proportional closed-loop feedback control of flow separation. *AIAA Journal*, 45(1):181–190, 2007.

M. Rajaee, S. K. F. Karlsson, and L. Sirovich. Low-dimensional description of free-shear-flow coherent structures and their dynamical behaviour. *Journal of Fluid Mechanics*, 258: 1–29, 1994.

D. Rempfer. On low-dimensional Galerkin models for fluid flow. *Theoretical and Computational Fluid Dynamics*, 14(2):75–88, 2000.

D. Rempfer and H. F. Fasel. Dynamics of three-dimensional coherent structures in a flat-plate boundary layer. *Journal of Fluid Mechanics*, 275:257–283, 1994.

C. Rethmel, J. Little, K. Takashima, A. Sinha, I. Adamovich, and M. Samimy. Flow separation control over an airfoil with nanosecond pulse driven DBD plasma actuators. In *49th AIAA Aerospace Sciences Meeting, AIAA Paper 2011-487*, 2011.

W. C. Reynolds and A. K. M. F. Hussain. The mechanics of an organized wave in turbulent shear flow. Part 3. Theoretical models and comparisons with experiments. *Journal of Fluid Mechanics*, 54(2):263–288, 1972.

H. Robbins and S. Monro. A stochastic approximation method. *Annals of Mathematical Statistics*, 22(3):400–407, 1951.

C. R. Rowley. *Modeling, Simulation, and Control of Cavity Flow Oscillations*. PhD thesis, California Institute of Technology, 2002.

C. R. Rowley. Model reduction for fluids, using balanced proper orthogonal decomposition. *Int. J. of Bifurcation and Chaos*, 15(3):997–1013, 2005.

C. R. Rowley and V. Juttijudata. Model-based control and estimation of cavity flow oscillations. In *44th IEEE Conference on Decision and Control*, 2005.

C. R. Rowley, T. Colonius, and R. M. Murray. Model reduction for compressible flows using POD and Galerkin projection. *Physica D*, 189:115–129, 2004.

C. R. Rowley, D. Williams, T. Colonius, D. R. Murray, and D. G. MacMynowski. Linear models for control of cavity flow oscillations. *Journal of Fluid Mechanics*, 547:317–330, 2006.

M. Samimy, I. Adamovich, B. Webb, J. Kastner, J. Hileman, S. Keshav, and P. Palm. Development and characterization of plasma actuators for high-speed jet control. *Experiments in Fluids*, 37(4):577–588, 2004.

M. Samimy, M. Debiasi, E. Caraballo, A. Serrani, X. Yuan, J. Little, and J. H. Myatt. Feedback control of subsonic cavity flows using reduced-order models. *Journal of Fluid Mechanics*, 579:315–346, 2007a.

M. Samimy, J.-H. Kim, J. Kastner, I. Adamovich, and Y. Utkin. Active control of high-speed and high-Reynolds-number jets using plasma actuators. *Journal of Fluid Mechanics*, 578: 305–330, 2007b.

M. Samimy, J.-H. Kim, J. Kastner, I. Adamovich, and Y. Utkin. Active control of a Mach 0.9 jet for noise mitigation using plasma actuators. *AIAA Journal*, 45(4):890–901, 2007c.

M. Samimy, J.-H. Kim, M. Kearney-Fischer, and A. Sinha. Acoustic and flow fields of an excited high Reynolds number axisymmetric supersonic jet. *Journal of Fluid Mechanics*, 656:507–529, 2010.

M. Samimy, M. Kearney-Fischer, J.-H. Kim, and A. Sinha. High speed and high Reynolds number jet control using arc filament plasma actuators for noise mitigation and for flow and noise diagnostics. In *49th AIAA Aerospace Sciences Meeting, AIAA Paper 2011-22*, 2011.

J. A. Sanders, F. Verhulst, and J. Murdock. *Averaging methods in nonlinear dynamical systems*, volume 59. Springer-Verlag, 2 edition, 2007.

S. Sanghi and N. Aubry. Mode interaction models for near-wall turbulence. *Journal of Fluid Mechanics*, 247:455–488, 1993.

M. Schlegel, B. R. Noack, P. Comte, D. Kolomenskiy, K. Schneider, M. Farge, D. Luchtenburg, J. Scouten, and G. Tadmor. Reduced-order modelling of turbulent jets for noise control. In C. et al. Brun, editor, *Numerical Simulation of Turbulent Flows and Noise Generation*, volume 104, pages 3–27. Springer, 2009.

H. Schlichting. *Boundary-Layer Theory*. McGraw Hill, 1968.

J. Seidel, S. Siegel, T. McLaughlin, and C. Fagley. Feedback flow control of a shear layer for aero-optic applications. In *48th AIAA Aerospace Sciences Meeting, AIAA Paper 2010-356*, 2010.

S. Siegel, J. Seidel, C. Fagley, D. M. Luchtenburg, K. Cohen, and T. McLaughlin. Low-dimensional modelling of a transient cylinder wake using double proper orthogonal decomposition. *Journal of Fluid Mechanics*, 610:1–42, 2008.

A. Sinha, K. Kim, J.-H. Kim, A. Serrani, and M. Samimy. Towards feedback control of high-speed and high-Reynolds number jets. In *4th AIAA Flow Control Conference, AIAA Paper 2008-3862*, 2008.

A. Sinha, K. Kim, J.-H. Kim, A. Serrani, and M. Samimy. Extremizing feedback control of a high-speed and high Reynolds number jet. *AIAA Journal*, 48(2):387–399, 2010a.

A. Sinha, A. Serrani, and M. Samimy. Initial development of reduced-order models for feedback control of axisymmetric jets. *International Journal of Flow Control*, 2(1):39–60, 2010b.

A. Sinha, A. Serrani, and M. Samimy. Development of empirical estimators for feedback control of axisymmetric jets. *Accepted for Publication in AIAA Journal*, 49(9), 2011.

L. Sirovich. Turbulence and the dynamics of coherent structures, Parts I-III. *Quarterly of Applied Mathematics*, XLV(3):561–590, 1987.

T. Suzuki and T. Colonius. Instability waves in a subsonic round jet detected using a near-field phased microphone array. *Journal of Fluid Mechanics*, 565:197–226, 2006.

G. Tadmor, O. Lehmann, B. R. Noack, and M. Morzynski. Mean field representation of the natural and actuated cylinder wake. *Physics of Fluids*, 22(3):034102, 2010.

G. Tadmor, O. Lehmann, B. R. Noack, L. Cordier, J. Delville, J.-P. Bonnet, and M. Morzynski. Reduced-order models for closed-loop wake control. *Proc. R. Soc. Lond. A*, 369: 1513–1524, 2011.

J. A. Taylor and M. N. Glauser. Towards practical flow sensing and control via POD and LSE based low-dimensional tools. *ASME Journal of Fluids Enginnering*, 126(3):337–345, 2004.

A. A. Tchieu, A. T. Kutay, J. A. Muse, A. J. Calise, and A. Leonard. Validation of a low-order model for closed-loop flow control enabled flight. In *4th AIAA Flow Control Conference, AIAA Paper 2008-3863*, 2008.

C. E. Tinney, F. Coiffet, J. Delville, A. M. Hall, P. Jordan, and M. N. Glauser. On spectral linear stochastic estimation. *Experiments in Fluids*, 41(5):763–775, 2006.

C. E. Tinney, P. Jordan, A. M. Hall, J. Delville, and M. N. Glauser. A time-resolved estimate of the turbulence and sound source mechanisms in a subsonic jet flow. *Journal of Turbulence*, 8(7):1–20, 2007.

C. E. Tinney, M. N. Glauser, and L. S. Ukeiley. Low-dimensional characteristics of a transonic jet. Part 1. Proper orthogonal decomposition. *Journal of Fluid Mechanics*, 612: 107–141, 2008a.

C. E. Tinney, L. S. Ukeiley, and M. N. Glauser. Low-dimensional characteristics of a transonic jet. Part 2. Estimate and far-field prediction. *Journal of Fluid Mechanics*, 615: 53–92, 2008b.

V. J. Torczon. *Multi-Directional Search: A direct search algorithm for parallel machines*. PhD thesis, Rice University, 1989.

V. J. Torczon. On the convergence of the multidirectional search algorithm. *SIAM J. Optim.*, 1(1):123–145, 1991.

V. J. Torczon. On the convergence of pattern search algorithms. *SIAM J. Optim.*, 7(1): 1–25, 1997.

T. C. Tung and R. J. Adrian. Higher-order estimates of conditional eddies in isotropic turbulence. *Physics of Fluids*, 23(7):1469–1470, 1980.

L. S. Ukeiley and M. K. Ponton. On the near field pressure of a transonic axisymmetric jet. *International Journal of Aeroacoustics*, 3(1):43–65, 2004.

L. S. Ukeiley, L. Cordier, R. Manceau, J. Delville, M. N. Glauser, and J.-P. Bonnet. Examination of large-scale structures in a turbulent plane mixing layer. Part 2. Dynamical systems model. *Journal of Fluid Mechanics*, 441:67–108, 2001.

Y. G. Utkin, S. Keshav, J.-H. Kim, J. Kastner, I. V. Adamovich, and M. Samimy. Development and use of localized arc filament plasma actuators for high-speed flow control. *Journal of Physics D: Applied Physics*, 40(3):685–694, 2007.

G. Vigo. The proper orthogonal decomposition applied to unsteady compressible Navier-Stokes equations. Technical Report 3385, INRIA Rapport de Recherche, 1998.

F. M. White. *Viscous fluid flow.* McGraw Hill, 2 edition, 1991.

O. Wiederhold, R. King, and B. R. Noack. Robust control in turbomachinery configurations. In R. King, editor, *Active Flow Control II*, pages 187–201. Springer Berlin / Heidelberg, 2010.

D. J. Wilde. *Optimum seeking methods.* Prentice Hall Inc., 1964.

K. B. M. Q. Zaman and A. K. M. F. Hussain. Turbulence suppression in free shear flows by controlled excitation. *Journal of Fluid Mechanics*, 103(1):133–159, 1981.

X. Zheng. *A low dimensional description of the axisymmetric jet mixing layer.* PhD thesis, Clarkson University, 1990.

X. Zheng and M. N. Glauser. A low dimensional description of the axisymmetric jet mixing layer. *ASME Computers in Engineering*, 2:121–127, 1990.